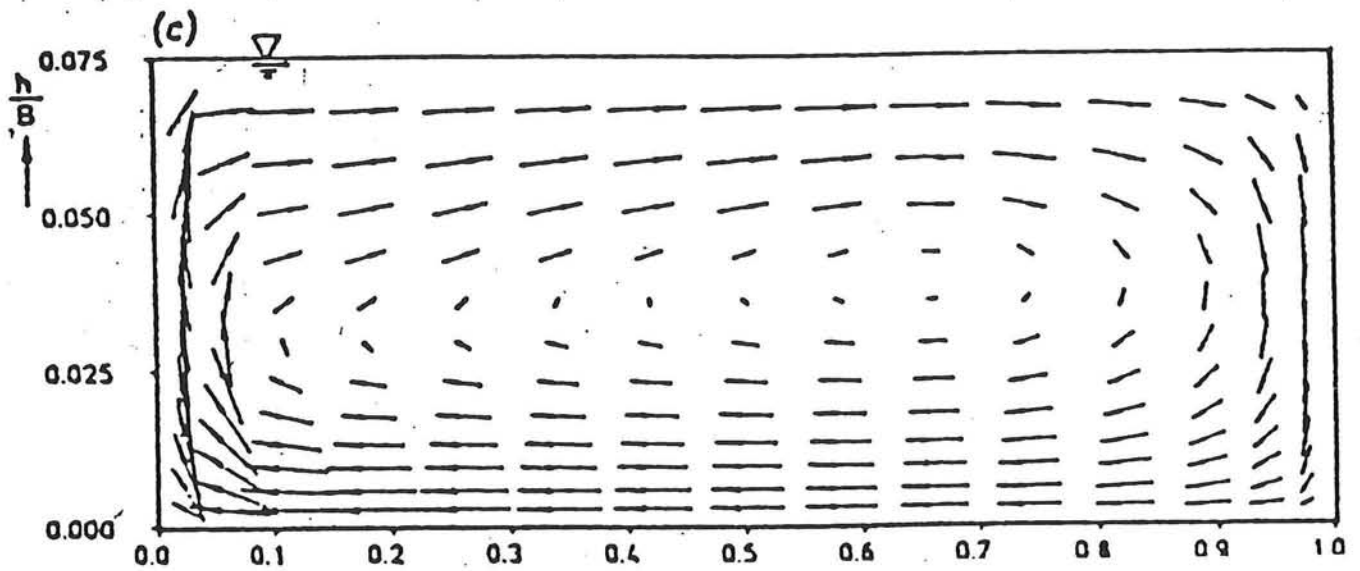


Three-dimensional modelling of secondary flow in river bends



Jan-Willem Jongbloed

Preface

This document is called the Masters Thesis. As such it serves as the graduation thesis, the final examination of the study of Fluid Mechanics, at the Faculty of Civil Engineering at Delft University of Technology in the Netherlands. The work which led to this thesis has partly been done at the Institute of Hydraulics at the University of Padua, Italy and partly at the Faculty of Civil engineering at Delft University of Technology in the Netherlands.

This project has been carried out under the supervision of prof. dr. ir. G.S. Stelling, prof. G. di Silvio, prof. dr. ir. J.A. Battjes, ir. R. Booij and dr. ir. Z.B.Wang.

Many people, in Padua as well as in Delft, have given me invaluable support, which was necessary to make my project a success. I want to thank all of them for the time and effort they have put into my project.

Jan-Willem E. Jongbloed

Delft, October 1996

Summary

The flow in a river bend has a large influence on the cross-sectional profile of the bend. Due to the curvature of the bend a secondary flow, which is perpendicular to the main flow, occurs. The secondary flow is directed outwards in the upper part of the cross-section and inwards in the lower part of the cross-section. It causes by means of the transverse transport of main flow momentum a redistribution of the main flow. This redistribution of the main flow and the sediment transport by the secondary flow cause a typical river bend profile, a steep sloping bank in correspondence with a large depth near the outer wall and a smoothly sloping bank in correspondence with a small depth near the inner wall. To be able to predict (the changes of) the profile and the position of a river bend one must understand the flow pattern and the related sediment transport. To account for the flow pattern several numerical simulation programs have been developed. Since, nowadays, it is impossible to calculate the flow exactly, due to the turbulence, it has to be modelled and some assumptions and approximations have to be made. At Delft Hydraulics a program package (Delft3D) has been developed to simulate these flow cases and their sediment transports.

In this thesis research has been done to what extent Trisula, the part that accounts for the prediction of the fluid movement, is capable of predicting the flow in river bends. At first a description of the flow pattern in river bends and a summary of the possibilities of the turbulence modelling are given as well as an abstract of the previous research, both numerically and experimentally, to gain insight in the phenomenon.

To verify Trisula an experiment in an 'infinite river bend' has been done at the University of Padua at the Institute of Hydraulics 'G Poleni'. Due to the sensitivity of the boundary conditions this experiment gave not satisfying results so the program had to be checked with other measurement. The measurements of De Vriend were used to verify the computational results of a strongly curved bend and the measurements of Booij were used to verify the computational results of a smoothly curved bend.

From the research to the simulation of the flow in river bends, it appeared that Trisula is able to predict the main features that occur in a river bend although the magnitude, especially of the radial velocities, is sometimes too small. The velocity distributions over the vertical and the development and decay of the secondary flow throughout a river bend are predicted rather well.

One of the most striking features is the impossibility of trisula to predict the counterrotating secondary flow near the outer wall at sufficiently large Dean numbers due to the incorrect modelling of the turbulence.

Preface	
Summary	
Contents	1
1. Introduction:	4
2. Secondary flow	5
2.1 Introduction	5
2.2 Mechanism of secondary flow	6
2.3 Velocity redistribution	7
2.4 Influence of the Dean number	8
2.5 Reverse secondary circulation	9
2.6 Mathematical description of the main flow and secondary circulation	10
3. Turbulence modelling	13
3.1 Introduction	13
3.2 Algebraic turbulence viscosity models	15
3.2.1 Constant eddy viscosity	15
3.2.2 Mixing-length hypothesis	15
3.2.3 Algebraic turbulence viscosity model of Trisula	16
3.3 Differential turbulence viscosity models	17
3.3.1 K-L models with a constant mixing length	17
3.3.2 K-L models with a differential expression for the mixing length	18
3.3.3 K- ϵ models	18
3.3.4 Reynolds stress models	20
3.4 Boundary conditions for the turbulent models	21
3.4.1 Wall boundaries	21
3.4.2 Free surface	22
3.4.3 Inlet	22
3.4.4 Outlet	22
3.4.5 Initial conditions	23
3.4.6 Grid	23
4. Previous research to flow in open channel bends	24
4.1 Experimental research	24
4.1.1 Longitudinal velocities	24
4.1.2 Secondary velocities	25
4.1.3 Counterrotating secondary flow	25
4.1.4 Sensitivity	26
4.1.5 Shear-stresses	26
4.2 Numerical research	27
4.3 Modelling of turbulence	30
5. Experimental study	31
5.1 Introduction	31

5.2 Requirements	32
5.3 Various solutions of the model	32
5.4 Experimental configuration	33
5.5 Instrumental equipment	36
5.6 Data discussion	36
5.6.1 Longitudinal velocities	36
5.6.2 Radial velocities	37
5.7 Conclusion of the experiment	37
6. Numerical research of river bend flows.	38
6.1 Introduction	38
6.2 Scope of the research	38
6.3 Comparison of the numerical results with experimental results	38
6.3.1 Configuration and input file of the strongly curved bend.	38
6.3.1.1 Grid.	39
6.3.1.2 Boundary conditions	39
6.3.1.3 Initial conditions.	39
6.3.1.4 Total calculation time and time step	39
6.3.1.5 Turbulence model.	40
6.3.1.6 Processes.	40
6.3.1.7 Output	40
6.4 Data discussion	40
6.5 Configuration and input file of the smoothly curved bend	41
6.6 Data discussion	42
6.7 Results of the numerical simulation of the flow in the strongly curved bend.	43
6.8 Sensitivity analysis	45
6.8.1 Strongly curved bend	45
6.8.1.1 Influence of the turbulence	46
6.8.1.2 Influence of the grid size in longitudinal direction.	48
6.8.1.3 Influence of the time step in the simulation	48
6.8.1.4 Influence of the radius of curvature	49
6.8.1.5 Influence of the inlet flow velocity	51
6.8.1.6 Influence of the cross-sectional profile	52
6.8.1.7 Influence of the Chézy coefficient	53
6.8.2 Smoothly curved bend	54
6.8.2.1 Influence of the turbulence models	54
6.8.2.2 Influence of the Chézy coefficient	55
6.8.2.3 Influence of the boundary condition (no-slip/partly -slip) at the side wall	56
7. Conclusions and recommendations	57
List of references	59
Appendices	
I K-ε model	

II	box dimensions
III	experimental data
IV	description of Trisula
V	description of the A.D.I. and numerical solution method of Trisula
VI	used grid and boundary conditions in the simulation
VII	used MD-file in the simulation
VIII	comparison of strongly curved bend with experimental data
IX	comparison of smoothly curved bend with experimental data
X	velocity distributions of the strongly curved bend throughout the bend
XI	influence of the used turbulence closure model in the simulation of the strongly curved bend
XII	influence of the grid size in the simulation of the strongly curved bend
XIII	influence of the time step in the simulation of the strongly curved bend
XIV	influence of the radius in the simulation of the bend
XV	influence of the inlet flow velocity in the simulation of the strongly curved bend
XVI	influence of the cross-sectional profile in the simulation of the strongly curved bend
XVII	influence of the Chézy coefficient in the simulation of the strongly curved bend
XVIII	influence of the used turbulence closure model in the simulation of the smoothly curved bend
XIX	influence of the Chézy coefficient in the simulation of the smoothly curved bend
XX	influence of the boundary condition at the side walls in the simulation of the smoothly curved bend

1. Introduction

Bends play an important role in a river like for example, for shipping, the problem of changing depth when passing from a straight reach to a bend or, especially important in urban areas, the tendency of moving outward. Therefore, it is sometimes desired to predict the behaviour of a bend; its future shape and position. To improve and control the situation structures may be needed. For proper predictions and a good design of the structures, if any, it is important to know the position and strengths of the peak shear-stresses at bends and how these parameters vary both with discharge and position around the bend. Longstream variations of the flow velocity, and therefore the shear-stress, can cause an imbalance between sediment input and output at a point, leading to erosion or deposition. This requires a good understanding of the entire flow and the related soil transport.

The flow in a river bend is a very complicated one. Due to the curvature of the bend a secondary flow occurs which rotates in the cross-sections perpendicular to the main flow direction, changing the distribution of the main flow and, by doing so, the cross-sectional shape. A different cross-sectional shape, in turn, influences the main flow distribution. This is a dynamical process that proceeds until a certain equilibrium is reached.

A lot of research has been done on the flow in river bends, mathematically as well as experimentally in laboratory flumes. At first the experiments were performed in flumes with a fixed configuration to measure the flow pattern. Later on a moveable bed was sometimes inserted to establish the soil transport.

Already in the early years numerical simulation programs existed which could calculate the flow. Since, compared to recent ones, computers were very slow, only one-dimensional programs were used. Later on two-dimensional programs were used and after these, the so-called two-and-a-half dimensional programs were used. Nowadays computers have become quicker and quicker, so it is possible to calculate the flow in a river bend in three dimensions within reasonable time. On the other hand when dealing with larger flow fields a fully three-dimensional numerical simulations will still require much calculation time, so if a less complicated model can give satisfying results these will be preferred. However, these numerical simulation programs have to be checked on their validity and functionality.

The scope of this study is to verify to what extent the numerical simulation program Trisula, which is based on the hydrostatic pressure assumption, is capable of simulating the flow in a river bend.

In the second chapter a description of the secondary flow and its influence on the main flow will be given to gain insight in the phenomenon. The third chapter describes the various features of the turbulence in these flows and the possibilities of modelling the turbulence. In chapter four the results of the previous research, experimentally as well as numerically, will be described. An experiment was done to simulate the secondary flow in an infinite river bend. This and the numerical simulation of this experiment will be described in chapter five. Chapter six deals with the simulation with Trisula of a river bend flow and the comparison with experimental results as well as a sensitivity analysis of the various parameters in such a flow case. In chapter seven the conclusions and recommendations will be given when simulating flows in river bends with Trisula.

2. Secondary flow

2.1 Introduction

Secondary flows are encountered in many engineering problems. In this section attention will be paid to the secondary flows in river bends.

The secondary flow in river bends is an important matter in river engineering not only for the flow itself, but especially for its effect on the main flow and therefore the bottom configuration. The effect on the main flow is a velocity redistribution which, depending on the main flow velocity and the curvature, decreases the velocities at the inner part of the cross-section and increases the velocities at the outer part of the cross-section [ref.5,17,18]. The secondary flow is directed outwards in the upper half and inwards in the lower half of the cross section (fig 2.1).

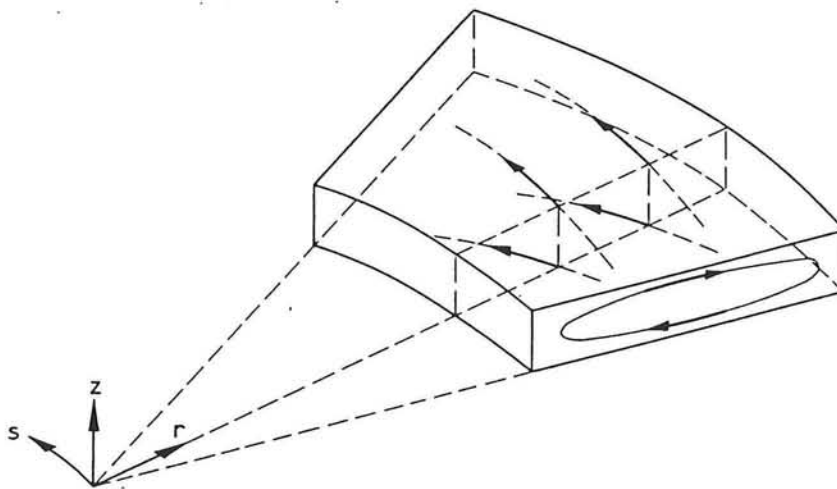


figure 2.1 (P.Ph. Janssen [ref 7])

The influence of the secondary flow on the cross-section is that it causes, by means of the redistribution of the main flow, a typical river bend cross-section which means a gently sloping sidewall at the inner part of the bend and a steep wall at the outer part of the bend. The outer part, due to the local scour because of the larger velocities and the inwards directed sediment transport due to the secondary flow, is relatively deep. On the contrary in the inner part the depth is small compared to the outer part [ref. 2]. It has been tried by several researchers to simplify the mathematical description of this complex flow [ref. 1,17,18]. This need of simplification is felt in river engineering, for instance, where the mathematical predictions of flow and bed topography in alluvial river bends requires multiple repeated flow computations with continually changing bottom configurations, so that a fully exact three-dimensional flow model would become too expensive.

In river bends the Reynolds numbers ($Re=UD/\nu$ where U is the flow velocity, D the depth of flow and ν the kinematic viscosity) are so large that a turbulent flow occurs. This seems to make the analysis of this problem more difficult but since for these flows the turbulent motion and the laminar motion are comparable the analysis was often made for laminar motion [ref.17,18]. Since the secondary flow and the velocity redistribution in laminar and turbulent curved flows are qualitatively the same it can also be applied to the latter. This can be explained by considering the following:

- in many turbulent flows the net convective exchange of momentum due to the velocity fluctuations can be modeled on the analogy of the molecular diffusion (Boussinesq hypothesis).
- the turbulent viscosity, though varying over the flow field, qualitatively corresponds with the molecular viscosity.
- both laminar and turbulent flows show the same helical flow pattern caused by the same mechanism [ref.17,18].

2.2 Mechanism of secondary flow

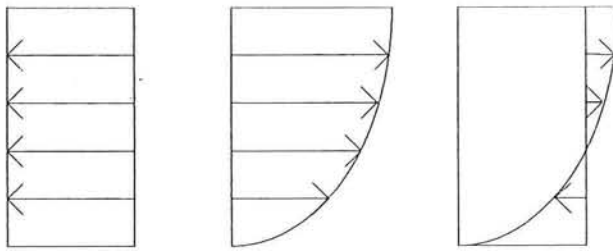
Here a cross-section with steeply sloping banks will be considered. In channels with mildly sloping banks the influence of the banks are less important. In the last case the transverse variations of the main velocity and the secondary flow are mainly due to the transverse variation of the flow depth when not too strongly curved bends are considered.

When a river passes through a bend there appear, due to the curvature of the bend, centrifugal accelerations which act on the liquid particles. Due to these centrifugal accelerations the liquid particles tend to move towards the outer wall. Therefore the water level becomes higher in the outer wall region and lower in the inner wall region. The slope of the free surface gives rise to a non-uniform pressure distribution in the cross-sections. The pressure increases towards the outer wall. Since the vertical accelerations are only small compared to the gravitational acceleration an approximately hydrostatic pressure distribution over the vertical is found. Therefore, the pressure gradient in the radial direction is approximately equal over the vertical. The centripetal accelerations would have counterbalanced completely the centrifugal accelerations were the longitudinal velocities determining their magnitude ($a_{\text{centrifugal}} \sim u^2$) equal at all points on the vertical. The non-uniform distribution of the longitudinal velocities is caused by the viscosity forces, which, in turn cause a non-uniform distribution of the centrifugal accelerations over the section; the flow velocities are largest near the free surface and therefore the centrifugal accelerations are largest near the free surface and decrease towards the bottom. An equilibrium in the separate points in a vertical does not occur (fig 2.2) which gives rise to a helical motion perpendicular to the main flow. This motion is directed according to the centrifugal accelerations, being larger, towards the outer wall in the upper part of the cross-section. In the lower part of the cross-section the motion is directed towards the inner wall since the centrifugal accelerations are smaller than the centripetal accelerations. A steady circulation will be established in the stream when the forces acting on the liquid particles are counterbalanced by the turbulent and viscous forces. With no viscosity and turbulence, but under the condition of decreasing longitudinal velocities with depth, the increase of the transverse velocities would be indefinite. Actually, in parallel with an increase of this velocity the viscous forces (turbulent and molecular) would also increase until an equilibrium is reached between these forces and the tangential accelerations caused by a non-uniform distribution of the centrifugal accelerations.

At the entrance and at the exit of a bend another motion occurs. At the entrance of a bend the slope of the free surface has to be built up and therefore the pressure gradient is negative in the inner wall region and positive in the outer wall region. Hence at the entrance of the bend, the motion is directed towards the inner wall in the entire cross-section resulting in a net flow towards the inner wall. Gradually this motion changes into a helical motion. Experiments [ref. 1] show that the establishment of a steady

velocity field at channel bends is asymptotic. The opposite is found at the exit of the bend where the pressure gradient is positive in the inner wall region and negative in the outer wall region since the slope of the free surface decreases and becomes zero at the straight reach downstream of the bend. An outward directed motion is found resulting in a net flow towards the outer wall.

After flowing through the bend, the stream reaches a new straight stretch where the energy of the transverse circulation is gradually dissipated under the action of the viscosity. When the transverse circulation is completely damped, the streamlines are restored to their original shape.



1. Influence of the centripetal accelerations 2. Influence of the centrifugal accelerations result of the superposition of curve 1 and 2

figure 2.2

Also other forces act on the liquid particles like the coriolis force and wind forces. The coriolis force is compared to the before-mentioned forces negligible if the width of the channel is not too large; coriolis forces only play a significant role if the width is several kilometers or more. These forces will be left out of the discussion because they only make the problem more complicated and do not give more insight in this phenomenon.

2.3 Velocity redistribution

The results of a secondary flow are that a considerable redistribution of the main velocity takes place.

Due to the secondary flow liquid particles near the free surface are transported towards the outer wall. These liquid particles contain larger velocities and momentum compared to the ones near the outer wall. This implies that everywhere in this region the fluid conveyed to a point by the secondary flow has a longitudinal momentum surplus with respect to the undisturbed flow in that point. The result is that the velocity in the outer wall region increases. Near the bottom the opposite occurs; liquid particles containing smaller velocities and momentum compared to the ones in the inner wall region are transported towards the inner wall reducing the velocity near the inner wall. Near the side walls the vertical convective transport of main flow momentum is important whereas in the central part of the cross-section the vertical transport is negligible. The vertical convection is the main cause of the velocity reduction in the inner wall region and the velocity increase in the outer wall region, whereas radial convection provides for an outward lateral interaction.

This effect of the secondary flow on the main flow can better be explained considering a figure with the streamlines of the secondary flow and the isovels of the main velocity (figure 2.3) [ref. 17]. From this figure it can be seen that near the bottom the differences of the velocities along the streamlines of the secondary flow are not large. At the inner wall these differences are larger and near the surface the streamlines are almost perpendicular to the isovels. The effect of the secondary flow depends on the distance between the isovels (the local main velocity gradient), the strength of the secondary flow and the sine of the angle of intersection between the main flow isovels and the streamlines of the secondary flow. In the wall region the velocity gradient is of the same order of magnitude throughout the vertical, so that the effect of the secondary flow will be relatively stronger in the upper part of the vertical. Consequently the shape of the main velocity profile becomes flatter near the surface.

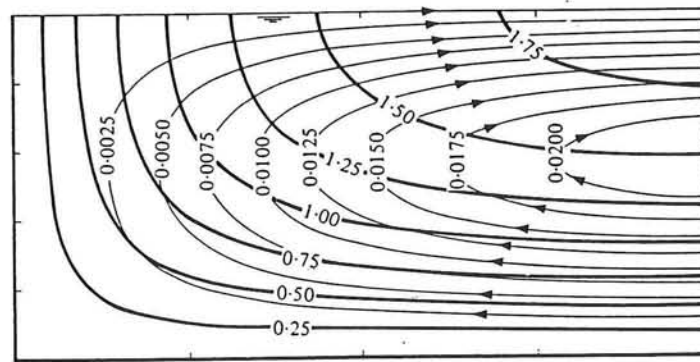


FIGURE 5. Main-flow isovels (—) and secondary-flow streamlines (—→) in the inner wall region of a shallow channel ($d/B = 0.1$).

figure 2.3 Secondary flow streamlines and isovels of main velocity (De Vriend [ref.17])

Experimental research confirms this explanation. At the entrance of a bend and in the early part of the inner wall region, the longitudinal velocity component increases accompanied by a steep fall of the free surface and the maximum velocity is found at the free surface at this position in the cross-section [ref. 4]. Later on due to the redistribution of the main velocity the maximum velocity shifts outward and at the end of a 180° curved bend the maximum velocity is found in the outer part of the cross-section [ref. 5,6,17,18]. In the outer wall region at the entrance of a bend the opposite is found. The longitudinal velocities decrease due to a positive pressure gradient.

2.4 Importance of the Dean number

If the Dean number, which is defined as $De = Re \sqrt{\delta}$ where $\delta = d/R_c$ and d is the mean depth and R_c is the radius of the channel axis [ref. 17], is small the influence of the redistribution is only observed close to the side walls. For $Dean=0$ the potential flow is approached [ref. 17]. The influence of the secondary flow on the main flow is a perturbation of the undisturbed main velocity distribution near the side walls. Increasing the Dean number the velocity is redistributed more and more in the entire

cross-section; the perturbations grow stronger and the lateral interaction grows more and more important, until the influence of the convection is felt throughout the entire cross-section.

The position of the velocity maximum depends on the Dean number and the position in the bend. In fully developed steady flow the velocity maximum moves towards the outer wall as Dean increases and for high Dean numbers it even lies below the surface (figure 2.4). Another interesting phenomenon is the movement of the center of circulation of the secondary flow. With increasing Dean number it moves downward and outward until $De \approx 25$ then the outward moving tendency is compensated by an inward one [ref 18].

The secondary flow increases, especially for intermediate and high Dean numbers, the overall boundary shear stress. This effect is often indicated as 'bend-resistance' [ref. 17].

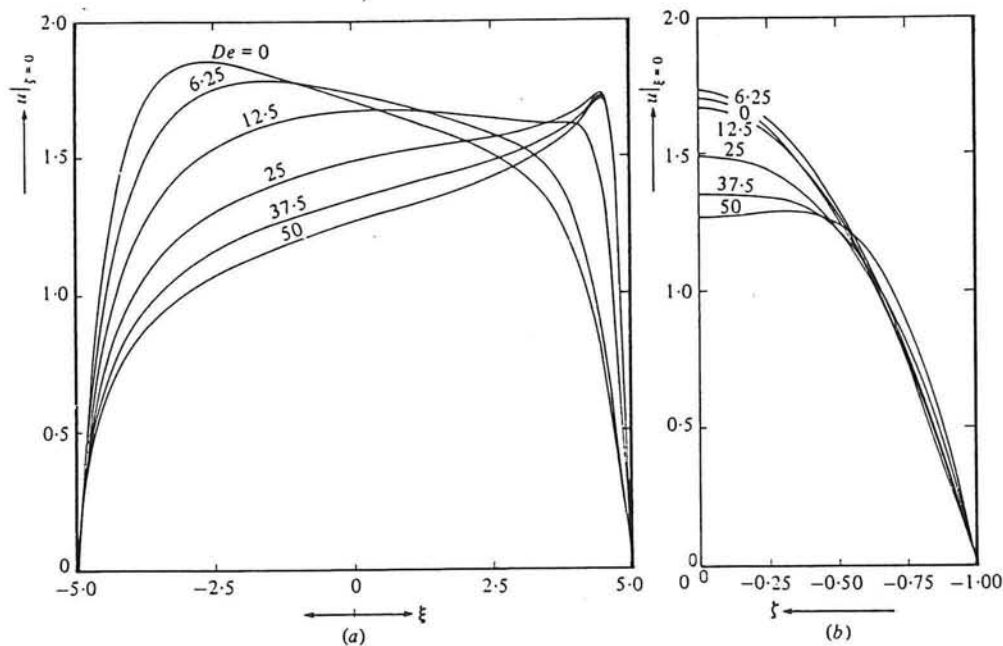


figure 2.4 Influence of the Dean number on the main velocity distribution (DeVriend [17])

For intermediate and high Dean numbers a velocity peak is observed in the outer wall region. This velocity peak is partly damped by the viscous forces. This is due to the outward extension of the low velocity region near the inner wall until it covers the greater part of the cross-section and the region influenced by the local velocity increase near the outer wall is compressed against the wall [ref. 18].

2.5 Reverse secondary circulation

At large Dean numbers, $Dean > \pm 50$, a reverse secondary circulation occurs (The Dean number in turbulent flows is calculated using the effective Reynolds number that means using the turbulent viscosity instead of the molecular viscosity). According to Engelund this effective Reynolds number can be estimated by:

$$Re_0 = 13 \frac{c}{\sqrt{g}} \quad (2.1)$$

where c is the Chezy-coefficient and g the gravitational acceleration.

In practice C/\sqrt{g} will range from 10 to 20 and the ratio channel width (B) to the radius of curvature (R) will not exceed 0.5 so a ratio of depth to width must be in the range of ± 0.5 for the Dean number to become around 50.

This reverse circulation occurs suddenly which means that when the Dean number is large enough and the reverse circulation is set in motion it intensifies itself as far as viscous terms permit. This reverse circulation occurs at the outer wall and is due to the fact that at large Dean numbers the velocity maximum lies below the water surface. If the velocity maximum over the vertical lies below the free surface and from that position the velocities decrease towards the outer wall, a countercirculating flow occurs. The fluid, at a certain distance below the surface containing the largest momentum, is split up when it comes near the side wall and moves partly upward and partly downward. The upward moving particles bend near the free surface and flow in the direction of the inner wall. The reverse secondary circulation and its convective influence gives rise to a further reduction of the main velocity at the surface which will make the difference between the maximum velocity region and the region at the surface only larger and by doing so the reverse circulation intensifies itself. In turbulent flows the counterrotating flow occurs in experiments at smaller Dean numbers than from simulations is found. This is probably due to the fact that near the side walls the turbulence is not isotropic (actually the turbulence is at no position isotropic). This leads to hydrodynamic instabilities near the side wall. It should also be born in mind that the Dean number in turbulent flows is defined using the effective Reynolds number so using the turbulent viscosity instead of the molecular viscosity. The turbulent viscosity is anisotropic and may therefore vary from one position to another and it may even vary on one position in different directions.

2.6 Mathematical description of the main flow and secondary circulation

A three-dimensional incompressible fluid flow can be described by four differential equation namely the conservation of mass and the three components of momentum or in other words the equation of continuity and the equations of Navier-Stokes for the three directions x,y,z . These equations can be written for the x,y,z -directions, however, since the problem here concerns a fluid flow in a river bend it seems more appropriate to write these equations in an Φ,R,z co-ordinate system. In this system R represents the distance from the centre of the river bend, Φ represents the angle between a certain begin angle and the direction in which the point (x,y) lies and z represents the vertical co-ordinate (fig 2.1 in which s represents Φ).

The system of equations in this co-ordinate system can be written as (following De Vriend):

$$\frac{1}{R} \frac{\partial v_\phi}{\partial \phi} + \frac{\partial v_R}{\partial R} + \frac{v_R}{R} + \frac{\partial v_z}{\partial z} = 0 \quad (2.2)$$

$$\frac{\partial v_\phi}{\partial t} + \frac{v_\phi}{R} \frac{\partial v_\phi}{\partial \phi} + v_R \frac{\partial v_\phi}{\partial R} + v_z \frac{\partial v_\phi}{\partial z} + \frac{v_R v_\phi}{R} = \quad (2.3)$$

$$\frac{1}{\rho} \left[\frac{1}{R} \frac{\partial \sigma_{\phi\phi}}{\partial \phi} + \frac{\partial \tau_{R\phi}}{\partial R} + \frac{\partial \tau_{\phi z}}{\partial z} + 2 \frac{\tau_{R\phi}}{R} \right]$$

$$\frac{\partial v_R}{\partial t} + \frac{v_\phi}{R} \frac{\partial v_R}{\partial \phi} + v_R \frac{\partial v_R}{\partial R} + v_z \frac{\partial v_R}{\partial z} - \frac{v_\phi^2}{R} = \frac{1}{\rho} \left[\frac{1}{R} \frac{\partial \tau_{R\phi}}{\partial \phi} + \frac{\partial \sigma_{RR}}{\partial R} + \frac{\partial \tau_{Rz}}{\partial z} + \frac{\sigma_{RR}}{R} - \frac{\sigma_{\phi\phi}}{R} \right] \quad (2.4)$$

$$\frac{\partial v_z}{\partial t} + \frac{v_\phi}{R} \frac{\partial v_z}{\partial \phi} + v_R \frac{\partial v_z}{\partial R} + v_z \frac{\partial v_z}{\partial z} = \frac{1}{\rho} \left[\frac{1}{R} \frac{\partial \tau_{\phi z}}{\partial \phi} + \frac{\partial \tau_{Rz}}{\partial R} + \frac{\partial \sigma_{zz}}{\partial z} + \frac{\tau_{Rz}}{R} \right] - g \quad (2.5)$$

In which the velocities are indicated by: v_ϕ is the longitudinal velocity, v_R is the radial velocity and v_z is the vertical velocity and $\sigma_{\phi\phi}$, σ_{RR} , σ_{zz} , $\tau_{\phi R}$, $\tau_{\phi z}$, τ_{Rz} represent the components of the stress tensor ρ is the density of the fluid and g is the acceleration due to gravity.

In this system of equations the time derivatives can be easily omitted if it concerns steady laminar flow. For steady turbulent flow this is impossible since turbulent flows are essentially time-dependent, though the turbulence averaged quantities do not vary with time. In that case the equations should be integrated over an interval much longer than the turbulence time scale. By doing so extra terms are introduced namely terms that are related to the time-mean products of the velocity fluctuations (see 'Turbulence'). These terms are called the Reynolds stress tensor. According to the Boussinesq hypothesis now an analogy of the relation between the viscous stress tensor and the rate of strain tensor for the molecular viscosity and the relation between the viscous stress tensor and the rate of strain for the turbulent viscosity is assumed. η is normally used in the viscous relation and η_t (the turbulent viscosity coefficient) in the turbulent relation. It should be noted that the molecular viscosity is a constant value whereas the turbulent viscosity coefficient varies from point to point in the flow and it even varies in the various directions. This makes the equations more complicated since at first the turbulent viscosity coefficient must be determined and additional terms, $\partial\eta_t/\partial\phi$, $\partial\eta_t/\partial R$ and $\partial\eta_t/\partial z$, appear in the equations and must be taken into account.

Furthermore represents p the isotropic pressure. The stress tensor can now be written as:

$$\sigma_{\phi\phi} = -p + 2(\eta + \eta_t) \left(\frac{1}{R} \frac{\partial v_\phi}{\partial \phi} + \frac{v_R}{R} \right) \quad (2.6)$$

$$\sigma_{RR} = -p + 2(\eta + \eta_t) \left(\frac{\partial v_R}{\partial R} \right) \quad (2.7)$$

$$\sigma_{zz} = -p + 2(\eta + \eta_t) \frac{\partial v_z}{\partial z} \quad (2.8)$$

$$\tau_{R\phi} = (\eta + \eta_t) \left(\frac{1}{R} \frac{\partial v_R}{\partial R} + \frac{\partial v_\phi}{\partial R} - \frac{v_\phi}{R} \right) \quad (2.9)$$

$$\tau_{Rz} = (\eta + \eta_t) \left(\frac{\partial v_R}{\partial z} + \frac{\partial v_z}{\partial R} \right) \quad (2.10)$$

$$\tau_{\phi z} = (\eta + \eta_t) \left(\frac{1}{R} \frac{\partial v_z}{\partial \phi} + \frac{\partial v_\phi}{\partial z} \right) \quad (2.11)$$

Where the velocities v_ϕ , v_R and v_z are now averaged over the turbulence and p is the turbulent averaged pressure. If these expressions for the Reynolds stress tensor are substituted in the equations of Navier-Stokes and the viscosity can be written as $\eta + \eta_t = A$ (in normal cases in river engineering the molecular viscosity is negligible except very close to the side walls) then after some elaboration and with using the continuity equation these equations are:

$$\begin{aligned} \frac{v_\phi}{R} \frac{\partial v_\phi}{\partial \phi} + v_R \frac{\partial v_\phi}{\partial R} + v_z \frac{\partial v_\phi}{\partial z} + \frac{v_R v_\phi}{R} = -\frac{1}{\rho} \frac{1}{R} \frac{\partial p}{\partial \phi} + \frac{A}{\rho} \left(\nabla^2 v_\phi - \frac{v_\phi}{R^2} + \frac{2}{R^2} \frac{\partial v_R}{\partial \phi} \right) + \\ \frac{1}{\rho} \left[\frac{2}{R} \frac{\partial A}{\partial \phi} \left(\frac{1}{R} \frac{\partial v_\phi}{\partial \phi} + \frac{v_R}{R} \right) + \frac{\partial A}{\partial R} \left(\frac{1}{R} \frac{\partial v_R}{\partial \phi} + \frac{\partial v_\phi}{\partial R} - \frac{v_\phi}{R} \right) + \frac{\partial A}{\partial z} \left(\frac{\partial v_\phi}{\partial z} + \frac{1}{R} \frac{\partial v_z}{\partial \phi} \right) \right] \end{aligned} \quad 2.12$$

$$\begin{aligned} \frac{v_\phi}{R} \frac{\partial v_R}{\partial \phi} + v_R \frac{\partial v_R}{\partial R} + v_z \frac{\partial v_R}{\partial z} - \frac{v_\phi^2}{R} = -\frac{1}{\rho} \frac{\partial \rho}{\partial R} + \frac{A}{\rho} \left(\nabla^2 v_R - \frac{v_R}{R^2} - \frac{2}{R^2} \frac{\partial v_\phi}{\partial \phi} \right) + \\ \frac{1}{\rho} \left[\frac{1}{R} \frac{\partial A}{\partial \phi} \left(\frac{1}{R} \frac{\partial v_R}{\partial \phi} + \frac{\partial v_\phi}{\partial R} - \frac{v_\phi}{R} \right) + 2 \frac{\partial A}{\partial R} \frac{\partial v_R}{\partial R} + \frac{\partial A}{\partial z} \left(\frac{\partial v_R}{\partial z} + \frac{\partial v_z}{\partial R} \right) \right] \end{aligned} \quad (2.13)$$

$$\begin{aligned} \frac{v_\phi}{R} \frac{\partial v_z}{\partial \phi} + v_R \frac{\partial v_z}{\partial R} + v_z \frac{\partial v_z}{\partial z} = -\frac{1}{\rho} \frac{\partial \rho}{\partial z} - g + \frac{A}{\rho} \nabla^2 v_z \\ + \frac{1}{\rho} \left[\frac{1}{R} \frac{\partial A}{\partial \phi} \left(\frac{\partial v_\phi}{\partial z} + \frac{1}{R} \frac{\partial v_z}{\partial \phi} \right) + \frac{\partial A}{\partial R} \left(\frac{\partial v_z}{\partial R} + \frac{\partial v_R}{\partial z} \right) + 2 \frac{\partial A}{\partial z} \frac{\partial v_z}{\partial z} \right] \end{aligned} \quad (2.14)$$

$$\text{in which } \nabla^2 = \frac{1}{R^2} \frac{\partial^2}{\partial \phi^2} + \frac{\partial^2}{R^2} + \frac{1}{R} \frac{\partial}{\partial R} + \frac{\partial^2}{\partial z^2} \quad (2.15)$$

3. Turbulence

3.1 Introduction

In the past chapters the problem of the fluid-movement in river bends have been discussed. This problem can be described by the equation of continuity and the equations of Navier Stokes. If the Reynolds-numbers become above a certain number (± 2000) a turbulent motion will appear. Normally in river flows the Reynolds numbers are much higher than this limit-number and so a turbulent flow occurs in these flows. For calculations of turbulent flows it is impossible to use the Navier Stokes equations in the form of (eq.3.4 /3.7) because for describing the flow in a proper way all length scales of the eddies have to be modelled. The largest length scales in a turbulent flow have a magnitude with the size of the flow domain and are determined by the boundary conditions of the flow. The smallest eddies have length scales that are determined by the scale at which the turbulent energy is transformed into heat; these have a magnitude of 10^{-4} m. So for making a calculation of a flow in three dimensions about 10^9 grid points have to be used to model an area of 1 cm^3 . Although the turbulence energy is transformed into heat by the smallest eddies it is the largest length scales that transport the turbulent motion and at these length scales the energy of the mean flow is passed on to the turbulent motion, therefore, these are the ones which have to be modelled. In turbulent models the length scale and the velocity scale of the largest eddies are parameters which characterise the motion.

The large eddies interact with the mean flow because the scales of both are similar, thereby extracting kinetic energy from the mean motion and feeding it into the large-scale turbulent motion. Due to vortex stretching the energy is passed on to smaller and smaller eddies until viscous forces become active and dissipate the turbulent energy. This process is called energy cascade. The large scale turbulent motion strongly depend on the boundaries of the flow and is therefore strongly anisotropic. In flows with large Reynolds numbers like the ones normally found in civil engineering the small scale turbulent motion (where the energy is dissipated) does not depend on the boundaries and is isotropic.

For obtaining a system of equations for turbulent motion the velocities and the pressure are thought of as a sum of mean velocity/pressure part and a fluctuating velocity/pressure part:

$$RE(=N.S.): \frac{\partial}{\partial t}(\rho \bar{u}_i) + \nabla_j(\rho \bar{u}_i \bar{u}_j) + \nabla_j \overline{\rho u_i' u_j'} + \nabla_i \bar{p} - \eta \nabla_j^2 \bar{u}_i = \bar{k}_i \quad (3.1)$$

where ρ is the fluid density, u_i the velocity in the i -direction, u_i' the turbulent part of the velocity in the i -direction, p the pressure, η the molecular viscosity of the fluid and k_i the external force acting in the i -direction.

To compress equation 3.1 the tensor notation is used. The indices i and j can take the value 1,2 and 3 indicating the different directions. A repeated index in the same term implies summation of the term over the three directions. The overbars indicate time averages.

The terms $\overline{\rho u_i' u_j'}$ are called stresses because they have the dimension of a stress.

The system of equations obtained consists of more unknown variables than equations so it is no more a closed system (which it is without the Reynolds stresses). The

solution of this problem is called the closure problem. Additional equations or expressions have to be given to solve this problem. These equations or expressions are called the turbulence model. In the literature a variety of solutions can be found from simple algebraic equations to systems of non linear differential equations.

In the closure models of the turbulence problem often a gradient-type transport is used. The turbulent viscosity is then based on the so-called Reynolds analogy. It is therefore assumed that

$$\overline{\rho u'_i u'_j} = -\rho \nu_t \left(\frac{\partial \bar{u}_j}{\partial x_i} + \frac{\partial \bar{u}_i}{\partial x_j} \right) \quad (3.2)$$

in which \bar{u}_i is the mean velocity of the flow since the velocity-scale and the length-scale depend on the largest eddies in the flow.

To solve the problem the viscosity has to be determined.

Speziale suggested the following frame work in order to account for the normal stresses. This frame work can be written as (following Speziale [ref 16]):

$$\overline{\rho u'_i u'_j} = -\frac{2}{3} \rho k \delta_{ij} + \rho \sqrt{k} l D_{ij} \quad (3.3)$$

in which

$$\delta_{ij} = \begin{cases} 1 & \text{if } i=j \\ 0 & \text{if } i \neq j \end{cases} \text{ the Kronecker delta} \quad (3.4)$$

and

$$D_{ij} = \frac{1}{2} \left(\frac{\partial v_j}{\partial x_i} + \frac{\partial v_i}{\partial x_j} \right) \quad (3.5)$$

The term involving the Kronecker delta is perhaps a somewhat unfamiliar addition to the eddy-viscosity expression; it is necessary to make the expression applicable also to normal stresses (when $i = j$). The second part involving the velocity gradients would yield the normal stresses

$$\overline{U_1^2} = -2\nu_t \frac{\partial u_1}{\partial x_1}, \quad \overline{U_2^2} = -2\nu_t \frac{\partial u_2}{\partial x_2}, \quad \overline{U_3^2} = -2\nu_t \frac{\partial u_3}{\partial x_3} \quad (3.6)$$

whose sum is zero because of the continuity equation. However all normal stresses are by definition positive quantities, and their sum is twice the kinetic energy k of the fluctuating motion.

$$k = \frac{1}{2} \left(\overline{U_1^2} + \overline{U_2^2} + \overline{U_3^2} \right) \quad (3.7)$$

Inclusion of the first part of the eddy viscosity expression assures that the sum of the normal stresses is equal to $2k$. The normal stresses act like pressure forces (i.e. perpendicular to the faces of a control volume), and because like the pressure itself, the

energy k is a scalar function, the first part constitutes a pressure. Therefore, when the frame-work equation is used to eliminate $\overline{u_i u_j}$ in the momentum equation this first part can be absorbed by the pressure-gradient term so that in effect the static pressure is replaced as unknown quantity by the pressure $P+2/3k$. Therefore the appearance of k in the frame-work does not necessitate the determination of k ; it is the distribution of the eddy viscosity ν_t that has to be determined.

The turbulence models can be divided in two main types of equations:

- algebraic turbulence viscosity models
- differential turbulence viscosity models

In the algebraic turbulence viscosity models a constant viscosity is used which is obtained by the product of a characteristic velocity and a characteristic length, or by simple relations between the gradient of the main velocity and a typical length-scale. The differential turbulence viscosity models compute the turbulence viscosity by means of differential equations which describe one or more characteristic quantities of the turbulence.

Hereafter the following turbulence closure models will be discussed:

Algebraic turbulence viscosity models

- given constant viscosity
- the mixing length model
- algebraic turbulence viscosity model of Trisula

Differential turbulence viscosity models

- K-L model with a constant mixing length
- K-L model with differential expressions for the mixing length L
- K- ϵ model

3.2 Algebraic turbulence viscosity models

3.2.1 Constant eddy viscosity

If a constant eddy viscosity is given no extra equations are needed to solve the system of equations so the computational time is reduced in confront of models where first the viscosity has to be determined. Especially when viscosity plays an unimportant role in the calculation of the flow the use of this type of model is often applied. The constant eddy viscosity is determined by using the fact that the dimensions of ν_t are m^2/s which is a velocity times a length. For this reason, normally, a characteristic length scale and a characteristic velocity-scale of the larger eddies are multiplied to obtain ν_t . Since a constant length-scale is used this model does not work very well for rivers and canals because ν_t differs to much with the depth of the flow (see 'previous experiments'). If, for example, a depth-averaged constant eddy viscosity is used than the viscosity at the bottom is far to large resulting in an estimation of the velocity which is to small. In large flow-fields with a relatively plane bottom a constant turbulent viscosity works rather well because in these cases the bottom-friction is far more important than the turbulent viscosity so the velocity-field is determined by the bottom-friction.

3.2.2 Mixing-length hypothesis

The first model to describe the distribution of the eddy viscosity, and thus the first proper turbulence model, was suggested by Prandtl in 1925. Therefore this model is called the Prandtl mixing-length model. He also suggested that the turbulence viscosity could be written as a velocity times a length. For the length he took a characteristic length

$$l = l_m \quad (3.8)$$

which is the so-called mixing length. The velocity is written as the gradient of the mean velocity of the flow multiplied by the mixing length.

$$v_t = l_m \left| \frac{d\bar{u}}{dz} \right| \quad (3.9)$$

if the velocity changes only in the z-direction

The turbulence viscosity can now be expressed as

$$v_t = l_m^2 \left| \frac{d\bar{u}}{dz} \right| \quad (3.10)$$

Because of its simplicity of application the model is useful if not too complicated flow-fields are calculated

3.2.3 Algebraic turbulence viscosity model of Trisula

Another type of turbulence model is used in the numerical simulation program Trisula [ref. 12]. It assumes the turbulent viscosity equal to a constant times a characteristic length times a velocity which is related to the kinetic turbulent energy.

$$v_t = c_v \sqrt{k} l \quad (3.11)$$

where k is

$$\sqrt{k} = \frac{1}{2} \sqrt{\left(\frac{\bar{u}_i}{u_i} \right)^2} \quad (3.12)$$

and the mixing length is written as (Bakhmetev, 1932)

$$l = k(z+d) \sqrt{1 - \frac{z+d}{h}} \quad (3.13)$$

where c_v is an empirical constant, k the Von Karman's constant, z the vertical coordinate above some horizontal plane of reference, d the water depth below some horizontal plane of reference and h the total water depth

To calculate k an algebraic equation is given which is

$$k = \frac{1}{\sqrt{c_\mu}} \left[(u_*^b)^2 \left(1 - \frac{z+d}{h} \right) (u_{*s})^2 \frac{z+d}{h} \right] \quad (3.14)$$

c_μ is an empirical constant, u_*^b is a modified form of the bed friction velocity, u_{*s} is the friction velocity at the free surface.

With this set of equations the problem is solvable.

The main (dis)advantages of these turbulent closure models are:

Advantages:

- * Because of their simplicity of application no extra differential equations are needed
- * If the mixing-length can be prescribed in a proper way then normally good results are obtained

Disadvantages:

- * In recirculating flows it is difficult to prescribe a proper mixing-length since the relations between the shear-stresses and the gradient of the velocity is too complicated.
- * If at a certain place the velocity-gradient is zero then also the turbulence viscosity is zero and therefore at these places no transport can take place
- * These models do not account for convection and diffusion of turbulence
- * The calculated viscosity is always positive whereas experiments [ref. Booij] showed that the viscosity is negative at certain positions in the flow.

3.3 Differential turbulence viscosity models

The differential turbulent viscosity models describe the transport of turbulent quantities by means of differential equations. They describe the transport of quantities k , the turbulent energy per unit mass, and/or ε , the dissipation of turbulent energy. The turbulence is not expressed anymore as a property of the mean velocity profile but as a turbulent quantity.

3.3.1 K-L models with a constant mixing length

The most simple K-L model is a differential equation for the kinetic energy k and a prescribed value of L . The problem is that still a constant length-scale has to be given which means that for rather complicated flows the determination of this length-scale can be very difficult and may contain errors for local solutions. It also has to be noted that the length L is not a constant, so a constant prescription would be wrong, since the eddies generated by a grid are convected downstream so that their size at any station depends on their initial size. Other processes influencing the length-scale are dissipation, which destroys the small eddies and thus effectively increases the eddy size and vortex stretching connected with the energy cascade, which reduces the eddy size. The equation for K is obtained by manipulating the Navier-Stokes equation and by making use of the continuity equation. The equation that follows is further simplified by neglecting the smaller terms (fluctuation of the external force) and by making some assumptions for the diffusion term and the dissipation term (see appendix I). The k -equation reads:

$$\frac{\partial k}{\partial t} + \frac{\partial}{\partial x_j} \left(u_j - \frac{v_t}{\sigma_k} \frac{\partial k}{\partial x_j} \right) + P + c_d \frac{k^{\frac{3}{2}}}{l} = 0 \quad (3.15)$$

$$\text{in which } p = -\overline{u_i u_j} \frac{\partial \bar{u}_i}{\partial x_j} \quad (3.16)$$

$$\text{and } v_t = C_v \sqrt{k} l \quad (3.17)$$

and σ_k and c_d are empirical constants for which normally are taken

$$\sigma_k = 1.0$$

$$c_d = 0.15$$

3.3.2 K-L models with a differential expression for the mixing length

Mostly the determination of the length L is done by means of a differential equation Z which contains the product of k to the power m and L to the power n [ref 15]

$$Z = k^m L^n \quad (3.18)$$

Since an equation for k already exists in this model the determination of L is possible; it is now a closed system.

A lot of combinations of L and k have been suggested like $Z = L$ an equation for the mixing length only, $Z = k^2/L$ (Kolmogorov ea.) an equation for the frequency, $Z = kL$ (Rotta ea.), $Z = k/L^2$ (Spalding, Saffman, ea.) an equation for a turbulence vorticity, $Z = k^{3/2}/L$ (Jones, Launder, Chou, Davidov, ea.) an equation for the dissipation rate. The differential equations which they give are all of the same form

$$\frac{\partial z}{\partial t} + u_i \frac{\partial z}{\partial u_i} = \frac{\partial}{\partial x_i} \left(\frac{\sqrt{kl}}{\sigma_z} \frac{\partial z}{\partial x_i} \right) + c_{z1} \frac{z}{k} P - c_{z2} z \frac{\sqrt{k}}{l} + S \quad (3.19)$$

in which P is the production of the kinetic energy and S represents a secondary source term and σ_z , c_{z1} and c_{z2} are empirical constants. Experiments showed that the secondary source term is important near walls but unimportant in free flows. The only combination for Z of k and L which does not require a secondary source term S is for $Z = k^{3/2}/L$. All the other combinations do need a near-wall correction term S. This is one of the reasons why this model is so often used. It is used in the form

$Z = C_\mu k^{3/2}/L = \varepsilon$; which is the dissipation rate of turbulent energy. This model is called the K- ε model which will be described hereafter.

The length L is calculated by an equation of Z (which will not be given here because there are, as shown previously several expressions for Z) but has the form of equation 3.19.

3.3.3 K- ε models

The K- ε model is a K-L model for which the physical meaning of the combination of k and L is the dissipation of turbulent kinetic energy. This type of K-L model is more used than the other K-L models because it has some great advantages in confront of the other K-L models it is, as said before, the only combination of K and L which does

not require a secondary source term so a simpler differential equation can be used. The physical character of this model is liked because now in the set of equations for K and ε an equation for the turbulent energy and an equation for its dissipation exists. The dissipation of energy ε is written as

$$\varepsilon = c_d \frac{k^{\frac{3}{2}}}{l} \quad (3.20)$$

Inserting this in the expression of the turbulent viscosity:

$$\nu_t = C_v \sqrt{k} l \quad (3.21)$$

The following expression for ν_t is:

$$\nu_t = c_v c_d \frac{k^2}{\varepsilon} = c_\mu \frac{k^2}{\varepsilon} \quad (3.22)$$

in which $c_\mu \cong 0.09$

The differential equation for ε is, like the equation for K , obtained by manipulating the Navier-Stokes equations and making some assumptions and simplifications for the diffusion and dissipation terms. It has to be noted that in this equation an analogy is assumed between diffusion of mass, momentum and turbulent energy and the dissipation of turbulent energy. This is a false assumption since the first three quantities are kept quantities on the contrary the turbulent dissipation is not [ref 3]. The K- ε model exists of two equations which are implicitly connected with each other.

$$\frac{\partial k}{\partial t} + \frac{\partial}{\partial x_j} \left(u_j - \frac{\nu_t}{\sigma_k} \frac{\partial k}{\partial x_j} \right) + P + \varepsilon = 0 \quad (3.23)$$

$$\frac{\partial \varepsilon}{\partial t} + \frac{\partial}{\partial x_j} \left(u_j \varepsilon - \frac{\nu_t}{\sigma_\varepsilon} \frac{\partial \varepsilon}{\partial x_j} \right) - \frac{\varepsilon}{k} (c_{1\varepsilon} P - c_{2\varepsilon} \varepsilon) = 0 \quad (3.24)$$

$$\text{in which } p = -\overline{u_i u_j} \frac{\partial \bar{u}_i}{\partial x_j} \quad (3.25)$$

and $\sigma_\varepsilon \cong 1.3, c_{1\varepsilon} \cong 1.44$ and $c_{2\varepsilon} \cong 1.92$

Because of the empirical constants that have to be used this model can only function well if these constants can be applied on several flow situations.

The K- ε model does very well in the analysis of thin turbulent shear flow since it reduces to the traditional eddy-viscosity models which were constructed for this purpose. Furthermore it is frame indifferent which means that it is of the same form whether or not the frame of reference is inertial. A shortcoming of this model is that it yields inaccurate predictions for the normal Reynolds stresses (see 'Reynolds stress model') which play an important role in recirculating an secondary flows. Also for turbulent flow over a backward-facing step the K- ε model yields inaccurate values for the separation-length. De Vriend suggested that the inaccurate modelling of the normal

Reynolds stresses could fairly be the reason why in a channel-bend the reverse circulation occurs at lower Dean numbers than predicted by the linear models.

3.3.4 Reynolds stress models

The Reynolds stress models are used to give a better prediction of the normal Reynolds stresses which, in a K- ϵ model, are equal in the three directions (x,y,z). This means that these models predict isotropic normal stresses. This is not the case in reality. To arrive at anisotropic normal stresses many researchers have searched for laws for the closure-models for a non-linear connection between the tensor of the turbulent stresses and the tensor of the deformation of the velocity. (Lumley 1970, Rodi 1982. ea.). These Reynolds stress models (second-order closure models) are far more implicit than the K- ϵ models so for second-order closure models the computational effort is more than doubled since transport equations must be solved for each individual component of the Reynolds stress tensor (Lumley 1978). Furthermore, in order to obtain these transport equations for the Reynolds stresses, closure models for the higher order turbulent correlation must be formulated which have uncertain physical foundations. The main advantage of the second-order closure models is the incorporation of the history-dependent non-local effects (through the convection and the viscous diffusion of the Reynolds stresses) which are known to play an important role in determining the structure of many important flows. Speziale (1984) posed that in order to find a good prediction of the secondary flow in channel bend the axial main velocity must give a non-zero transverse normal Reynolds stress difference $\tau_{yy} - \tau_{zz}$. In the Reynolds stress model approach the frame-work is like the one of the approach K- ϵ plus some non-linear terms. This frame-work has the form:

$$\overline{\rho u'_i u'_j} = -\frac{2}{3} \rho k \delta_{ij} + {}_D \tau_{ij} \quad (3.26)$$

in which ${}_D \tau_{ij}$ is a traceless tensor and the transport equation is formulated in such a way that $K > 0$ (Lumley 1978). According Speziale this expression for the Reynolds stress model frame-work writes:

$$\begin{aligned} \overline{\rho u'_i u'_j} = & -\frac{2}{3} \rho k \delta_{ij} + \rho \sqrt{k} l \overline{D_{ij}} + \\ & c_d \rho l^2 \left(\overline{D_{im} D_{mj}} - \frac{1}{3} \overline{D_{mn} D_{mn}} \delta_{ij} \right) + c_e \rho l^2 \left(\overset{\circ}{D_{ij}} - \frac{1}{3} \overset{\circ}{D_{mm}} \delta_{ij} \right) \end{aligned} \quad (3.27)$$

$$\text{in which } l = c \frac{k^{\frac{3}{2}}}{\epsilon}, \quad (3.28)$$

$$\overline{D_{ij}} = \frac{1}{2} \left(\frac{\partial v_j}{\partial x_i} + \frac{\partial v_i}{\partial x_j} \right) \quad (3.29)$$

$$\frac{\overset{\circ}{D}_{ij}}{\partial t} = \frac{\partial \overline{D}_{ij}}{\partial t} + \bar{v} \nabla \overline{D}_{ij} - \frac{\partial v_i}{\partial x_k} \overline{D}_{kj} - \frac{\partial v_j}{\partial x_k} \overline{D}_{ki} \quad (3.30)$$

3.4 Boundary conditions for the turbulent models

Some of the before-mentioned models need just like other models boundary conditions. The algebraic models can be determined immediately because they only depend on the gradient of the mean velocity. The K-L models (and also the K- ϵ models) need some boundary conditions for K and/or L (ϵ) if L (ϵ) is to be calculated by a differential equation.

There are four kinds of boundaries to be considered, namely inlet, outlet, walls and the free surface boundaries.

3.4.1 Wall boundaries

At the wall the velocities are in reality equal to zero and in the vicinity of the wall large velocity gradients occur. Should the first grid-point be defined at the wall than, for proper resolution, a very small grid distance have to be used at this location. For this reason the first grid-point is defined at some distance from the wall. This implies that from this first grid-point to the wall a function for the velocity has to be given. Another reason for not calculating to close to the wall is that in the viscous sublayer viscous effects are important so that the high-Reynolds number model is not applicable anymore.

The near-wall region can be separated in three regions [ref. 3] in which either the viscous shear stresses or the turbulent shear stresses or both are important. At the wall a region can be found where the turbulent shear stresses can be neglected (the so-called viscous sublayer). Further from the wall a region can be distinguished where neither of them can be neglected (buffer layer) and after this region a region can be distinguished where the viscous shear stresses can be neglected (turbulent boundary layer). A boundary condition and the first grid point should preferably be placed in the last region.

Experimentally [Reichardt, Laufer] it has been found that for smooth walls this first grid point should be placed at $y^+ \cong 30$ [ref 3] where y^+ is defined as $y^+ = yU_*/\nu$, y is the distance from the wall, U_* is the friction velocity and ν is the kinematic viscosity. For hydraulically rough walls the value for y^+ must be larger.

The boundary conditions for K and ϵ are found by posing that near the wall the convection and diffusion of the turbulence can be neglected. Then it follows that locally the production of turbulent energy is equal to the dissipation of the turbulent energy. For k is the next boundary condition obtained [ref. 12, 14]

$$k = \frac{u_*^2}{\sqrt{C_\mu}} \quad (3.31)$$

with $C_\mu \cong 0.09$

and for the dissipation ϵ is then found

$$\varepsilon = \frac{u_*^3}{\kappa y} \quad (3.32)$$

This boundary condition can be applied for smooth and rough walls since the roughness parameter enters in the condition via the friction velocity U_*

3.4.2 Free surface

When the Froude number is small the free surface can be approximated by a frictionless flat plane: the so-called rigid-lid approximation [ref. 9]. In case of a rectangular channel the surface is a plane of symmetry parallel to the bottom. Implementing this approximation does not mean that surface elevation changes are neglected but are rather taken into account in an indirect manner. As a result of the constraint imposed on the flow by the fictitious rigid lid, nonzero pressure gradients in the radial and vertical directions are predicted at the boundary. This treatment involves a certain error, mainly in continuity, because superelevated regions are implicitly considered hydrodynamically passive. Experience [McGuirk and Rodi, 1977] has shown that the error is small if the maximum super-elevation does not exceed approximately 10% of the total channel depth.

At the free surface the impermeability of the water surface (vertical velocities are zero) and the vanishing of the shear stress tangent to this surface (derivative in the vertical direction of the radial and longitudinal velocities are zero) are formulated:

On the water-surface in absence of wind the boundary conditions for the turbulence parameters are taken [ref. 12]:

$$\begin{aligned} \varepsilon &= 0 \\ \text{and } k &= 0 \end{aligned}$$

3.4.3 Inlet

Across this boundary, distributions of all velocities and of the turbulence parameters need to be prescribed. Ideally, all distributions should originate from measurements; but this is rarely possible in practice and some, if not most of the distributions, need to be guessed or estimated on the basis of physical reasoning.

An experimental distribution of k is rarely available, while an ε -distribution can only be obtained indirectly from measurements of other turbulent quantities. Fortunately, both exert little influence on the predictive accuracy, and considerable latitude is given to their estimation [ref. 9]. The boundaries must lie at a distance, long enough for the flow to smooth out the boundary conditions, from the positions of interest.

3.4.4 Outlet

The same reasoning as for the inlet boundary conditions can be given.

3.4.5 Initial conditions

Usually it is assumed that initially the model is at rest (cold start) and initial boundary conditions are prescribed which are wrong and after some calculation time, the spin-up (warming-up), the real values are calculated. These wrong initial values have to be an approximation of the expected values.

3.4.6 Grid

Some problems may arise when trying to model turbulent flows. Since only a limited number of grid-points can be used, resulting in a coarser grid-size the larger is the flow field. Therefore some additional processes occur, which are represented by the diffusivity, which have nothing to do with turbulence. At first it should be noted that all convective motions within the mesh, such as recirculation zones, can not be resolved and must be accounted for by the diffusivity.

Another phenomenon is the numerical diffusion which occurs because of the discretisation that is made. The approximation of the differential equation by difference equations introduces errors which act to smooth out variations of the dependent variables and thus effectively increases the diffusivity. This numerical or false diffusion is larger for coarser grids.

4. Previous research to flow in open channel bends

In this section a brief description will be given of the past research on secondary flow in river bend flows. For the modelling of these flows special attention will be paid to the modelling of the turbulence.

The ratio of the depth of flow to the width of flow was usually supposed to be small and often turbulent motion was assumed.

In the literature a lot of proposed numerical simulation models and experiments can be found for this type of flow.

4.1 Experimental research

More than 100 years ago it was already known that in channel bends a certain secondary flow occurred. The first experiments which were carried out to this phenomenon were made by Thomson in 1879. Later on Engels (1900) did the same experiments which were only of a qualitative nature. The experiments they both did were done in a channel bend and at certain places near the outer wall (A_1 , A_2 , A_3) they dropped some wetted coal. It turned out that this coal was moved downstream and ended near the inner wall at points B_1 , B_2 , B_3

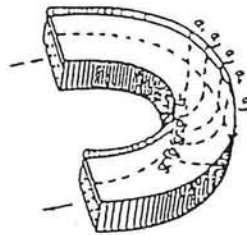


Figure 4.1 First experiment to secondary flow by Thomson

Mockmore, in 1943, carried out experimental investigations on the pattern of velocity distribution in a rectangular flume having two 180° bends, connected by a straight element. The results of his experiments gave rise to the following conclusions.

They confirmed the presence of a helical (screw) movement in bends, while the helix possesses a rather complicated character. Also was concluded that the longitudinal velocities were in approximately the first half of the bend larger in the inner half of the cross-section and in the second half of the bend they were larger in the outer half of the cross-section. Nearly three quarters of the way down the bend an eddy or a stagnation zone appeared at the convex (inner) wall, which led to the deposition of sediment at this spot and to the formation of a shoal.

4.1.1 Longitudinal velocities

According experimental research it appears that the deviation of the resultant flow before the flow enters the bend is negligible. At the entrance of the bend in the inner

part of the cross-section a steep fall of the free surface was observed accompanied by an increase of the velocity there.

Even before the bend starts, the effect of the bend is observed in the straight approach reach in as much as the difference in surface elevation across the width of the channel is observed [ref 5, 6, 17]. From experiments, it was found that in strongly curved bends the maximum longitudinal velocity prevails near the inner wall region between sections $\theta \cong 0^\circ$ to $\theta \cong 45^\circ$ after which it gradually shifts towards the outer wall with increasing magnitude. In mildly curved bends the maximum longitudinal velocity is, in the beginning of the bend, found in the centre of the cross-section and shifts towards the outer wall with increasing magnitude. In the early part of the inner wall the velocity increases with increasing θ and z/h [ref 5]. A transverse slope which is always found whether the bend is strongly or mildly curved is largest for strongly curved bends and is often found to arrive at its maximum near the inner wall at $\theta \cong 90^\circ$ considering 180° curved bends. In the central and the outer wall region the velocities decrease until $\theta \cong 90^\circ$ whereas the velocities in the inner wall region increase. Further downstream the velocities in the central and outer wall region increase and the ones in the inner wall region decrease. The overall longitudinal velocity maximum was found to be near the outer wall at a cross-section downstream of the bend exit for both strongly and mildly curved bends [ref 5, 6, 17].

4.1.2 Secondary velocities

The spiral motion originates at the outer wall near the surface at the early reaches of the bend and is shifted toward the inner wall in the developing zone. The spiral motion in the early developing zone is of very low strength. It develops to its full strength in the central region and, towards the exit of the bend, it starts decaying, near the inner wall and is then shifted towards the outer wall. The early secondary flow consists of a flow which is mainly directed toward the inner wall resulting in a net flow in that direction. When passing through the bend more and more a spiral motion develops. When arriving at the end of the bend (if the bend is a 180° one) the opposite occurs and the spiral motion is gradually changed after $\theta \cong 120^\circ$ in a motion which is mainly directed toward the outer wall resulting in a net fluid flow in that direction.

Secondary velocities are typically one order of magnitude smaller than the bulk primary velocity [ref 2].

Rozovskii found the vertical velocities near the inner and outer wall to be of the same order of magnitude as the radial velocity in the central part.

4.1.3 Counterrotating secondary flow

The single cell of secondary circulation is well understood. However the pattern is sensitive to the presence of any pre-existing circulation. In a series of meanders, if the bends are linked by relatively deep reaches, the flow cell of one bend can appear as a relict cell at the next bend downstream. Its sense of rotation is than opposite to that of the main cell of that next bend. Small cells of reverse circulation have also been observed at the outer banks of single bends in channels. Rozovskii concluded that this cell is a wall effect, extending over a region of one or two depths of flow from the bank, but negligible in bends with large width-depth ratios. However because it has probably a significant effect on the stability of the outer bank, the cell is an important

subject. De Vriend [ref 17, 18] showed that the counterrotating cell in the outer wall region relied heavily on the Dean number. He found that the counterrotating cell appears suddenly when the Dean number is approximately 50. Considering both the isovel patterns and the direct measurements from the field measurements it appears that as discharges increases, the dimensions of the outer bank cell increases but its lateral extent does not exceed one or two times the depth of flow [ref 2].

The same velocity distributions for both longitudinal and secondary velocities in the bend were found when a non-rectangular cross-sectional profile was considered. Kalkwijk and De Vriend [ref 10] showed this in a typical river profile in experiments in the laboratory and Bathurst, Thorne and Hey [ref 2] found the same in real river bends. The results of the secondary circulations are that, together with Rozovskii, they support the suggestion that these cells appear where the bank is steep but not where it shelves.

4.1.4 Sensitivity

The experiments by Choudhary and Narasimhan [ref. 5]. were aimed for prediction of the influence of several parameters. It appeared that an increase of the Froude number or B/h resulted in a decrease of the ratio of the longitudinal velocity to the mean longitudinal velocity. The secondary flow which initiates at the outer wall is shifted towards the inner wall. In the latter half of the inner wall region the opposite occurs and an increase of θ or an increase of R/R_c is accompanied by a decrease of the ratio of the longitudinal velocity to the mean longitudinal velocity. The stronger the curvature of the bend, the larger the drop of the pressure and the larger the increase of the velocity in the inner wall region at the entrance of the bend.

This rate of decay of the secondary flow is faster for wide channels than for narrow channels. The secondary flow occurs earlier with increasing Froude number and also the growth of it occurs earlier and its intensity is higher for narrow channels than for wide channels. The maximum ratio of the radial velocity to the mean longitudinal velocity reduces with increasing Froude numbers.

4.1.5 Shear-stresses

Relatively low shear-stresses are found at places where upwelling and low velocity occur. This is near the inner bank. The stronger the downwelling, the greater the compression of isovels near the bed and therefore the bigger the shear-stress. Peak values of shear-stress associated with the core of maximum velocity are generally one and one half to two and one-half times as large as the mean shear-stress at the sections. The shear-stress peak associated with the core of maximum velocity lies nearer the inner bank than does the core itself. This is probably because the cross-over of the shear-stress peak towards the outer bank that occur at some point is delayed, relative to the cross-over of the core of maximum velocity, by inertial effects.

As discharge increases the maximum shear-stress is associated to the maximum velocity since the secondary circulation remains approximately constant but the primary velocities increase. As can be concluded from the distribution over the cross-section, regarding the high and low shear-stress zones, the typical profile of a river

bend, deep and having a steep wall near the outer side and not deep having a smooth wall near the inner side, is rather obvious.

4.2 Numerical research

In the early studies some approximations were made to be able to solve this flow problem numerically. The assumption of axial symmetry was the one most frequently made in previous analyses [ref. 1, and Rozovskii (Flow of water in bends of open channels, 1965)] but even then, solutions for the cross-sectional velocity field relied heavily on the partial or total neglect of inertia and a prescription of a uniform or empirically deduced eddy-viscosity distribution. It is clear that the assumption of axial symmetry precludes any statement on the streamwise development and decay of surface slope, transverse circulation and radial asymmetry in the tangential velocity maximum. For strongly curved flows this is a severe drawback but for weakly curved flows the influence is of less importance. An aspect which has received very little attention in most of the previous studies is the accurate representation of turbulence effort. Most of these studies made use of an indirect determination of the eddy-viscosity field on the base of an assumed logarithmic or power-law vertical distribution of the tangential velocity. Some others made use of an even more easy eddy viscosity namely a constant one. On the other hand some research has been done to the justification of the use of the various turbulence models and the determination of the turbulent quantities in this flow case.

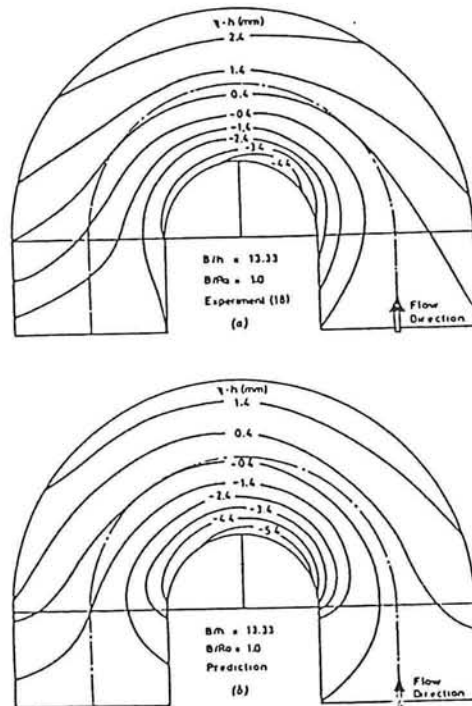


Figure 4.2 The surface slope in a channel bend [ref. 9]

Leschziner and Rodi [ref. 9] made use of a tight 180° bend with a rectangular cross-section and straight inlet and outlet. They searched for a three-dimensional solution with a finite difference procedure of Patankar and Spalding (1972). With this scheme downstream changes of pressure (or surface elevation) do not influence upstream conditions. In strongly curved flow it is this transmission that is responsible for the formation of the transverse slope and motion in the straight reaches preceding and following the bend. The strong radial asymmetry in the tangential velocity profiles and its reversal are also almost entirely due to this transmission process. The results of the surface slope and the depth averaged tangential velocities by experiment and calculation are given here. The transverse slope reaches its maximum at $\theta \approx 90^\circ$

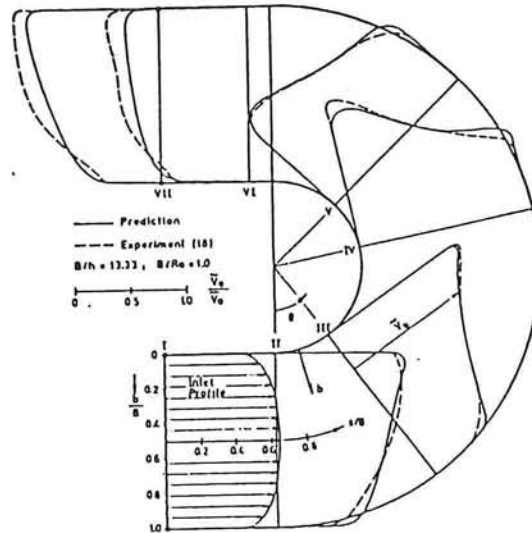
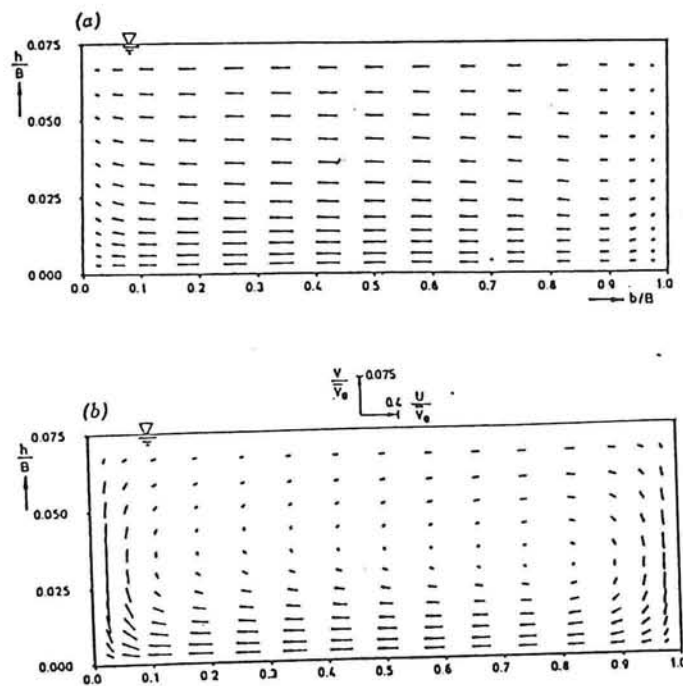


Figure 4.3 The longitudinal velocities in a channel bend [ref. 9]

The secondary flow was calculated; for four different positions the results were as follows.



figuur 6

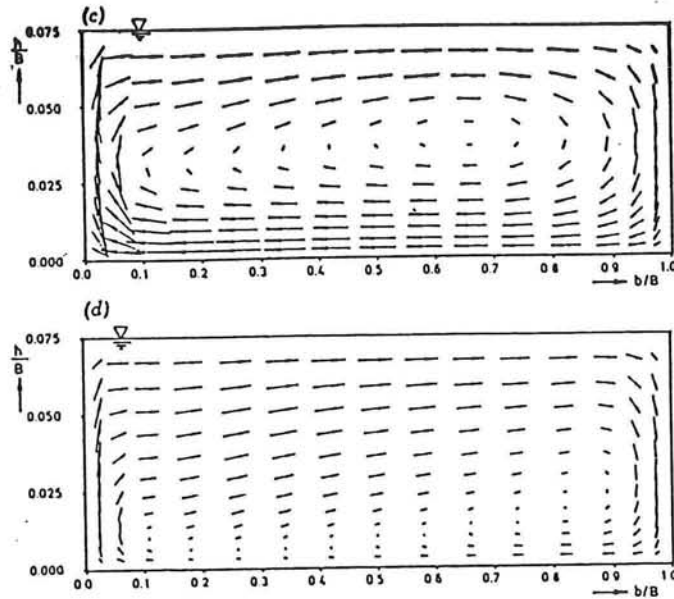


Figure 4.4 The secondary flow in a bend at four positions [ref. 9]

The first figure shows the beginning of the bend until $\theta \cong 15^\circ$. The build up of the surface slope (figure 4.2) implies negative pressure gradients $\partial p / \partial \theta$ accompanied by fluid acceleration near the inner bank and positive $\partial p / \partial \theta$ accompanied by fluid deceleration near the outer bank. By continuity, radial differences in longitudinal fluid accelerations cause a lateral (in this case inward) motion which, mainly due to the inertial term balances the differences between the centrifugal force and the lateral pressure gradient as the latter slowly approaches a limiting value and then decays. The same phenomenon was found experimentally by Choudhary and Narasimhan [ref 5]. They found that even before the bend starts the effect of the bend is observed in the straight approach reach in as much as the difference in the surface elevation is observed.

In the second figure the secondary motion is slowly starting, however, the inward motion is still influencing the spiral motion as can be seen because the inward velocities are larger than the outward velocities resulting in a net transport of fluid towards the inner wall.

In the third figure for $\theta \cong 40^\circ$ until $\theta \cong 130^\circ$ the secondary motion seems to be fully developed.

The last figure shows the decay of the secondary flow and an outward bounded flow resulting in a net flow towards the outer wall.

It can be concluded that there is a continuous build-up or decay of the transverse slope within the bend so that no distinct region exists in which a state of axial symmetry exists. Also it is seen that the velocity maximum occurs at the beginning of the bend near the inner wall and throughout the bend it is shifted due to the secondary flow toward the outer wall.

The influence of the Dean number was researched numerically by De Vriend [ref 17, 18]. It appeared that in fully developed flows an increase in the Dean number results in an increase of the longitudinal velocities in the outer wall region and a decrease in the inner wall region. The influence of the secondary flow on the main flow depends strongly on the Dean number. For low Dean numbers the influence of the secondary flow is limited to the regions near the walls and the central region remains practically

undisturbed. When increasing the Dean number the influence is felt throughout the entire cross-section. When further increasing the Dean number the velocity maximum is not found anymore at the free surface but below it. This maximum below the free surface gives rise to a reverse countercirculating current in the upper part of the cross-section near the outer wall. This reverse circulation reduces the velocity near the surface which therefore increases the intensity of the reverse circulation. The width of the reverse circulation is found not to be larger than one or two times the depth of flow [ref 18].

Although these are the results of models they were confirmed by the experiments.

4.3 Modelling of turbulence

As mentioned earlier, the turbulence was often modelled by means of a constant viscosity and a gradient type transport was assumed. Lately some research has been done to the turbulent quantities as they appear in the equations 4.1. Using

$$\frac{\tau_{i,j}}{\rho} = \overline{u'_i u'_j} = -\nu_{ij} \left(\frac{\partial \overline{u}_i}{\partial x_j} + \frac{\partial \overline{u}_j}{\partial x_i} \right)$$

The turbulent viscosity was calculated in the vertical by means of the measured velocity gradients and the measured quantities $\overline{u'_i u'_j}$. It appeared that the turbulent viscosity was negative over a large distance of the vertical. The explanation is that, especially near the bottom, upwards moving parcels have negative longitudinal and radial turbulent parts of the velocities ($u_i = u'_i + \overline{u}_i$) and positive turbulent parts of the vertical velocities and vice versa [ref 4]. Therefore, the quantities $\overline{u'v'}$ are positive whereas the quantities $\overline{u'w'}$ and $\overline{v'w'}$ are negative. From graphs of these turbulent viscosities it can be observed that the three eddy viscosities are far from equal and the use of an isotropic eddy viscosity is not justified. This is a phenomenon that can not be reproduced by the turbulent models. This means that the turbulent can not be modelled correctly, however, it depends on the flow case whether a correct representation of the turbulence is important or not.

5 Experimental study

5.1 Introduction

In a real river the secondary flow develops and, if the bend is long enough, a fully developed stage will be reached. To investigate this phenomenon, a situation of a fully developed flow and sediment transport should be researched. This fully developed stage is in principle reproduced by an infinite long bend so the initial developing part is left out of consideration. Besides the spatial adaptation, however, a time adaptation should be considered, long enough for the water and the bottom to reach an equilibrium. To further reduce complications, in the beginning, a non-erodible bed was used. After that an erodible bed should be used to research the bottom shape for such a flow. An equilibrium is reached when the sediment transport in a certain point is such that the same amount of sediment is taken away as is put down by the flow.

In the literature a lot of experiments on secondary flow and bottom shape in river bends are described but they were usually done in finite river bends. A few ones have measured in infinite long bends [ref. Booij, 1994].

5.2 Requirements

When researching the secondary flow in an infinite long bend, a uniform velocity distribution along each streamline ($du/ds=0$) is needed. Since this study was done to secondary flow in bends, which are very sensitive to disturbances in the main flow velocity distribution, the most careful attention was paid to this part of the problem. Also for uniform sediment transports between the different cross-sections a uniform flow is required so an equilibrium can be reached and no feeding of sediment is needed. The problem is how to set the water in motion without creating much disturbances. For making the water flow and to keep it in motion the velocity of the water that enters in the annular flume has to be larger than the velocity of the water that flows in the annular flume. This means that at the point where the water enters in the annular flume a non-uniform distribution of the velocity occurs. When this non-uniformity is small then after a certain, small distance the flow will be uniform again. These will be the positions where the measurements must be done. If the non-uniformity is too large it will be felt throughout the entire annular flume. For making the measurements with a velocity-meter possible a simple and accessible configuration is needed.

The velocities were measured by a velocity-meter which measures by means of a magnetic field. This velocity meter was inserted in the water from above so the surface had to be free.

The velocity of the flow has to be a realistic one. This means that the velocity in a froude-scale must be one which in reality can be expected to occur in a river bend.

5.3 Various solutions of the model

An annular flume was made to simulate an infinite long bend. The problem for this flow-case was how to set the water in motion and how to keep the water in motion. As said before the way it is set in motion should not create much disturbances and differences in velocities in the various cross-sections. A solution was to make a little mill that rotates and sets the upper part of the cross-section in motion. The upper part will set the rest of the water in motion by means of the vertical turbulent exchanges of momentum. Once the water flows uniformly over the entire depth the mill will only have to maintain the movement of the flow which is slowed down by the friction forces on the walls and the bottom. Since these losses of flow velocity are only small the difference in water-level before and after the mill can be small.

Another solution of making the water flow was to make small tubes in the side wall which would inject water in the annular flume under a small angle with the direction of the flow. The problem is that the holes had to be small and therefore a concentration of high velocity occurs resulting in too large disturbances.

In the beginning a solution of putting a few perforated vertical tubes in the cross-section has been tried. The water entered in the flow through small holes in the direction of the flow. Because the total area of the holes was small compared to the cross-sectional area the velocity of the water that was injected had to be large and therefore concentrated flows in this section occurred again. This disturbance was so large that it was felt in the rest of the annular flume.

The last solution and the one used in the experiment was the one of a box in the upper part of the cross-section with one open side through which the water enters in the flow. The advantage is that the area of the total cross-section compared to the area of the inlet flow is compared to the other proposed solutions relatively small so the

difference in inlet velocity and flow velocity can be small. This last solution will be better described in the following part.

5.4 Experimental configuration

For the investigations of the secondary flow in a developed flow an annular flume with a rectangular cross-section was constructed by means of an external circular pipe and a circular pipe placed in the centre of the first one (see fig. 1 and 2). The side walls were made of Plexiglas and the bottom of sand. The inlet of the water in the annular flume was done by a box which was as large as the width of the flow and occupied one third of the depth (appendix II 'dimensions of the box') and about 30° of the area of the annular flume. The downstream side of the box in the flow direction was open to let the water enter into the annular flume, the rest of the box was closed because of the higher pressure in it and therefore forcing that the water left the box only from the open side. On top of the box the feeding tube connected it to a pump. On the closed side of the box another box was made where the water was taken out by the pump. On the open side of both boxes a filter was inserted to make sure that a uniform inlet and outlet flow occurred. Later on this filter was changed by another filter made of little stones to force a larger pressure drop over the filter. After this one a filter of smaller material was made to increase the pressure drop over the filter. This filter was made of sand. The pressure inside the box was higher than the pressure outside. Because the water entered the box concentrated in one small place with a high velocity, the pressure was not uniform inside the box and therefore the velocity through the filter and in the annular flume was not uniform. To deal with this problem a filter should be made to force through it a pressure drop, much larger than the pressure differences inside the box. By doing so the influence of the pressure differences inside the box would become less important and the water would enter more uniformly in the annular flume. The uniform flow is needed to make sure that as less disturbances as possible occur in the annular flume and so the velocity gradient will also be as small as possible. The bottom of the box means an extra wall in the flow which should not be present in a real infinite bend so extra friction occurs. In order to have a sufficient free length in the flume this part had to be as small as possible. On the other side the box could not be too small otherwise the filter had to be reduced and that would mean reducing the pressure drop. A smaller filter would require an even finer filter to obtain the same pressure drop. The pressure inside the box may not be excessive for reasons of the strength of the box.

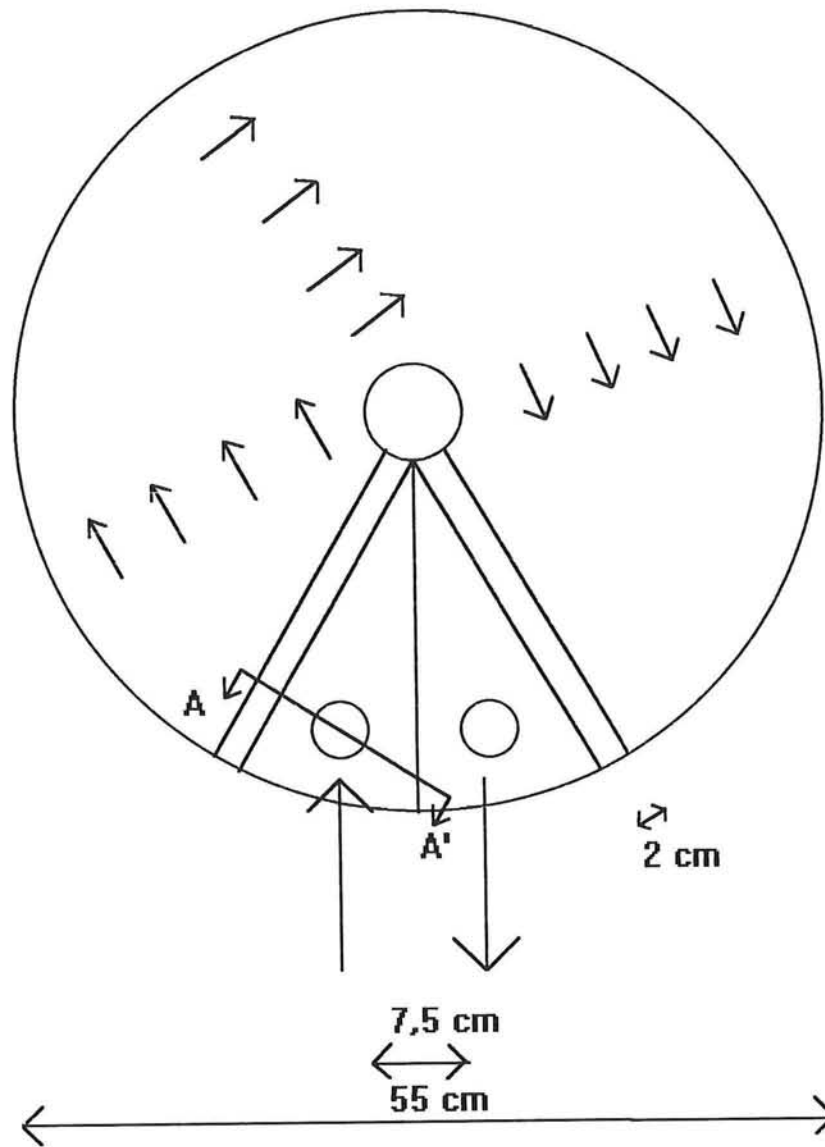


figure 1: experimental configuration of the annular flume

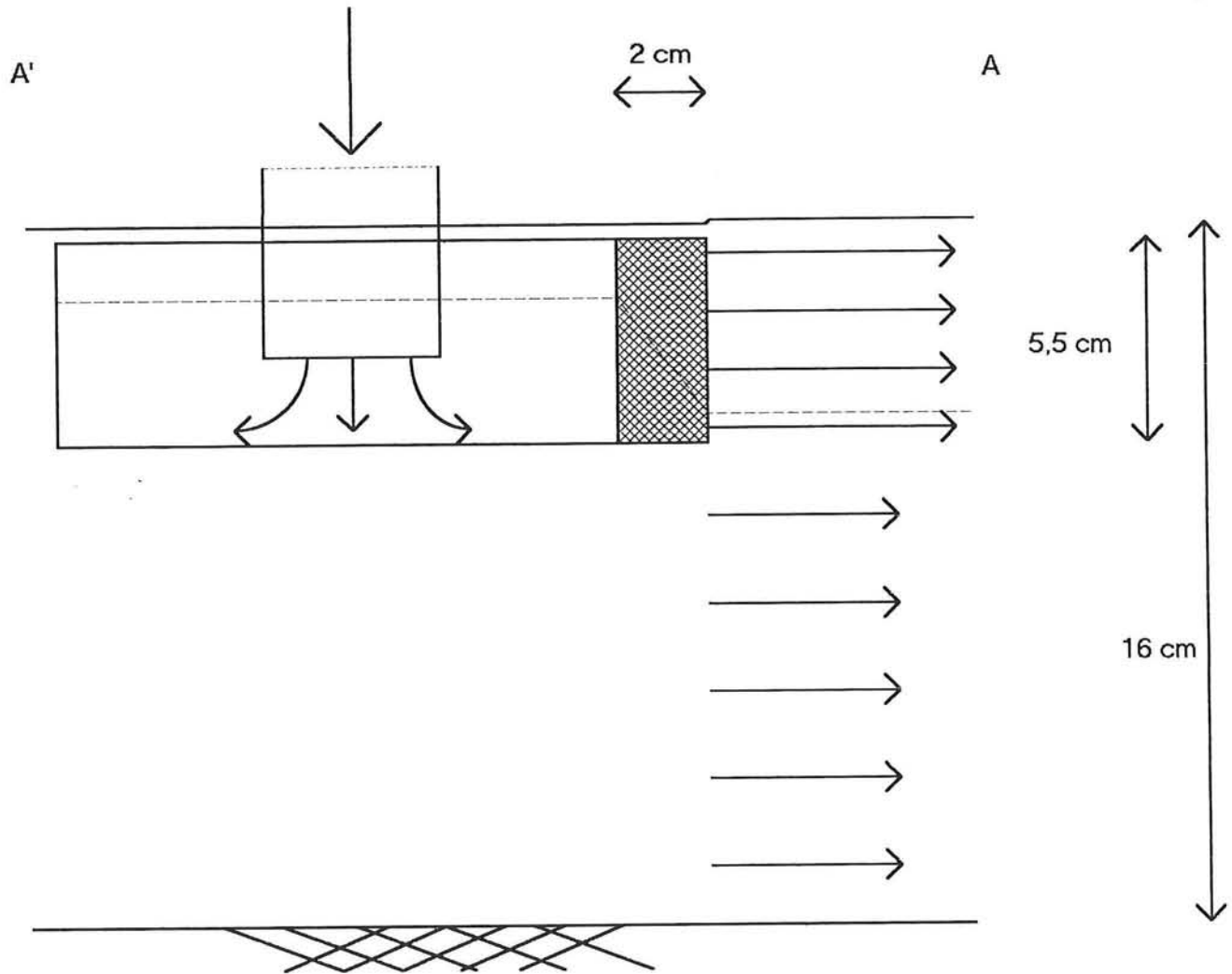


figure 2: cross-section A-A'

The dotted line in figure 2 represents the pressure distribution inside the box, the filter and the flow. Inside the box fluctuations of the pressure are present because the water is injected only in a relatively small part of the box. The inlet flow in the flume would not be uniform if very little or no resistance in the filter were present and the water could flow away immediately. The non-uniform distribution of the pressure inside the box however is not designed in this figure. They should be small compared to the pressure drop over the filter. In the beginning of the experiment the gravel filter ($d_{\text{mean}} \cong 2 \text{ mm}$) was too coarse which means that the pressure drop was only a few millimetres. After inserting sand in the filter ($d_{\text{mean}} \cong 0,5 \text{ mm}$) the pressure drop was of the order of 0,5 m depending on the size of the sand, like can be calculated in the following:

The pressure variations inside the box are of the order of $V^2 / 2g$ which has to be much smaller then the pressure drop over the filter which is of the order of $i \Delta h$ so:

$$V^2 / 2g \ll i \Delta L$$

where V is the flow velocity in the tube, g the gravitational acceleration, i the angle of the slope of the piezometric line over the filter and ΔL the width of the filter.

V can now be calculated easily because during the experiments the discharge is known and constant (40 litres per minute) and also the width of the tubes are known. ΔL can be measured from the filter in the box so the only unknown parameter is i which can be found from graphics showing the Reynolds number against a parameter f which equals:
 $f = 2gid/V^2$

where f is the friction number and d the diameter of the material. When the latter is known the problem is solved.

It was found that the pressure drop over the filter, expressed in meters water-height, in this experiment was 0,40 m using a mean diameter of the sand of 500 μm . A mean diameter of 250 μm resulted in a pressure drop of 1,20 m water-height. The pressure due to the inflow velocity in the box was (again in meters water-height).

$V^2/2g = Q/(\frac{1}{2}D)^2 \pi/60 \text{ s} = 40 \cdot 10^{-3} / (\frac{1}{2} 1,5 \cdot 10^{-2})^2 \pi/60 = 0,77 \text{ m}$ with D is the diameter of the tube and Q the discharge.

So the sand must have a diameter smaller than $\pm 100 \mu\text{m}$.

To avoid an excessive pressure, however, this was not done because a much stronger box is needed then.

5.5 Instrumental equipment

The experiment was done in a deep tank made of Plexiglas with a height of 1 m and a diameter of 0,55 m. In the centre a small tube was placed with a diameter of 0,075 m. The bottom of the flume was made of sand with a mean diameter of 4 mm. The measurements were made with a four quadrant electromagnetic liquid velocity meter which measures the velocity in the two horizontal directions by means of a magnetic field. An electronic signal is given to a control-unit that, in turn, gives another signal to a connected computer. The computer transforms this signal to a velocity and records it. The measurements are not continuously but up to 20 data can be gathered in a second so an almost continuous signal is obtained.

5.6 Data discussion

The horizontal components (U , V) of the flow velocity have been measured in 3 sections at different distances from the box inlet, namely at $\phi = 5^\circ$, $\phi = 160^\circ$ and $\phi = 210^\circ$.

5.6.1 Longitudinal velocities

Section $\phi = 5^\circ$.

This section gives an idea of the distribution of the flow velocity at the inlet of the water in the annular flume and therefore of the boundary conditions.

Due to the concentrated jet leaving the box, the longitudinal velocities in this section are far from uniform (figure 3). A velocity concentration is found at the height of the bottom of the box, 6 centimetres below the free surface. In the part of the cross-section below the box the longitudinal velocities in the outer part are somewhat larger then the ones in the inner part of the cross-section.

Section $\phi = 160^\circ$ and $\phi = 210^\circ$.

The distribution of the longitudinal velocities shows that the velocities increase with increasing depth. The largest velocities are found near the bottom and the smallest velocities near the free surface (figures 5,7). In the computer computation the opposite is found. In the cross-section at 210° the velocities are also measured near the outer wall. It appears that the velocities in this part of the cross-section are larger than the ones in the middle and the inner part.

5.6.2 Radial velocities

When observing the figures of the radial velocity (figures 4,6,8) it can be seen that the velocities near the inner wall are mostly directed towards the outer wall. The velocities near the outer wall are mostly directed towards the inner wall or are nearly zero, at least in the middle and lower part of the vertical. All the radial velocity distributions tend to become smaller, if they are positive, or more negative, if they are negative, very near to the bottom.

5.7 Conclusion of the experiment

The first results of the experiment showed a very non-uniform distribution of the velocities just after the box. It has been tried to make this distribution more uniform but also in the end the distribution was not uniform. The velocities in the other sections are strongly influenced by this distribution so a proper interpretation of the results will be difficult. In all the data the velocities distributions showed the largest velocities near the bottom and the smallest near the free surface. The radial velocities are even more difficult to interpret because the error of the used instrument was of the same order of magnitude as the measured data so care should be taken when drawing conclusions.

A even finer filter should have been used but because of the larger pressure in the box this was not done. The box was not constructed for too large pressures. When trying to arrive at a more uniform inlet flow without increasing the pressure inside the box, the non-uniform distribution of the pressure in the box can be changed by using a larger tube that connects the pump with the box. Ideal would be a tube as large as the area of the box so the pressure would be uniform.

At first the scope of the experiment was to compare the results of a numerical simulation of Trisula with the results of the experiment. However, the results of the experiment can not be reproduced by the numerical simulation since the boundary conditions (inlet and outlet flow) in the experiment were different from the ones that could have been posed in a numerical simulation. Hence, a comparison of the experiment and the simulation is not valid.

6. Numerical research of river bend flows.

6.1 Introduction

In this section the flow in a river bend will be researched numerically. For this research an arbitrary configuration of the bend is taken. The configuration is chosen such that it could fairly be a existing one. Two different configurations are chosen; the first is a strongly curved bend ($R/b=2.5$) and the second is a smoothly curved bend ($R/b=8.2$).

To investigate the numerical approximation and the assumptions and approximations made by the program, the results of the numerical simulation have to be compared, at least qualitatively, with the results of measurements in existing river bends. The features that occur in real river bends are described in chapter 4.

The various input parameters are changed one at a time to investigate their influence on the flow. Also the difference between a rectangular (laboratory) cross-section, a channel cross-section with sloping side walls and a river bend cross-section are researched for the strongly curved case.

The three dimensional numerical simulation is done with Trisula; a simulation program for hydrodynamic flows and transports in two and three dimensions (appendix IV).

6.2 Scope of the research.

The simulation program Trisula is a part of a program package which calculates the flow and sediment transport in various (large) flow cases. The scope of this research is to check its validity and functionality of a three-dimensional numerical simulation of the flow in river bends.

6.3 Comparison of the numerical results with experimental results

In this section the results of a numerical simulation will be compared to the ones of experimental research. At first the configuration and the input files of the bends will be given.

6.3.1 Configuration and input file of the strongly curved bend.

In this section the input parameters of the MD-file of the strongly curved bend, which hereafter will be referred to as the standard bend, will be given and the choices of the various input values will be explained. Next the changes in a MD-file for a changing flow case will be described.

The MD-file for the standard bend is given in appendix VII.

The standard bend is a bend of 180° with a straight inlet and outlet channel. The cross-section is a rectangular one. The radius of the middle of the bend is equal to 250 m, its width is 100 m and its depth is uniform and equals 10 m.

Upstream of the bend the boundary condition is a uniform inlet flow of 1 m/s and downstream the boundary condition is a constant water depth of 10 m.

The initial conditions are a constant water depth of 10 m and zero-velocities everywhere in the flow.

6.3.1.1 Grid.

The schematisation is done with a curvilinear grid. The number of grid points in the ξ -, η - and σ -direction are taken respectively 38, 22 and 20. This means that the number of grid points in the longitudinal direction of the bend equals 37, in the radial direction 21 and in the vertical direction 20 (one extra grid point is required for imposing the boundary conditions at N_{\max} and M_{\max}). The longitudinal grid points are posed such that the straight reach upstream and downstream of the bend consists of 6 computational cells each with a constant length of 250m. The bend is divided in 24 computational cells of $7,5^\circ$.

These numbers are chosen such to obtain a clear pattern of the velocities in the various cross-section perpendicular to the main flow direction. The grid sizes (in the bend) in the radial and longitudinal direction are of the same order of magnitude, namely 5 m respectively ± 30 m. Upstream and downstream of the bend the longitudinal grid sizes are taken much larger. A smaller grid size in the longitudinal direction will increase the total simulation time and does not increase the accuracy (see sensitivity analysis). Later on the influence of the grid size on the accuracy will be investigated by increasing and decreasing the number of grid points.

6.3.1.2 Boundary conditions

The boundary conditions for this flow case are a constant inlet flow (1,0 m/s) at the upstream boundary and a constant water elevation (0,0 m) at the downstream boundary. Since the inlet flow is a uniform one the straight reach before the bend was taken long enough (150 times the water depth) for the flow to reach at a steady, uniform distribution of the velocities before entering the bend. The straight reach downstream of the bend was also taken long enough to smooth out the boundary condition at this position and to be able to calculate the velocities after the exit of the bend. Were the downstream boundary condition posed at the exit of the bend then the boundary condition would be a horizontal free surface at this place which does not correspond with the slope of the free surface in a real river bend.

6.3.1.3 Initial conditions.

The initial water elevation was taken constant and equal to 0,0 m (this means that the depth of flow was 10m everywhere in the flow).

6.3.1.4 Total calculation time and time step.

In the numerical simulation of the flow in this river bend the calculation time was always taken so large that the oscillations of the water level were smaller than 10^{-3} m. This was the case after a simulation time of approximately 400 minutes. The time step was taken 0.05 minute.

(Because this version of Trisula was not the appropriate one for the simulation of a river bend flow the number of errors was larger when calculating with a larger time step and sometimes the program even stopped the calculation. This is the reason for the small time step. The Courant-number in this case is:

$$C = V\Delta t / \Delta x = 1,0 \cdot 0,05 \cdot 60 / 30 = 0,1$$

where C is the Courant-number, V the main velocity, Δt the time step and Δx the grid size.)

Turbulence model.

To model the turbulence, four turbulent closure models are available in Trisula. In this case the k- ϵ model was applied because of the good results this model has given in the past when calculating river bend flows [ref 15]. The influence of the turbulent model will be investigated in the sensitivity analysis.

Processes.

No extra processes were defined as they would only make the simulation more complex and do not give more insight in the phenomenon.

Output

The positions where the output was defined as a series in time were defined on a few arbitrary positions in the flow to check whether the oscillations in the water level were small enough ($< 1 \cdot 10^{-3}$ m) to assume a constant uniform flow in time.

6.4 Data discussion

The results of the simulation have to be checked with measured results. These results are the measurements of De Vriend for a strongly curved bend. They are taken at three verticals in the cross-section; 0,1 times the width from the inner wall, halfway of the bend and at 0,1 times the width from the outer wall. The longitudinal velocities are given three meters upstream of the bend, throughout the bend at 0°, 45°, 90°, 135° and at 180° and three and six meters downstream of the bend. The radial velocities are given at the same positions except for the ones upstream and at the entrance of the bend. Over the vertical ten measured points are given. The results of the comparison are given in appendix VIII

Longitudinal velocities

The comparison of the measured velocities with the calculated ones show that in the inner wall region the predictions are rather well in the lower part of the cross-section. In the upper part the experimental velocities strongly decrease towards the free surface whereas the predicted velocities show a nearly vertical line of the distribution. In the inner wall region, the experimental velocities are upstream and in the early part of the bend smaller than the predicted ones. On the contrary, in the final part and downstream of the bend the experimental velocities are larger.

In the entire cross-section the maximum velocities are experimentally found to lie below the free surface whereas the predicted maximum velocities lie near the free surface.

Downstream of the bend the results differ the most; near the outer wall the magnitudes of the velocities are very different and in the middle of the cross-section the shapes of the velocity distributions are not the same, whereas they are practically equal in the rest of the bend.

Radial velocities

The radial velocities can not be checked because the magnitudes of the measured velocities were not known. The shapes of the velocity distributions, however, are known. It can be observed that in the inner and central part of the cross-section the shapes are practically the same. The position in the vertical where the velocities are zero are in the early part of the bend predicted rather well whereas their differences increase towards the exit and downstream of the bend.

The predicted radial velocities in the outer wall region are totally wrong, the counterrotating cell, which is present in the experiment, is not shown by the simulation.

Conclusions

The radial velocities are predicted rather well upstream and in the early part of the bend. Towards the exit and downstream of the bend their differences increase. The differences between the predicted velocities in the inner wall region and the ones in the outer wall region are larger than the differences between the measured ones. Near the free surface the predicted velocities are wrong, they remain practically the same in the upper half whereas the measured ones decrease towards the free surface.

The shape of the radial velocity distributions are in the inner wall and central region rather well. In the outer wall region, however, they are totally wrong.

6.5 Configuration and input file of the smoothly curved bend.

In this section the input parameters of the MD-file of the strongly curved bend will be given and the choices of the various input values will be explained. Next the changes in a MD-file for a changing flow case will be described.

The standard bend is a bend of 180° with a straight inlet and outlet channel. The cross-section is a rectangular one. The radius of the middle of the bend is equal to 410 m, its width is 50 m and its depth is uniform and equals 5 m.

Upstream of the bend the boundary condition is a uniform inlet flow of 1 m/s and downstream the boundary condition is a constant water depth of 5 m.

The initial conditions are a constant water depth of 5 m and zero-velocities everywhere in the flow.

The computational grid, the boundary conditions and the initial conditions are equal to the ones used in the strongly curved bend simulation.

The computational time step was taken larger. As mentioned before the program was not the appropriate one for a river bend calculation. This means that the stronger the curvature of the bend the smaller the time step to avoid too many errors in the calculation. Hence, the calculational time step in the smoothly curved bend simulation was taken larger. The total

simulation time had to be of the same order of magnitude (400 minutes) as in the strongly curved bend simulation. Therefore the total calculation time could be reduced.

6.6 Data discussion

Longitudinal velocities

From the figures in appendix XI it is observed that the longitudinal velocities in the wall regions are predicted too large. In the middle of the cross-section they are in the greater part of the vertical predicted very well. Near the bottom and near the free surface they are too large. The measured data show that in the inner wall region the maximum velocity lies below the free surface whereas the simulation predicts a nearly vertical distribution of the longitudinal velocities.

Radial velocities

The radial velocities are predicted too small in the greater part of the cross-section. The measured data show a counterrotating secondary flow near the outer wall and therefore the velocities near the free surface are directed towards the inner wall whereas the velocities predicted by the simulation are directed towards the outer wall. This means that no counterrotating secondary cell is predicted. Furthermore it is observed that the differences of the measured and predicted velocities are slightly larger near the bottom than near the free surface and larger in the central part of the cross-section than near the side walls. The point in the vertical where the velocities are zero is predicted too low.

Conclusions

Near the side walls the distributions of the radial velocity component are predicted rather well whereas the longitudinal velocity component is predicted better in the central part of the cross-section. As an approximation the results of the simulation are rather well, however, the velocity differences in the vertical and the counterrotating cell are not predicted well. The differences between the longitudinal component of the measured and the predicted velocity is in the order of magnitude of 10% whereas the radial component shows differences in the order of magnitude of 33%.

6.7 Results of the numerical simulation of the flow in the strongly curved bend.

The standard bend is a strongly curved bend; its ratio of radius of curvature to width is $250/100=2,5$. The Dean number of this bend is $De=Re_{\text{turb}} \sqrt{\varepsilon} = U \cdot D / \nu_{\text{turb}} \sqrt{(d/R)} \cong 1,0 \cdot 10,0 / 0,05 \sqrt{(10/250)} = 40$

where Re_{turb} is the turbulent Reynolds number ($U \cdot D / \nu_{\text{turb}}$), ε is d/R , U is the main flow velocity, D is the depth of flow, ν_{turb} is the turbulent viscosity and R is the radius of curvature. The positions where the velocities are given are in the middle of the computational cells. This means that at the cell boundaries the velocities can only be obtained by means of interpolation between two cells. The velocities are therefore not given exactly at the entrance and the exit of the bend because these are boundaries of computational cells. Inside the bend the positions where the results are given are all obtained by interpolation.

Two velocity distributions are given in each straight reach; at 375m and 125m upstream and downstream of the bend. Inside the bend the velocity distributions are given at $\phi = 3,75^\circ, 45^\circ, 90^\circ, 135^\circ, 177,25^\circ$

The width of the bend is divided in 20 computational cells; from grid point 1 until 21 (see Appendix VI for the positions of the points). The velocities are given at 6 positions; at grid point 3, 6, 10, 13, 17 and 20 which are at respectively 7,5m, 22,5m, 42,5m, 57,5m, 77,5m and 92,5m from the inner wall. The results of the velocities are shown in appendix X.

Longitudinal velocities

Upstream of the bend the distribution of the longitudinal velocities is already under its influence. The velocities are largest near the inner wall and towards the outer wall they gradually become smaller. At 375m upstream of the bend the differences in the longitudinal velocities are small but at 125m upstream of the bend they become larger. This is due to a pressure drop near the inner wall and a larger pressure near the outer wall. The form of their distributions remains practically the same. At $\phi = 3,75^\circ$ the same can be observed, the difference in inner and outer wall velocities has become larger. The flow behaves like a potential flow.

Following the bend until $\phi = 45^\circ$, the velocities increase near the inner wall and decrease near the outer wall except for the ones very near to the wall. Their distributions change due to the secondary flow. Near the outer wall an increase in the velocities in the lower half of the cross-section and a decrease in the upper half can be observed. Near the inner wall the same is found, even stronger than near the outer wall; here the velocity maximum even lies below the free surface. The maximum velocity at the free surface does not lie anymore at the inner wall but a small distance from it.

At $\phi = 90^\circ$, the change of the distribution of the velocities near the walls are extended towards the middle of the cross-section. Only in the middle of the cross-section the velocity distribution remains practically undisturbed. The maximum velocity near the free surface has shifted more and more toward the middle of the cross-section.

At $\phi = 135^\circ$, the entire cross-section is under the influence of the secondary flow and the distributions of the velocities are all changed. The maximum velocity near the free surface lies in the middle of the cross-section and the maximum of the velocities in the vertical near the walls lies below the free surface.

Close to the exit of the bend, at $\phi = 177,25^\circ$, the opposite is found as at $\phi = 3,75^\circ$, the maximum velocity lies near the outer wall and decreases towards the inner wall.

Downstream of the bend the difference in inner and outer wall velocity increases. Their distributions become more logarithmic ones; like the ones found upstream of the bend.

In the figures of appendix X is shown how the longitudinal velocities change near the inner and outer wall upstream and downstream of the bend.

From the figures upstream of the bend it can be observed that at first the velocity distribution needs to adapt to the flow situation; series 1 for the two figures are the boundary condition. The following series differ more and more from each other and finally at 125m upstream of the bend the velocities near the inner wall are much larger than the ones near the outer wall.

Downstream of the bend the opposite is found except that the velocity distributions in the cross-section at the outlet boundary do not have to be equal (as imposed in the program at the upstream boundary). The largest velocities are found near the outer wall. A pressure drop near the outer wall increases the velocities at this position. An increase in the maximum velocity is therefore found at the free surface near the outer wall. Actually this is where the overall maximum velocity is found. Further downstream the velocities gradually shift towards a steady uniform logarithmic distribution.

Radial velocities

It has been observed that the bend is already felt upstream of the bend. At 375m upstream of the bend the radial velocities are directed towards the outer wall but are very small (order of magnitude of mm/s). At 125m upstream of the bend the velocities are all directed towards the inner wall. As observed by the longitudinal velocities a pressure drop near the inner wall occurs at the entrance of the bend. Hence, the radial velocities are all directed towards the inner wall.

At the position $\phi = 3,75^\circ$ the radial velocities are not everywhere directed towards the inner wall but a net flow in the inner wall direction is found still due to the pressure drop at the entrance of the bend.

At $\phi = 45^\circ$ the velocity distribution is the same everywhere; in the lower half the velocities are directed towards the inner wall and in the upper half towards the outer wall. Here the largest velocities are those at the bottom and at the free surface near the inner wall. They become smaller towards the outer wall.

At $\phi = 90^\circ$ the radial velocity distributions show the same shape as the ones at $\phi = 45^\circ$, however, the magnitudes of the velocities have become slightly smaller. The velocities in the middle of the cross-section are larger than the ones near the walls.

At $\phi = 135^\circ$ the magnitudes of the velocities have become even smaller than the ones at $\phi = 90^\circ$ but the shape of the distribution remains the same. The velocities near the walls are the smallest and the ones in the middle of the cross-section are the largest.

All the cross-sections show that zero-velocities are found below the middle of the vertical. From this point until the bottom the radial velocities sharply increase; the largest radial velocities lie near the bottom.

The radial velocity distribution at $\phi = 177,25^\circ$ shows that a net transport of water occurs towards the outer wall. As was found by the longitudinal velocities a pressure drop near the outer wall at the exit of the bend is the reason for this transport. Also at this position the velocities in the middle of the cross-section are the largest and the ones near the walls the smallest.

Downstream of the bend the direction of the velocities is roughly the same but the velocities in the lower half of the cross-section do not increase much anymore towards the bottom. Actually near the bottom they become smaller. Therefore, the maximum velocities are not

found anymore at the bottom but at the free surface and the position of the zero-velocities in the vertical is above the upper half of the vertical. The magnitude of the radial velocities at 375m downstream of the bend is only a few percents of the one in the bend.

Vertical velocities

Considering the figures of the vertical velocities it can be observed that the magnitude of these velocities are much smaller than the horizontal ones. Since these velocities are very small care should be taken when interpreting the velocities near the side walls (as said before Trisula does not impose a shear stresses at the side walls). Therefore they could be strongly different when using shear stresses at the side walls.

In all the cross-sections the vertical velocities in the middle of the cross-section are smaller than the ones near the inner and outer wall. Their order of magnitude is mm/s whereas the main velocity is in the order of magnitude of m/s.

Conclusions

Although the results of this simulation are not compared with measured data (which is done for this flow case in a few cross-sections in chapter 6.4) and, hence, it is not possible to make a quantitative analysis, a qualitative analysis is possible.

It appears that the high velocity region shifts from the inner wall towards the outer wall, however, the simulation predicts that this region lies in the outer wall region between $\phi \cong 135^\circ$ and $\phi \cong 177,25^\circ$. In reality the high velocity region appears to lie in the outer wall region at smaller angles [ref 18]. The longitudinal velocity distributions at the entrance and at the exit of the bend show the same pattern as the one in experiments as well as the development and decay of the secondary flow along the bend [ref 9].

The overall maximum velocity is found both in the simulation and in experiments near the outer wall and downstream of the bend. As mentioned in chapter 6.4, the counterrotating cell is absent in the simulation which is present in experiment [ref 18].

6.8 Sensitivity analysis.

6.8.1 Strongly curved bend

The flow in the standard bend has been simulated, but since a lot of assumptions and approximations, like the modelling of the turbulence, are made the influences of these assumptions and approximations will be investigated in this section. Besides this the change of the configuration of the bend will be investigated; a channel with a non-rectangular cross-section will be used as well as a different radius of the bend. Also the influence of the boundary conditions will be investigated.

From the past chapters it has become clear that a change in radius, flow velocity or depth (and therefore a change in the Dean-number) strongly influences the secondary flow as well as the main flow.

The cases that are researched are the following:

1. The influence of different turbulence closure models and different values for the horizontal turbulent eddy viscosity on the velocities and the vertical turbulent eddy viscosity. The figures are shown in appendix XI
2. The influence of different grid-sizes in longitudinal direction on the accuracy of the velocities. The figures are shown in appendix XII
3. The influence of different time steps on the velocities. The figures are shown in appendix XIII
4. The influence of different radii of curvature on the distribution of the velocities. The figures are shown in appendix XIV
5. The influence of different inlet flow velocities on the pattern of the velocities. The figures are shown in appendix XV
6. The influence of the profile (various channel profiles, river profile). The figures are shown in appendix XVI
7. The influence of the Chézy coefficient. The figures are shown in appendix XVII

6.8.1.1 Influence of the turbulence.

The influence of the turbulence will be investigated by comparing the numerical results of the longitudinal, radial and vertical velocities for different turbulent models as well as by comparing the vertical eddy viscosity distributions.

The modelling of the turbulence in Trisula consists of two parts; one part is (the constant value of) the horizontal turbulent eddy viscosity and the other part is the vertical turbulent eddy viscosity for which a turbulence closure model has to be chosen. The influence of the horizontal turbulent eddy viscosity has been investigated with different values for this parameter and using a constant vertical turbulent eddy viscosity.

In this analysis seven different way to model the turbulence are considered. The four turbulence models are used and the two-dimensional (horizontal) turbulence is investigated. In appendix XI seven series are plotted. They are the results of the calculation with the following closure models:

- | | |
|----------|---|
| Series 1 | The k-ε model and the horizontal eddy viscosity $\nu_h = 1 \cdot 10^{-2} \text{ m}^2/\text{s}$. |
| Series 2 | The k-L model and the horizontal eddy viscosity $\nu_h = 1 \cdot 10^{-2} \text{ m}^2/\text{s}$. |
| Series 3 | A constant value for the vertical viscosity coefficient $\nu_v = 1 \cdot 10^{-6} \text{ m}^2/\text{s}$ and the horizontal eddy viscosity $\nu_h = 1 \cdot 10^{-2} \text{ m}^2/\text{s}$. |
| Series 4 | A constant value for the vertical viscosity coefficient $\nu_v = 1 \cdot 10^{-2} \text{ m}^2/\text{s}$ and the horizontal eddy viscosity $\nu_h = 1,0 \text{ m}^2/\text{s}$. |
| Series 5 | A constant value for the vertical viscosity coefficient $\nu_v = 1 \cdot 10^{-6} \text{ m}^2/\text{s}$ and the horizontal eddy viscosity $\nu_h = 1,0 \text{ m}^2/\text{s}$. |
| Series 6 | A constant value for the vertical viscosity coefficient $\nu_v = 1 \cdot 10^{-6} \text{ m}^2/\text{s}$ and the horizontal eddy viscosity $\nu_h = 10,0 \text{ m}^2/\text{s}$. |
| Series 7 | The algebraic model. |

The velocities will be compared one with another at three grid points in the cross-section at $\phi=90^\circ$; at grid point 6, 11 and 16.

The vertical eddy viscosity distributions will be compared one with another at the 2nd, 3rd and 11th grid point.

Data discussion.

Longitudinal velocities

The velocities are largest in the inner wall region for every velocity distribution except for the 6th series which shows an almost uniform velocity distribution in the cross-section. The largest differences in velocities between the inner and outer wall region are predicted by series 2, though, also series 1 predicts them (especially in the inner wall region and in the middle of the cross-section) larger than the other ones. These two series are also the only ones that calculate the velocity maximum in the inner wall region below the free surface. The velocity distributions for series 3, 4, 5 and 7 give the same results in the inner wall region and in the middle of the cross-section, however, series 4 gives slightly smaller velocities in the outer wall region.

Radial velocities

Again the largest velocities are predicted by series 2 and (slightly less) by series 1 whereas the smallest velocities are given by series 6. In the inner wall region and in the middle of the cross-section the series 3, 4, 5 and 7 do match very well. In the outer wall region series 4 predicts velocities that are much larger than the ones calculated by the other models. All the velocity distributions are approximately straight lines.

Vertical velocities

Considering the figures in appendix XI it can be observed that large differences are calculated by the various models. In the inner wall region all the models calculate positive (upward) velocities and negative (downward) velocities in the outer wall region. The magnitudes of the velocities differ very much; largest velocities are given by series 1 in the inner wall region as well as in the outer wall region. The upward velocities of series 1 and 2 are approximately twice as large as their downward ones, whereas the absolute values of the vertical velocities calculated by the other models, except series 7, are nearly equal. Series 7 shows the contrary of the series 1 and 2 and is in the outer wall region approximately twice as large as in the inner wall region. In the middle of the cross-section all the velocities are directed downward except for series 6 which is still upward. The magnitude of the velocities in the middle of the cross-section are smaller than the ones in wall regions.

Vertical eddy viscosity coefficient

The results of the vertical eddy viscosity coefficient are given at the grid point in the middle of the cross-section, at the first grid point from the inner wall and at the second grid point from the inner wall. These points are chosen mainly to determine the influence of the side walls on the turbulence.

It is seen that the turbulence eddy viscosity is only different when it is calculated with the k- ϵ model. The other models, as well as a varying constant eddy viscosity values, give practically the same results when the predicted values of one model are compared in the central part of the cross-section and the inner wall region.

Conclusion

A large horizontal eddy viscosity coefficient (series 6) results in a uniform flow along the streamlines and in the cross-section. The velocities are not much redistributed resulting in a

small difference in the longitudinal velocities in the cross-section, because only small exchanges of flow momentum occurs. Also the radial velocities are small due to the large horizontal eddy viscosity coefficient. The centre of the secondary flow lies in the outer wall region (series 6) since the vertical velocities in the middle of the cross-section are directed upward whereas all the other models predict downward directed velocities in the middle of the cross-section and, hence, the centre of secondary flow in the inner wall region. The latter can also be the reason for the larger vertical velocities in the inner wall region predicted by the other models compared to series 6.

The integral of the radial velocities in the cross-section is for every series, except series 4, approximately zero. This means that all these models predict that the slope of the free surface is steady and fully developed.

6.8.1.2 Influence of the grid size in longitudinal direction.

The analysis concerns only the change in grid size inside the bend; upstream and downstream the same size and number of the grids are used. The used grid sizes are the one of the standard case where the bend is subdivided in 24 pieces so $\Delta x = \pi R / 24$ ($\Delta \phi = 7,5^\circ$) each and a grid size two times as large so $\Delta x = \pi R / 12$ ($\Delta \phi = 15^\circ$). The velocities are taken at the positions 125m upstream of the bend, at $\phi = 90^\circ$ and 125m downstream of the bend at the 3rd, 10th and 20th grid point. Figures are shown in appendix XII

Data discussion.

Longitudinal velocities

Upstream of the bend the velocity distributions do match very well. Making the grid size two times as large does not affect the distributions at this position. Downstream of the bend, again, the velocities do match very well.

Radial velocities.

Upstream of the bend the radial velocities are very small compared to the ones at $\phi = 90^\circ$. They do differ one from another but the differences in absolute values are very small.

At $\phi = 90^\circ$ and downstream of the bend the same phenomenon can be observed. The velocity distributions are approximately the same for the different grid sizes except for the ones in the outer wall region. They show much smaller velocities for the flow with the largest grid size.

Conclusion

Increasing the grid size and making it two times larger than the one in the standard case does not affect the accuracy of the computation. Using an even coarser grid, four times as large (not shown in the figures), changes the velocity distributions in the bend but hardly upstream and downstream of the bend. A coarser grid gives larger velocities in the middle of the cross-section and smaller (longitudinal and radial) velocities near the walls.

6.8.1.3 Influence of the time step in the simulation.

The simulation starts with all velocities set to zero. At the upstream boundary a flow enters the computational area and causes oscillations in the water level. The amplitude of the oscillations have disappeared or have become less than a certain value after the spin-up time of the model. At this time the computational results can be taken. A larger time step would reduce the simulation time needed to arrive at this situation.

The influence of the time step in the simulation is investigated by comparing the numerical results of various simulations with 5 different time steps. The full time steps were $\Delta t=0,05\text{min}$, $\Delta t=0,5\text{min}$, $\Delta t=1,0\text{min}$, $\Delta t=2,0\text{min}$ and $\Delta t=4,0\text{min}$; this means that the Courant numbers (Courant number= $V\Delta t/\Delta x \approx 1\Delta t/33$) are respectively 0,09 0,9 1,8 3,6 and 7,2. The longitudinal and the radial velocities in the middle of the cross-section at $\phi=90^\circ$ and 125m downstream of the bend will be considered here. The figures are shown in appendix XIII

Data discussion

Longitudinal velocities

The figures show that the longitudinal velocities increase over the entire depth for increasing time step. The differences between the velocities calculated with $\Delta t=0,05\text{min}$ and $\Delta t=0,5\text{min}$ are approximately zero in both the cross-sections. Increasing the time step to 4 minutes the differences at $\phi=90^\circ$ deviate $\pm 3\%$ from the velocities calculated with $\Delta t=0,05\text{min}$. At 125m downstream of the bend these differences are even smaller.

Radial velocities

The opposite is found for the radial velocities for which the differences between the various velocity distributions are smallest at $\phi=90^\circ$. At $\phi=90^\circ$ the absolute values of the velocities calculated with the largest time step are slightly larger than the ones calculated with the smallest time step. On the contrary, at 125m downstream of the bend the velocities calculated with the largest time step are larger over the entire vertical; this means that the absolute values of the velocities near the bottom are slightly smaller whereas they are slightly larger near the free surface than the ones predicted with the smallest time step

Conclusions

The influence of the time step does play an important role in the computation since the used version of Trisula was not the appropriate one for a river bend simulation. On the contrary it does not play an important role for the accuracy of the calculation when using time steps up to 1 minute. Larger time steps give small changes. Considering the smallest and largest time step, the largest was 80 times as large as the smallest however the largest difference in the velocities was $\pm 3\%$.

6.8.1.4 The influence of the radius of curvature.

In the literature the influence of the radius of curvature has been described. With this analysis will be investigated whether Trisula shows the same phenomena of the velocity pattern, the slope of the free surface and the development and decay of the secondary flow as found by experiments for changing radii of curvature.

The influence of the different radii of curvature are investigated for 5 different radii of curvature; $R=125\text{m}$, $R=250\text{m}$, $R=500\text{m}$, $R=1000\text{m}$ and $R=1500\text{m}$ which will be referred to as respectively flow case 1, 2, 3, 4 and 5. The results of the simulation of the horizontal velocities are taken at three cross-sections along the bend; at $\phi=3,75^\circ$, $\phi=90^\circ$ and $\phi=177,25^\circ$. In these cross-sections the 6th, 11th and 16th grid point are taken. The figures are shown in appendix XIV

Data discussion.

Longitudinal velocities.

From the figures it appears that at $\phi=3,75^\circ$ the velocities increase in the inner wall region and decrease in the outer wall region for decreasing radius of curvature. They all decrease from the inner wall towards the outer wall, however, for the largest radii of curvature the longitudinal velocity distributions are nearly uniform in the cross-section. The velocity distributions in the inner wall region are steeper than the ones in the middle and outer wall region. The maximum velocities are found at the free surface.

At $\phi=90^\circ$ the largest velocities for the first flow case are, like at $\phi=3,75^\circ$, found in the inner wall region. The velocity distributions of the other flow cases show an outward movement of the high velocity region; for case 1 the maximum velocity lies in the middle of the cross-section and for the cases 4 and 5 the maximum velocity is found in the outer wall region. Considering the cases 3, 4 and 5, the maximum velocities in the vertical are found below the free surface, whereas in the first two cases they lie at the free surface except for the distribution in the inner wall region for $R=250\text{m}$ where the maximum velocity lies below the free surface. Again, the velocity distributions for the cases 4 and 5 match rather well.

Near the exit of the bend, at $\phi=177,25^\circ$, the velocities increase from the inner wall towards the outer wall. Every distribution shows the same pattern; the velocity close to the bottom is smallest and the maximum velocity in the vertical lies below the free surface. The largest difference between the maximum velocity in the vertical and the velocity at the free surface is found in the first case and decreases with increasing radius. The distributions of the cases 4 and 5 are slightly different in the outer wall region but do match very well in the central and the inner wall region.

Radial velocities

The radial velocities are in the lower part of the cross-section directed towards the inner wall and are directed towards the outer wall in the upper part of the cross-section except for the first case where they are directed towards the inner wall everywhere in the cross-section. All the velocity distributions show that the velocities are largest in the middle of the cross-section and smallest in the outer wall region although the distributions of the cases 4 and 5 hardly differ in the various parts of the cross-section. The integral of the velocity of the two largest radii equals approximately zero whereas the integral of the other radii show an increasing negative value with decreasing radius which means a net flow towards the inner wall.

At $\phi=90^\circ$ the magnitude of the velocities of the first three cases has increased reasonably whereas it has increased only slightly in the last two cases. The largest flow velocities in the first case are found in the inner wall region and they decrease towards the outer wall. On the other hand the contrary is observed for the flow cases 4 and 5. The flow cases 2 and 3 have the largest velocities in the middle of the cross-section. The last two cases show that the largest positive velocities are not found at the free surface but below it.

At $\phi=177,25^\circ$ the velocities are mostly directed towards the outer wall. The integral of the velocities in the cross-section is approximately zero for the cases 4 and 5 and increases with decreasing radius. The first case shows a large net flow towards the outer wall (the contrary is found at $\phi=3,75^\circ$). The velocity magnitudes are far more larger then the ones at $\phi=3,75^\circ$. All the radial velocities show that at $\phi=90^\circ$ and $\phi=177,25^\circ$ an increasing radius results in decreasing absolute velocities.

Conclusions

Trisula does not simulate a counterrotating secondary flow that occurs in the upper half of the cross-section near the outer wall when the Dean number is larger then approximately 50. Since the wall shear stresses are assumed zero this counter rotating secondary flow will not occur.

It appears that all the flow cases show a transverse displacement along the bend of the high velocity zone from the inner wall towards the outer wall. Therefore, at the exit of the bend, the maximum longitudinal velocities lie in the outer wall region, except for the first flow case. The longitudinal velocity distributions in the vertical changes from approximately logarithmic at the entrance of the bend to a distribution with the maximum velocity below the free surface more downstream. This change starts in the inner wall region and extends to the outer wall.

The intensity of the radial velocities increases for all flow cases along the bend. Though the same mechanism can be found for the net inward and outward flow at respectively the entrance and the exit of the bend their values differ strongly. The ratio of the (absolute) radial velocity at the exit of the bend to the (absolute) radial velocity at the entrance of the bend increases with decreasing radius of curvature from approximately 1 for the flow case with $R=1500m$ to approximately 3 for the flow case with $R=125m$.

6.8.1.5 Influence of the inlet flow velocity

The inlet flow velocity changes the velocities inside the bend. The velocity is one of the parameters that determine the Dean number. Here, the influence of the various inlet flow velocities will be investigated. Because the velocities in the bend are different for different inlet flow velocities the analysis is done for normalised velocities; this means that the values are given as the flow velocities divided by the inlet flow velocity. The used inlet flow velocities are 1m/s, 2m/s, 4m/s and 0,5m/s represented by respectively series 1, 2, 3 and 4.

The normalised longitudinal and radial velocities are taken in the cross-section at $\phi=90^\circ$ at the grid points 3, 6, 10, 13, 17 and 20. The figures are shown in appendix XV.

Data discussion.

Longitudinal velocities

In the inner wall region at grid point 3 the series 2 and 3 that represent the larger velocities predict a velocity maximum below the free surface whereas the series 1 and 4 predict them at the free surface. At the 6th grid point the same is found although the velocity maximum predicted by series 2 and 3 lies higher in the vertical then at the 3rd grid point. The series 1, the standard case, shows a slight decrease in the velocity distributions from the inner wall towards the outer wall. Compared to these distributions the series 4 shows smaller velocities in the inner wall region and larger ones in the outer wall region but they still decrease towards

the outer wall. This means that its differences between inner and outer wall velocities are smaller than the ones in the standard case. Considering the series 2 and 3 it can be observed that their differences between the inner and outer wall region are larger than the ones in the standard case. The shape of their distributions are the same in the entire cross-section.

Radial velocities

The distributions of the radial velocities differ slightly in the central part of the cross-section and reasonably near the side walls when the inlet flow velocity is changed. The adimensional velocity increases with increasing inlet flow velocity. The difference is larger near the bottom than near the free surface. It can also be observed that the position in the vertical where the radial velocities are zero lies higher for increasing inlet flow velocity.

Conclusion

A changing inlet flow velocity changes the distributions of the adimensional velocities. This is due to the changing Dean number. An increasing inlet flow velocity increases the turbulent viscosity coefficient, however, in the simulation the Dean number does not increase linearly with increasing velocity; the increase is much smaller. Would the turbulent viscosity coefficient vary linearly with a varying velocity then the Dean number would remain the same. As the turbulent viscosity coefficient does not increase as the inlet flow velocity it can be concluded that the Dean number increases resulting in a different velocity distribution shape.

6.8.1.6 Influence of the cross-sectional profile.

The influence of the cross-sectional shape was investigated by changing the profile. 5 different profiles were considered:

1. The initial rectangular cross-section
2. A channel profile with side walls 1:1 and a plane bottom
3. A channel profile with side walls 1:2 and a plane bottom
4. A channel profile with side walls 1:3 and a plane bottom
5. A river profile with a parabolic cross-section in the straight parts and a gradually changing profile, with steep side walls and a large depth near the outer wall and a smoothly sloping side wall and a small depth near the inner wall, at the entrance of the bend. The results are taken at $3,75^\circ$ downstream of the entrance of the bend, halfway of the bend and $3,75^\circ$ upstream of the exit of the bend

Hereafter, these profiles will be referred to as profile 1, 2, 3, 4 and 5 respectively.

The results of the simulations are shown in appendix XVI.

Data discussion.

Longitudinal velocities

The largest differences in the velocity distributions are found near the side walls. This is due to the different flow depths, however, the shapes of the distributions are approximately equal except for the river profile which, near the side walls, increases more with depth than the other ones. An interesting feature is that near the side walls, at $\phi=90^\circ$ and at the exit of the bend, the difference in maximum velocity, which lies below the free surface (or the distribution is nearly

vertical), and the velocity at the free surface is the largest for profile 1 whereas the opposite is found (or there is hardly any difference) in the middle of the cross-section.

In the middle of the cross-section hardly any differences are found between the profiles except for profile 5 since this one has a different flow depth in the middle of the cross-section. Although having a larger flow depth in the middle of the cross-section, the velocity at the free surface in profile 5 is not larger than the other ones.

Radial velocities

The distributions of the radial velocity are all the same except for the one of profile 5. They all show that already at $7,5^\circ$ downstream of the bends entrance and $7,5^\circ$ before the bends exit the secondary motion is present. There is approximately no net transport in radial direction at the entrance whereas there is a net outward transport near the exit of the bend. Profile 5 shows the contrary; a strong outward motion at the bends entrance and an inward motion at the bends exit. The radial velocities of profile 1 are near the bottom and near the surface slightly larger than the other ones.

Conclusions

The most striking feature of this research is the distribution of the radial velocities for profile 5; the river cross-section. It shows exactly the opposite as one would expect to occur in a bend. An explanation can be found by considering that the bottom configuration in this case is implied and can be wrong for this flow case. In a real bend this may be different and the cross-sectional shape can change in time and adapt to the flow. In the simulation the cross-sections change when entering the bend from parabolic, and therefore symmetric, to asymmetric the cross-section having a larger depth near the outer wall. The flow is therefore forced to flow in the outward direction. This may be the same in reality on the other hand it can fairly be true that in the simulation this change of cross-sectional shape occurred over a too short distance. From the figures of the longitudinal and radial velocities it can be observed that the side walls do have some influence on the flow, however, the distributions of both the longitudinal and radial velocities remain practically the same, especially away from the side walls.

6.8.1.7 The influence of the Chézy coefficient

The simulations of the other cases were all done with a Chézy coefficient of $65 \text{ m}^{1/2}/\text{s}$. In this investigation the Chézy coefficient is taken equal to $40 \text{ m}^{1/2}/\text{s}$ and $95 \text{ m}^{1/2}/\text{s}$. The results of the simulation are shown in appendix XVII. (The figures differ from the previous figures; the previous figures showed distributions in cross-sections perpendicular to the main flow whereas the figures in appendix XVII show them along the streamlines.) The results of the longitudinal velocities are taken at 125m upstream of the bend, at $\phi=3,75^\circ$, $\phi=45^\circ$, $\phi=90^\circ$, $\phi=135^\circ$, $\phi=177,25^\circ$, at 125m and at 375m downstream of the bend

Data discussion.

Longitudinal velocities

From the figures it is observed that the longitudinal velocities decrease with increasing Chézy coefficient. Actually at the entrance of the bend and near the inner wall the largest velocities

are found for a Chézy coefficient of $40 \text{ m}^{1/2}/\text{s}$ and the smallest for a Chézy coefficient of $95 \text{ m}^{1/2}/\text{s}$. This pattern gradually changes and at the exit of the bend the smallest velocities are found for a Chézy coefficient of $65 \text{ m}^{1/2}/\text{s}$. In the middle of the cross-section and near the outer wall the velocity distributions for the Chézy coefficient equals $40 \text{ m}^{1/2}/\text{s}$ show the largest velocities and the ones for the Chézy coefficient equals $95 \text{ m}^{1/2}/\text{s}$ show the smallest velocities.

Radial velocities

The radial velocities show the same pattern for the various Chézy coefficients, however, the values near the free surface and the bottom are larger for the case with a Chézy coefficient of $40 \text{ m}^{1/2}/\text{s}$ and decrease with increasing Chézy coefficient.

Conclusions

In real rivers the formula of Chézy is usually applied to give rough estimates of the flow velocity. In this formula an increasing Chézy coefficient corresponds with an increasing velocity. In the simulation of a river bend flow the opposite is found for both the longitudinal and radial velocities. The shape of the velocity distribution of the simulation with a Chézy coefficient of $40 \text{ m}^{1/2}/\text{s}$ shows that the velocity is redistributed reasonably throughout the bend whereas the shape of the velocity distribution of the simulation with a Chézy coefficient of $95 \text{ m}^{1/2}/\text{s}$ shows that the velocity hardly changes throughout the bend.

6.8.2 Smoothly curved bend

The following cases have been researched for this flow case.

1. The influence of the turbulence and changing values for the constant viscosity. The figures are shown in appendix XVIII.
2. The influence of the Chézy coefficient. The figures are shown in appendix XIX.
3. A no-slip/partly free-slip boundary condition at the side walls. The figures are shown in appendix XX.

6.8.2.1 The influence of the turbulence models.

In the case of a strongly curved bend the turbulence showed not to play an important role in the distribution of the velocities. Since the bend here concerned is a smoothly curved one the influence can possibly play a more important role. The four turbulent closure models of Trisula have all been applied. When simulating with a constant value for the eddy viscosity coefficient an estimated depth averaged value was used. Since the calculated values are to be confronted with measured data which were available for the cross-section at 135° this is the position in the bend where the computational results are given. The figures are shown in appendix XVIII.

Data discussion

Longitudinal velocities

The largest differences between the velocity distributions in the inner wall region and in the outer wall region was found when the k- ϵ model was used. The smallest differences were given with k-L model. In the middle of the cross-section the velocity distributions are practically the same for all the models. Especially the simulations with the algebraic closure model and the constant eddy viscosity coefficient give results which differ very little one from another.

Radial velocities

The velocity distributions calculated with a constant turbulence viscosity coefficient, the k-L model and the algebraic closure model give practically the same results. The k- ϵ model gives velocities which are larger near the bottom and near the free surface. The position in the vertical where the velocity is zero is for all the models the same except for the distribution near the outer wall calculated with the k- ϵ model.

Conclusions

The turbulence has become more important in this flow case than in the case of a strongly curved bend. The k- ϵ model gives results that are different from the other models (larger velocities) whereas the other models predict very much the same results.

6.8.2.2 Influence of the Chézy coefficient

The Chézy coefficient, the coefficient that accounts for the bottom friction, is normally in river flow a very important parameter. Therefore this parameter is likely to play an important role in river bend flows. In the strongly curved flow case it was a change in this parameter that had the most influence on the velocity distributions. The figures are shown in appendix XIX.

Data discussion

Longitudinal velocities

The differences between the velocities near the inner wall and the outer wall are larger for the simulation with Chézy coefficient equals 65 m^{1/2}/s than with 95 m^{1/2}/s. The overall largest velocities are in the entire cross-section predicted with a Chézy coefficient equal to 40 m^{1/2}/s. The shape of the velocity distributions with a Chézy coefficient equal to 65 m^{1/2}/s and 95 m^{1/2}/s is the same; increasing from the bottom to half way of the vertical and then rather steep towards the free surface. The one with a Chézy coefficient equal to 40 m^{1/2}/s is less steeper; smaller velocities near the bottom and larger near the free surface are observed.

Radial velocities

The magnitude of the radial velocities increase with decreasing Chézy coefficient generally. The velocities predicted with a Chézy coefficient equal to 40 m^{1/2}/s and 65 m^{1/2}/s are nearly the same in the middle of the cross-section whereas their differences increase towards the side walls. The velocities with Chézy coefficient equal to 95 m^{1/2}/s are smaller everywhere in the cross-section.

Conclusions

An increase in the Chézy coefficient results in straight river flows in an increase of the velocities. In the simulation of a river bend this is not the case. Actually the opposite is found. The differences of the velocities predicted with the different values of the Chézy coefficient increase towards the outer wall.

6.8.2.3 The influence of the boundary condition (no-slip/partly slip) at the side wall

From the side wall to the first calculational grid point a relation must be found to account for this area. A no-slip condition (velocities at the side wall are zero) can be imposed; a condition which is physically correct. The figures are shown in appendix XX.

Data discussion

Longitudinal velocities

Close to the inner wall the predictions of the velocities are practically the same for the different boundary conditions. In the central part of the cross-section the velocities predicted with a no-slip condition are smallest and the largest ones are predicted with a partly-slip condition with a roughness length of $1 \cdot 10^{-4}$ m. Close to the outer wall the velocities with a no-slip condition are largest whereas the smallest are predicted with a partly-slip condition with a roughness length of $1 \cdot 10^{-4}$ m.

Radial velocities

The velocity distributions away from the side walls are equal for all the imposed boundary conditions. Near the free surface and near the inner wall the velocities predicted with a no-slip condition are slightly larger whereas they are smaller near the outer wall.

Conclusions

The boundary condition does not play an important role in the prediction of the radial velocities and also for the prediction of the longitudinal velocities the differences are small. The radial velocities are practically the same and the longitudinal velocities vary only slightly. The simulation with a no-slip condition gives the best results with the measured data.

7. Conclusions and recommendations

Conclusions

It can be concluded that the velocities predicted by the numerical simulation program Trisula give a rather good approximation of the reality. Qualitatively, the program give good results, it is capable of predicting the main features occurring in river bend flows except for the counterrotating secondary flow at sufficiently large Dean numbers, however, care should be taken when interpreting the quantitative results of the simulation as they may differ reasonably from experimental results. The velocity distributions differ strongly for changing radius of curvature. Strongly curved bends show at the entrance of the bend, a high velocity region near the inner wall which gradually moves towards the outer wall. Secondary velocities are relatively strong and the maximum velocity lies below the free surface. Increasing the radius of curvature results in relatively smaller secondary velocities as well as a displacement of the high velocity region at the entrance of the bend towards the central part of the bend. The most striking feature is the influence of the Chèzy coefficient. An increase in the Chèzy coefficient results in a decrease of the main velocities.

In strongly curved bends the longitudinal velocities give a rough approximation of the reality; the order of magnitude of the velocities is rather well, however, the shapes of the velocity distributions differ strongly from experimental ones, especially in the upper part and near the exit of the bend. The displacement of the high velocity zone from the inner wall region towards the outer wall is predicted well, however, in reality this occurs over a shorter distance.

The predictions of the eddy viscosity coefficient is wrong, however, its influence on the prediction is very small, only a large constant value of the eddy viscosity coefficient results in less redistributed velocities throughout the bend.

The time step in the simulation does hardly affect the accuracy of the predictions as well as the grid size, if not a very coarse grid is used.

An increase of the inlet flow velocity increases the Dean number and by doing so the pattern of the velocity distributions.

The influence of the cross-sectional profile is small and is only felt near the side walls. In the central part of the cross-section the velocity predictions remain practically equal.

In smoothly curved bends the prediction of the longitudinal velocities is very well in the central and outer wall region. Close to the inner wall they are predicted too large. The radial velocities are predicted far too small ($\pm 30\%$) and near the outer wall even their direction is wrong due to the lack of the counterrotating cell in the prediction.

The turbulence plays a more important role than in the flow in a strongly curved bend.

The boundary conditions at the side walls do hardly affect the distributions of the velocities in the cross-section; a no-slip condition gives the best results when they are compared with experimental data.

The main problem in the experiment was the inlet and outlet boundary condition. A non-uniform inlet and outlet flow velocity, due to a non-uniform pressure distribution inside the inlet and outlet

boxes, resulted in disturbances that were too large and could not be smoothed out throughout the annular flume. Therefore, a uniform steady flow was not reached.

Recommendations

Future research should be done to the following:

- * The flow pattern should be compared with experimental data at more positions in the bend to investigate the redistribution of the main flow and the development and decay of the secondary flow throughout the bend.
- * A combination of the turbulence, the boundary conditions at the side walls and the Chèzy coefficient should be searched for which the flow is predicted the best.
- * An important part in the sediment transport is the velocity very close to the bottom and side walls. A closer look to the velocities at these positions should be taken.
- * A finer grid near the bottom and the side walls should be used.
- * If one wants to do experimental research to the flow pattern in an infinite river bend as was done in this research, more attention should be paid to the boundary conditions. The filters in the inlet and outlet boxes have to be refined and, hence, the boxes must be constructed stronger.

When using the numerical simulation program Trisula for determining the flow pattern, it depends on the flow case whether the results should at best be used as approximations of the reality or as rough estimates of the velocity distribution. Roughly, a decrease in radius of curvature results in a decrease of the accuracy of the predictions.

Literature

1. A.K. Ananyan - Fluid flows in bends of conduits 1965
2. J.C. Bathurst / C.R. Thorne / R.D. Hey - Secondary flow and shear stress at river bends 1979 (j. of hydr. div.)
3. R. Booij - Turbulentie in de waterloopkunde 1992
4. R. Booij / J. Tukker - 3-dimensional laser doppler measurements in a curved flume
5. U.K. Choudhary / S. Narasimhan - Flow in 180° open channel rigid boundary bends 1977 (j. of hydr. div.)
6. J.R.D. Francis / A.F. Asfari - Velocity redistribution in wide, curved open channel flows 1971 (j. of hydr. res.)
7. P.Ph. Jansen - Principles of river engineering 1994
8. B.E. Launder / D.B Spalding - Mathematical models of turbulence 1972
9. M.A. Leschziner / W. Rodi - Calculation of strongly curved open channel flow 1979 (j. of hydr. div.)
10. J.P.Th. Kalkwijk / H.J. de Vriend - Computation of the flow in shallow river bends 1980 (j. of hydr. res.)
11. N.E. Kondrat'ev et. al. - River flow and river channel formation 1959
12. Manual Trisula 1994
13. Pennekamp/Booij
14. G. Pezzinga - Applicazione del modello K- ϵ non lineare allo studio di circolazioni secondarie 1990 (convegno di idraulica e costruzioni idrauliche-Cosenza)
15. W. Rodi - Turbulence models and their application in hydraulics 1980
16. Ch. G. Speziale - On non-linear K-L and K- ϵ models of turbulence 1986 (j. of fluid mech.)
17. H.J. de Vriend - Velocity redistribution in curved rectangular channels 1980 (j. of fluid mech.)
18. H.J. de Vriend - Steady flow in shallow channel bends 1981(thesis)

Appendix I

The continuity equation and the Reynolds (is the Navier-Stokes equation with the turbulent quantities) for the mean flow are:

$$\bar{C} : \nabla_j \bar{v}_j = 0$$

$$RE (= N.S.): \frac{\partial}{\partial t} (\rho \bar{v}_i) + \nabla_j (\rho \bar{v}_i \bar{v}_j) + \nabla_j q_{ij} + \nabla_i \bar{p} - \eta \nabla_j^2 \bar{v}_i = \bar{k}_i$$

The continuity equation and the Reynolds equations for the fluctuating (turbulent) flow are:

$$C' : \nabla_j v'_j = 0$$

$$Re' : \frac{\partial}{\partial t} (\rho v'_i) + \nabla_j (-\rho \bar{v}_i v'_j + \rho \bar{v}_i v'_j + \rho v'_i \bar{v}_j + \rho v'_i v'_j) + \nabla_i p' - \eta \nabla_j^2 v'_i = k'_i$$

To obtain the energy of the mean respectively the turbulent flow the Navier-Stokes equations of the mean respectively fluctuating flow must be multiplied by \bar{v}_i respectively v'_i . With use of the continuity equation and given that

$$q = q_m + q_t$$

$$q_m = \frac{1}{2} \rho \overline{v_j v_j}$$

$$q_t = \frac{1}{2} \rho \overline{v'_j v'_j}$$

it can be deduced that

$$E_m : \frac{\partial \bar{q}_m}{\partial t} + \nabla_j (\bar{v}_j \bar{q}_m) + \nabla_j \left(\overline{p v_j} + \overline{v_i (-\eta (\nabla_i v_j + \nabla_j v_i))} + q_{ij} \bar{v}_i \right) = q_{ij} \nabla_j \bar{v}_i - \frac{\eta}{2} \overline{(\nabla_i v_j + \nabla_j v_i)^2} + \bar{k}_i \bar{v}_i$$

$$E_t : \frac{\partial q_t}{\partial t} + \nabla_j (\bar{v}_j q_t) + \nabla_j \left(\overline{p' v'_j} + \overline{v'_i (-\eta (\nabla_i v'_j + \nabla_j v'_i))} + \frac{1}{2} \rho \overline{v'_i v'_i v'_j} \right) = -q_{ij} \nabla_j \bar{v}_i - \frac{\eta}{2} \overline{(\nabla_i v'_j + \nabla_j v'_i)^2} + \bar{k}'_i \bar{v}'_i$$

- A change of q_t in time
 B convection of q_t by the mean flow
 C diffusive transport by the pressure and viscosity shear-stress-fluctuations and turbulent velocity-fluctuations
 D contribution of the Reynolds-stresses
 E dissipation to the heat-motion
 F contribution of the fluctuations of external forces

To obtain a differential transport equation for the turbulent kinetic energy per unit mass k the equation for the turbulent fluctuations of q_t is manipulated in such a way that a useful equation remains; that means an equation which only contains the variables k and l (or ϵ) the gradients of the mean velocity and some empirical constants. In order to arrive at such an equation the following steps are made:

At first all diffusive transports, the term C in the E_t -equation, are replaced by one gradient-type transport-term

$$\nabla_j \left(\overline{p' v'_j} + \overline{v'_i (-\eta (\nabla_i v'_j + \nabla_j v'_i))} + \frac{1}{2} \rho \overline{v'_i v'_i v'_j} \right) = -\frac{\rho v_t}{\sigma_k} \nabla_j k$$

in which for the constant σ_k is often taken 1.0

Secondly the term E is modified by the following steps: the dissipation occurs at the smallest turbulent length-scales but the amount of dissipation depends on the exchange from the larger turbulent length-scales to smaller ones. Considering the dimensions the term E is replaced by:

$$\frac{\eta}{2} \overline{(\nabla_i v_j' + \nabla_j v_i')^2} = c_d \rho \frac{k^{\frac{3}{2}}}{l}$$

in which l depends on the large length-scales

If the term F is neglected (the fluctuations of the external forces can be assumed small) and the remaining equation is divided by ρ the following transport equation for the turbulent kinetic energy per unit mass is obtained:

$$\frac{Dk}{Dt} = \nabla_j \left(\frac{\nu_t}{\sigma_k} \nabla_j k \right) + \nu_t \left[(\nabla_{ji} \bar{v}_i)^2 + (\nabla_j \bar{v}_i)(\nabla_i \bar{v}_j) \right] - c_d \frac{k^{\frac{3}{2}}}{l}$$

with $\frac{Dk}{Dt} = \frac{\partial k}{\partial t} + v_j \nabla_j k$

which is only written in a slightly different form but is the same as

$$\frac{\partial k}{\partial t} + \frac{\partial}{\partial x_j} \left(u_j - \frac{\nu_t}{\sigma_k} \frac{\partial k}{\partial x_j} \right) + P + c_d \frac{k^{\frac{3}{2}}}{l} = 0$$

in which $P = -\overline{u_i u_j} \frac{\partial \bar{u}_i}{\partial x_j}$

and

$$\overline{u_i u_j} = -\nu_t \left(\frac{\partial \bar{v}_j}{\partial x_i} + \frac{\partial \bar{v}_i}{\partial x_j} \right)$$

Appendix II

Dimensions of the box

It is important that a small difference between the inlet velocity and the flow velocity occurs so only a small distance is needed for the flow to arrive at a fully developed flow. This means that a relation has to be found between the discharge of the inlet and the flow on one side and the height of the box and the depth of flow on the other side. An optimum can then be found for the height of the box and the inlet discharge.

Consider the following schematization of the box and assume that

- the difference in water level upstream the box (section 1) and downstream of the box (section 2) divided by the longitudinal distance is the slope of the water level in longitudinal direction.
- the pressure distribution is hydrostatic everywhere
- the friction of the bottom and the walls can be taken together as one constant friction coefficient f
- the mean depth of flow is the mean of the water level upstream of the box and the water level downstream of the box
- the radial slope of the water level is left out of consideration
- the water level at the position of the exit of the box is equal to the water level upstream of the box; a certain distance downstream of the box the water level is larger (see figure II.1).

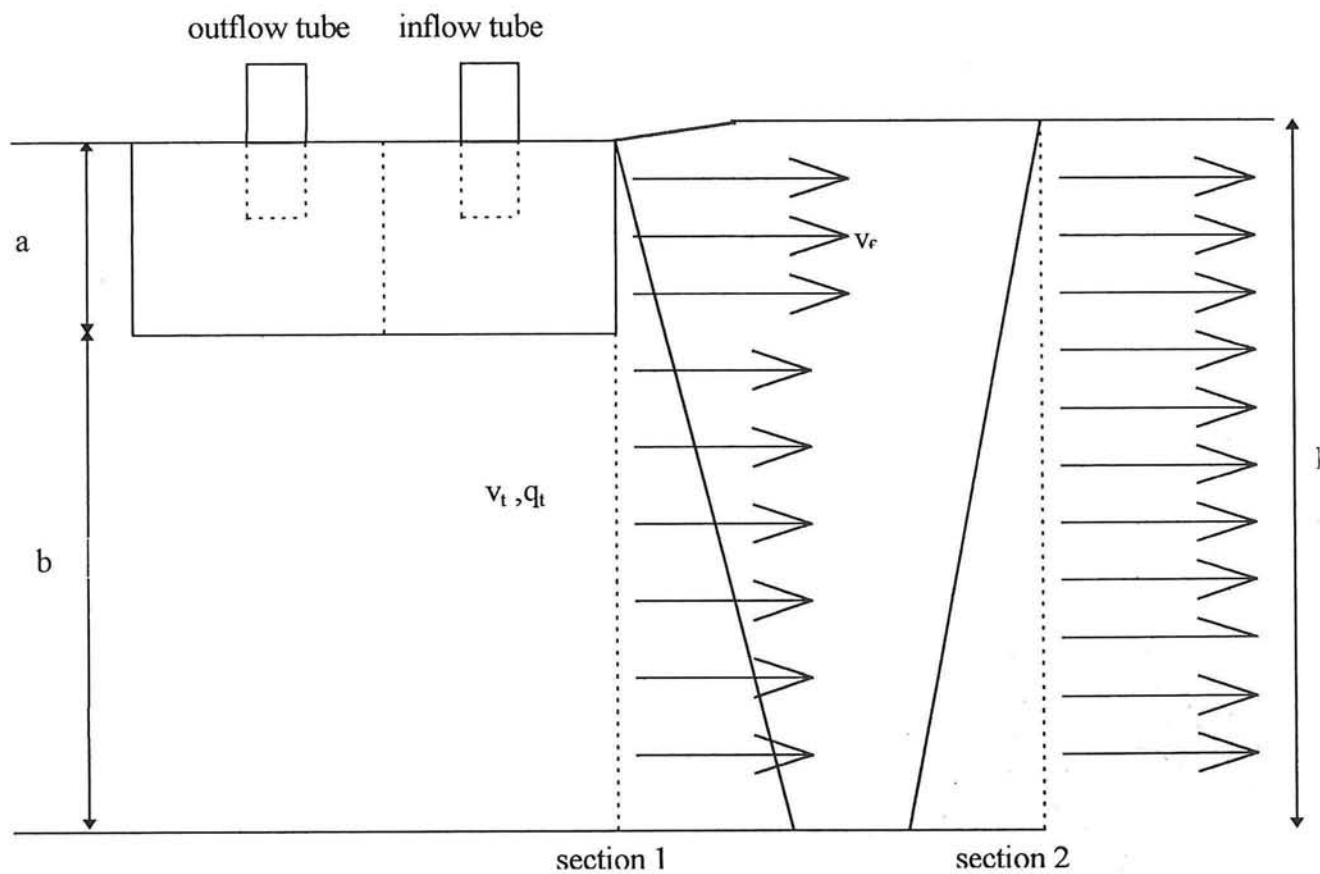


Figure II.1

When considering the two cross-sections 1 and 2 this yields the following equation:

$$\frac{1}{2} \rho g (h_1^2 - h_2^2) = \rho q v_2 - \rho q_f v_f - \rho q_t v_t \Leftrightarrow$$

$$\frac{1}{2} (h_2^2 - h_1^2) = \frac{1}{g} \left[\frac{q_f^2}{a} + \frac{q^2}{b} + \frac{q_f^2}{b} - \frac{q^2}{h_2} - \frac{2qq_f}{b} \right] \Leftrightarrow$$

$$(h_2 - h_1) \frac{(h_2 + h_1)}{2} = \frac{q^2}{gh} \left[\left(\frac{q_f}{q} \right)^2 \left(\frac{1}{a} + \frac{1}{b} \right) h + \left(\frac{1}{b} - \frac{1}{h_2} \right) h - 2h \left(\frac{q_f}{q} \right) \frac{1}{b} \right] \Leftrightarrow$$

$$(h_2 - h_1) = \frac{q^2}{gh^2} \left[\left(\frac{q_f}{q} \right)^2 \left(\frac{1}{a} + \frac{1}{b} \right) h + \left(\frac{1}{b} - \frac{1}{h_2} \right) h - 2h \left(\frac{q_f}{q} \right) \frac{1}{b} \right] \quad (\text{II.1})$$

where ρ is the density of the fluid, g the gravitational acceleration, h_1 the water depth upstream of the box, h_2 the water depth downstream of the box, q the discharge in the tank, v_2 the flow velocity downstream of the box, q_f the discharge of the box, v_f the flow velocity through the filter, q_t the discharge below the box, v_t the flow velocity below the box, a the height of the box, b the depth of flow below the box and h the mean depth of flow $(h_2 + h_1)/2$.

Now $h_2 - h_1$ is written as $\Delta h = i L$ where i is the angle of the water level slope and L is the longitudinal length of the flow.

$$i l = f \frac{v^2}{8g} 2\pi R \quad (\text{II.2})$$

so it follows that

$$f \frac{v^2}{8g} 2\pi R = \frac{q^2}{gh^2} \left[\left(\frac{q_f}{q} \right)^2 \left(\frac{1}{a} + \frac{1}{b} \right) h + \left(\frac{1}{b} - \frac{1}{h_2} \right) h - 2h \left(\frac{q_f}{q} \right) \frac{1}{b} \right] \Leftrightarrow$$

$$\left(\frac{b}{h} \right) \frac{fq^2 \pi R}{4h^2} = \frac{q^2}{h} \left[\left(\frac{q_f}{q} \right)^2 \left(\frac{h}{a} \right) + \left(1 - \frac{b}{h} \right) - 2 \left(\frac{q_f}{q} \right) \right] \Leftrightarrow$$

$$\left(\frac{b}{h} \right) \left(\frac{f\pi R}{4h} + 1 \right) = \left[\left(\frac{q_f}{q} \right)^2 \left(\frac{h}{a} \right) - 2 \left(\frac{q_f}{q} \right) + 1 \right] \Leftrightarrow$$

$$\left(\frac{q_f}{q} \right)^2 \left(\frac{h}{a} \right) - 2 \left(\frac{q_f}{q} \right) + \left(1 - \left(\frac{b}{h} \right) \left(\frac{f\pi R}{4h} + 1 \right) \right) = 0 \quad (\text{II.3})$$

In the next figure the relation between q_f/q and a/h is shown.

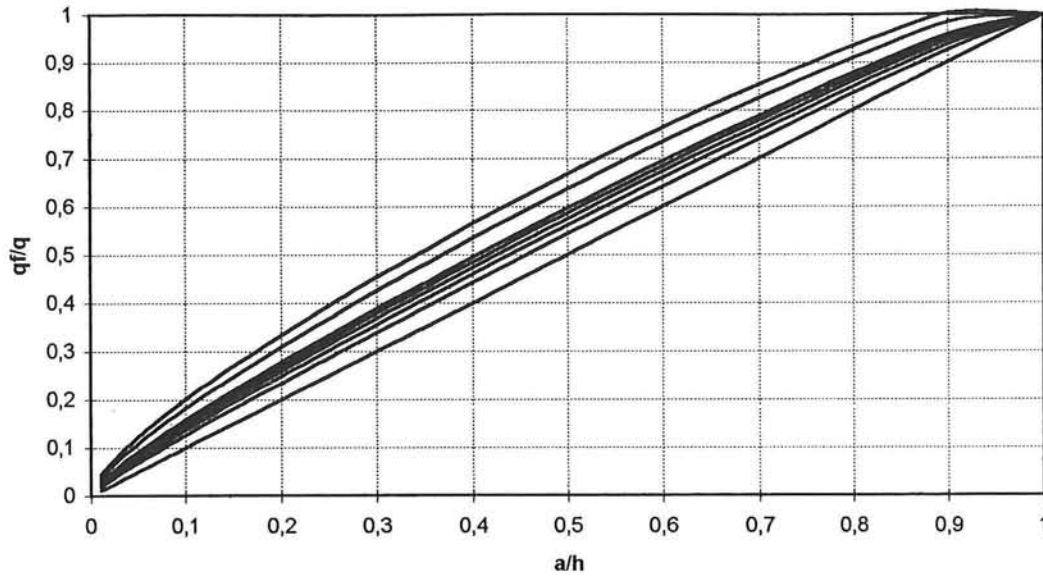


Figure II.2

Obviously when the height a equals the depth of flow h the discharge q_f equals the discharge of the entire flow. On the other hand when the height of the box is almost zero and a/h is zero, q_f/q equals zero.

When the friction coefficient f equals zero the relation between q_f/q and a/h is linear which can be shown easily by considering the a,b,c-formula. It appears that $q_f/q = a/h$ which is logical because without friction the inlet and the flow velocities are the same (the discharge is height multiplied by flow velocity). The lines shown in this figure represent $f=0$ (straight line), $f=0.01$, $f=0.02$, $f=0.03$, $f=0.04$, $f=0.05$, $f=0.1$ and $f=0.15$ where an increasing value of f results in an increasing value of q_f/q for a constant value of a/h .

To find the inlet and flow velocities a graphic will be made of the discharges expressed in depth times velocity. Therefore equation II.2 becomes:

$$\left(\frac{v_f a}{vh}\right)^2 \left(\frac{h}{a}\right) - 2\left(\frac{v_f a}{vh}\right) + \left(1 - \left(\frac{b}{h}\right)\left(\frac{f\pi R}{4h} + 1\right)\right) = 0 \Leftrightarrow$$

$$\left(\frac{v_f}{v}\right)^2 \left(\frac{a}{h}\right) - 2\left(\frac{v_f}{v}\right)\left(\frac{a}{h}\right) + \left(1 - \left(\frac{b}{h}\right)\left(\frac{f\pi R}{4h} + 1\right)\right) = 0 \Leftrightarrow$$

$$\left(\frac{v_f}{v}\right)^2 - 2\left(\frac{v_f}{v}\right) + \left(\frac{h}{a}\right)\left(1 - \left(\frac{b}{h}\right)\left(\frac{f\pi R}{4h} + 1\right)\right) = 0 \Leftrightarrow$$

$$\left(\frac{v_f}{v}\right)^2 - 2\left(\frac{v_f}{v}\right) + \left(\left(\frac{h}{a}\right) - \left(\frac{h}{a} - 1\right)\left(\frac{f\pi R}{4h} + 1\right)\right) = 0 \Leftrightarrow$$

$$\left(\frac{v_f}{v}\right)^2 - 2\left(\frac{v_f}{v}\right) + \left(\left(\frac{f \pi R}{4 h}\right)\left(1 - \frac{h}{a}\right) + 1\right) = 0 \quad (\text{II.4})$$

To check this formula the value of the friction f is taken equal to 0 which means that there is no friction. It appears that for every value of the inlet velocity, the relation $v_f/v = 1$ so the flow velocity is always the same as the inlet velocity.

For non-zero, positive values of the friction f the relation v_f/v to a/h has the vertical axis as its asymptote as shown in the following graph. The lines shown in this figure represent $f=0$ (straight line), $f=0.01$, $f=0.02$, $f=0.03$, $f=0.04$, $f=0.05$, $f=0.1$ and $f=0.15$ where an increasing value of f results in an increasing value of v_f/v for a constant value of a/h .

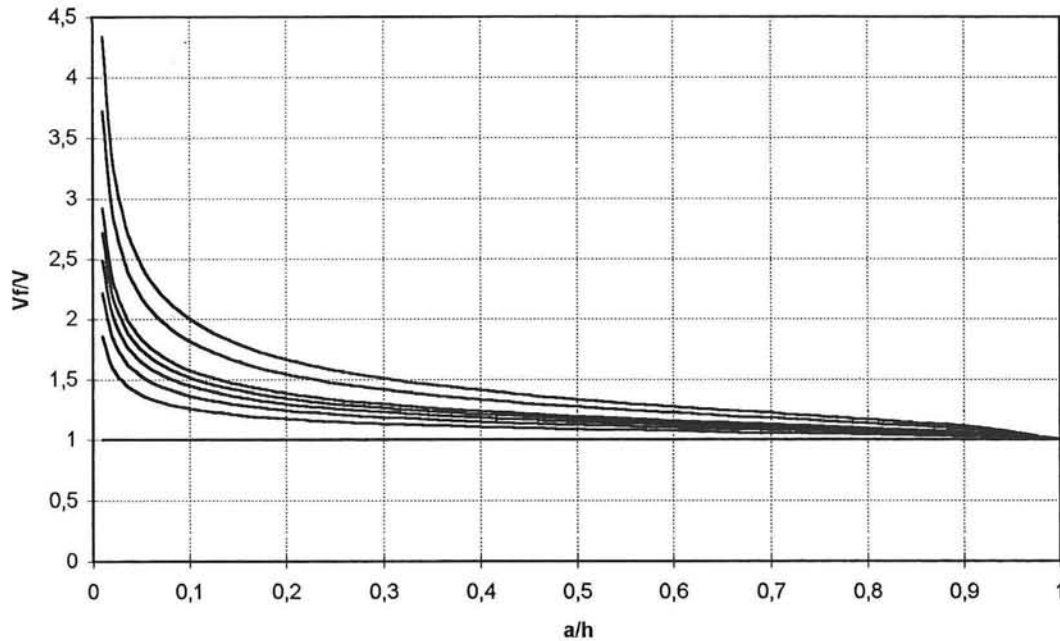


Figure II.3

To make sure that as less disturbances as possible occur in the tank the inlet flow velocity must be as close as possible to the flow velocity in the tank. From the figure II.3 it can be found that the relation a/h must then be as large as possible. On the other side this large values of a/h result in values of q_f/q close to 1. The velocities in the tank may not be too small because of the accuracy of the used velocimeter. Therefore the discharge in the tank may not be too small which means that for values of q_f/q close to 1 the discharge in the box would be large. A large discharge in the box results in a large velocity in the feeding tube since its dimensions can not be changed because of the lack of space at the position where the tube is connected to the box. The pressure inside the box would increase, since it is related to the square of the flow velocity in the feeding tube, and this is not possible for reasons of its strength.

An optimum had to be found for the values of v_f/v , q_f/q and a/h . In the experiment these values were taken:

$a/h=0,33$ and the friction coefficient was approximately 0.02.

According to these graphics $q_f/q \cong 0,4$ and $v_f/v \cong 1,25$
 $q_f = 40 \text{ liters/min} / 0,23 \text{ m} = 2,90 \text{ liters/s/m} = 2,90 \cdot 10^{-3} \text{ m}^3/\text{s/m}$

N.B. if no recirculating flows are present then
 $(q_f/q) = (a/h) (v_f/v)$

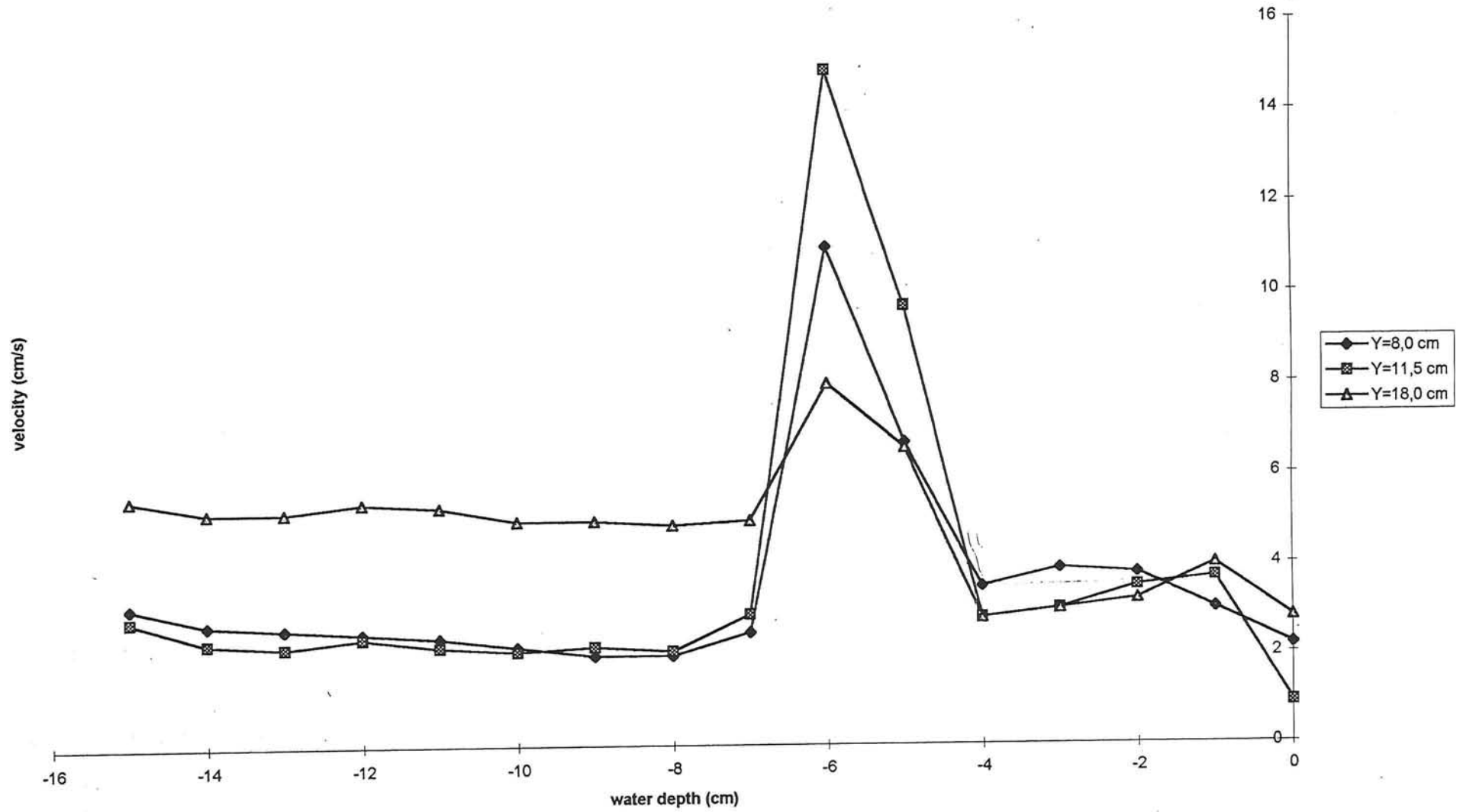
Appendix III

In this appendix the results of the experimental research will be given.

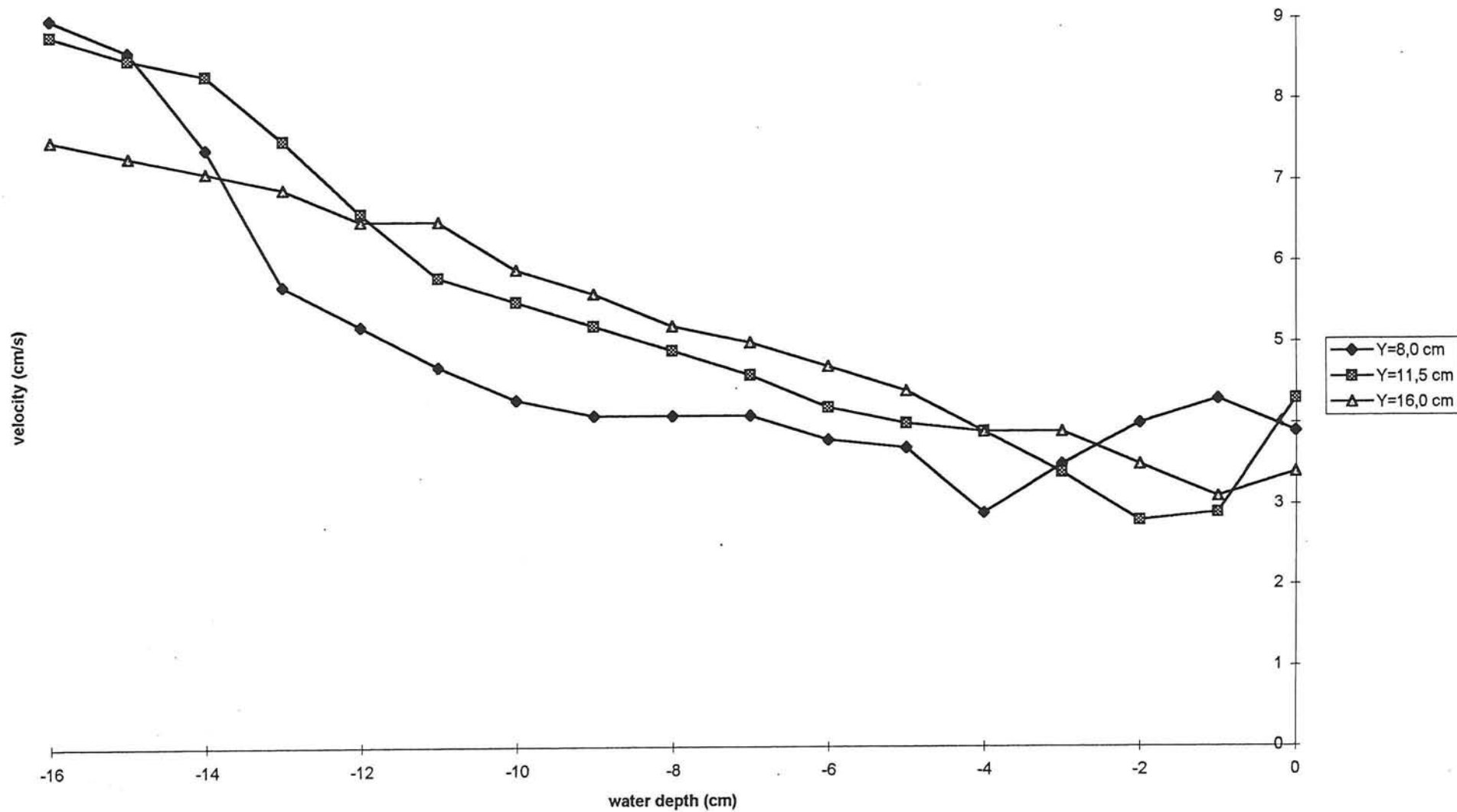
The distances are taken in longitudinal direction such that 0° is at the exit of the feeding box. In radial direction is the positive spatial direction, as well as the positive velocity direction, towards the outer wall.

The first figures of the longitudinal and the radial velocity distribution are taken at 2 cm downstream of the exit of the feeding box for reasons of the magnitude of the velocimeter. 2 cm corresponds approximately with 5° .

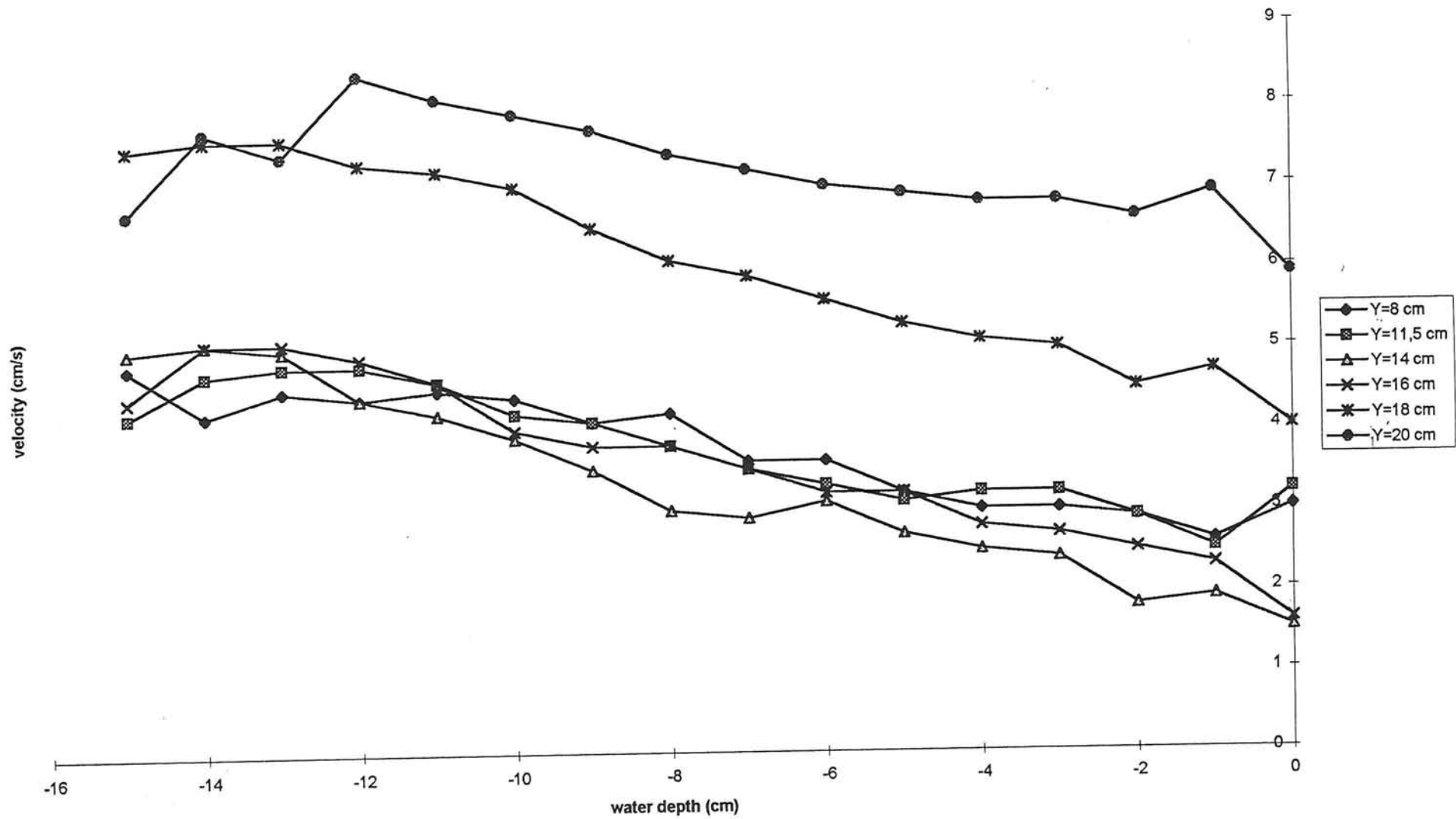
experimental longitudinal velocities 2cm after the box



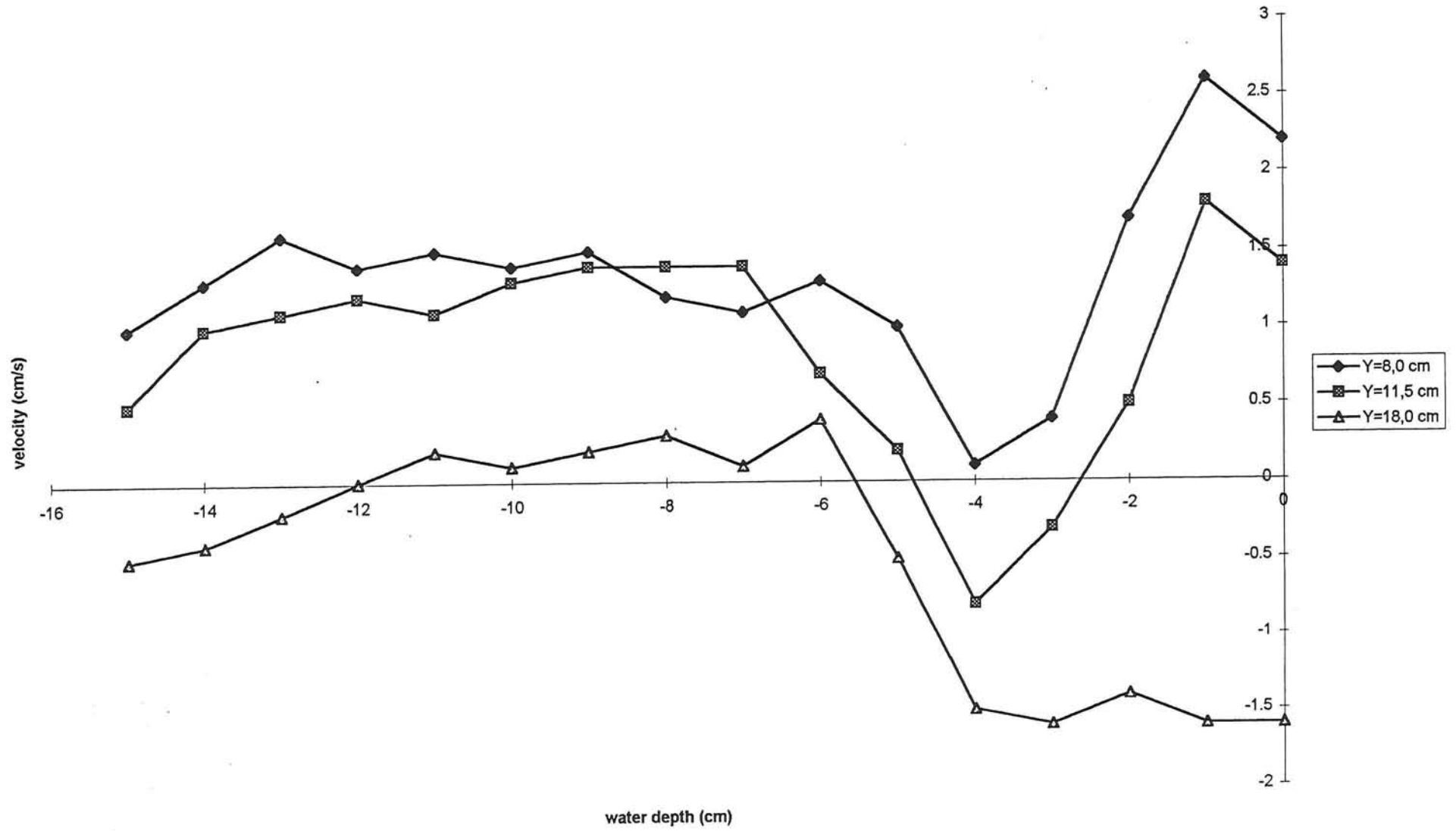
experimental longitudinal velocities $\phi=180^\circ$



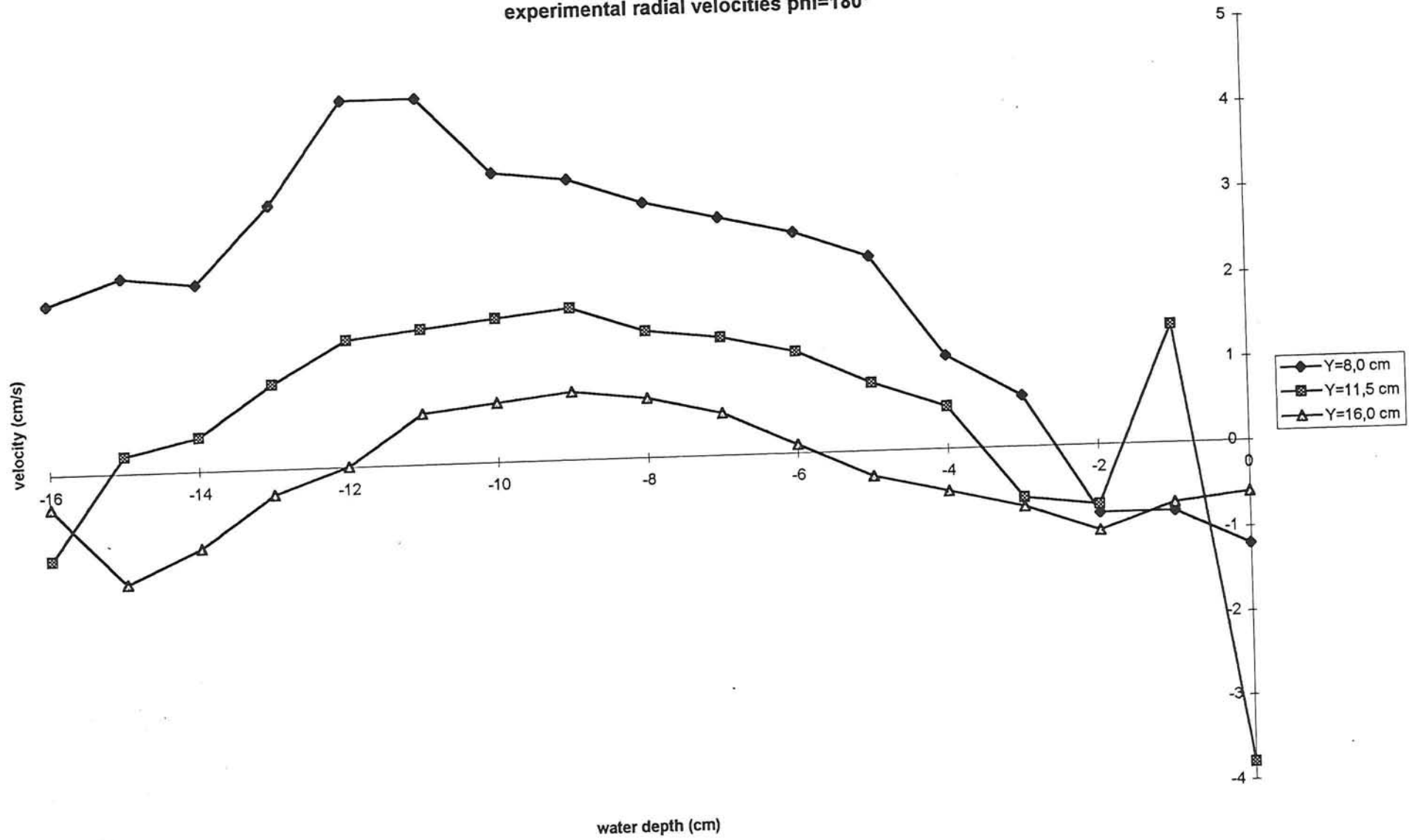
experimental longitudinal velocities at $\phi=225^\circ$



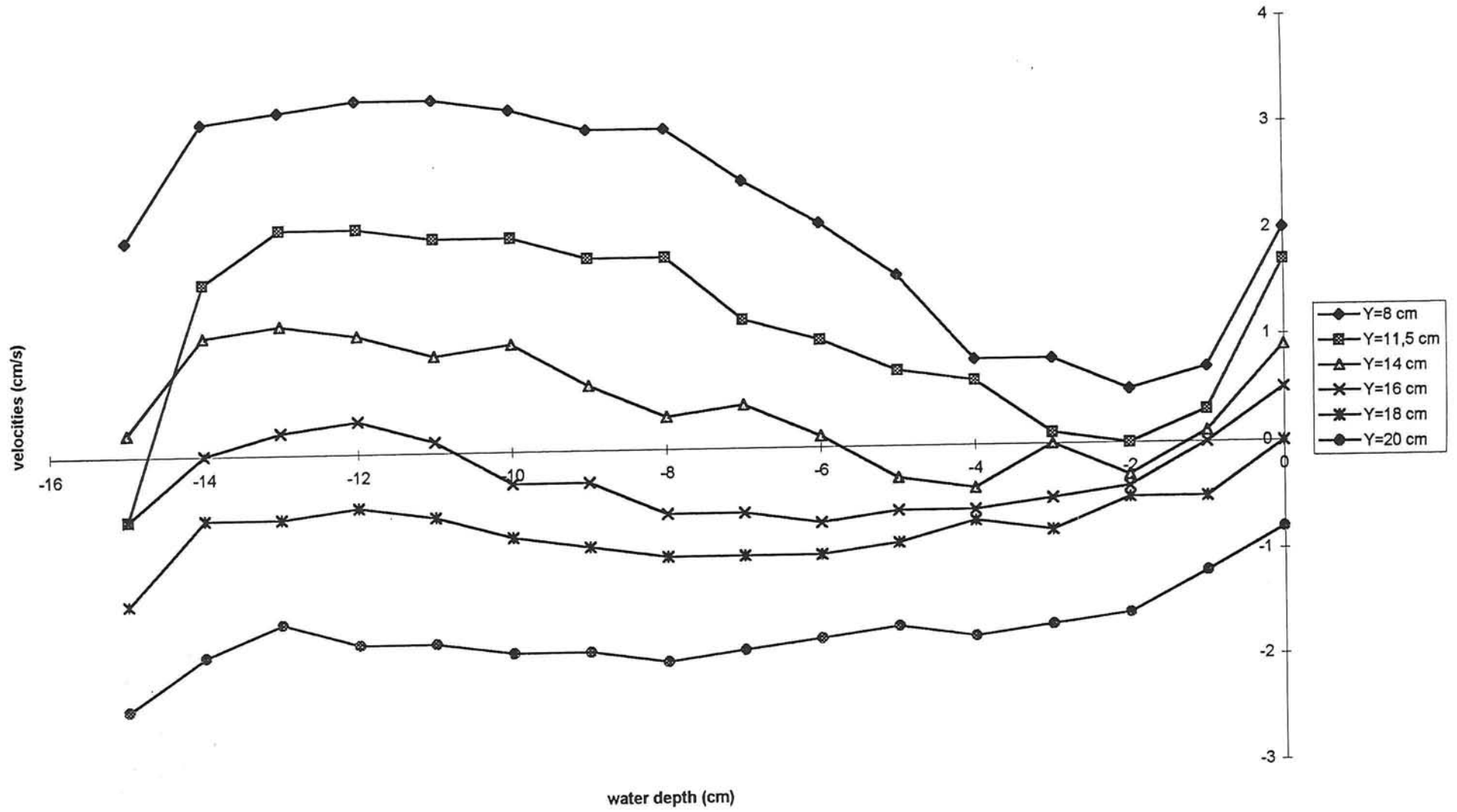
experimental radial velocities 2 cm after the box



experimental radial velocities $\phi=180^\circ$



experimental radial velocities at $\phi=225^\circ$



Appendix IV

Description of the program Trisula.

Trisula is a program which is a part of the program package Delft3d. Trisula calculates the flow pattern that can be used as input for morphological models or sediment transport models. Its main purpose is the two-dimensional (depth-averaged) and three-dimensional simulation of tidal and wind driven flow, including the effect of density differences in shallow seas, coastal areas, estuaries, rivers and lakes. In these cases the horizontal length scales are significantly larger than their vertical length scales.

The grid that is used in the simulation can be formulated in a Cartesian frame of reference or in spherical coordinates on the globe.

Trisula is based on a finite difference scheme using a system of equations that consists of the horizontal momentum equations, the continuity equation and transport equations. The flow equations are solved for an incompressible fluid under the shallow water assumption. This system of equations is solved using the Alternating Direction Implicit technique (appendix VII).

For the discretisation of the horizontal gradients a staggered grid is used. This means that in the centre of a (continuity) cell the water level is defined, the depth points are defined on the corners and the flow velocities on the faces.

The advantage of a staggered grid is that two independent sets of values are calculated so, without lack of accuracy, one can be left out of consideration. Another advantage is that it prevents spatial oscillations in water levels [Stelling, 1984]. In the three-dimensional simulation a so-called σ -coordinate [Phillips 1957] in the vertical direction is used defined as: $\sigma = (z - \zeta) / (\zeta + d)$ where z is the vertical coordinate, ζ the water level above some horizontal plane of reference and d the water depth below some horizontal plane of reference. This means that over the entire flow the same amount of grid numbers are defined in the vertical direction. For each layer, a set of coupled conservation equations is solved.

The equations used in Trisula are (in orthogonal curvilinear coordinates):

the depth-averaged continuity equation;

$$\frac{\partial \zeta}{\partial t} + \frac{1}{\sqrt{G_{\xi\xi}} \sqrt{G_{\eta\eta}}} \frac{\partial [(d + \zeta) U \sqrt{G_{\eta\eta}}]}{\partial \xi} + \frac{1}{\sqrt{G_{\xi\xi}} \sqrt{G_{\eta\eta}}} \frac{\partial [(d + \zeta) V \sqrt{G_{\xi\xi}}]}{\partial \eta} = 0$$

The momentum equations in the horizontal ξ - and η -directions:

$$\begin{aligned}
& \frac{\partial u}{\partial t} + \frac{u}{\sqrt{G_{\xi\xi}}} \frac{\partial u}{\partial \xi} + \frac{v}{\sqrt{G_{\eta\eta}}} \frac{\partial u}{\partial \eta} + \frac{w}{d+\zeta} \frac{\partial u}{\partial \sigma} + \frac{uv}{\sqrt{G_{\xi\xi}}\sqrt{G_{\eta\eta}}} \frac{\partial \sqrt{G_{\xi\xi}}}{\partial \eta} - \\
& \frac{v^2}{\sqrt{G_{\xi\xi}}\sqrt{G_{\eta\eta}}} \frac{\partial \sqrt{G_{\eta\eta}}}{\partial \xi} - f v = -\frac{g}{\sqrt{G_{\xi\xi}}} \frac{\partial \zeta}{\partial \xi} + \\
& \frac{1}{\sqrt{G_{\xi\xi}}} \frac{\partial}{\partial \xi} \left(\frac{2 v_h}{\sqrt{G_{\xi\xi}}} \left(\frac{\partial u}{\partial \xi} + \frac{\partial u}{\partial \sigma} \frac{\partial \sigma}{\partial \xi} \right) \right) + \\
& \frac{1}{\sqrt{G_{\eta\eta}}} \frac{\partial}{\partial \eta} \left(v_h \left(\frac{1}{\sqrt{G_{\eta\eta}}} \left(\frac{\partial u}{\partial \eta} + \frac{\partial u}{\partial \sigma} \frac{\partial \sigma}{\partial \eta} \right) + \frac{1}{\sqrt{G_{\xi\xi}}} \left(\frac{\partial v}{\partial \xi} + \frac{\partial v}{\partial \sigma} \frac{\partial \sigma}{\partial \xi} \right) \right) \right) + \\
& \frac{1}{(d+\zeta)^2} \frac{\partial}{\partial \sigma} \left(v_v \frac{\partial u}{\partial \sigma} \right)
\end{aligned}$$

$$\begin{aligned}
& \frac{\partial v}{\partial t} + \frac{u}{\sqrt{G_{\xi\xi}}} \frac{\partial v}{\partial \xi} + \frac{v}{\sqrt{G_{\eta\eta}}} \frac{\partial v}{\partial \eta} + \frac{w}{d+\zeta} \frac{\partial v}{\partial \sigma} + \frac{uv}{\sqrt{G_{\xi\xi}}\sqrt{G_{\eta\eta}}} \frac{\partial \sqrt{G_{\eta\eta}}}{\partial \xi} - \\
& \frac{u^2}{\sqrt{G_{\xi\xi}}\sqrt{G_{\eta\eta}}} \frac{\partial \sqrt{G_{\xi\xi}}}{\partial \eta} + f u = -\frac{g}{\sqrt{G_{\eta\eta}}} \frac{\partial \zeta}{\partial \eta} + \\
& \frac{1}{\sqrt{G_{\xi\xi}}} \frac{\partial}{\partial \xi} \left(v_h \left(\frac{1}{\sqrt{G_{\eta\eta}}} \left(\frac{\partial u}{\partial \eta} + \frac{\partial u}{\partial \sigma} \frac{\partial \sigma}{\partial \eta} \right) + \frac{1}{\sqrt{G_{\xi\xi}}} \left(\frac{\partial v}{\partial \xi} + \frac{\partial v}{\partial \sigma} \frac{\partial \sigma}{\partial \xi} \right) \right) \right) + \\
& \frac{1}{\sqrt{G_{\eta\eta}}} \frac{\partial}{\partial \eta} \left(\frac{2 v_h}{\sqrt{G_{\eta\eta}}} \left(\frac{\partial v}{\partial \eta} + \frac{\partial v}{\partial \sigma} \frac{\partial \sigma}{\partial \eta} \right) \right) + \frac{1}{(d+\zeta)^2} \frac{\partial}{\partial \sigma} \left(v_v \frac{\partial v}{\partial \sigma} \right)
\end{aligned}$$

The vertical momentum equation reduces under the shallow water assumption to a hydrostatic pressure equation (vertical accelerations of the fluid are much smaller than the gravitational acceleration):

$$\frac{\partial P}{\partial \sigma} = -g \rho H$$

The vertical velocities are in a three-dimensional simulation computed from the continuity equation:

$$\frac{\partial \zeta}{\partial t} + \frac{1}{\sqrt{G_{\xi\xi}}\sqrt{G_{\eta\eta}}} \frac{\partial \left[(d+\zeta) u \sqrt{G_{\eta\eta}} \right]}{\partial \xi} + \frac{1}{\sqrt{G_{\xi\xi}}\sqrt{G_{\eta\eta}}} \frac{\partial \left[(d+\zeta) v \sqrt{G_{\xi\xi}} \right]}{\partial \eta} + \frac{\partial w}{\partial \sigma} = 0$$

where:

- ξ horizontal curvilinear spatial coordinates (-)
- η horizontal curvilinear spatial coordinates (-)
- σ scaled vertical coordinate $(z-\zeta) / (\zeta+d)$ (-)

ζ	the water level (m)
$\sqrt{G_{\xi\xi}}$	a coefficient used to transform curvilinear to rectangular coordinates (m)
$\sqrt{G_{\eta\eta}}$	a coefficient used to transform curvilinear to rectangular coordinates (m)
d	the water depth below some horizontal plane of reference (m)
U	the depth averaged velocity in the ξ -direction (m/s)
V	the depth averaged velocity in the η -direction (m/s)
u	flow velocity in the ξ -direction (m/s)
v	flow velocity in the η -direction (m/s)
w	flow velocity in the σ -direction (-)
f	coriolis coefficient (1/s)
g	gravitational acceleration (m/s ²)
ν_h	horizontal eddy viscosity (m ² /s)
ν_v	vertical eddy viscosity (m ² /s)
P	hydrostatic water pressure (kg/m/s ²)
ρ	density of water (kg/m ³)

Solution method of Trisula

In the three-dimensional simulation the horizontal velocities of the adjacent vertical layers are coupled by the advection term and the vertical viscosity term. To prevent instabilities induced by the vertical viscosity term, a fully implicit integration is used for the vertical exchange terms.

At first the velocities of the layers are expressed in the water levels. These are substituted in the depth-averaged continuity equation. Together with the momentum equations the water levels are calculated. The equations for the water levels are solved with an Alternating Direction Implicit technique (A.D.I.). This means that the water levels are calculated implicitly along grid lines in the ξ - and η -direction in an alternating way. In the first half time step is calculated implicitly in one direction and explicitly in the other direction. The next half time step changes the direction in which is calculated implicitly and explicitly. By doing so, only tri-diagonal systems of equations along grid lines have to be solved. The solved water levels are substituted in the momentum equations to calculate the horizontal velocities. These velocities are substituted in the continuity equation to calculate the vertical velocities.

With regard to the full time step the discretisation is second order accurate [manual Trisula].

The horizontal and vertical viscosity need to be prescribed. The horizontal viscosity is a superposition of the '2D-turbulence' and the '3D-turbulence' ; $\nu_h = \nu^{2D} + \nu_v$. ν_v is referred to as three-dimensional turbulence and is computed following the turbulence closure model that is used in the simulation. The turbulence closure models differ in their description of the turbulent kinetic energy k , the dissipation of energy ϵ , and/or the mixing length L .

The other part of the two-dimensional turbulence, the so-called sub-grid scale turbulence, has to be prescribed, it takes account for that part that is not resolved by the horizontal grid. In Trisula four different turbulence closure models exist;

- a constant value for ν_v

- a combination of two zero order schemes which uses algebraic/analytical formulas to determine k and L .
- a first order turbulence scheme which uses an algebraic expression for L and a transport equation to determine k ; the so-called k - L model
- a second order turbulence closure model which uses transport equations for both k and ϵ . From these two quantities the mixing length L which is now a property of the flow is determined.

The last three models make use of the eddy viscosity concept of Kolmogorov and Prandtl. The eddy viscosity has the following form:

$$\nu_v = c_\mu L \sqrt{k}$$

where

- c_μ is a constant determined by calibration (-)
- L the mixing length (m)
- k turbulent kinetic energy (m^2/s^2)
- ϵ dissipation of turbulent kinetic energy (m^2/s^3)

The description of the turbulent models is done in the chapter 4.

Assumptions with respect to Trisula

Trisula is like all simulation programs an approximation of the reality. The for a river bend flow important assumptions and approximations which are used in formulating the equations in the used version of Trisula are:

The shallow water assumption: the vertical momentum equation is reduced to the hydrostatic pressure relation. Vertical accelerations are assumed to be small compared with the gravitational acceleration and are not taken into account.

The fluid (water) is assumed to be incompressible.

The momentum of discharges are neglected

In three-dimensional computations the effect of three-dimensional turbulence on the vertical exchange of momentum and mass is modelled through a vertical eddy viscosity and eddy diffusivity coefficient (eddy viscosity concept), by means of an algebraic, k - L or k - ϵ turbulence model.

The horizontal viscosity terms are reduced to a biharmonic operator along coordinate lines

The tangential shear stress is zero (free slip) for all lateral boundaries (this is a result of the hydrostatic pressure assumption)

At the bed a slip boundary condition is assumed

Input in a simulation with Trisula.

For making a proper calculation of a river bend flow with a numerical simulation the input values are very important. In Trisula a number of input values and choices of solution methods have to be given like initial values, boundary conditions, values for physical properties, which turbulent and transport model will be used, grid configuration, time step and total calculation time, depth values, roughness values, definition of the calculational area etc.. Some of these input values must be inserted before a simulation can start while for others default values are taken.

The input file, the so-called Master Definition file or MD-file, contains all the necessary data required for defining a model and running the simulation program. This MD-file is made with the pre-processor which supports in preparing a correct and complete MD-file.

The exact description and explanation of the various input parameters of a MD-file is given in appendix VII. Since Trisula is a numerical simulation program for two- and three-dimensional flows one has to choose between a two- and a three-dimensional simulation. In this research the scope was to simulate the flow in three dimensions so the description of the input parameters will all be made with respect to a three-dimensional simulation.

Grid.

In Trisula it is possible to choose between three different horizontal coordinate systems:

1. a Cartesian rectangular coordinate system (x, y)
2. an orthogonal curvilinear coordinate system (ξ, η)
3. a spherical coordinate system (χ, ϕ)

The last one is a special case of an orthogonal curvilinear coordinate system.

When an orthogonal curvilinear grid is chosen Trisula reads this coordinate system and changes it in a rectangular coordinate system (Appendix VI). Due to this translation some additional terms occur in the equations that calculate the flow. In Trisula, two more grid points in the horizontal directions must be defined then computational cells are present. One extra grid point is needed because a computational cell is defined as the area between four depth grid points; it can be easily seen that with N_{grid} points $N-1$ computational cells exist. A second extra grid point is needed for defining the boundary conditions at the grid points where $N=N_{max}$ and $M=M_{max}$ (Appendix VI).

In the vertical direction a scaled coordinate σ is used.

The distances between the adjacent grid points can be chosen by the user in the horizontal direction as well as in the vertical direction. In this way the thickness of the lowest layers can be chosen smaller than the upper ones. In the vertical direction the number of layers is constant and therefore the relation between the relative thickness of one layer to another is constant.

The definition of the grid is only a maximum of the computational area. The total computational grid enclosure must also be given. This means that the open and closed boundary positions must be given. Later on the open boundaries, if any, have to be defined and the rest of the computational grid enclosure is assumed closed.

The water depth can be given as a constant depth for every grid point or can vary from one grid point to another.

In the computational area the possibility exists of defining thin walls, dry points, discharges and wells.

Initial conditions.

Two different ways of defining the initial conditions are possible. The first one is that for every grid point in the computational grid enclosure the water depth must be given while the velocities are set to zero. The second one is the use of a restart file containing the final data of all the variables of a previous computation.

Boundary conditions.

Boundary conditions must be given for every open boundary. Every boundary has to be defined by a type of the boundary and a forcing type of the boundary. Also the beginning and the end of the boundary in the computational area have to be defined.

A choice must be made between four types of boundaries; a water elevation, a current, a flux and a Riemann/radiation type. The boundary is driven by one of the following forcing types of boundary condition; a harmonic, a times series or an astronomical driven boundary.

It is possible to let the wind act on the flow; the air density, a wind stress coefficient and the angle of the direction of the wind and the flow must then be given.

Total calculation time and time step.

The starting time of the computation as well as the time to stop the simulation must be given. The full integration time step must be defined; the number of time steps is calculated by the program. Once the time step is defined it is fixed so it is impossible to calculate with varying time steps.

Turbulence models.

As said before one has to choose between four different turbulent closure models for the vertical turbulent eddy viscosity; a constant value, the zero-order k-L model, the first-order k-L model and the k- ϵ model.

The constants in the last three models are already implemented in the program.

The constant value of the horizontal eddy viscosity must also be given as well as the horizontal diffusivity.

Processes.

The possibility exists in Trisula to use models for heat, salinity or a user defined constituent.

Output

In Trisula one has to specify the quantities that have to be stored. Trisula offers the possibility to store during the computation so a time series can be obtained but then a position in the computational domain or a cross-section must be defined for which these quantities have to be stored.

The grid coordinates of the position or in case of a cross-section the grid number in the direction perpendicular to this cross-section must be given as well as the time at which the quantities have to be stored.

Communication file.

As Trisula takes part in the program package Delft3D it has to be able to 'communicate' with the other programs. This is done by means of a communication file. One has to specify whether Trisula has to make a communication file or not.

Restart.

Like the communication file one can make a restart file. This restart file will store the final results of the calculation.

Appendix V

The discretisation in the vertical is done with the so-called σ -coordinate $\sigma = (z - \zeta) / (d + \zeta)$; $-1 \leq \sigma \leq 0$. The equations to solve these flow problems (without the coriolis and wind forces) will be given in a Cartesian coordinate system.

The depth averaged continuity equation

$$\frac{\partial \zeta}{\partial t} + \frac{\partial(H\bar{u})}{\partial x} + \frac{\partial(H\bar{v})}{\partial y} = 0 \quad \text{V.1}$$

The momentum equations in the horizontal directions

$$\frac{\partial}{\partial t}(\rho u) + \frac{\partial}{\partial x}(\rho u^2) + \frac{\partial}{\partial y}(\rho uv) + \frac{\partial}{\partial z}(\rho uw) + \frac{\partial}{\partial x}q_{xx} + \frac{\partial}{\partial y}q_{xy} + \frac{\partial}{\partial z}q_{xz} + \frac{\partial}{\partial x}p = 0 \quad \text{V.2}$$

$$\frac{\partial}{\partial t}(\rho v) + \frac{\partial}{\partial x}(\rho uv) + \frac{\partial}{\partial y}(\rho v^2) + \frac{\partial}{\partial z}(\rho vw) + \frac{\partial}{\partial x}q_{yx} + \frac{\partial}{\partial y}q_{yy} + \frac{\partial}{\partial z}q_{yz} + \frac{\partial}{\partial y}p = 0 \quad \text{V.3}$$

The continuity equation (used by Trisula to calculate the vertical velocities)

$$\frac{\partial \zeta}{\partial t} + \frac{\partial u}{\partial x} + \frac{\partial v}{\partial y} + \frac{\partial w}{\partial z} = 0 \quad \text{V.4}$$

The solution procedure of Trisula consists of the following steps (the terms q_{xx} , q_{xy} , q_{xz} , q_{yx} , q_{yy} and q_{yz} are the molecular and turbulent viscosity forces):

First the velocities are expressed in water levels with the A.D.I. method.

In the A.D.I. method one time step is divided in two half time steps. In the first half time step the depth averaged velocity in the x-direction and the water levels are calculated implicitly (equation V.5 and V.6) and the depth averaged velocity in the y-direction (equation V.7) is calculated explicitly. The semi-discretized equations are:

$$\frac{\zeta^{*,q+1} - \zeta^n}{\Delta t / 2} + \frac{\partial \left(H^{*,q+1} \int_{-1}^0 u^* d\sigma \right)}{\partial x} + \frac{\partial \left(H^n \int_{-1}^0 v^n d\sigma \right)}{\partial y} = 0 \quad \text{V.5}$$

$$\int_{-1}^0 \left(\frac{u^* - u^n}{\Delta t / 2} + u^* \frac{\partial(u^n)}{\partial x} + v^* \frac{\partial(u^n)}{\partial y} + \frac{H^{*,q}}{H^{*,q+1}} g \frac{\partial(\zeta^{*,q+1})}{\partial x} - v_h \frac{\partial^2(u^n)}{\partial x^2} - v_h \frac{\partial^2(u^n)}{\partial y^2} \right) d\sigma = 0 \quad \text{V.6}$$

$$\int_{-1}^0 \left(\frac{v^* - v^n}{\Delta t / 2} + u^n \frac{\partial(v^*)}{\partial x} + v^n \frac{\partial(v^*)}{\partial y} + \frac{2 w^n}{H^n} \frac{\partial(v^*)}{\partial \sigma} + g \frac{\partial(\zeta^n)}{\partial y} \right) d\sigma = 0 \quad \text{V.7}$$

$$\int_{-1}^0 \left(-v_h \frac{\partial^2(v^*)}{\partial x^2} - v_h \frac{\partial^2(v^*)}{\partial y^2} - \frac{2 v_v}{(H^n)^2} \frac{\partial^2(v^*)}{\partial \sigma^2} \right) d\sigma = 0$$

$$\frac{\partial(w^*)}{\partial \sigma} + \frac{\zeta^* - \zeta^n}{\Delta t / 2} + \frac{\partial(H^* u^*)}{\partial x} + \frac{\partial(H^n v^n)}{\partial y} = 0 \quad \text{V.8}$$

In the next half time step changes the direction in which is calculated implicitly and explicitly.

$$\frac{\zeta^{n+1,q+1} - \zeta^*}{\Delta t / 2} + \frac{\partial \left(H^* \int_{-1}^0 u^* d\sigma \right)}{\partial x} + \frac{\partial \left(H^{n+1,q+1} \int_{-1}^0 v^{n+1} d\sigma \right)}{\partial y} = 0 \quad \text{V.9}$$

$$\int_{-1}^0 \left(\frac{u^{n+1} - u^*}{\Delta t / 2} + u^* \frac{\partial(u^{n+1})}{\partial x} + v^* \frac{\partial(u^{n+1})}{\partial y} + \frac{2 w^*}{H^*} \frac{\partial(u^{n+1})}{\partial \sigma} + g \frac{\partial(\zeta^*)}{\partial x} \right) d\sigma = 0 \quad \text{V.10}$$

$$\int_{-1}^0 \left(-v_h \frac{\partial^2(u^{n+1})}{\partial x^2} - v_h \frac{\partial^2(u^{n+1})}{\partial y^2} - \frac{2 v_v}{(H^*)^2} \frac{\partial^2(u^{n+1})}{\partial \sigma^2} \right) d\sigma = 0$$

$$\int_{-1}^0 \left(\frac{v^{n+1} - v^*}{\Delta t / 2} + u^{n+1} \frac{\partial(v^*)}{\partial x} + v^{n+1} \frac{\partial(v^*)}{\partial y} + \frac{H^{n+1,q}}{H^{n+1,q+1}} g \frac{\partial(\zeta^{n+1,q+1})}{\partial x} \right) d\sigma = 0 \quad \text{V.11}$$

$$\int_{-1}^0 \left(-v_h \frac{\partial^2(v^*)}{\partial x^2} - v_h \frac{\partial^2(v^*)}{\partial y^2} \right) d\sigma = 0$$

$$\frac{\partial(w^{n+1})}{\partial \sigma} + \frac{\zeta^{n+1} - \zeta^*}{\Delta t / 2} + \frac{\partial(H^* u^*)}{\partial x} + \frac{\partial(H^{n+1} v^{n+1})}{\partial y} = 0 \quad \text{V.12}$$

where

- u^* the velocity in the x-direction at $t=n+\Delta t/2$
- u^n the velocity in the x-direction at $t=n$
- v^* is the velocity in the y-direction at $t=n+\Delta t/2$
- v^n is the velocity in the y-direction at $t=n$
- w^* the velocity in the σ -direction at $t=n+\Delta t/2$
- w^n the velocity in the σ -direction at $t=n$
- H^* the water depth at $t=n+\Delta t/2$
- ζ^* the elevation of the free surface at $t=n+\Delta t/2$
- g the gravitational acceleration
- v_h the horizontal eddy viscosity coefficient
- v_t the vertical eddy viscosity coefficient
- σ the normalised vertical coordinate $\sigma = (z-\zeta) / (d+\zeta)$
- q an iteration coefficient ($q=0, \dots, Q$; in Trisula $Q=1$).

N.B. The pressure terms are multiplied with $H^{*,q} / H^{*,q+1}$, c.q. $H^{n+1,q} / H^{n+1,q+1}$ making the system of equations linearly and mass conserving.

The advantage of this method is that by doing so only tridiagonal systems of equations along grid lines have to be solved for which an efficient algorithm, double sweep or Thomas algorithm, exists.

(So far the water levels and the depth averaged velocities are obtained. A two-dimensional solution is obtained. To arrive at a three-dimensional solution the next steps are done.)

The next step is that the resolved water levels are subsequently back-substituted in the momentum equations for the separate layers (V.6, V.7, V.10, V.11 without the integration over the depth) to calculate the horizontal velocities in the entire flow domain.

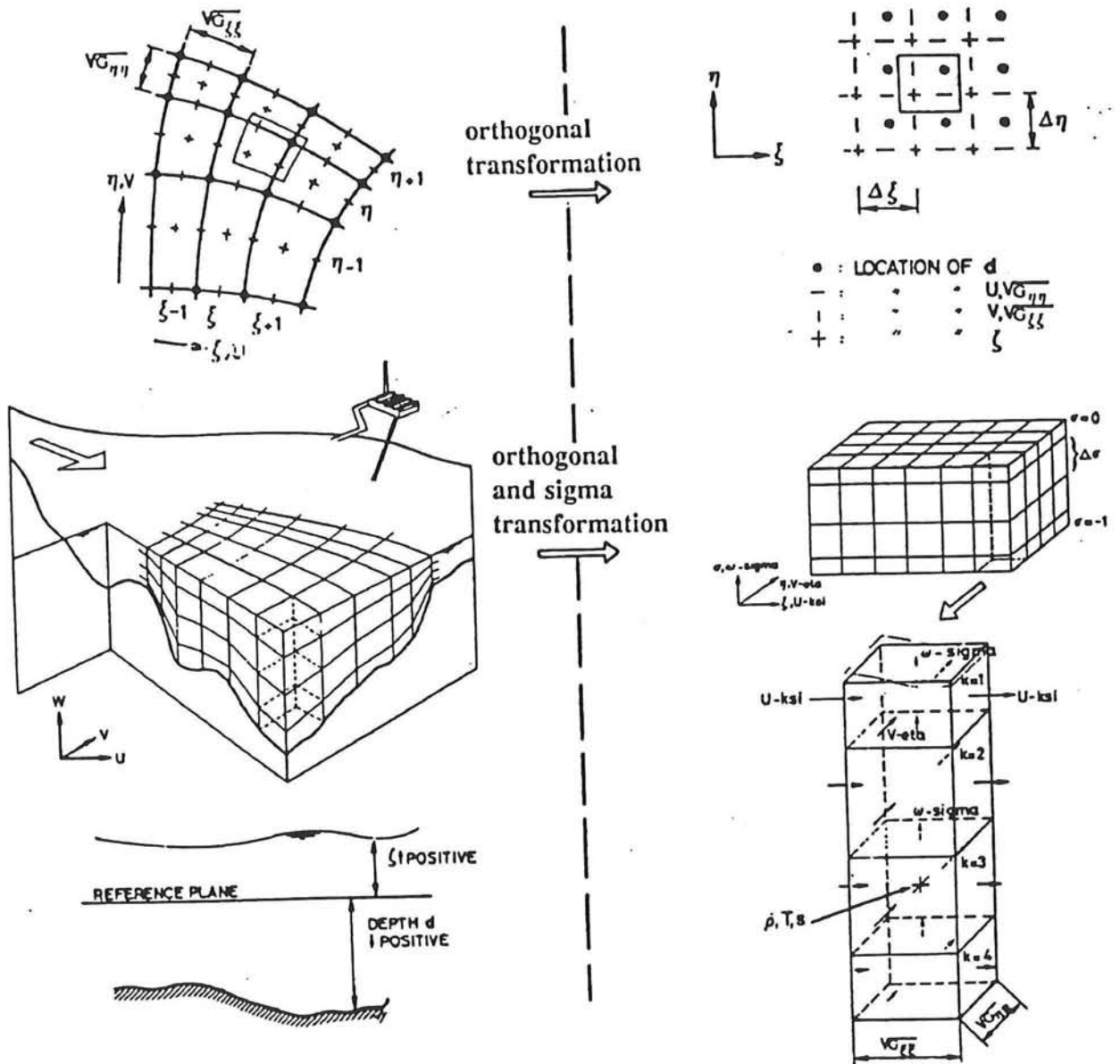
The last step is the substitution of the resolved velocities and water levels in the continuity equation (V.8, V.12) to calculate the vertical velocities.

Appendix VI

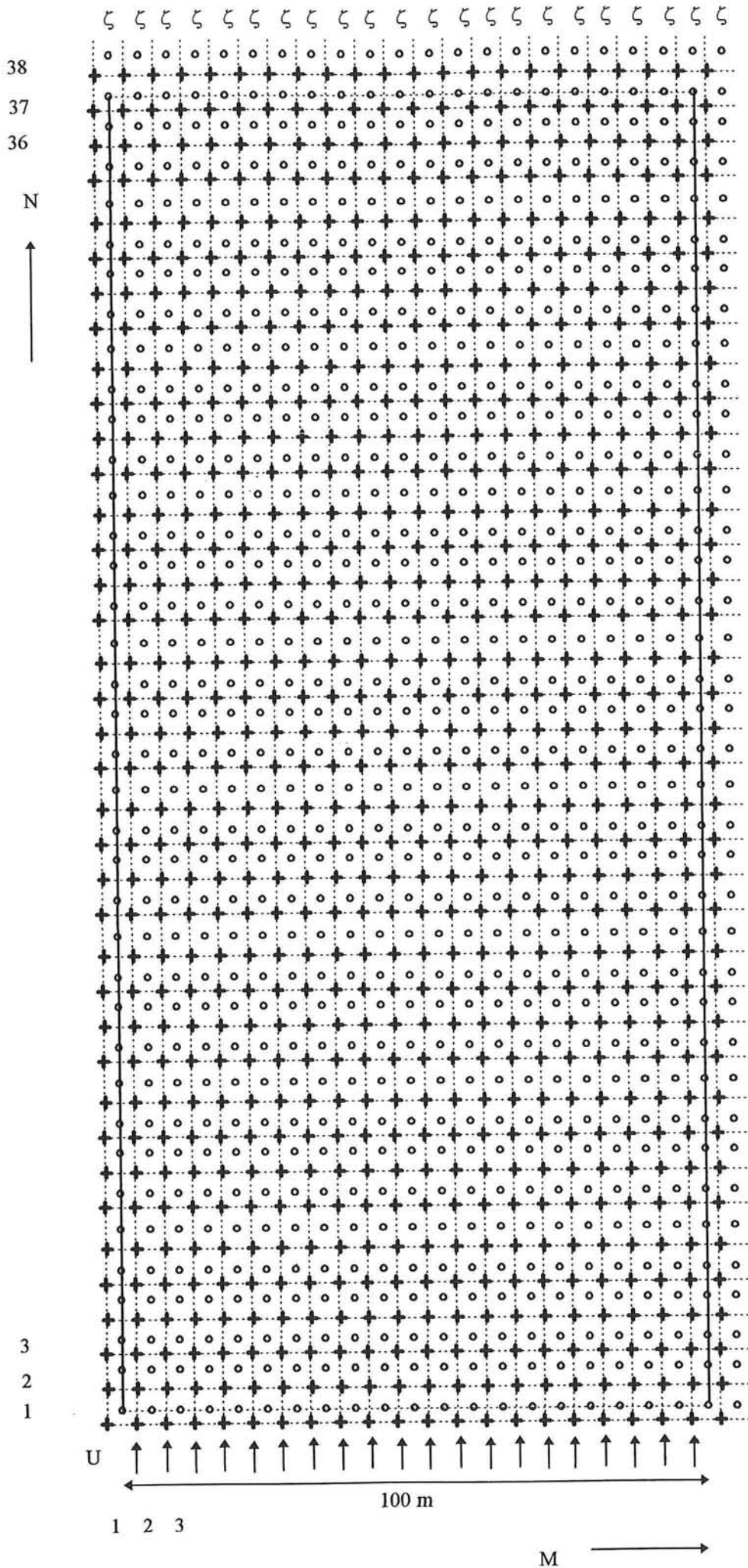
The transformation from a real configuration to a schematic grid configuration as well as the curvilinear grid configuration and the imposed boundary conditions of the bend used in this research.

physical space

transformed space



Orthogonal and Sigma transformation




```

Datbnd= #T#
MNBnd = 2 38 21 38
Alpha = 0.0000
ProfU = #Uniform #
Label = # # # #
INPPAR ADDPROC HEATMOD
Ktemp = 0
Fclou = [.]
Sarea = [.]
TURBMOD Tkemod= #K-epsilon #
RGDWALL Irov = 0
Z0v = [.]
TIDFORCE Tidfor= # # # #
# # #
USERDEF Nprcus= [ ]
Prcusr= # #
NUM-PAR Nprin= [ ] [ ] [ ] [ ]
Eps = [.]
Iter = 2
Dryflp= #NO #
Dryflc= 0.1000
RUNTIME Itdate= #1996-05-08#
Tunit = #M#
Dt = 0.0500
Tstart= 0.0000
Tstop = 0.0500
INIR Restid= #043#
INIF Filic = # #
FMtic = #FR#
INII LEVEL Zeta0 = 0.0000
OTHERS U0 = [.] [.] [.] [.] [.] [.] [.] [.]
[.] [.] [.] [.] [.] [.] [.] [.]
[.] [.] [.] [.]
V0 = [.] [.] [.] [.] [.] [.] [.] [.]
[.] [.] [.] [.] [.] [.] [.] [.]
[.] [.] [.] [.]
S0 = [.]
T0 = [.]
C01 = [.]
C02 = [.]
C03 = [.]
C04 = [.]
C05 = [.]
I0 = [.]
BNDCOND GENERAL SMOOTH Tlfsmo= 0.0000
HYDROAT Filana= # #
Filcor= # #
HYDROHF FilbcH= # #
FmtbcH= #FR#
HYDROHI FREQ Omega = [.]
CMPNENT Ampab = [.] [.]
Phsab = [.] [.]
HYDROTF FilbcT= # #
FmtbcT= #FR#
HYDROTI TsbcT = 0.0000
Ampab = 1.0000 1.0000
Ampab = 0.0000 0.0000
HYDROTI TsbcT = 200.000
Ampab = 1.0000 1.0000
Ampab = 0.0000 0.0000
PROCESF FilbcC= # #

```

		FmtbcC= #FR#
	PROCESI	TsbcC = [.]
		Sab = [.] [.] [.] [.]
		ProfC = [.] #Uniform #
		Tab = [.] [.] [.] [.]
		ProfC = [.] #Uniform #
		Cab1 = [.] [.] [.] [.]
		ProfC = [.] #Uniform #
		Cab2 = [.] [.] [.] [.]
		ProfC = [.] #Uniform #
		Cab3 = [.] [.] [.] [.]
		ProfC = [.] #Uniform #
		Cab4 = [.] [.] [.] [.]
		ProfC = [.] #Uniform #
		Cab5 = [.] [.] [.] [.]
		ProfC = [.] #Uniform #
	THRLMAN	Rettis= [.]
		Rettib= [.]
	PHYSCOF HYDRO GENERAL	Ag = 9.8130
		Rhow = 1000.0000
	BEDSTR XYGEN	Roumet= #C#
	XYVAR	Filrgh= # #
		Fmtrgh= #FR#
	UNIFORM	Ccofu = 65.0000
		Ccofv = 65.0000
	VIDIF 2D-SPV	Filedy= # #
		Fmtedy= #FR#
	2D-UNIF	Vicouv= 0.0100
		Dicouv= 1.0000
	3D-UNIF	Vicoww= 0.000001
		Dicoww= 0.000001
	WIND	Wstres= [.] [.] [.] [.]
		Rhoa = [.]
	PROCESS DENSITY	Alph0 = [.]
		Tempw = 0.0000
		Salw = 0.0000
	SECFLOW	Betac = [.]
		Equili= #N#
	ROUWAVE	Rouwav= # #
	PARTICL GENERAL	Par1 = [.]
		Par2 = [.]
	GROUP	Npari = [.]
		Tpar = [.] [.]
		XYpar = [.] [.]
	SPECIAL BARRIER GENERAL	Ergc1 = [.]
		Cofbar= [.] [.] [.] [.] [.] [.]
	SERIESF	Filbar= # #
		Fmtbar= #UN#
	SERIESI	Tsbar = [.] [.] [.] [.]
	WEIRLOS GENERAL	Ticrou= [.]
		Thetac= [.]
		Rfelag= [.]
		Rfelng= [.]
		Lwdry = #MEAN#
	COEFF	Hkruv = [.] [.]
		Crouv1= [.] [.]
		Crouv2= [.] [.]
		Lwtype= # #
	DISCHF	Fildis= # #
		Fmtdis= #FR#

DISCHI	Tsdis = [.] [.]		
	Cqs = [.]		
	Cqt = [.]		
	CqcN = [.] [.] [.] [.] [.]		
METEO HEAT SERIESF	Filtmp= # #		
	Fmttmp= #FR#		
TEMINT	Temint= #Y#		
SERIESI	Tstmp = [.] [.]		
WIND SPACEVA	Wnsvwp= #N#		
SERIESF	Filwnd= # #		
	Fmtwnd= #FR#		
WINDINT	Wndint= #Y#		
SERIESI	Tswnd = [.] [.] [.]		
USERDEF FILES	Filusr= # #		
REALCONS	Rcours= [.]		
INT.CON	Icours= [.]		
CHARCONS	Ccours= # #		
OUTPUT SITE STATION	Namst = #6,10 #		
	MNst = 6 10		
STATION	Namst = #6,16 #		
	MNst = 6 16		
STATION	Namst = #6,21 #		
	MNst = 6 21		
STATION	Namst = #6,26 #		
	MNst = 6 26		
STATION	Namst = #6,31 #		
	MNst = 6 31		
STATION	Namst = #6,36 #		
	MNst = 6 36		
CROSS	Namcrs= # #		
	MNcrs = [.] [.] [.] [.]		
QNTTY MAP	SMhydr= #YYYYY#		
	SMproc= #NNNNNNNNNN#		
	SMderv= #YYYN#		
HIS	SHhydr= #YYYY#		
	SHproc= #NNNNNNNNNN#		
	SHderv= #NNYN#		
	SHflux= #NNNN#		
FOURIER	Filfou= # #		
FILES PRINT MAP	Prmap = [.]		
HISTORY	Prhis = [.] [.] [.]		
STORE MAP	Flmap = 0.0000 0.0500 0.0500		
HISTORY	Flhis = 0.0000 0.0500 0.0000		
COMM	Flpp = 0.0000 0.0000 0.0000		
RESTART	Restrt= #Y#		

Explanation of the MD-file input parameters

The MD-file can be divided in six main groups of input parameters:

IDENT	the code of the version of Trisula that will be used
RUNID	means the run identification code which is used to name the MD-file
PROCESS	means the prescription of certain processes which can occur in the flow or can act on the flow
DOMAIN	means the parameters and the file names that define the computational domain and the flow configuration including types and places of the boundaries
INPPAR	here the values of the parameters and file names of the initial and boundary conditions, the processes, the physical quantities and the turbulent closure model have to be given as well as the total calculation time and time step in the simulation
OUTPUT	here the points and cross-sections for which the computational results will be stored and the time that they have to be stored must be given

Some of these six groups are divided in other groups of input parameters. To start with the main group Domain this subdivision is (Processes are not given in this flow case so it will be left out of consideration):

GRID	means the definition of the computational domain.
COMGRDF	means the attribute file containing the computational grid enclosure
COMGRDI	input values of grid coordinates of computational grid enclosure
SPECIAL	are the special discharges in the flow or special objects in the flow
DEPTH	means the depth of flow
DEFBNDF	file containing the position and type of the boundaries
DEFBNDI	values of the position and type of the boundaries

The main group Inppar is subdivided into:

ADDPROC	means the additional processes in the flow like heat model, turbulence model
NUM-PAR	are the numerical parameters of the simulation
RUNTIME	total simulation time and time step
INIR	run identification code of the restart file
INIF	file containing the results of an earlier computation to restart that calculation
INII	initial values for the additional processes
BNDCOND	starting and stopping time of the boundary conditions and their values
PHYSCOF	values of the various physical coefficient in the simulation
DISCHF	file containing the values and their starting and finishing time of the discharges
DISCHI	values and their starting and finishing time of the discharges
METEO	values for wind and heat models

In the main group of the output the subdivision is as follows:

SITE	grid point where the results must be stored
QNTTY	the quantities that have to be stored
FILES	starting time and time interval at which the quantities have to be stored

In this part the most important input parameters for this flow case will be described. The flows in this research do not contain extra processes (f.e. salt, heat, density) and the influence of the weather is not considered so their input parameters will be left out of consideration and therefore not every input parameter of the MD-file will be explained. When a blank value is given for a parameter it means that it is not considered.

Ident	version of Trisula that will be used
Runid	run identification code
MNKmax	maximum number of grid points in the computational domain
Thick	is the thickness of the layers in the vertical direction in percents of the total water depth

Filcco	means the input file where the coordinates of the grid points in an x-and y-coordinate system are given.
Anglat	position of the model on the earth globe (degrees north)
Grdang	angle of orientation of the model (degrees)
Mngrd	coordinates of points defining the computational grid enclosure
Depuni	uniform depth value (m)
Nambnd	name of the boundary section
Typbnd	type of the open boundary (water elevation, current, flux or Riemann/Radiation type)
Datbnd	forcing type of the boundary condition (harmonic, astronomical or time series driven)
Mnbnd	begin and end coordinates of the open boundary section
Alpha	semi reflective open boundary coefficient
ProfU	vertical profile for velocity/flux at open boundaries (logarithmic, uniform)
Tkemode	selection flag for the desired turbulence closure model
Irov	flag to (de)activate partial slip conditions at closed boundaries (0 means no slip)
Iter	maximum number of iterations applied to solve the continuity equation
Dryflp	flag for extra drying/flooding check criterion
Dryflc	threshold depth for drying/flooding check criterion (m)
ltdate	reference simulation date
Tunit	(fixed) unit of all time parameters in the simulation (minutes)
Dt	full integration time step (min)
Tstart	start time of the simulation (min)
Tstop	time to stop the simulation (min)
Restid	run identification code of the restart file
Zeta0	uniform initial condition for the water elevation (m)
U0	uniform initial condition for the velocities in the x-direction (m/s)
V0	uniform initial condition for the velocities in the y-direction (m/s)
S0	uniform initial condition for salinity (kg/m^3)
T0	uniform initial condition for temperature ($^{\circ}\text{C}$)
CO1..CO5	uniform initial condition for user defined constituent (kg/m^3)
I0	uniform initial condition for spiral motion intensity (m/s)
Tlfsmo	time interval to smooth the hydrodynamic boundary condition (min)
TsbcT	time parameter in the time-series for the hydrodynamic boundary condition
Ampab	magnitude of the hydrodynamic open boundary values
Ag	gravitational acceleration (m/s^2)
Rhow	density of the fluid (kg/m^3)
Roumet	bottom friction formulation to be used (Manning, White-Colebrook, Chézy or
bottom	roughness formulation)
Ccofu	uniform bottom roughness coefficient in x-direction
Ccofv	uniform bottom roughness coefficient in y-direction
Vicouv	uniform horizontal eddy viscosity (m^2/s)
Dicouv	uniform horizontal eddy diffusivity (m^2/s)
Vicoww	uniform vertical eddy viscosity (m^2/s)
Dicoww	uniform vertical eddy diffusivity (m^2/s)
Namst	name of the monitoring stations
Mnst	coordinate of the monitoring stations
Smhydr	output flags for hydrodynamic quantities
Smproc	output flags for constituent and turbulent quantities
Smderv	output flags for derived quantities
Shflux	output flags for fluxes across cross-sections
Flmap	start, interval and stop time to store overall computation results
Flhis	time interval to store computed history data
Flpp	start, interval and stop times for the hydrodynamic data base or the communication
file	
Restrt	flag to write a restart file

Appendix VIII

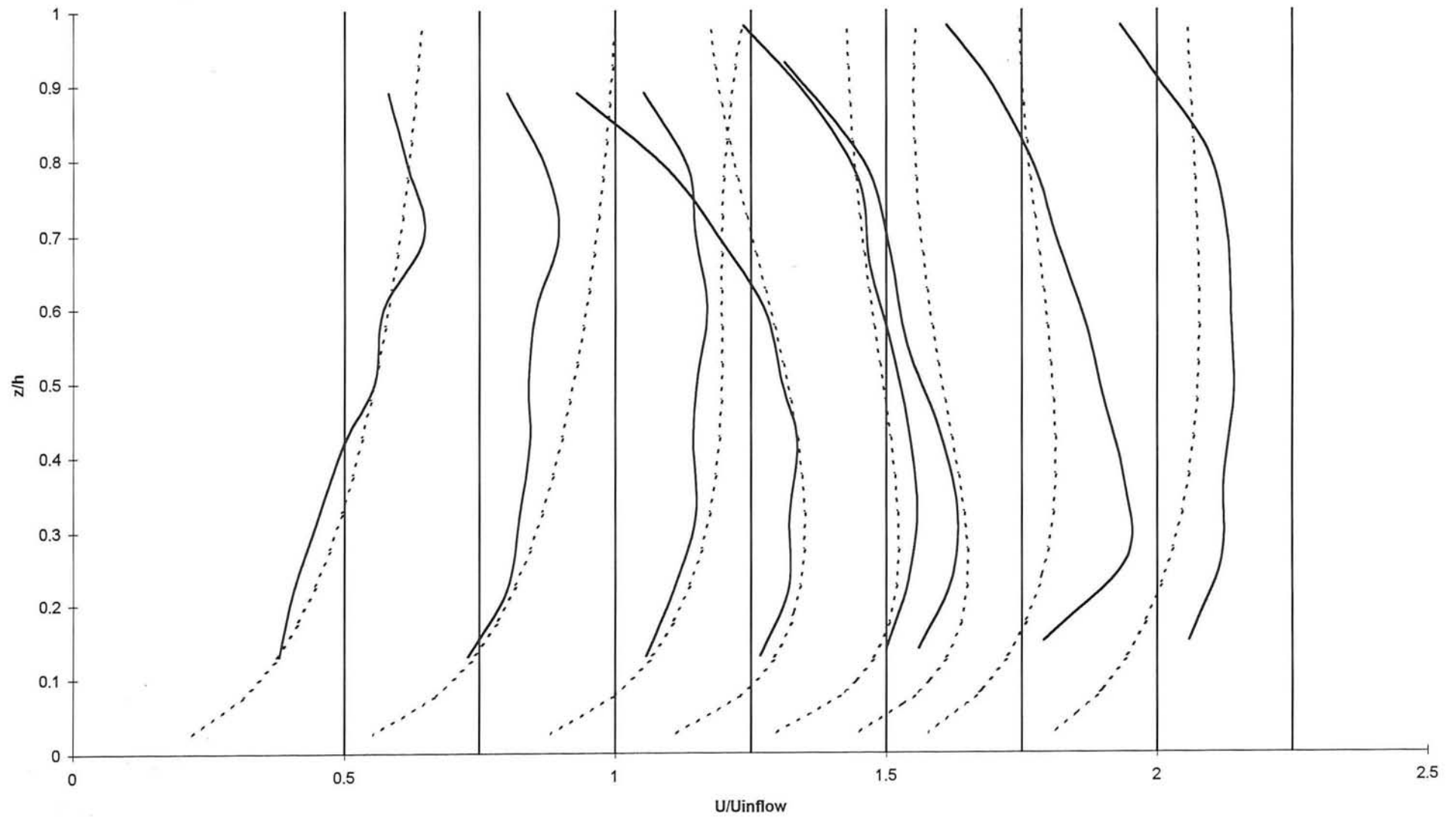
In this appendix the figures of the comparison of the numerical simulation of the strongly curved river bend and the measured data of De Vriend [ref 18] are shown.

In these figures are:

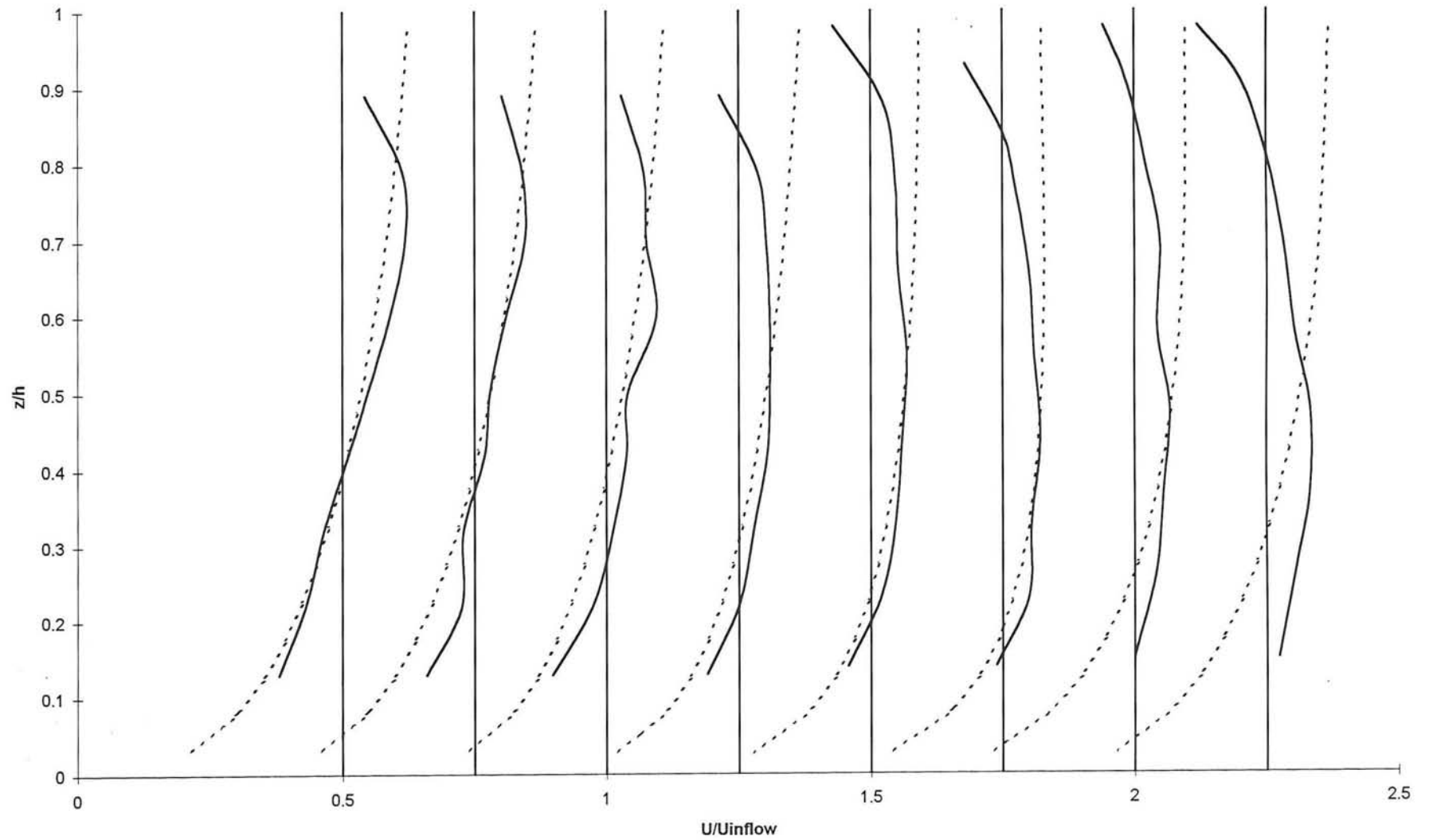
————— the experimental data
..... the prediction of the numerical simulation

N.B. All the velocity distributions have their own vertical axis. This vertical axis represent the main velocity (in case of the radial velocity distributions this main velocity is zero). The scale of the velocity is only shown for the first velocity distribution.

comparison of longitudinal velocities in the inner wall region ($\kappa \text{si} = -4$) of experiment/simulation with Chezy = $65 \text{ m}^{1/2} / \text{s}$

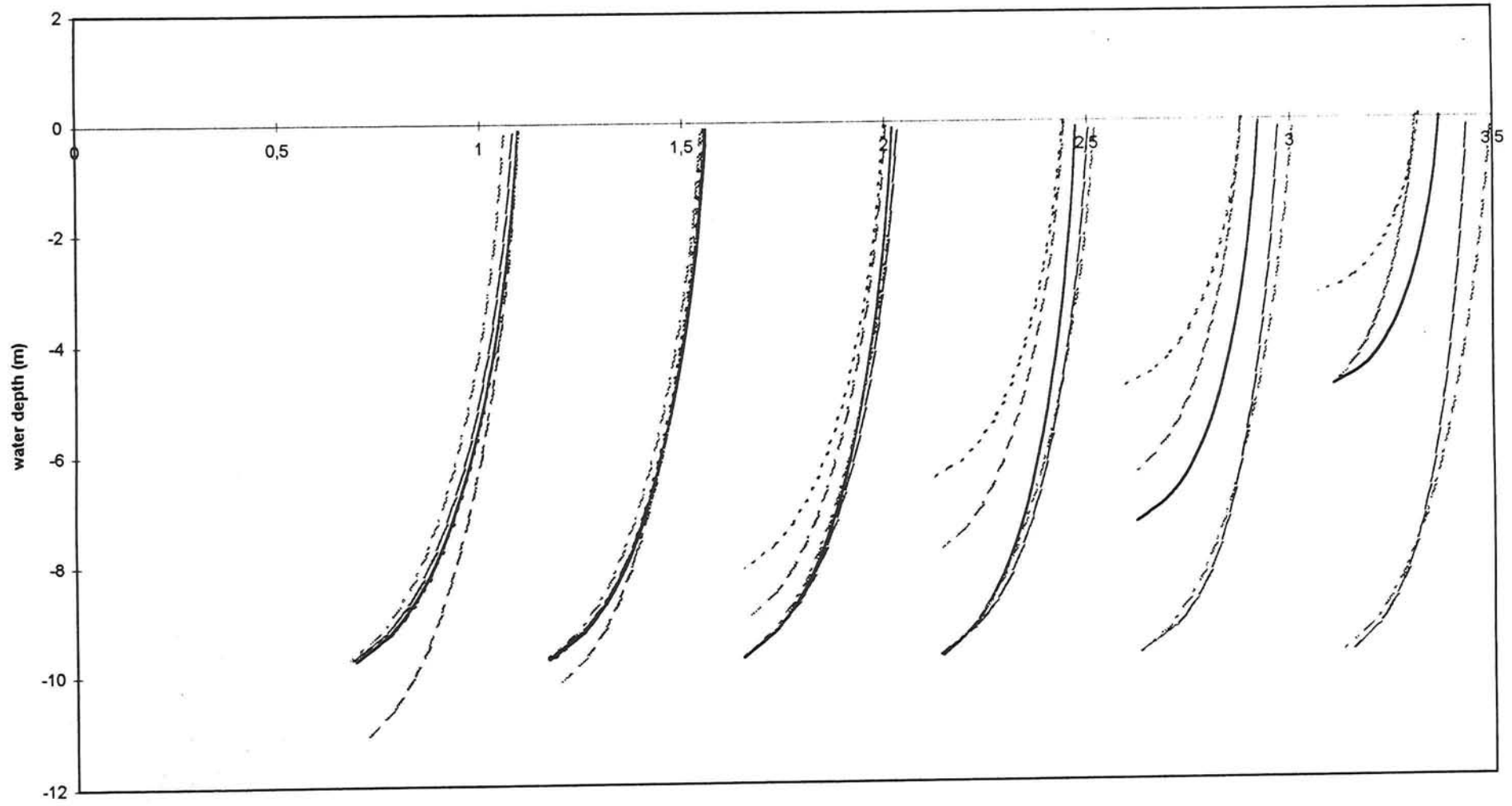


comparison of longitudinal velocities in the middle of the cross-section (ksi=0) of experiment/simulation with Chezy=65 m^{1/2}/s



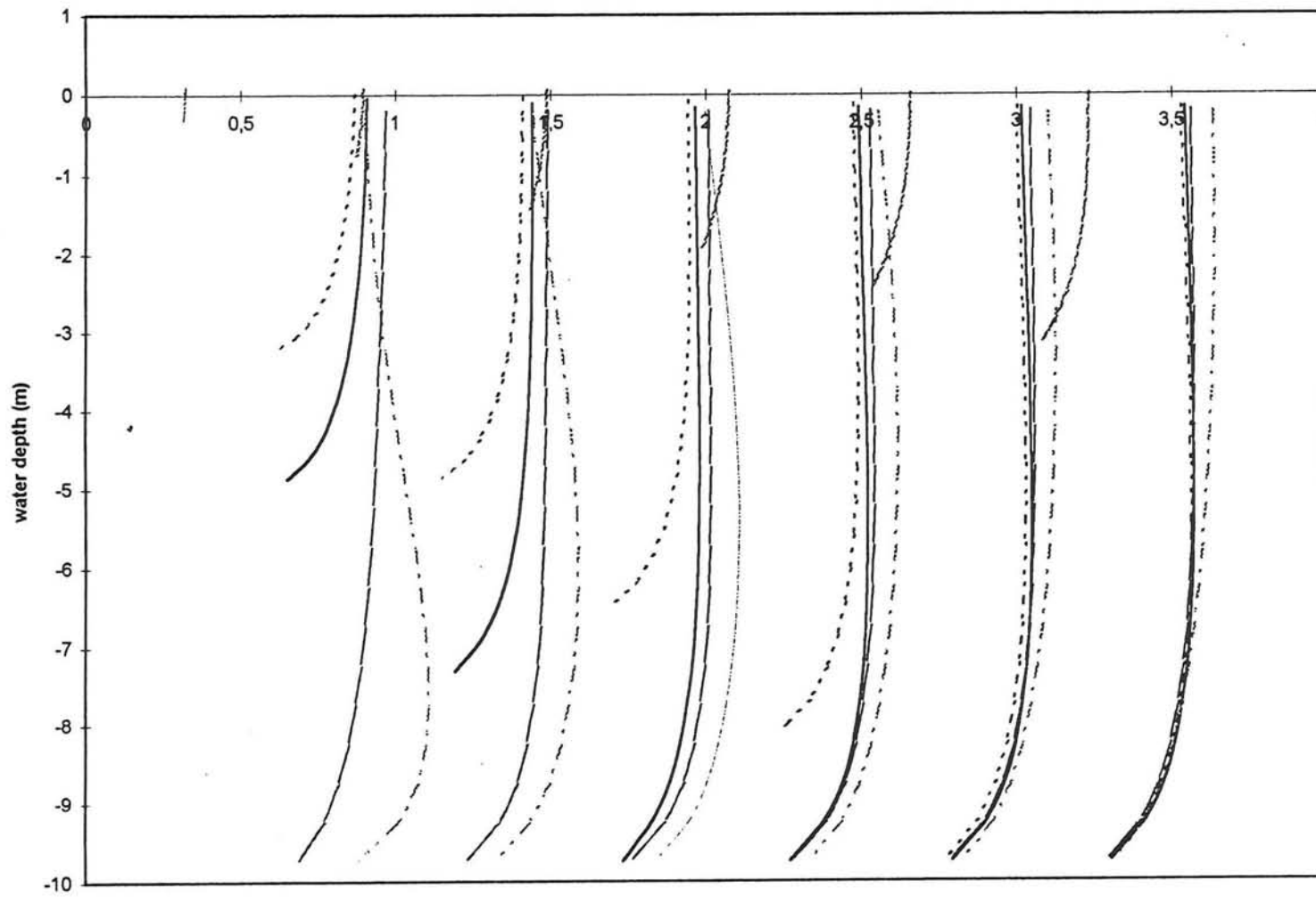
longitudinal velocities near the outer wall at $\phi=7,5$

velocity (m/s)



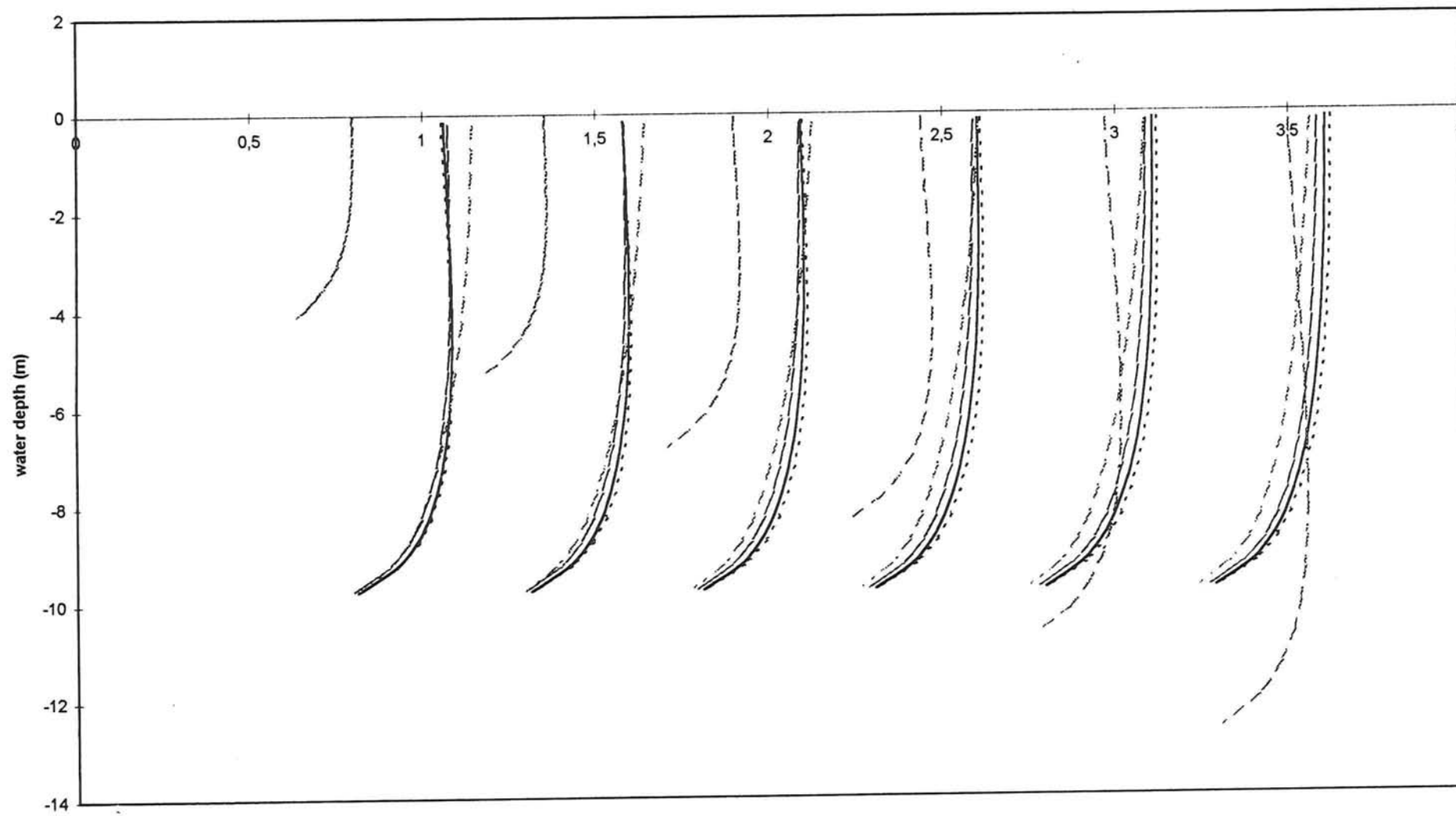
longitudinal velocities near the inner wall at $\phi=90$

velocity (m/s)

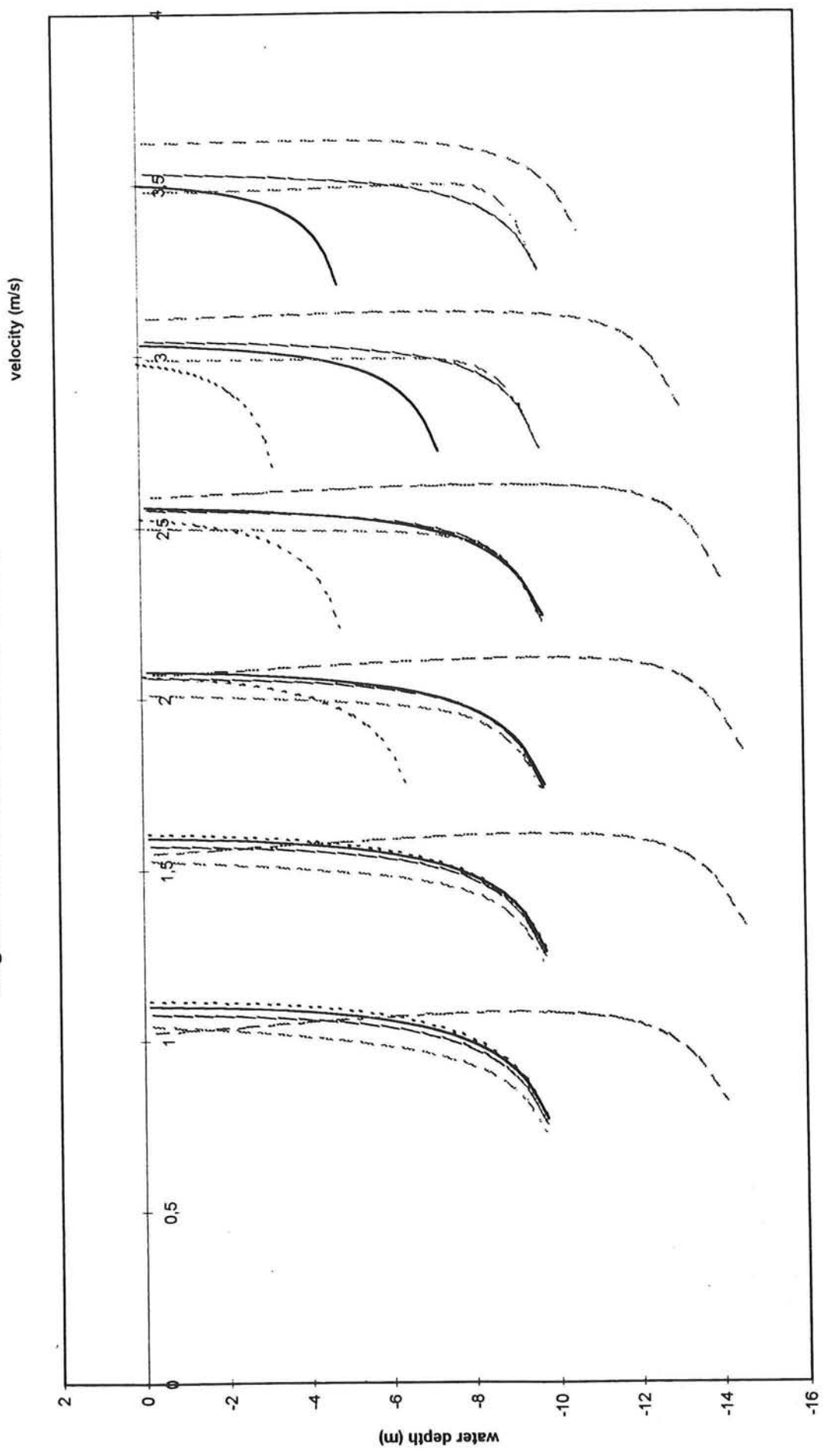


longitudinal velocities in the middle of the cross-section at $\phi=90$

velocity (m/s)

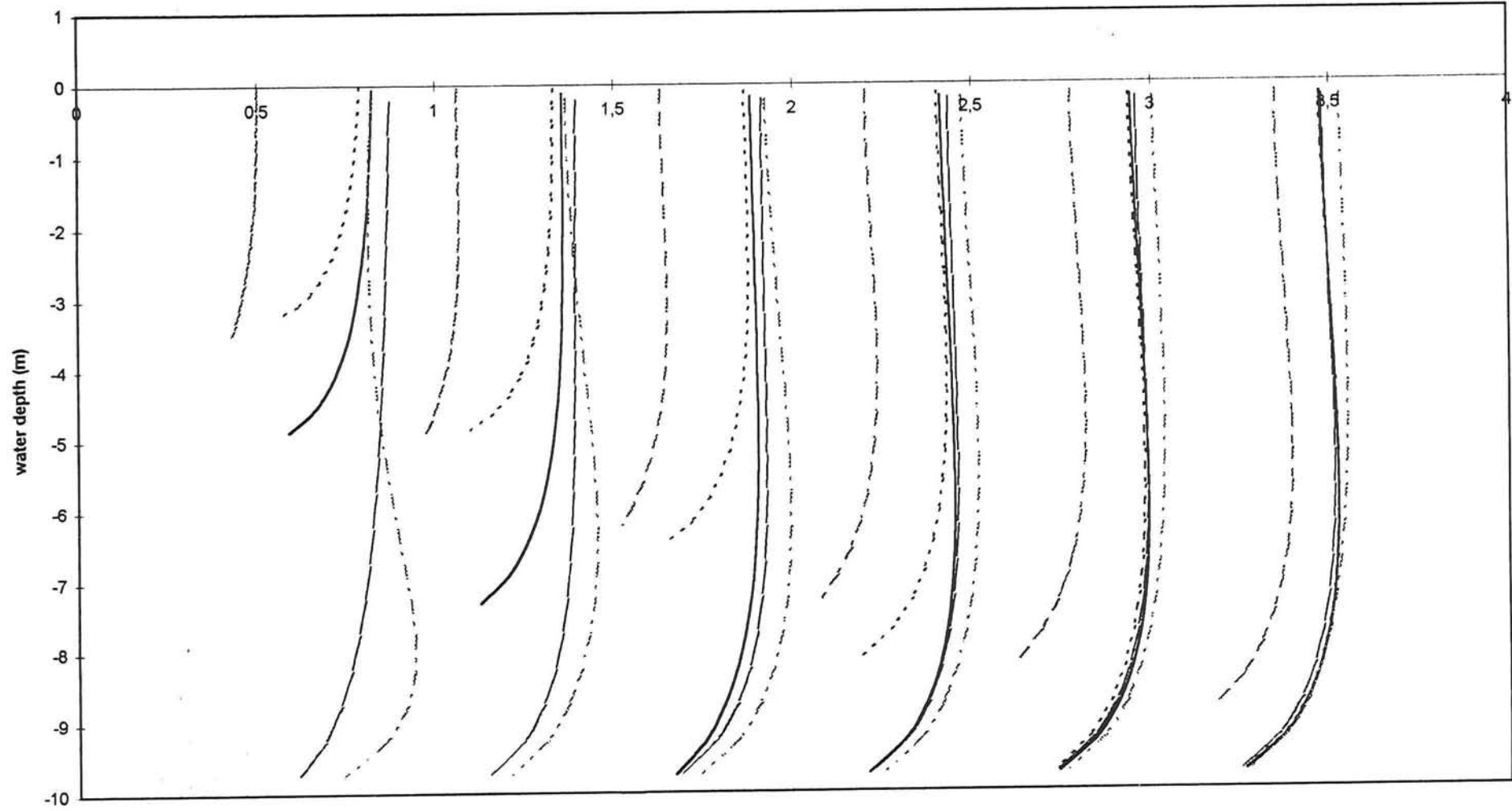


longitudinal velocities near the outer wall at $\phi=90$

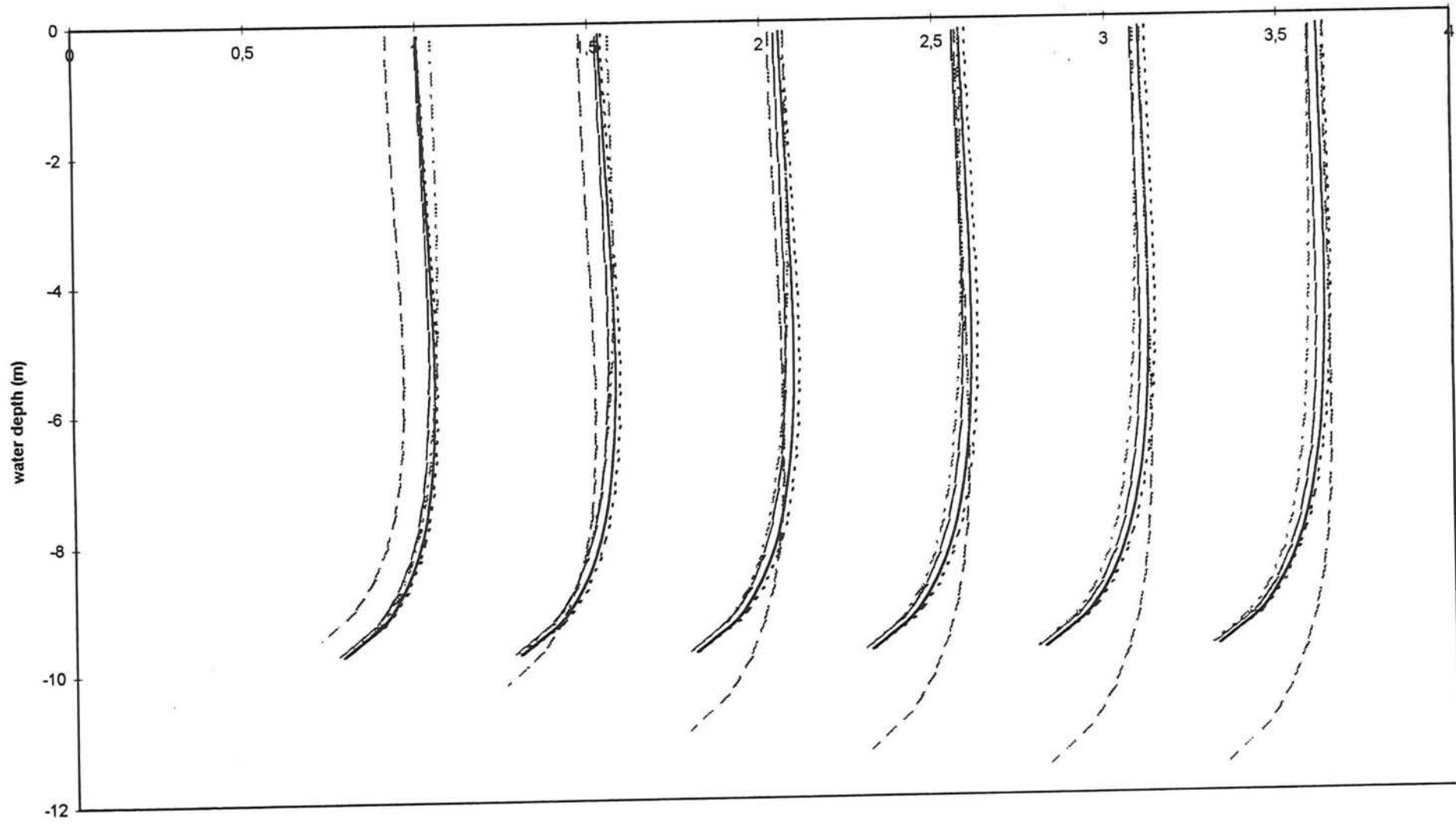


longitudinal velocities near the inner wall at $\phi=172,5$

velocity (m/s)

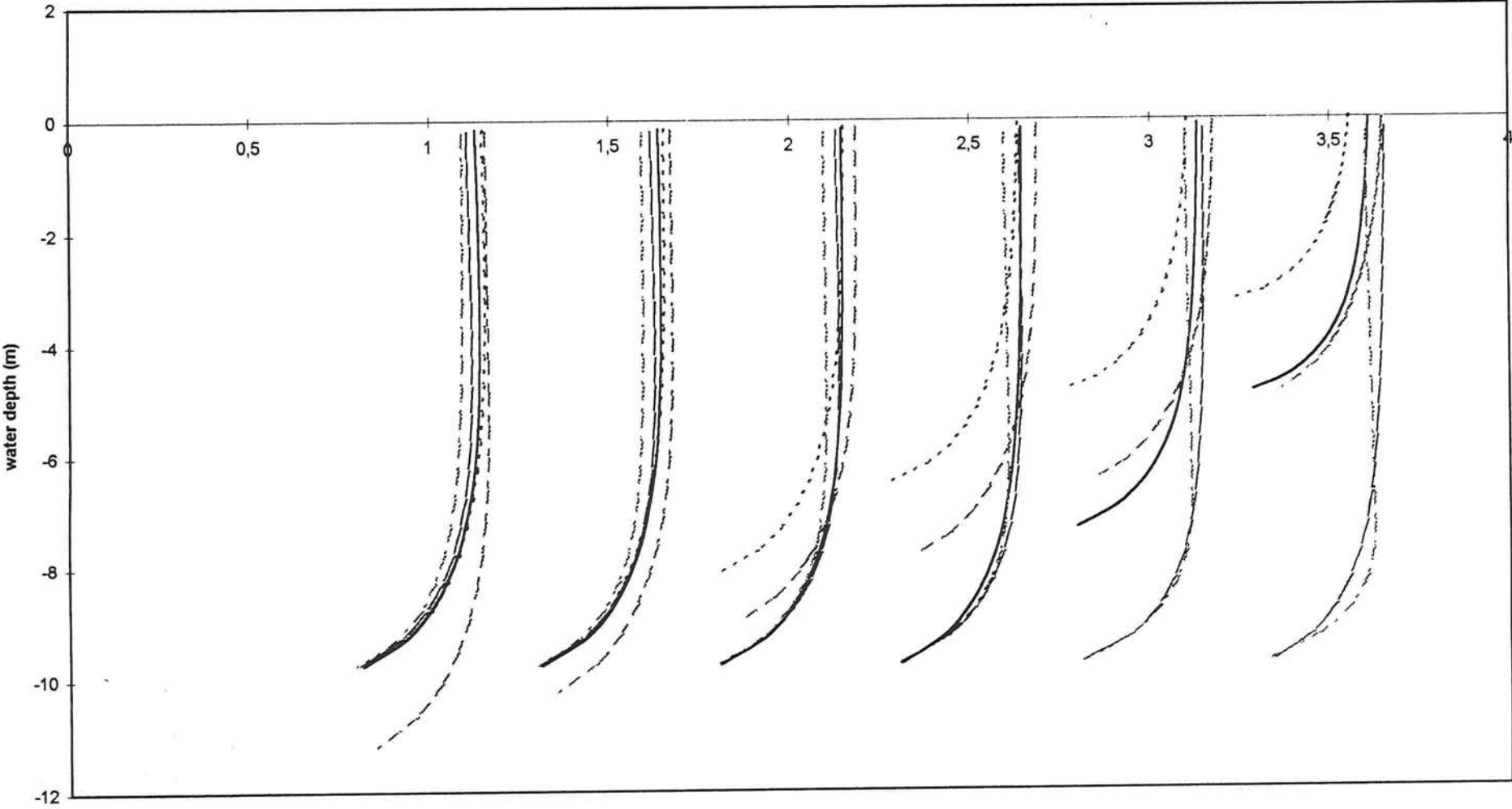


longitudinal velocities in the middle of the cross-section at $\phi=172,5$ velocity (m/s)

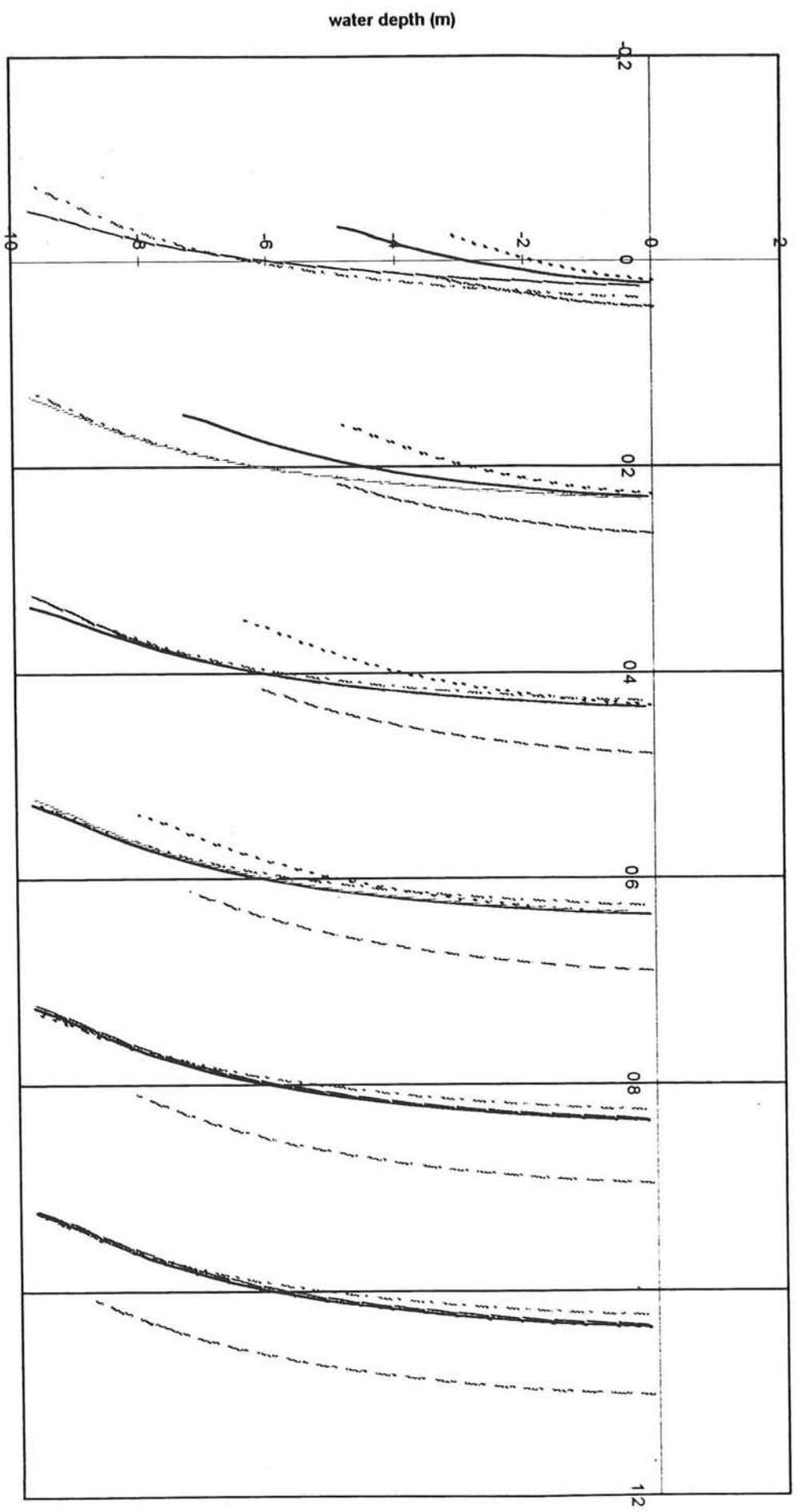


longitudinal velocities near the outer wall at phi=172,5

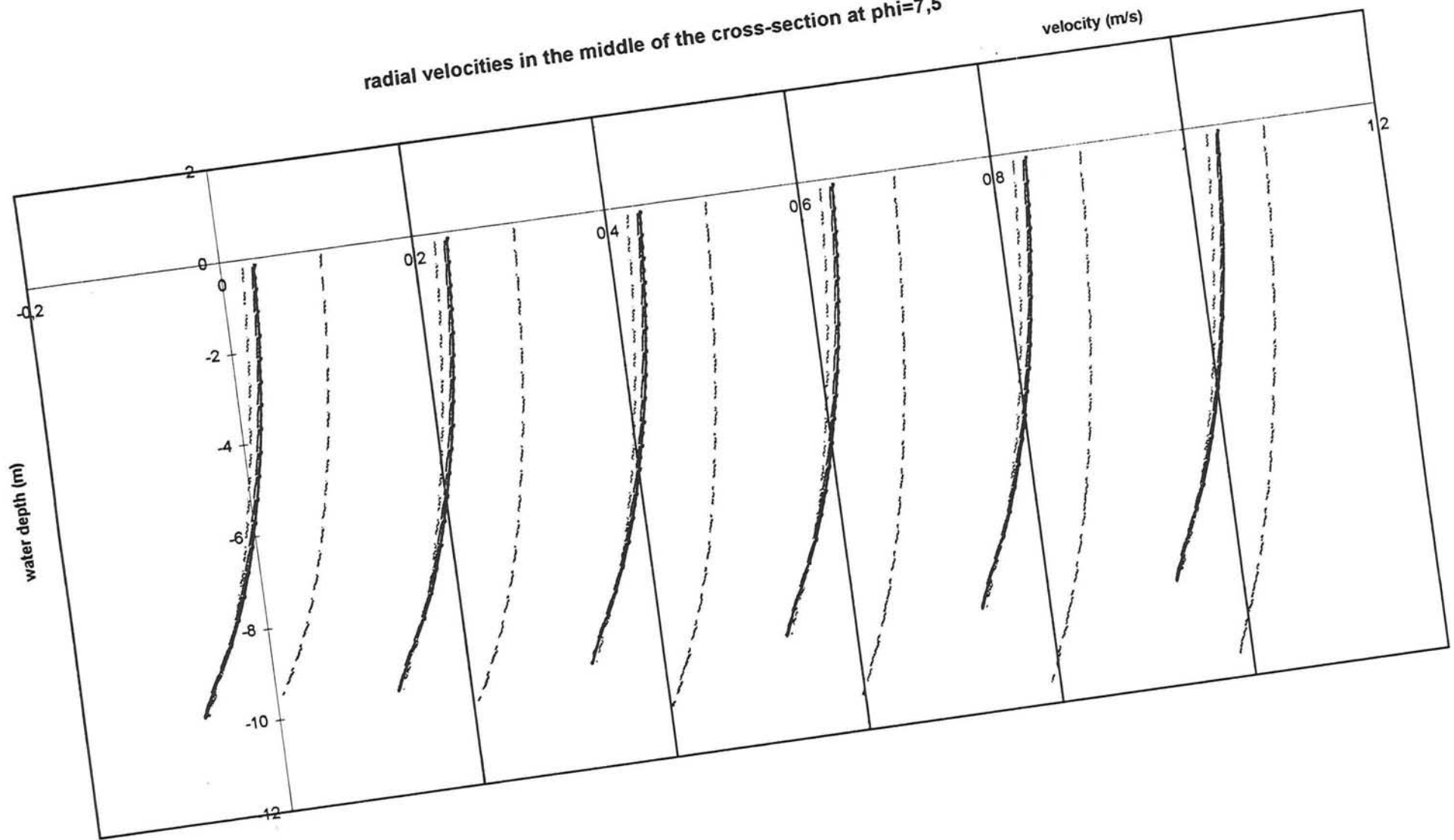
velocity (m/s)



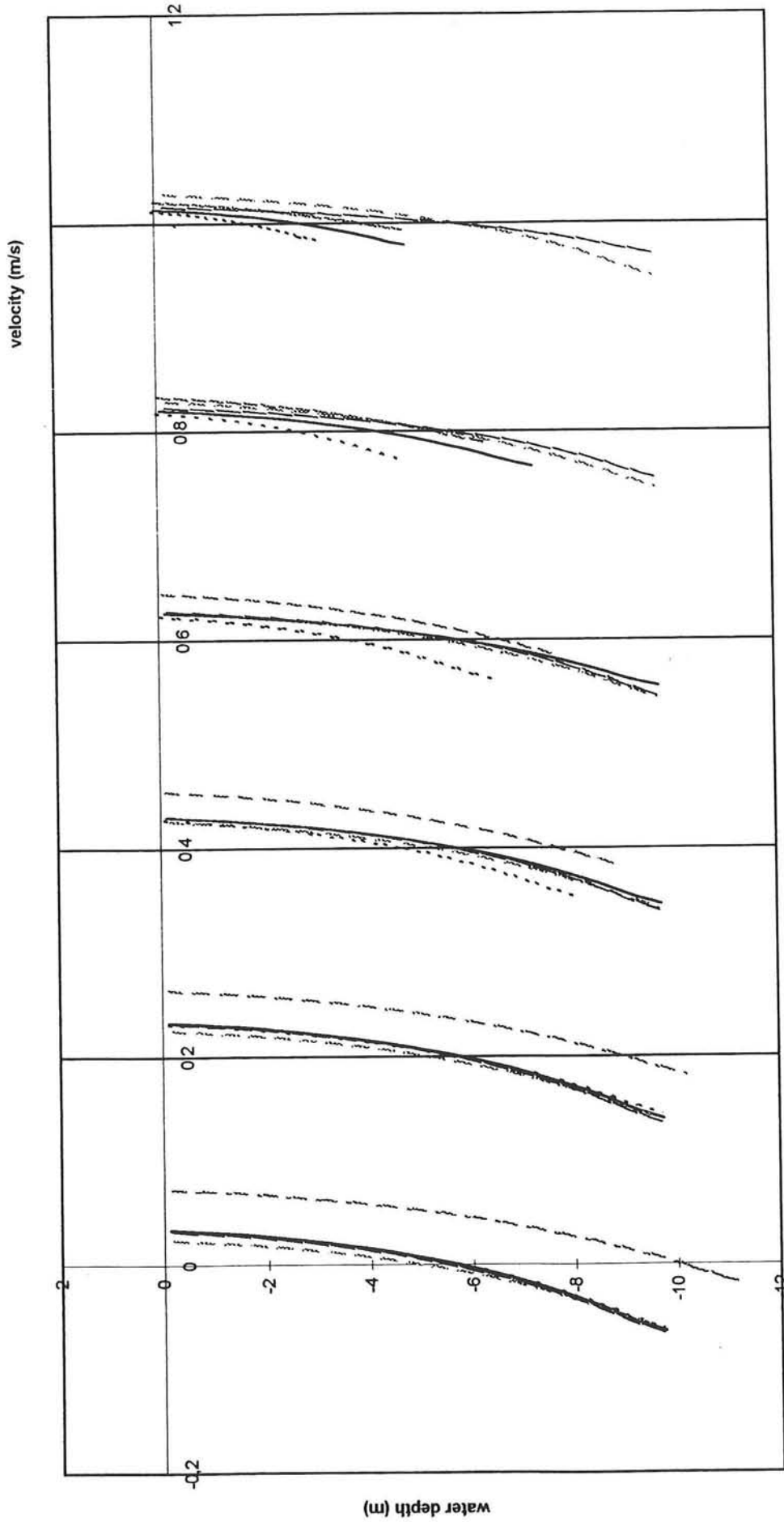
radial velocities near the inner wall at $\phi=7,5$



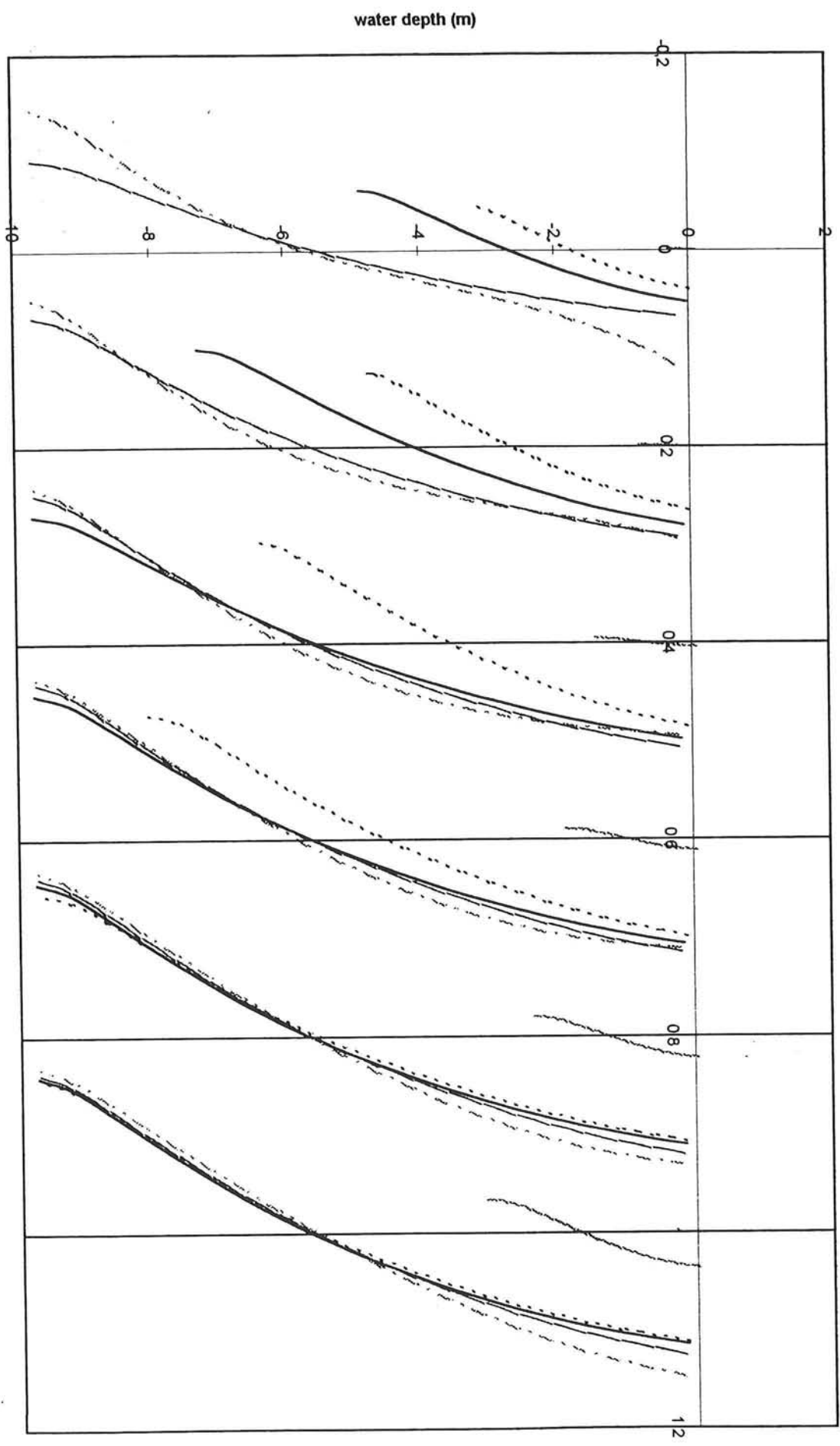
radial velocities in the middle of the cross-section at $\phi=7,5$



radial velocities near the outer wall at $\phi=7,5$

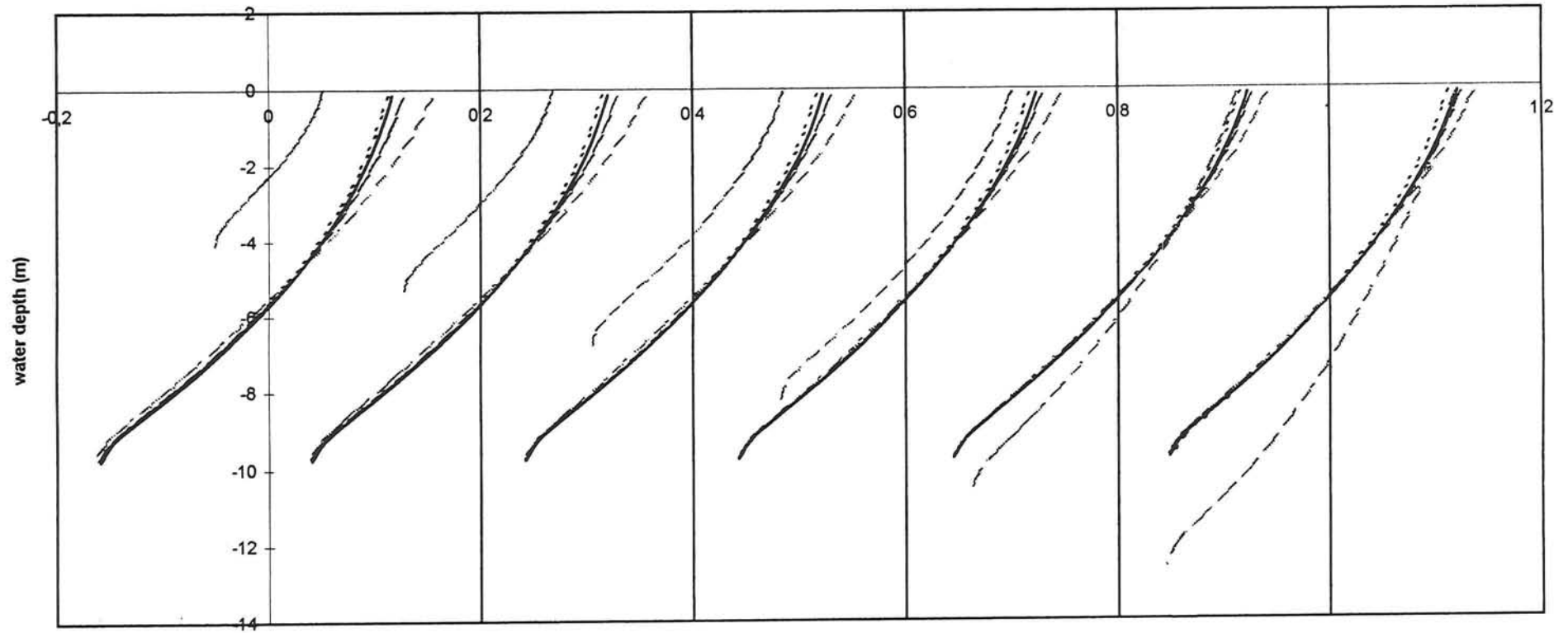


radial velocities near the inner wall at $\phi=90$



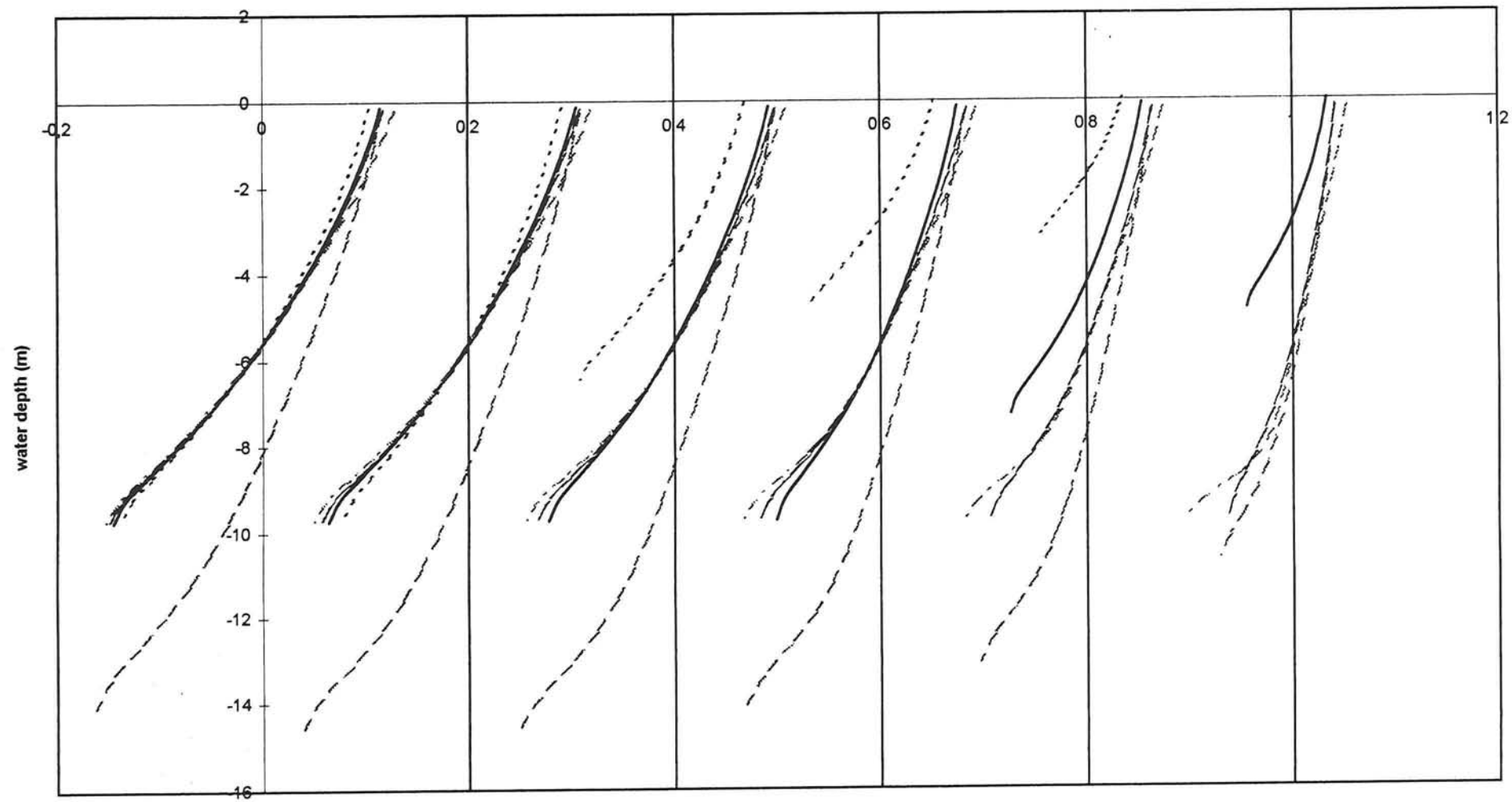
radial velocities in the middle of the cross-section at phi=90

velocity (m/s)



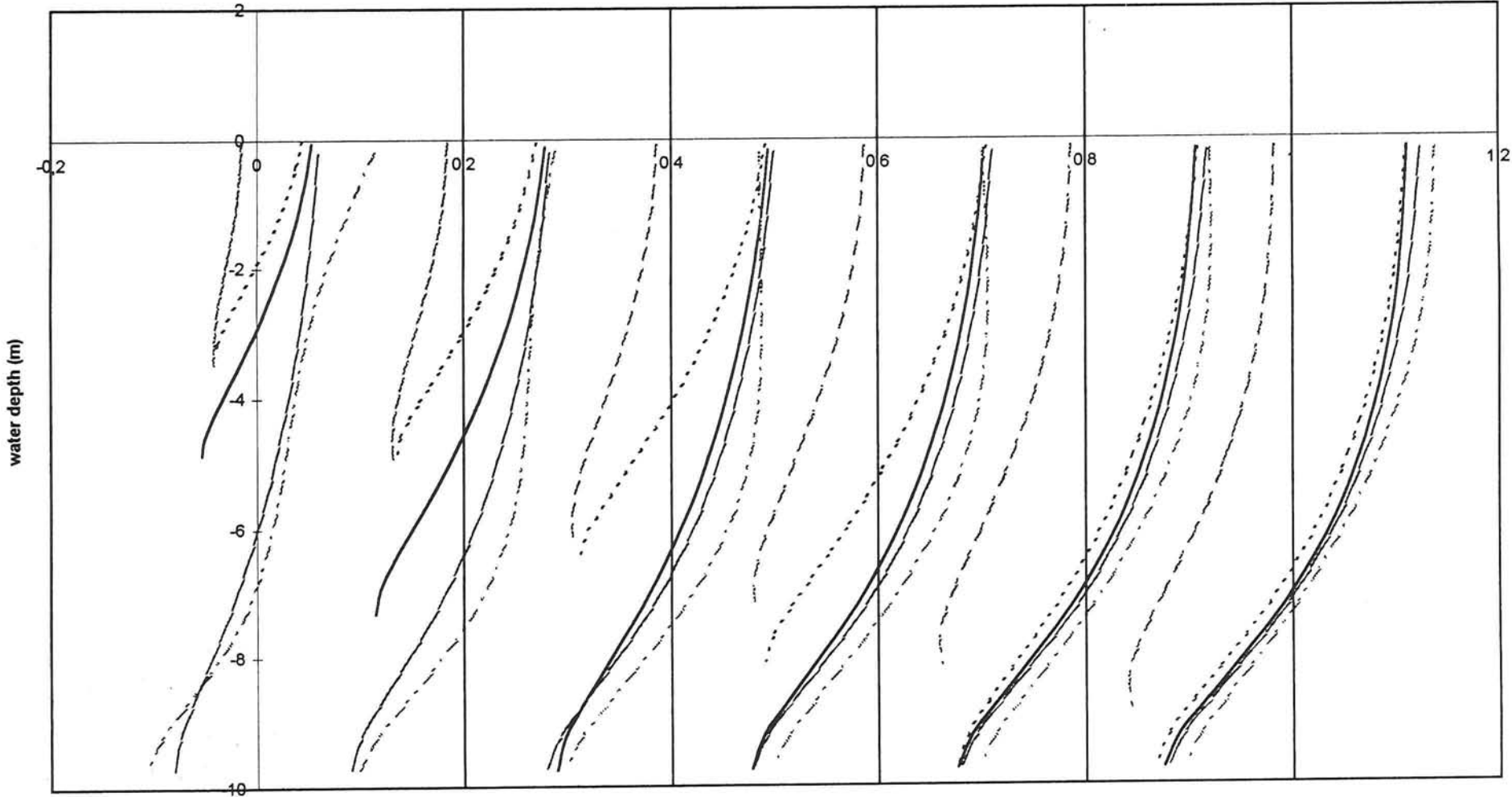
radial velocities near the outer wall at phi=90

velocity (m/s)

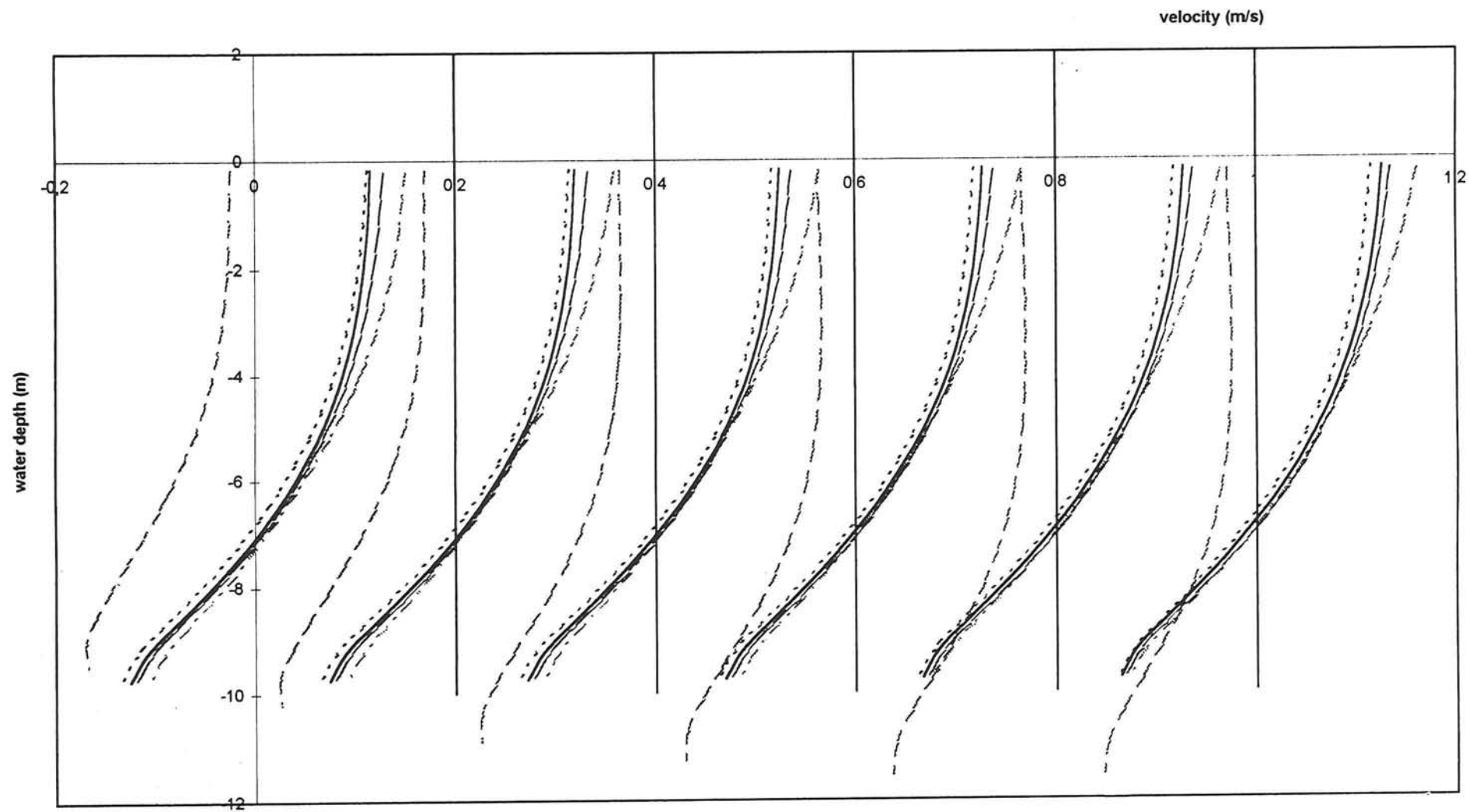


radial velocities near the inner wall at $\phi=172,5$

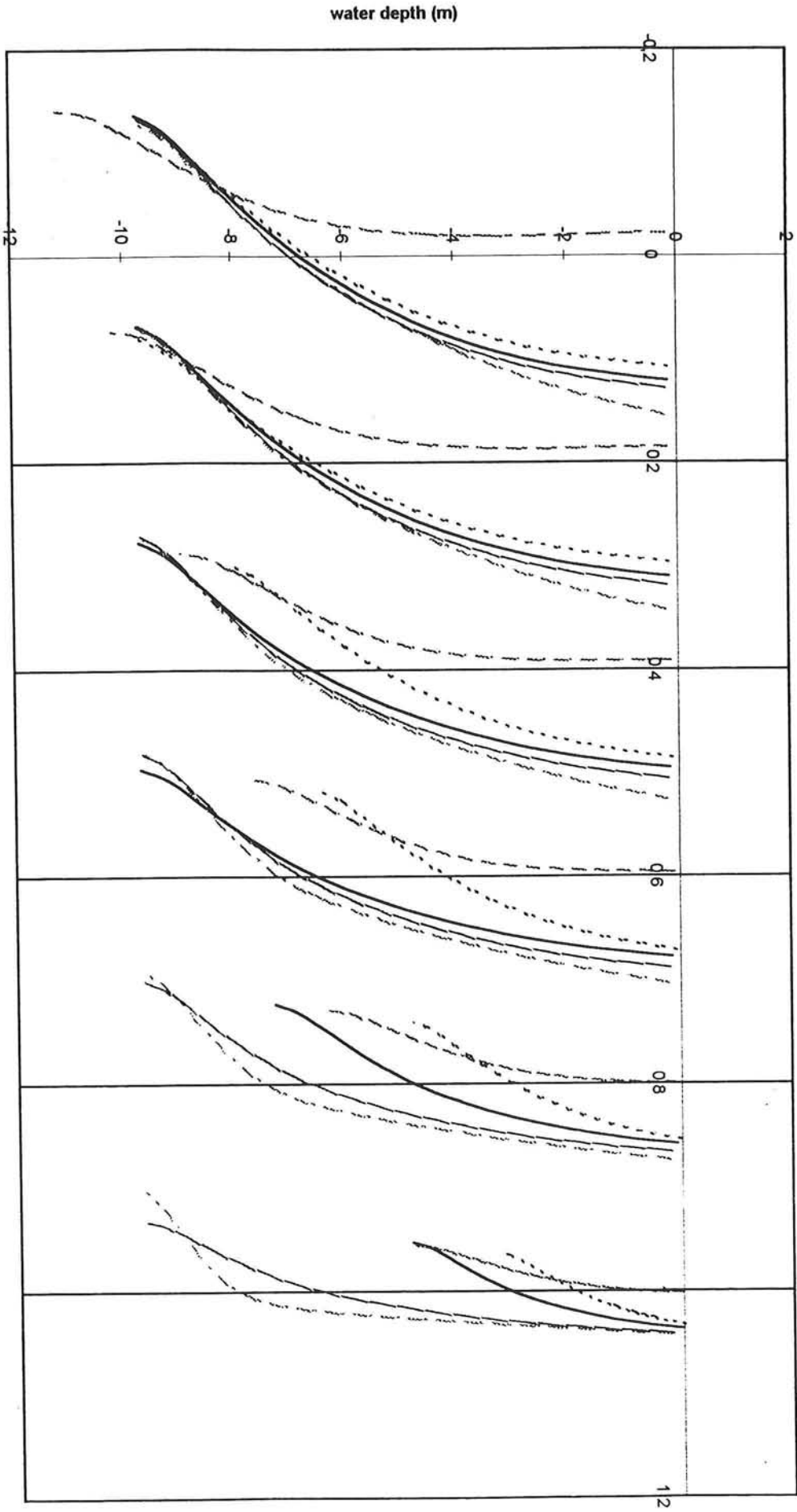
velocity (m/s)



radial velocities in the middle of the cross-section at phi=172,5



radial velocities near the outer wall at $\phi=172.5$



Appendix XVII

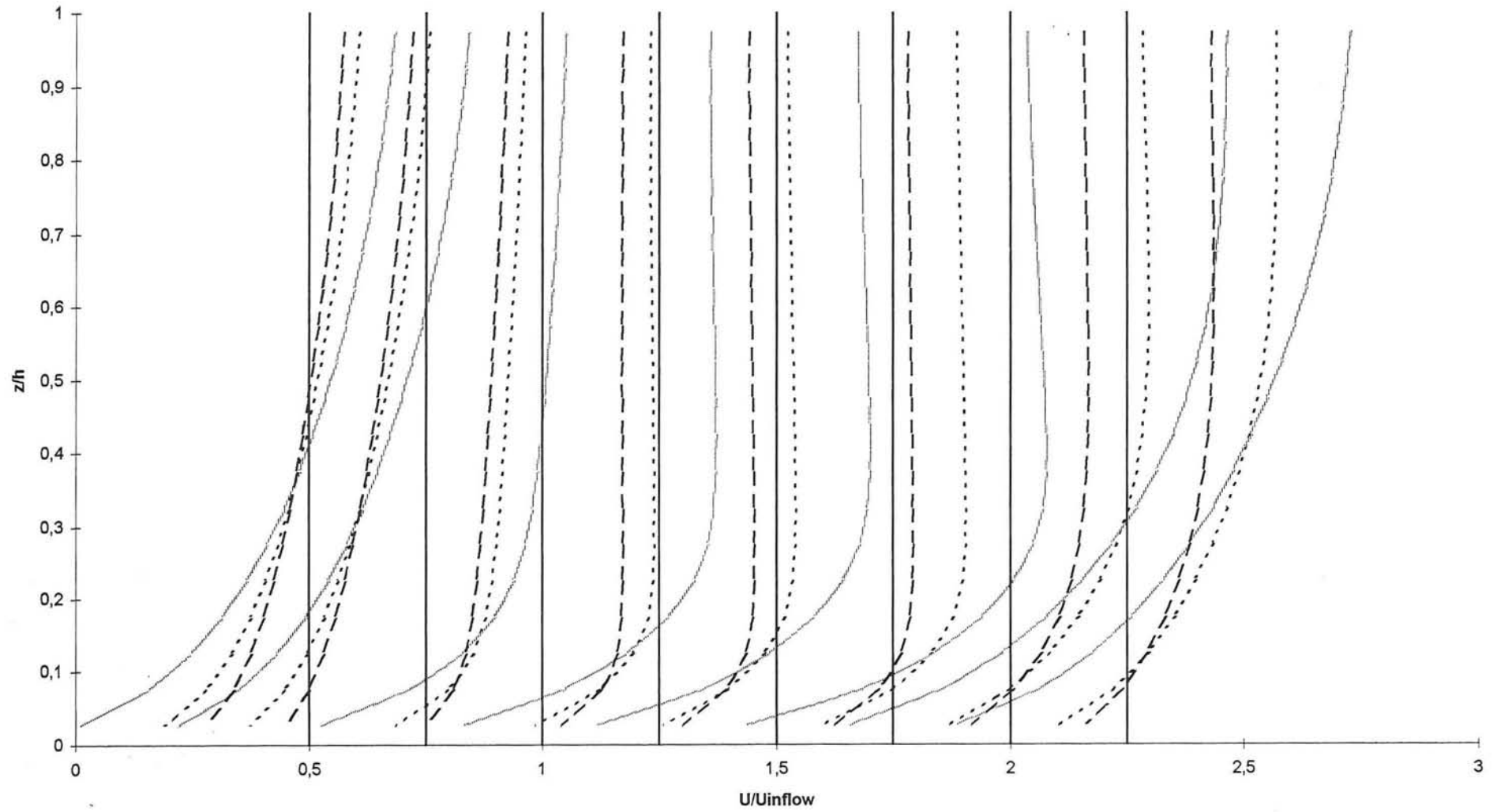
These figures show the influence of the Chézy coefficient in the simulation of the strongly curved bend.

The results are given along the longitudinal direction for three positions in the cross-section; at a distance 0,1 times the width from the inner wall, in the middle of the cross-section and at a distance 0,1 times the width from the outer wall.

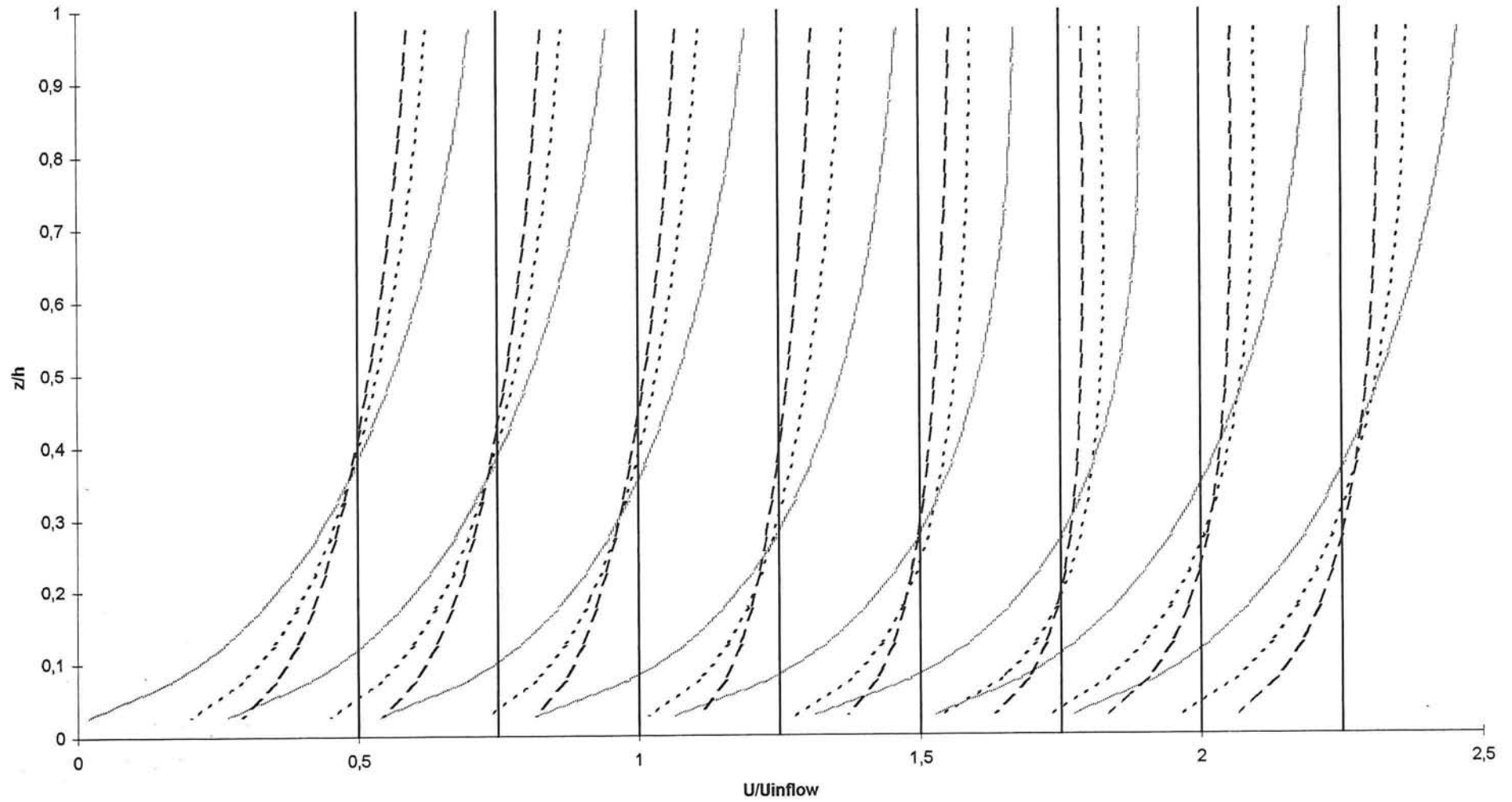
- Chézy coefficient equal 40 m^{1/2}/s
- Chézy coefficient equal 65 m^{1/2}/s
- Chézy coefficient equal 95 m^{1/2}/s

N.B. All the velocity distributions have their own vertical axis. This vertical axis represent the main velocity (in case of the radial velocity distributions this main velocity is zero). The scale of the velocity is only shown for the first velocity distribution.

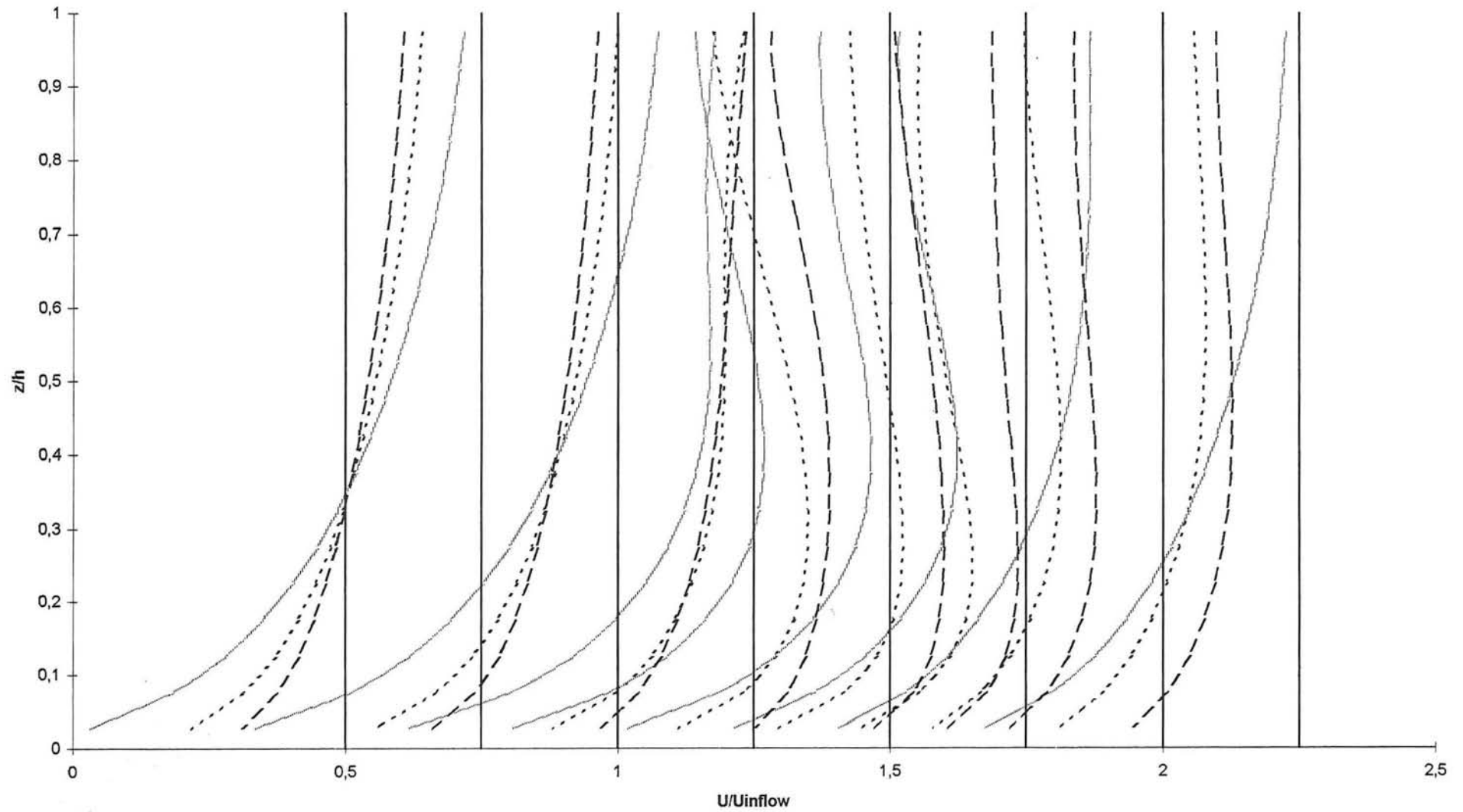
longitudinal velocity in the outer wall region ($k_{si}=4$) for chezy=40/65/95 $m^{1/2}/s$



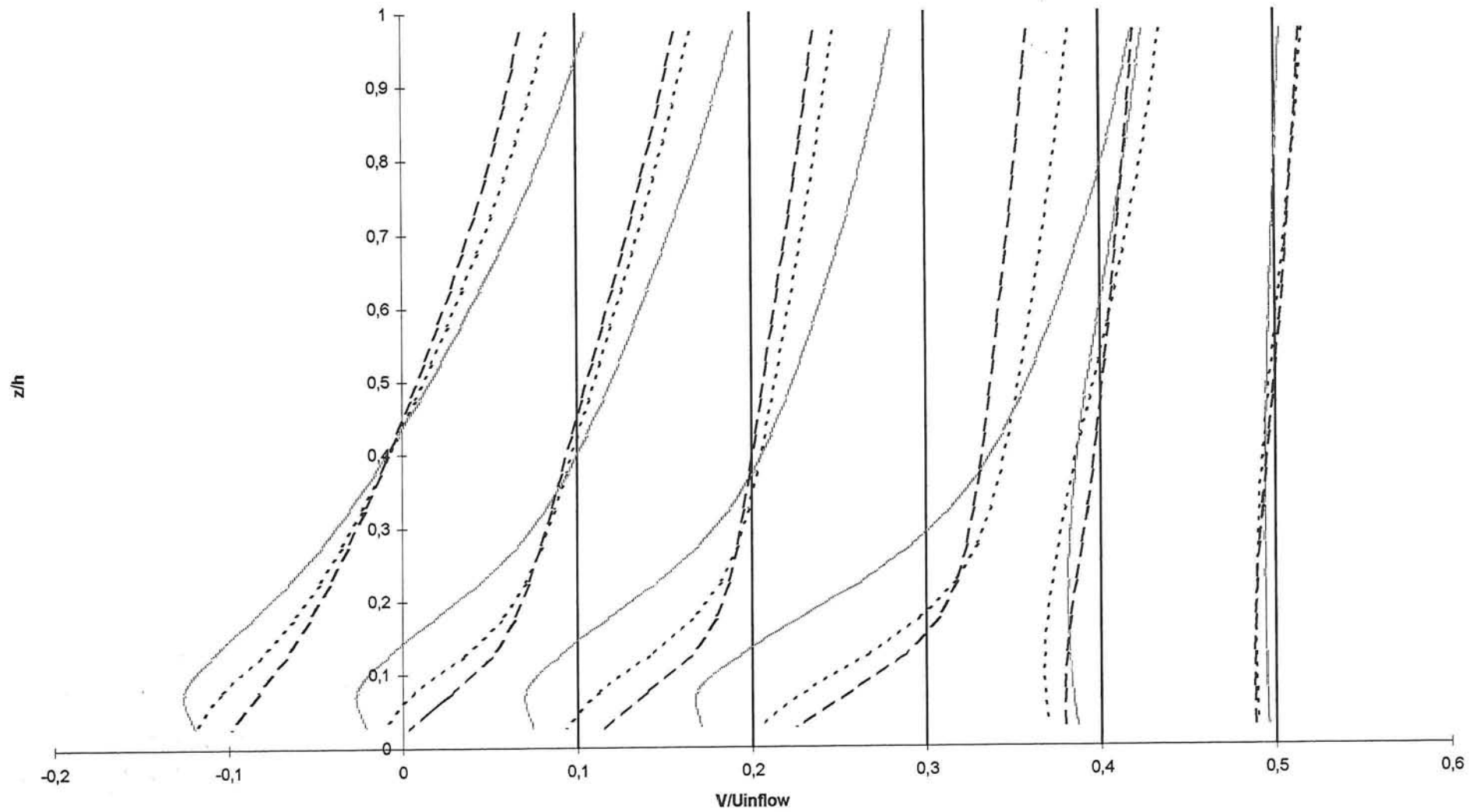
longitudinal velocity in the middle of the cross-section ($\kappa=0$) for chezy=40/65/95 $m^{1/2}/s$



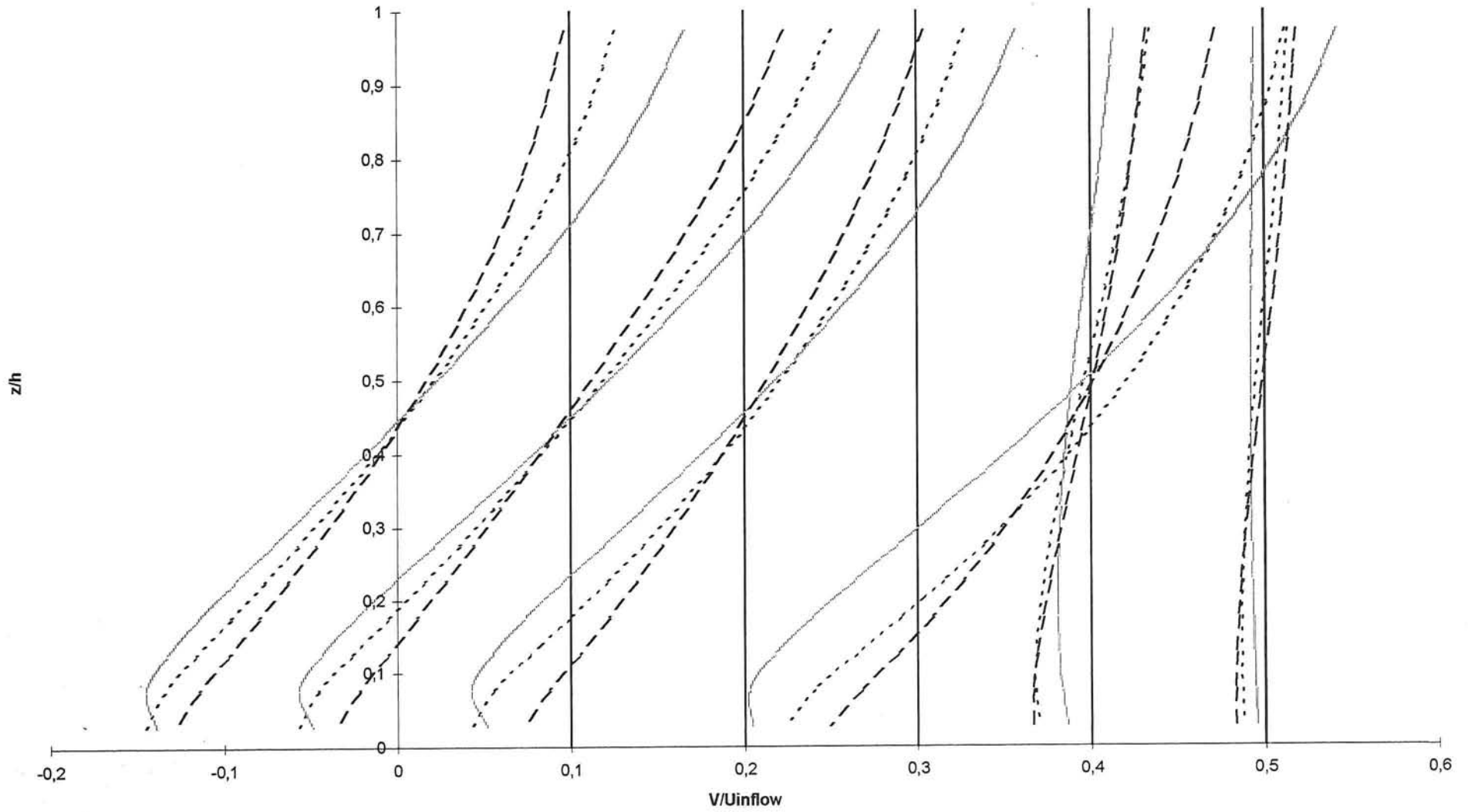
longitudinal velocity in the inner wall region ($\text{ksi}=-4$) for chezy=40/65/95 $\text{m}^{1/2}/\text{s}$



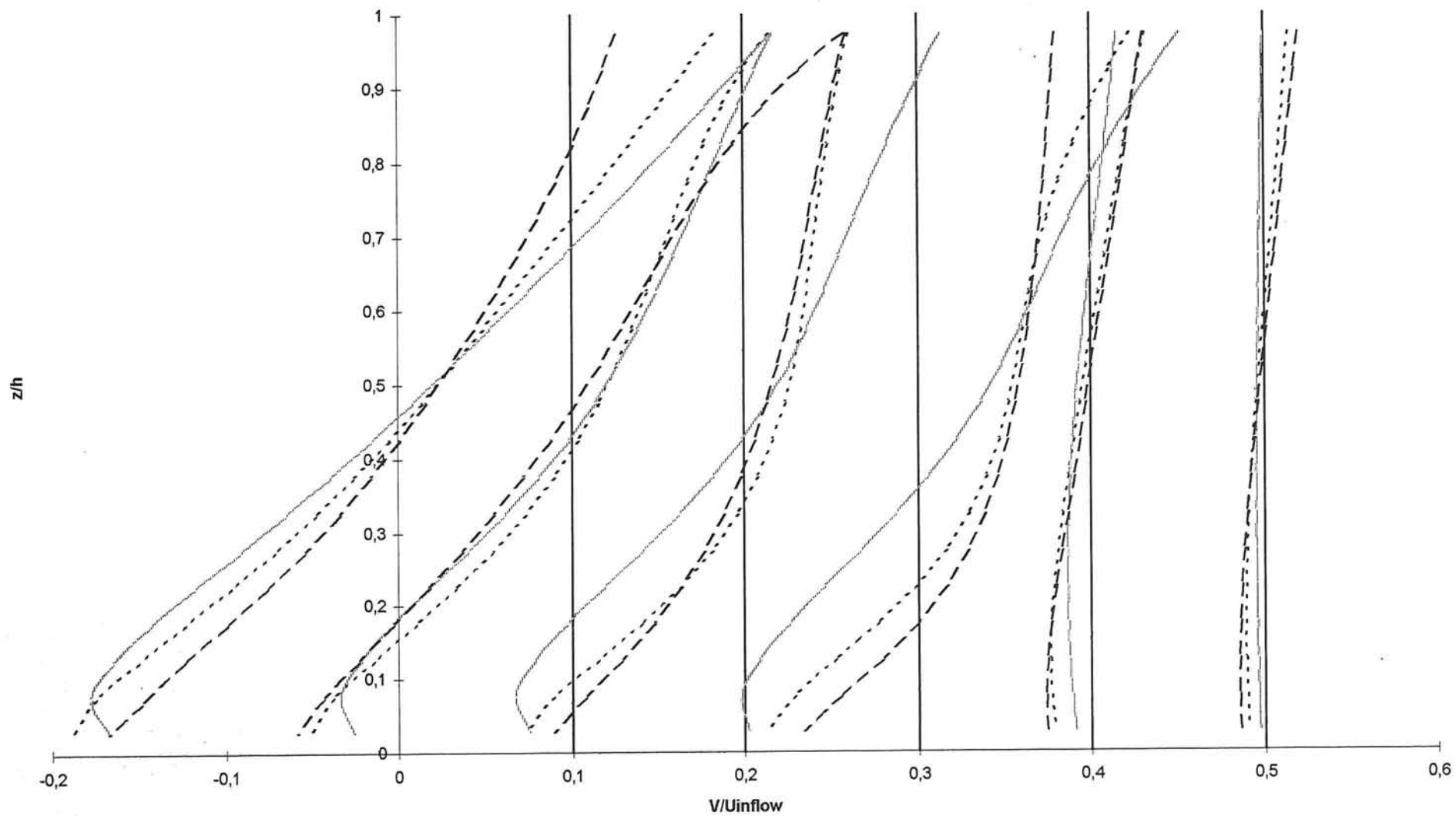
radial velocities near the outer wall (ksi=4) with chezy=40/65/95 m^{1/2} /s



radial velocities in the middle of the cross-section (ksi=0) with chezy=40/65/95 m^{1/2} /s



radial velocities near the inner wall ($\text{ksi}=-4$) with $\text{chezy}=40/65/96 \text{ m}^{1/2} / \text{s}$



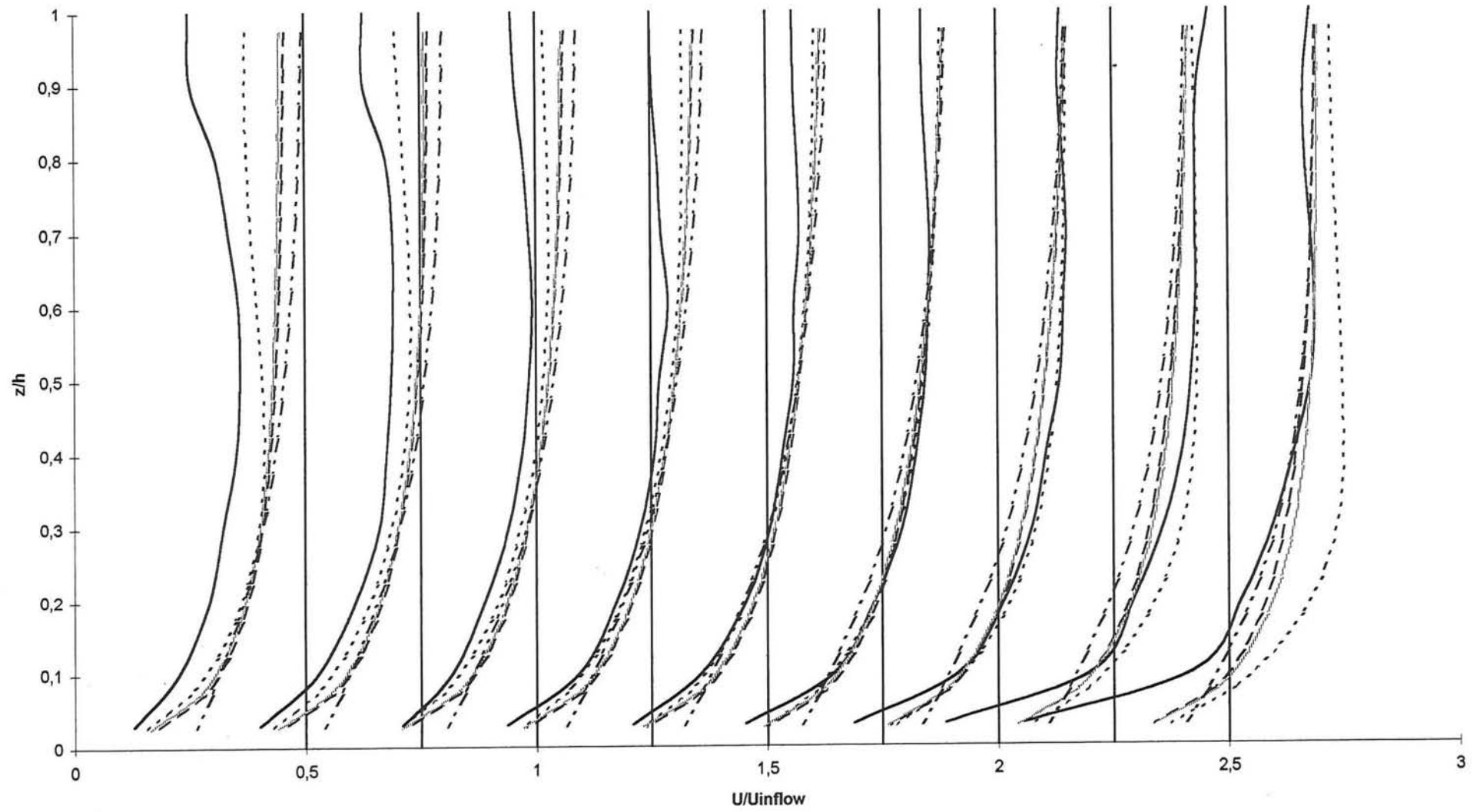
Appendix XVIII

These figures show the influence of the turbulence in the simulation of the smoothly curved bend.

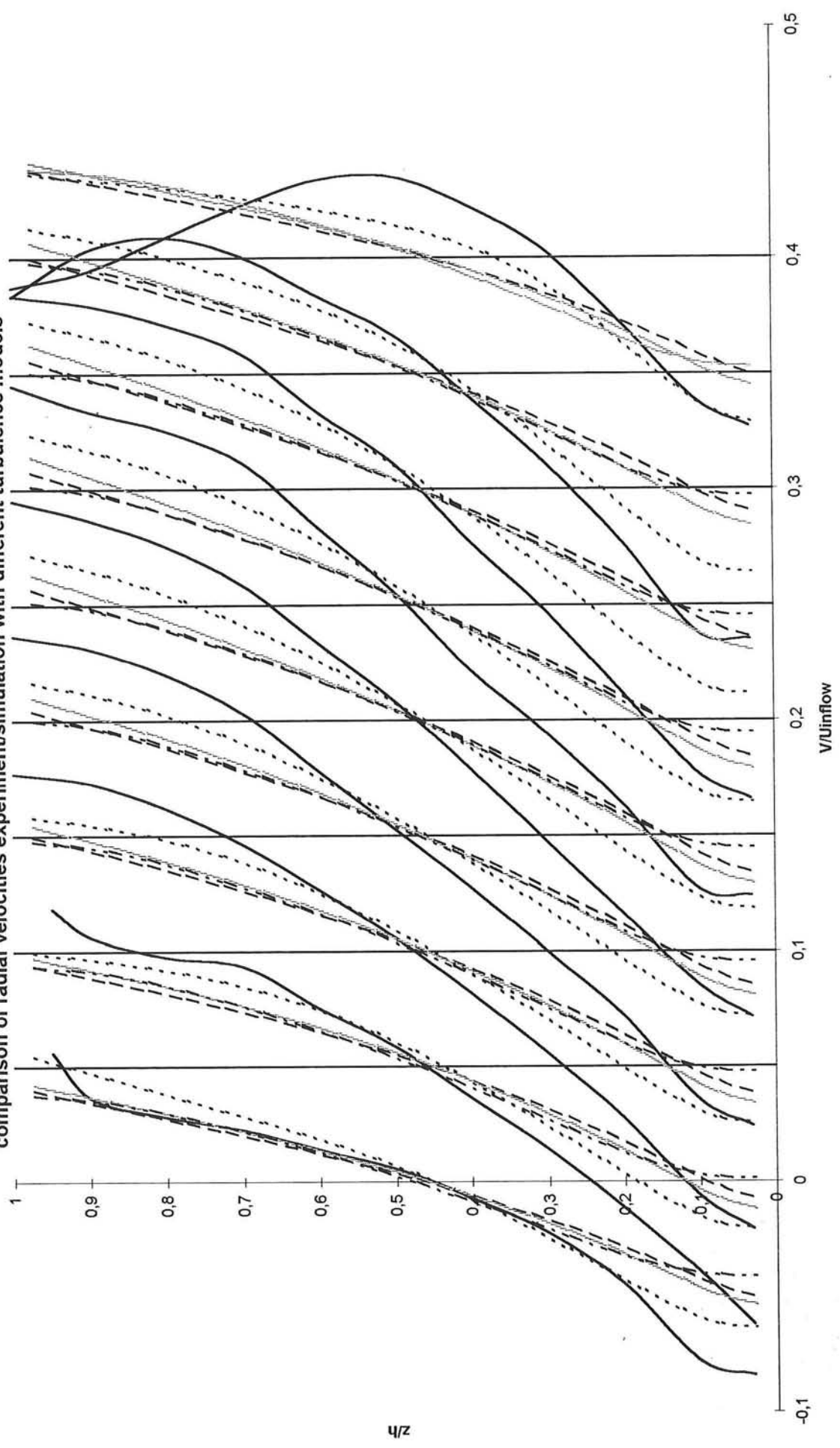
- k- ϵ model
- k-L model
- algebraic model
- constant vertical eddy viscosity coefficient (depth averaged= $0,02 \text{ m}^{1/2}/\text{s}$)
- experimental data

N.B. All the velocity distributions have their own vertical axis. This vertical axis represent the main velocity (in case of the radial velocity distributions this main velocity is zero). The scale of the velocity is only shown for the first velocity distribution.

comparison of longitudinal velocities experiment/simulation with different turbulence models



comparison of radial velocities experiment/simulation with different turbulence models



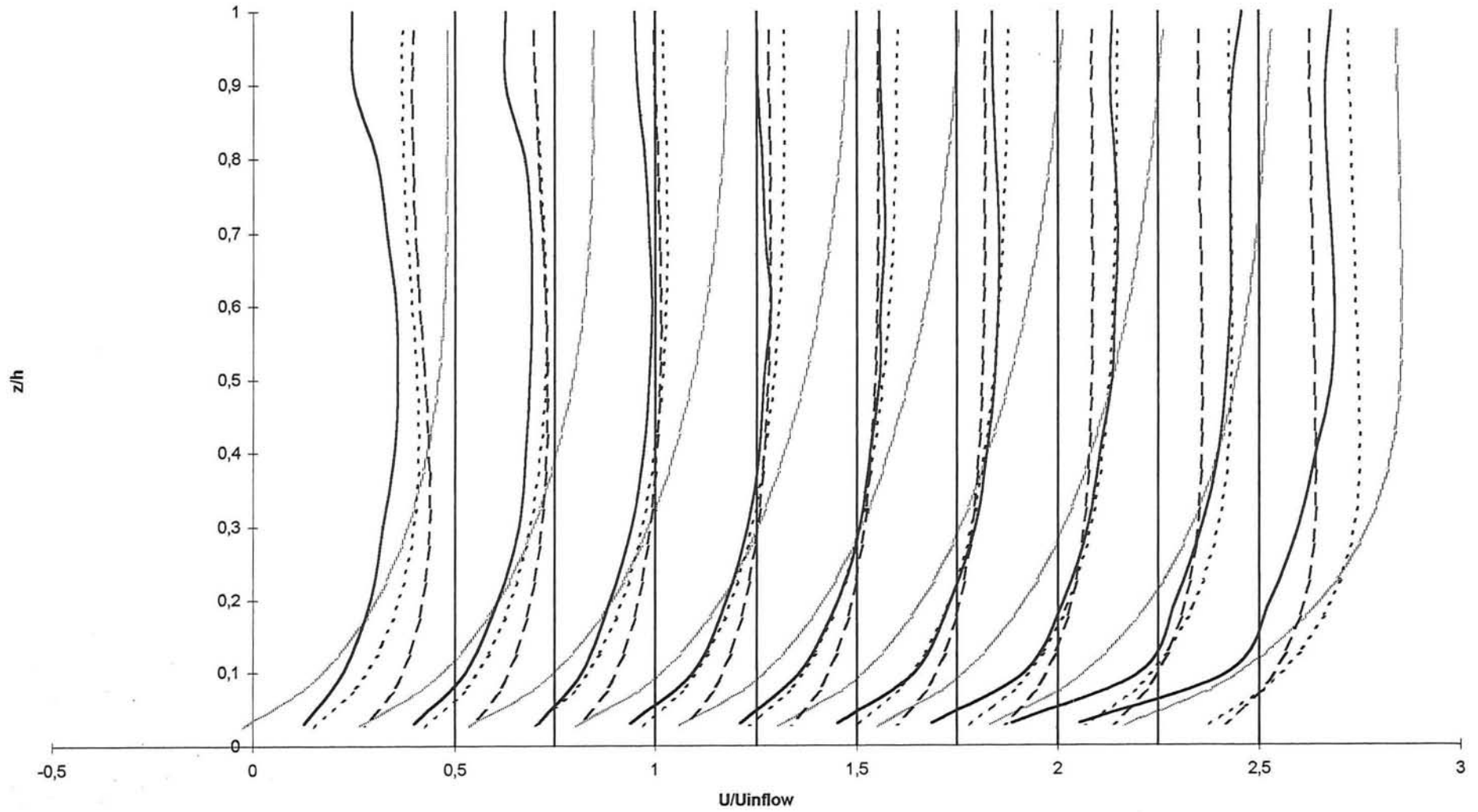
Appendix XIX

These figures show the influence of the Chézy coefficient in the simulation of a smoothly curved bend.

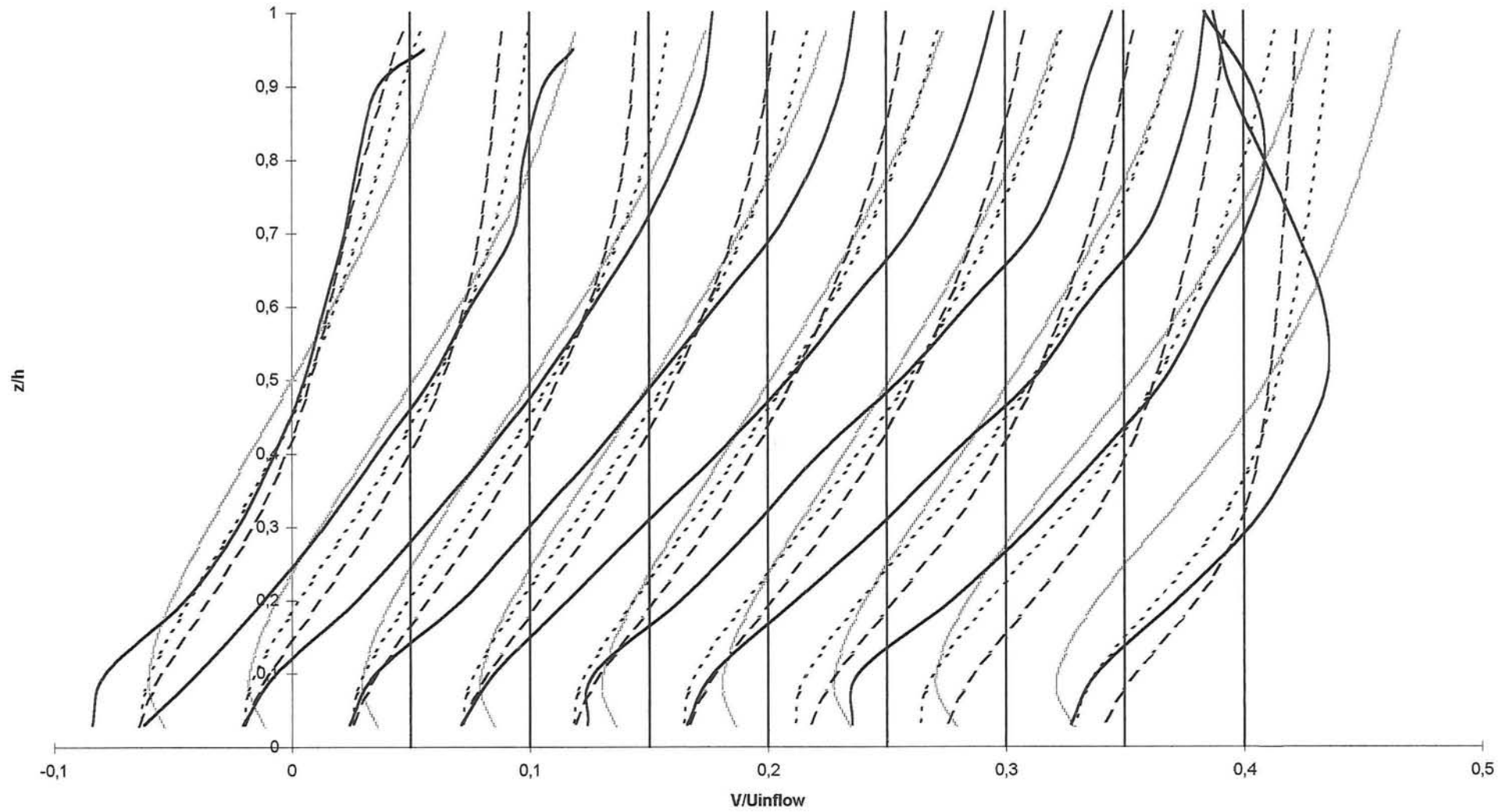
- Chézy coefficient equal $40 \text{ m}^{1/2}/\text{s}$
- Chézy coefficient equal $65 \text{ m}^{1/2}/\text{s}$
- Chézy coefficient equal $95 \text{ m}^{1/2}/\text{s}$

N.B. All the velocity distributions have their own vertical axis. This vertical axis represent the main velocity (in case of the radial velocity distributions this main velocity is zero). The scale of the velocity is only shown for the first velocity distribution.

comparison of longitudinal velocities experiment/simulation with chezy=40/65/95 m^{1/2} /s



comparison of radial velocities experiment/simulation with chezy=40/65/95 m^{1/2} /s



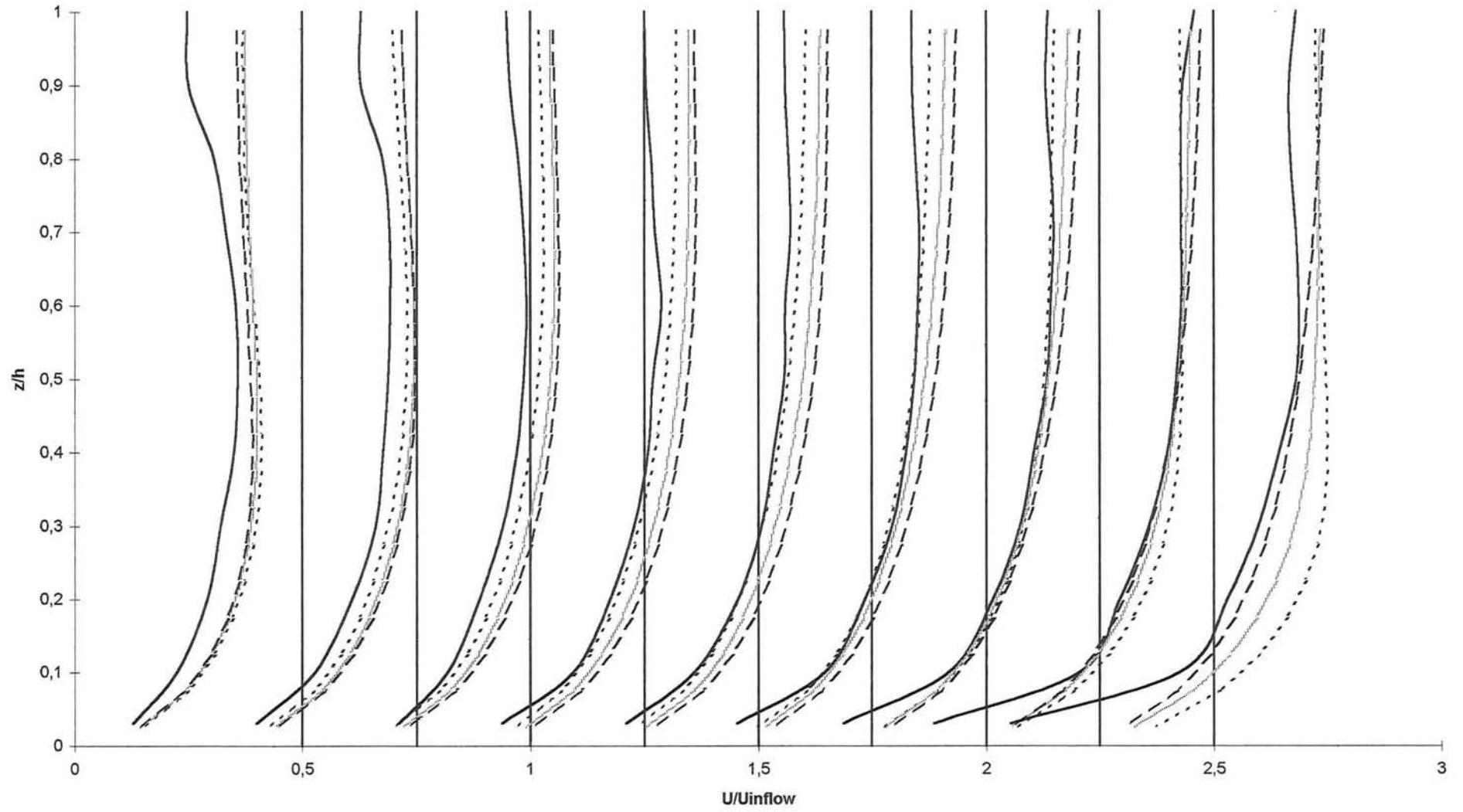
Appendix XX

These figures show the influence of the boundary condition at the side walls (no-slip/partly free-slip)

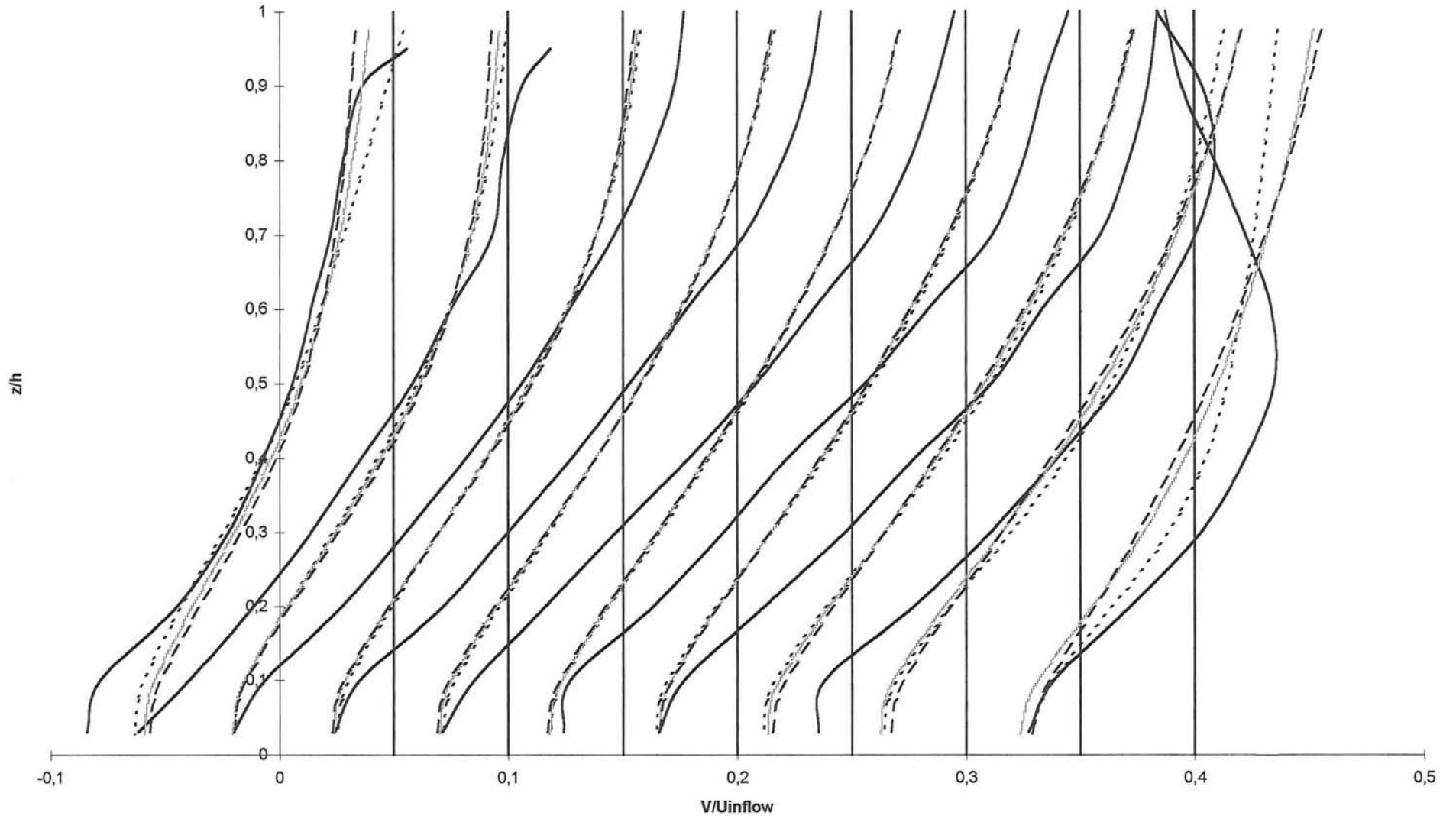
- no-slip
- free-slip; roughness length= 1.10^{-3} m
- free-slip; roughness length= 1.10^{-4} m
- experimental results.

N.B. All the velocity distributions have their own vertical axis. This vertical axis represent the main velocity (in case of the radial velocity distributions this main velocity is zero). The scale of the velocity is only shown for the first velocity distribution.

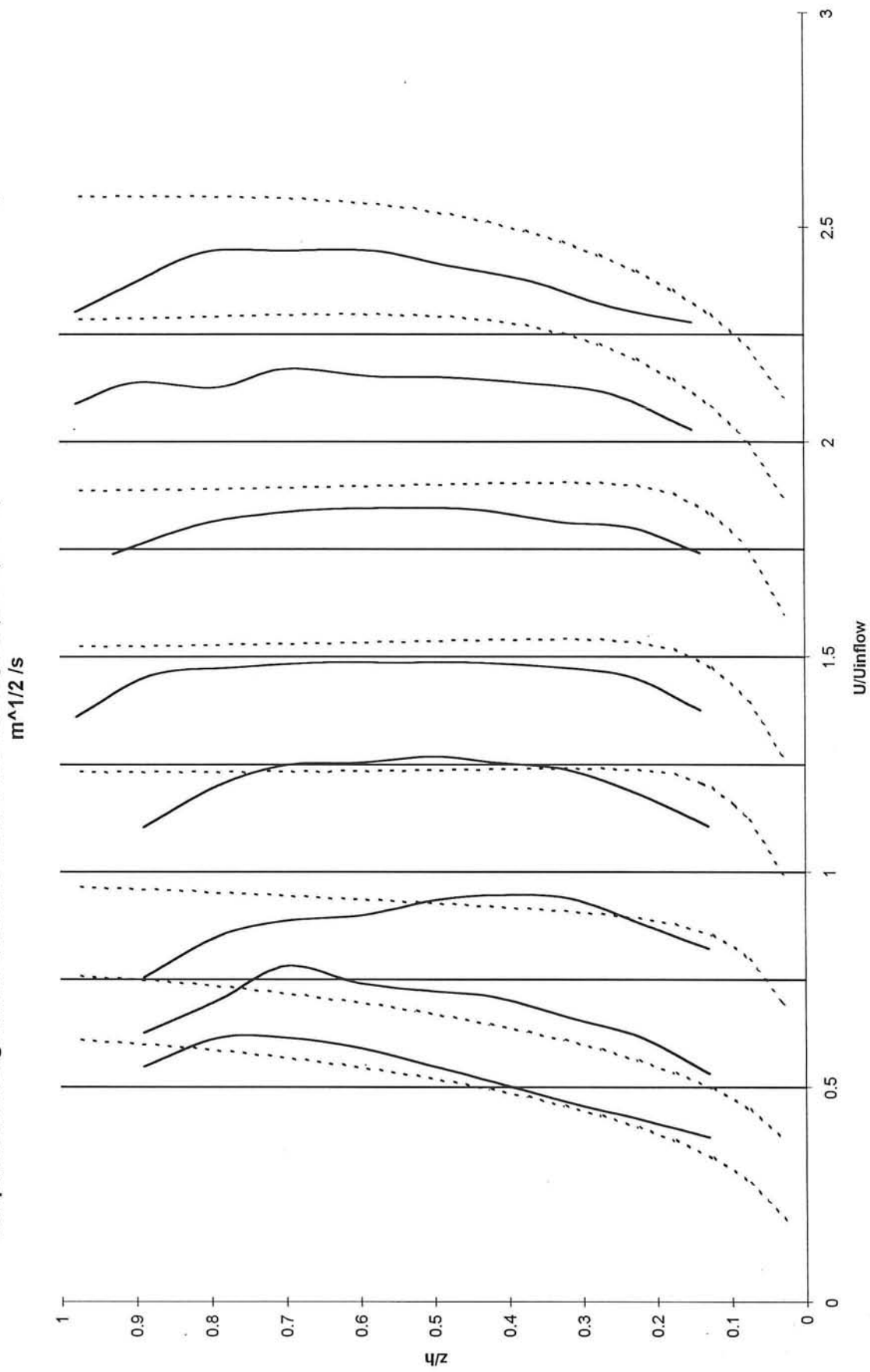
comparison of longitudinal velocities experiment/simulation with no-slip/partly-slip at the side walls



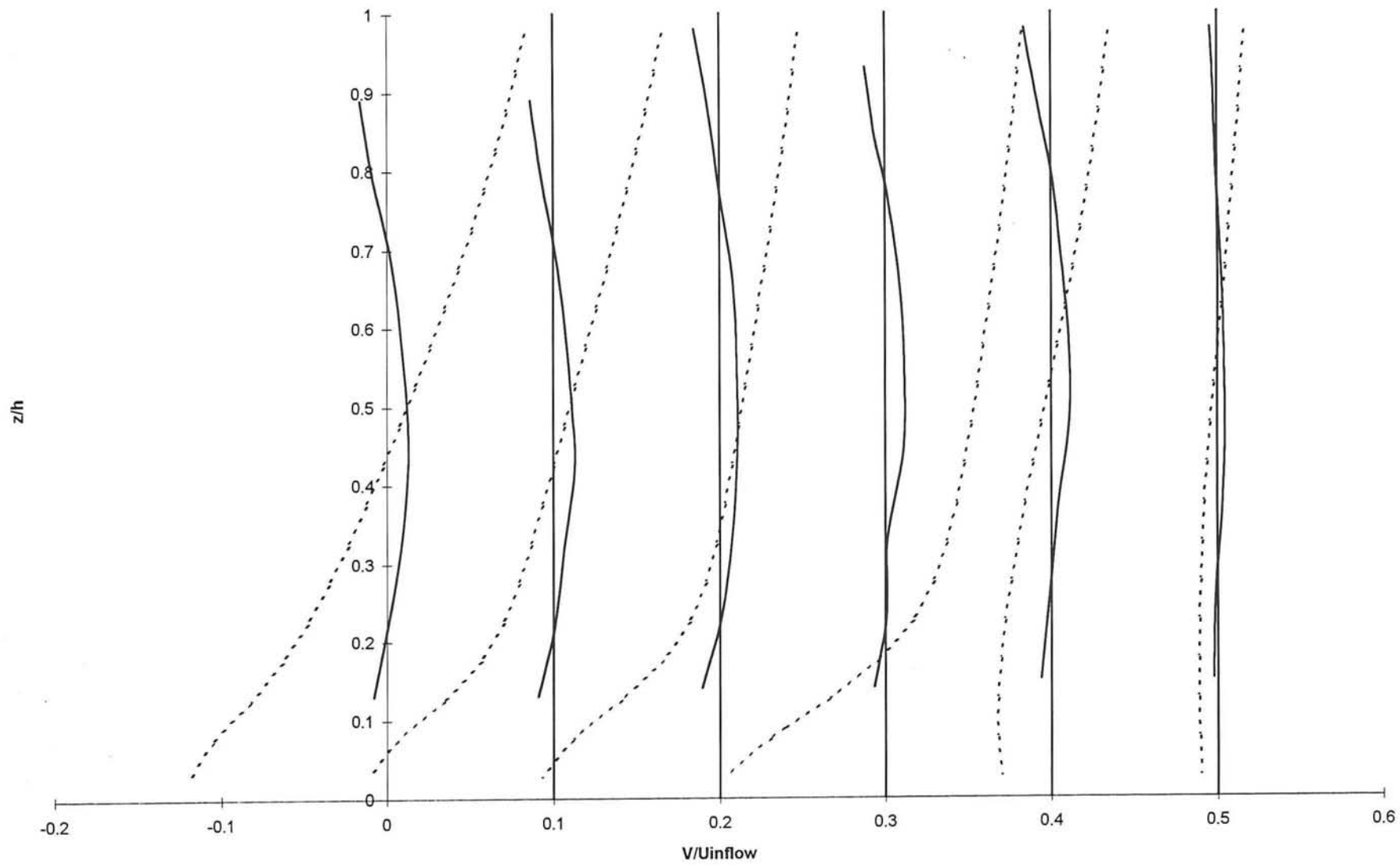
comparison of radial velocities experiment/simulation with no-slip/partly-slip at side walls



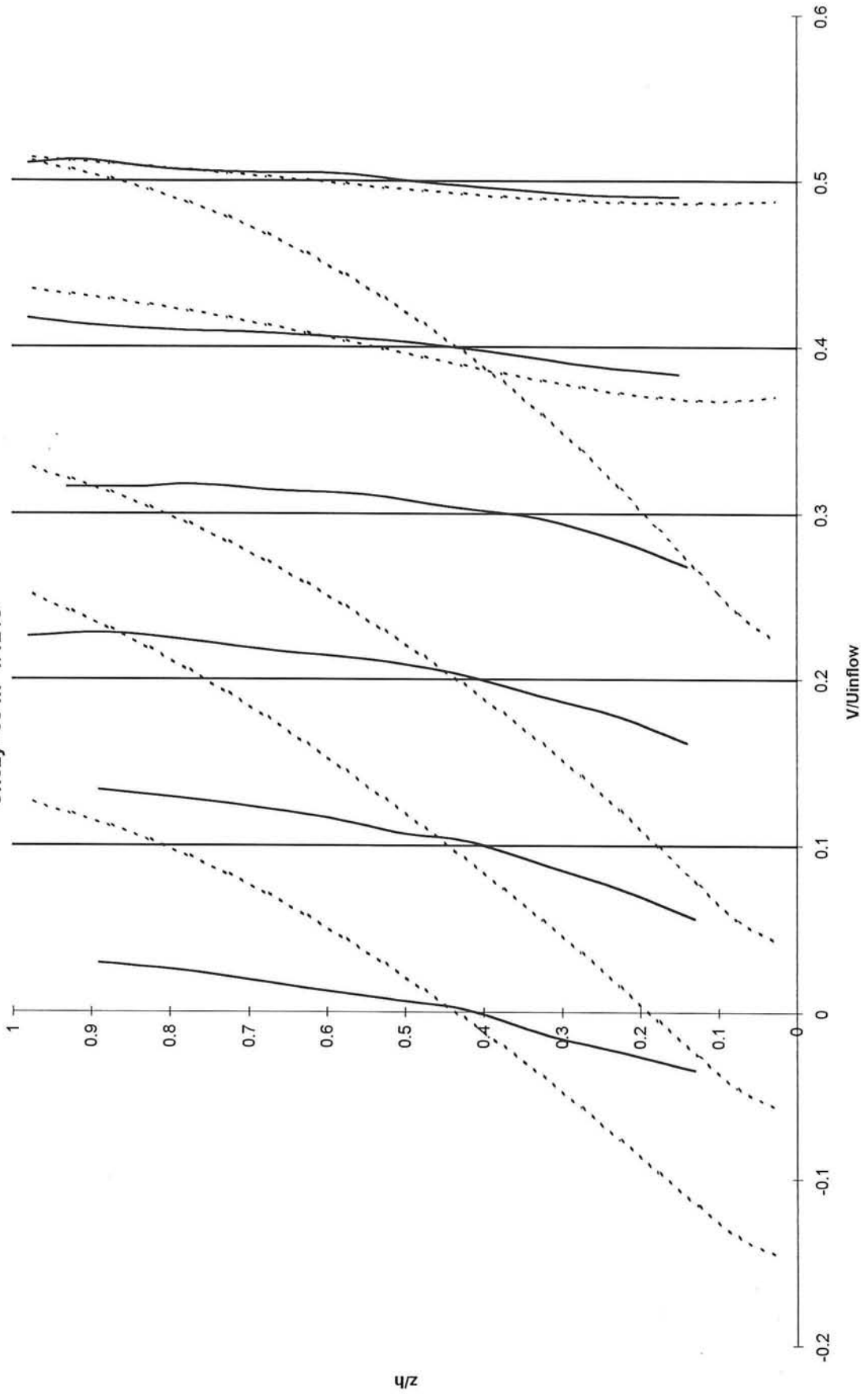
comparison of longitudinal velocities in the outer wall region (ksi=4) of experiment/simulation with Chezy=65



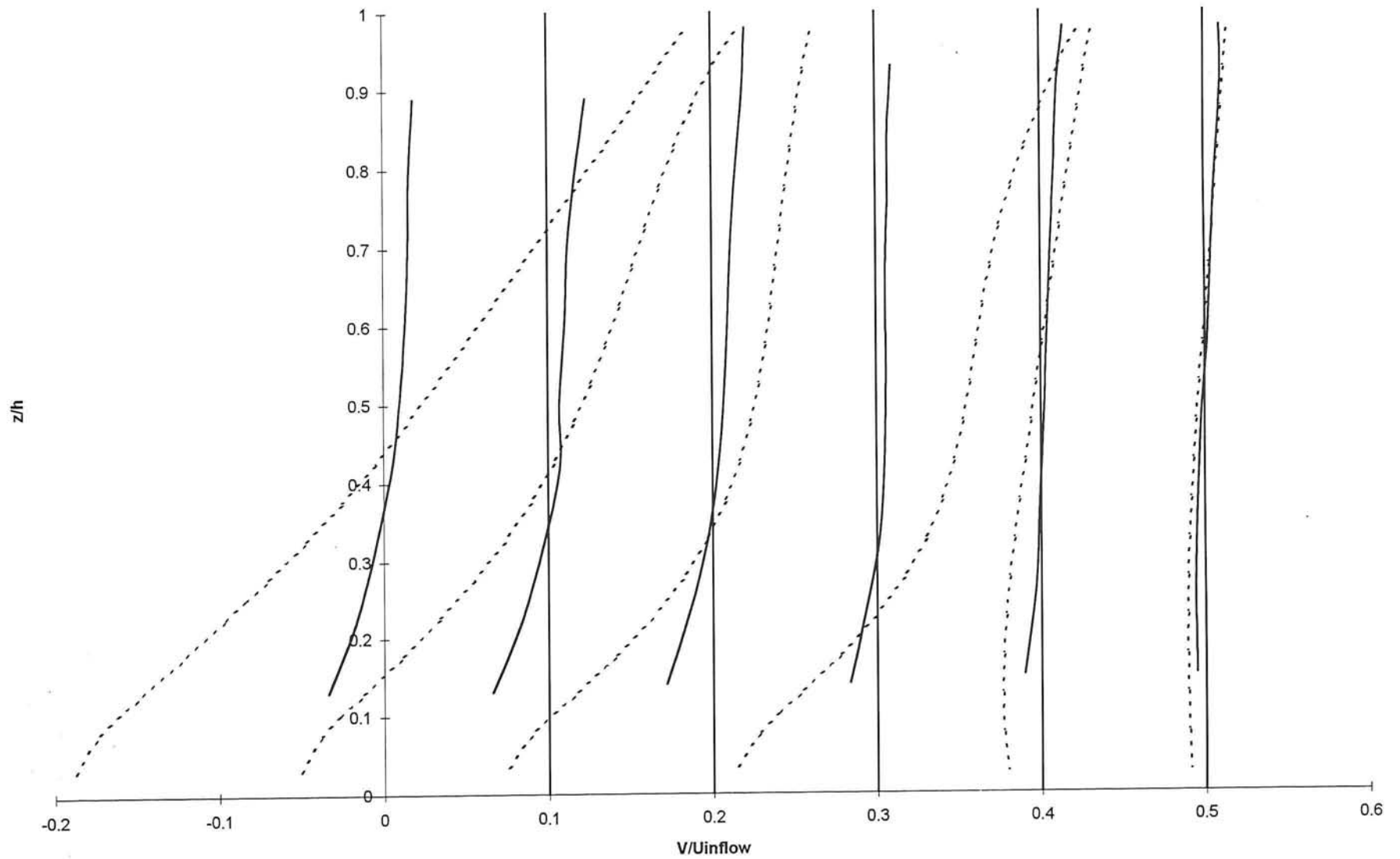
comparison of radial velocities near the outer wall ($k_{si}=4$) of experiment/simulation with $Chezy=65 \text{ m}^{1/2} / \text{s}$



comparison of radial velocities in the middle of the cross-section ($\text{ksi}=0$) of experiment/simulation with
Chezy=65 $\text{m}^{1/12} / \text{s}$



comparison of radial velocities near the inner wall ($k_{si}=4$) of experiment/simulation with Chezy=65 m^{1/2} /s



Appendix IX

In this appendix the figures of the comparison of the numerical simulation of the smoothly curved river bend and the measured data of Booij [ref 4] are shown.

In these figures are:

—————

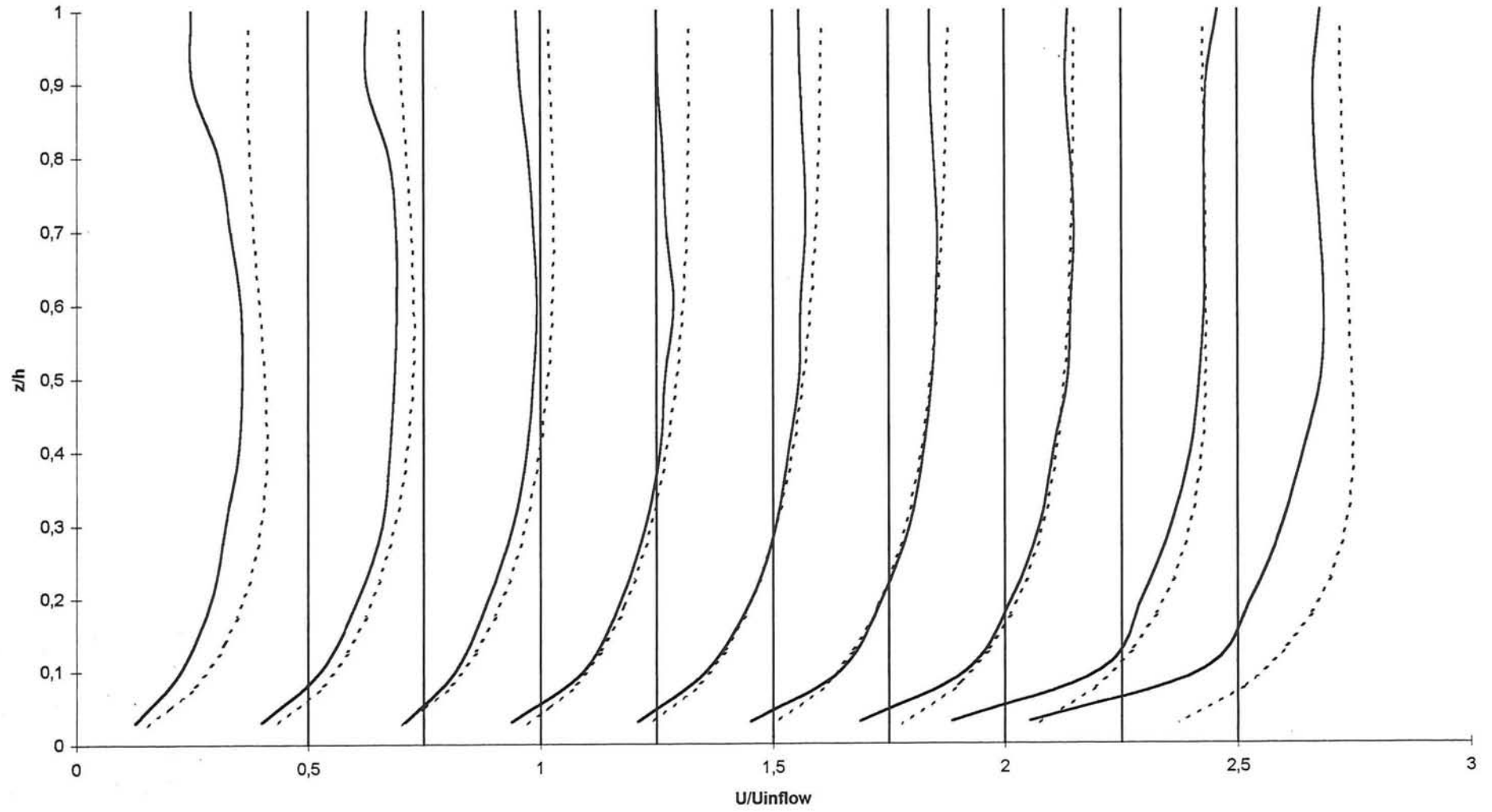
the experimental data

.....

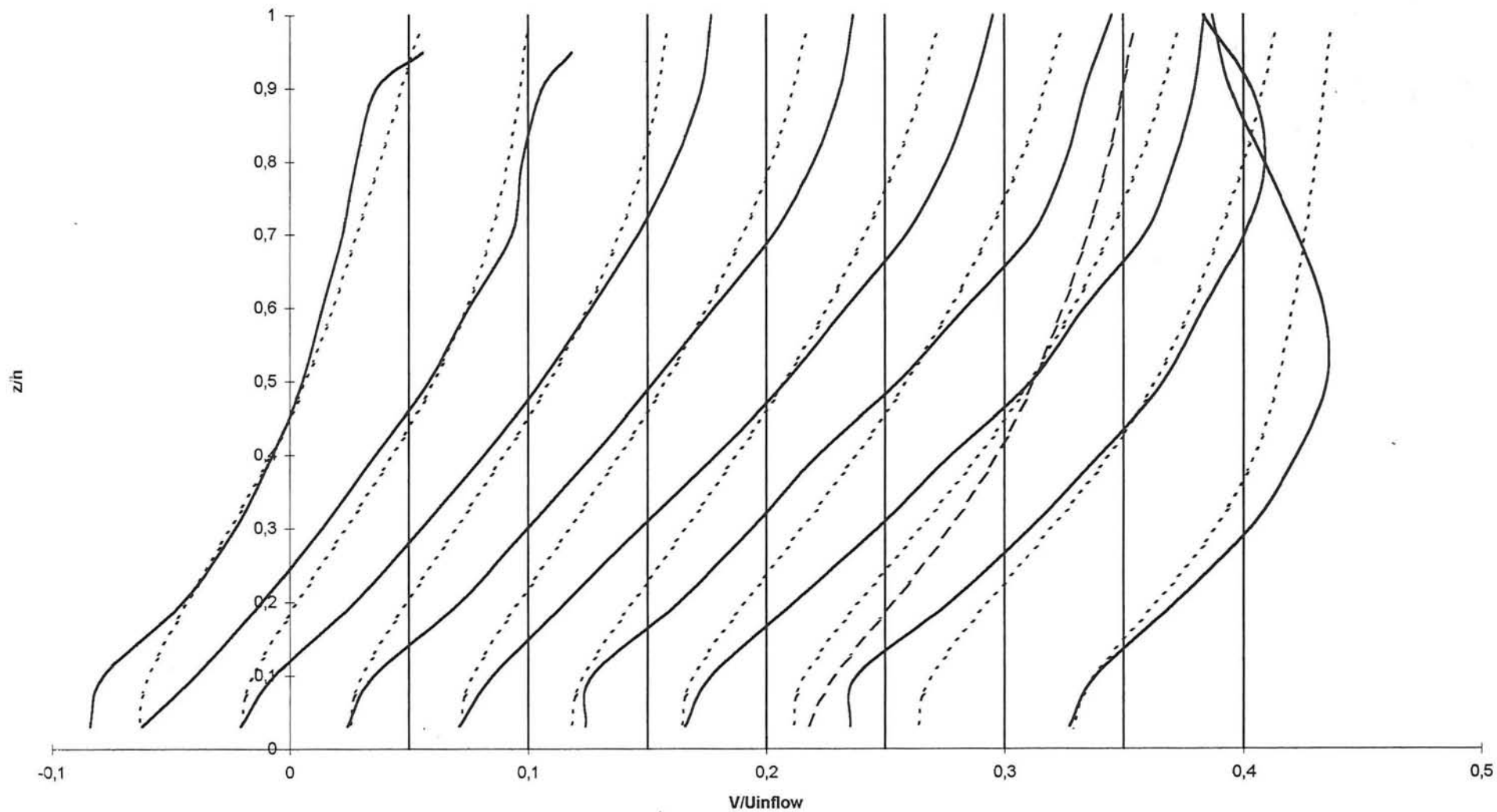
the prediction of the numerical simulation

N.B. All the velocity distributions have their own vertical axis. This vertical axis represent the main velocity (in case of the radial velocity distributions this main velocity is zero). The scale of the velocity is only shown for the first velocity distribution.

comparison of longitudinal velocities experiment/simulation with chezy=65 m^{1/2} /s



comparison of radial velocities experiment/simulation with chezy=65 m^{1/2} /s



Appendix X

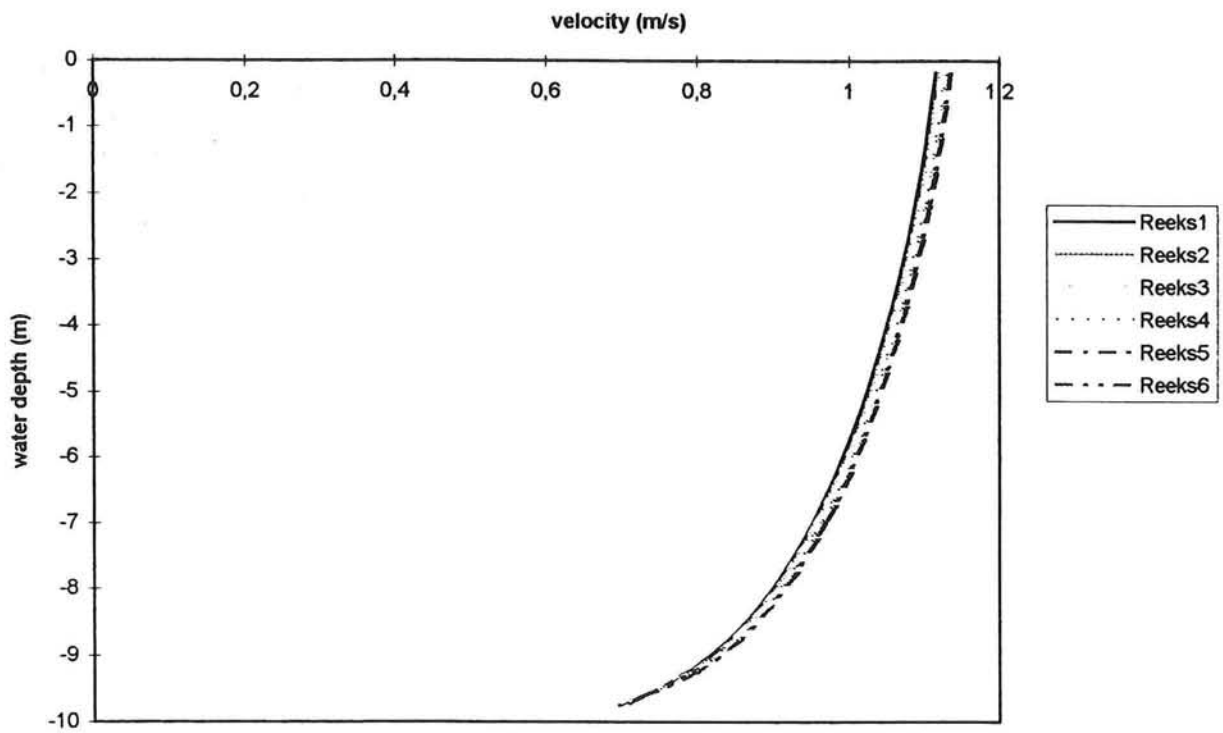
In these figures the results of the velocity distribution over the vertical of the numerical simulation of the strongly curved bend are shown at several positions upstream of the bend, in the bend and downstream of the bend. They are taken at 375m and 125m upstream and downstream of the bend. Inside the bend the velocity distributions are given at $\phi = 3,75^\circ, 45^\circ, 90^\circ, 135^\circ, 177,25^\circ$

The velocity distributions are given at 6 positions;

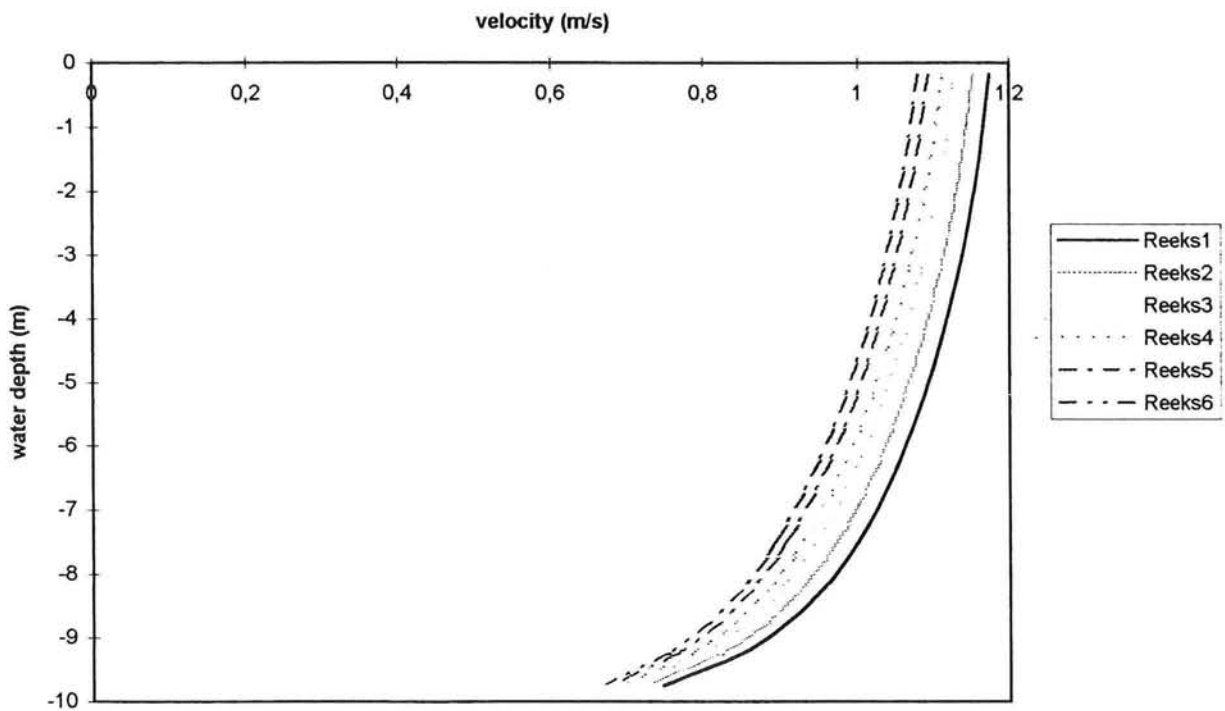
reeks 1	grid point 3 (7,5 m from the inner wall)
reeks 2	grid point 6 (22,5 m from the inner wall)
reeks 3	grid point 10 (42,5 m from the inner wall)
reeks 4	grid point 13 (57,5 m from the inner wall)
reeks 5	grid point 17 (77,5 m from the inner wall)
reeks 6	grid point 20 (92,5 m from the inner wall)

The last four figures are figures with six velocity distributions along a longitudinal line.

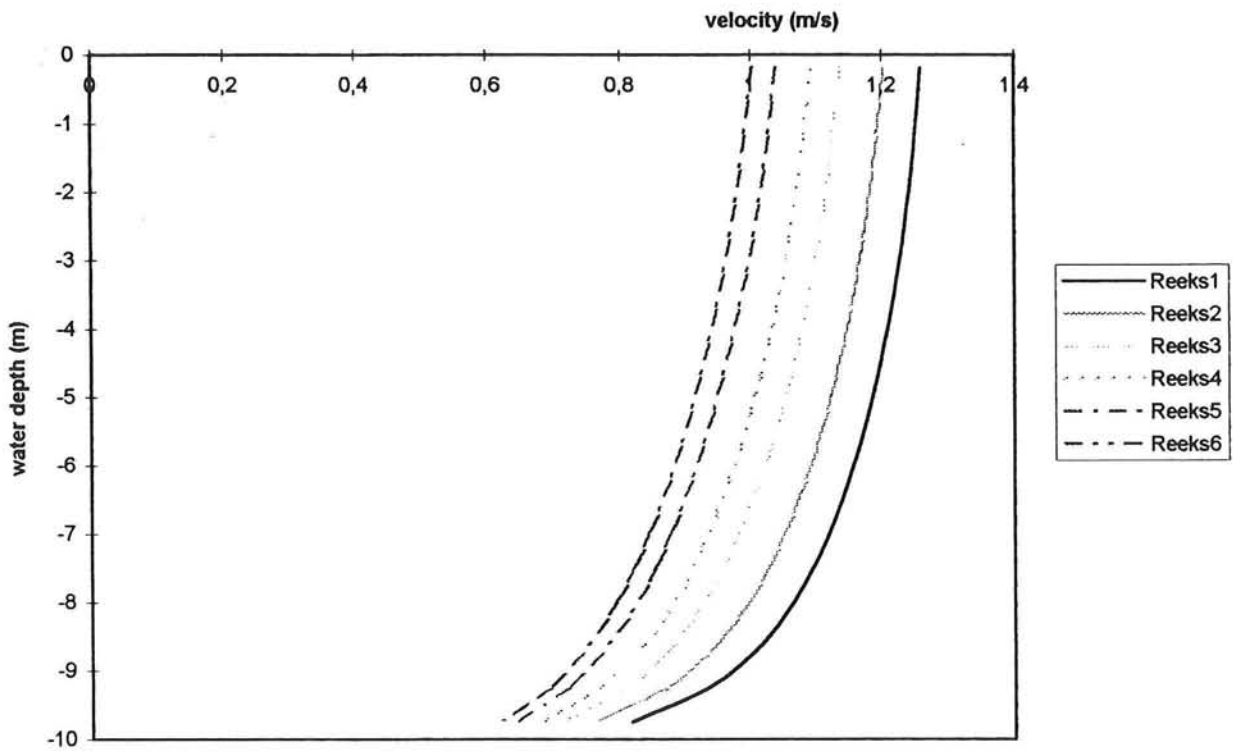
longitudinal velocities at 375 m upstream of the bend



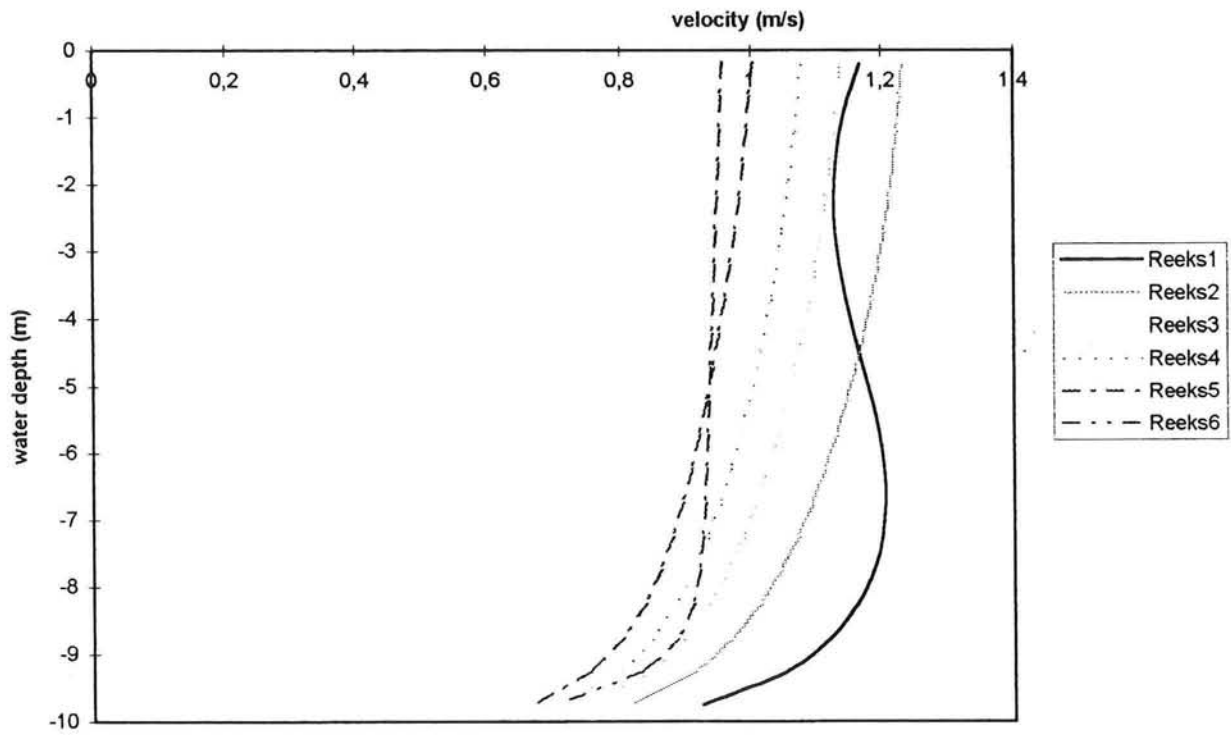
longitudinal velocities 125 m upstream of the bend



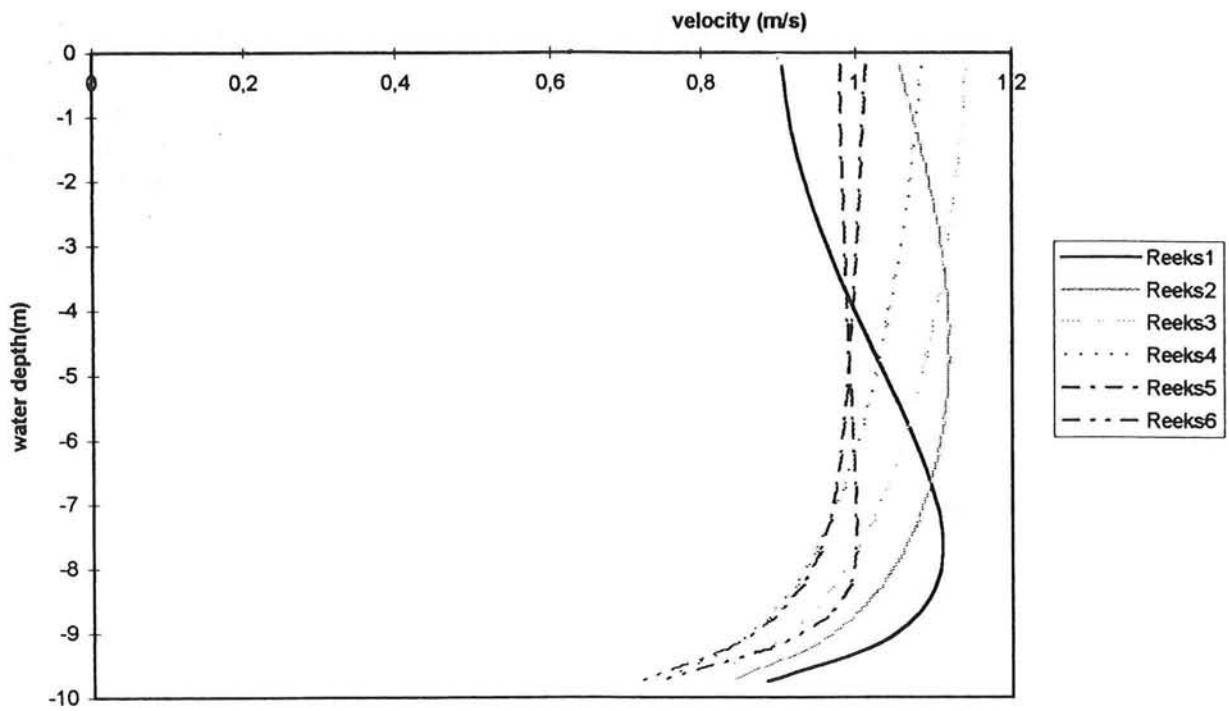
longitudinal velocities at $\phi=3,75$



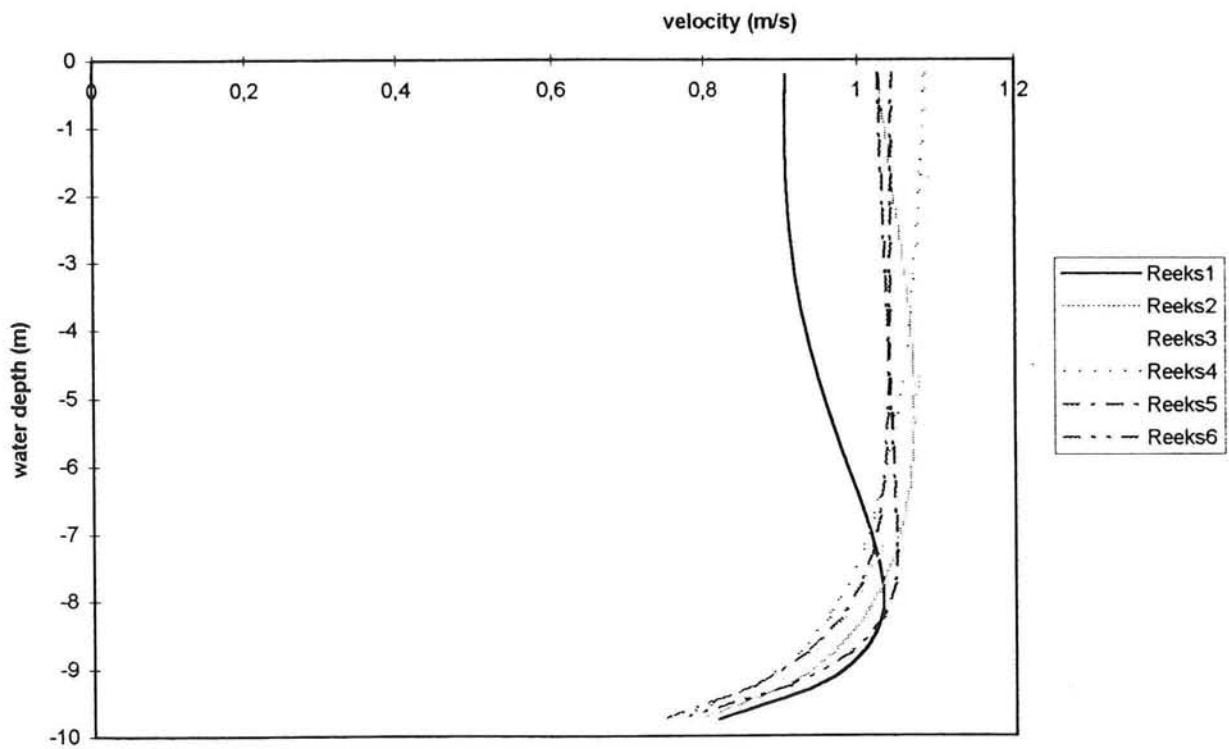
longitudinal velocities at $\phi=45$



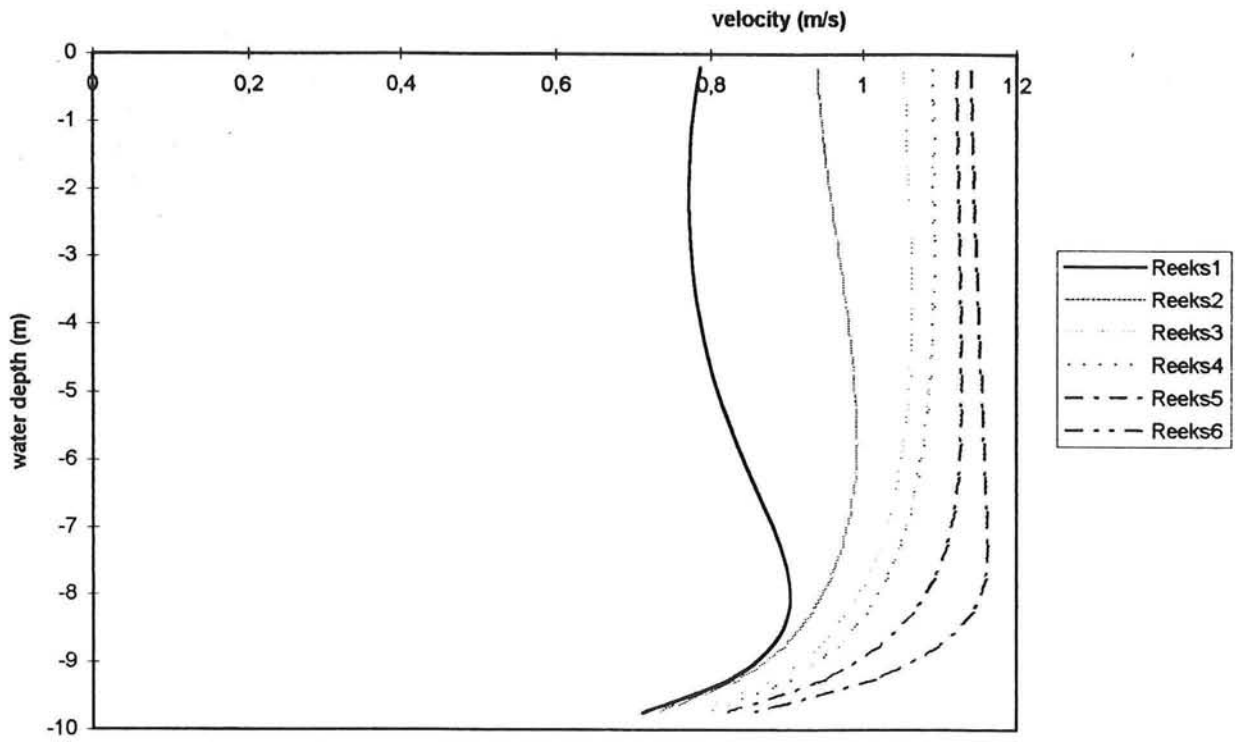
longitudinal velocities at phi=90



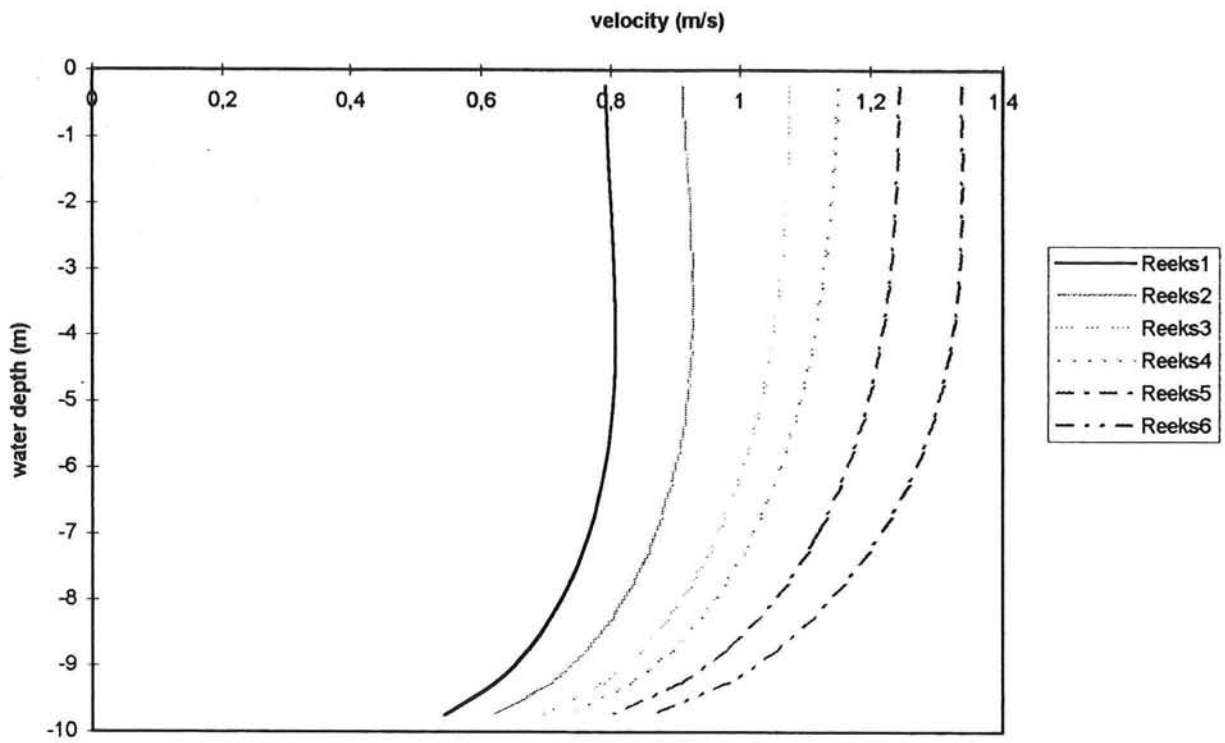
longitudinal velocities at phi=135



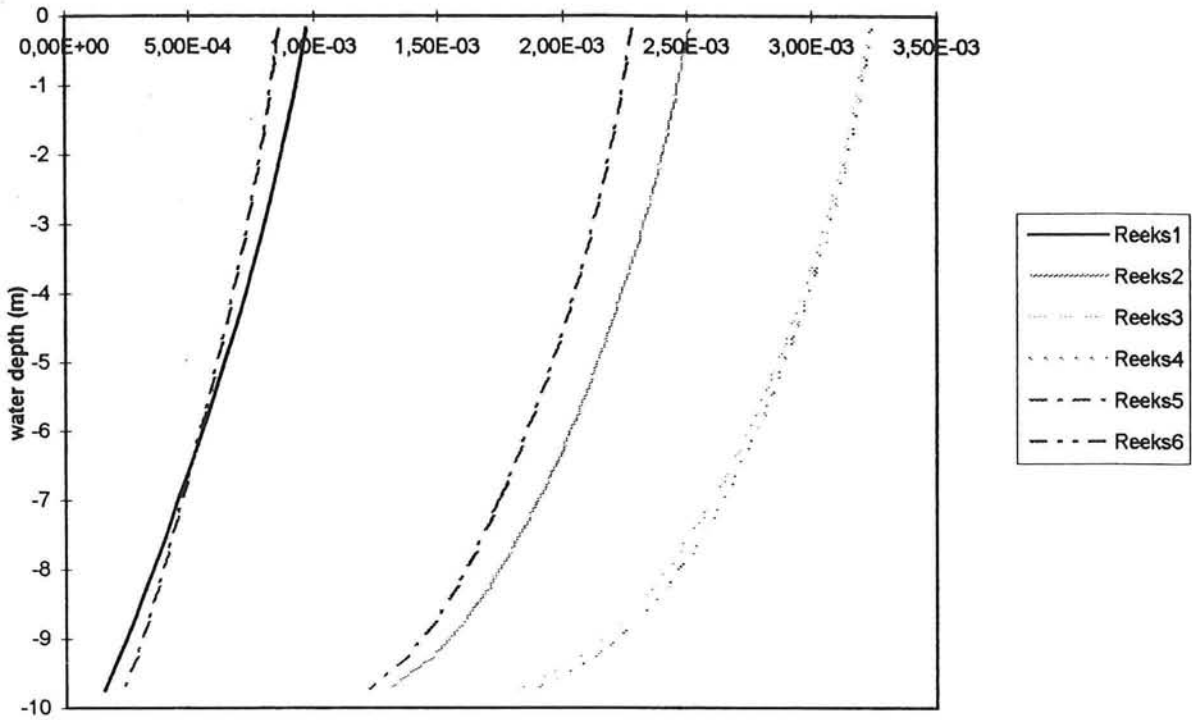
longitudinal velocities at $\phi=177,25$



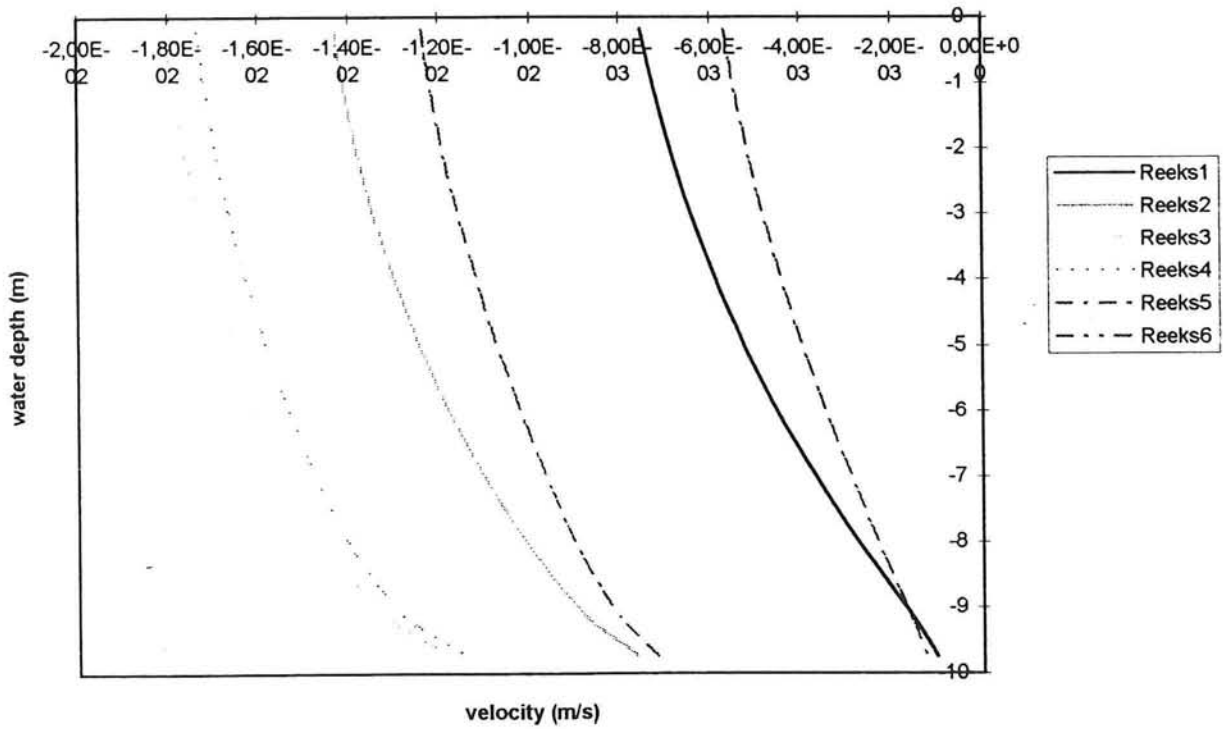
longitudinal velocities 375 m downstream of the bend



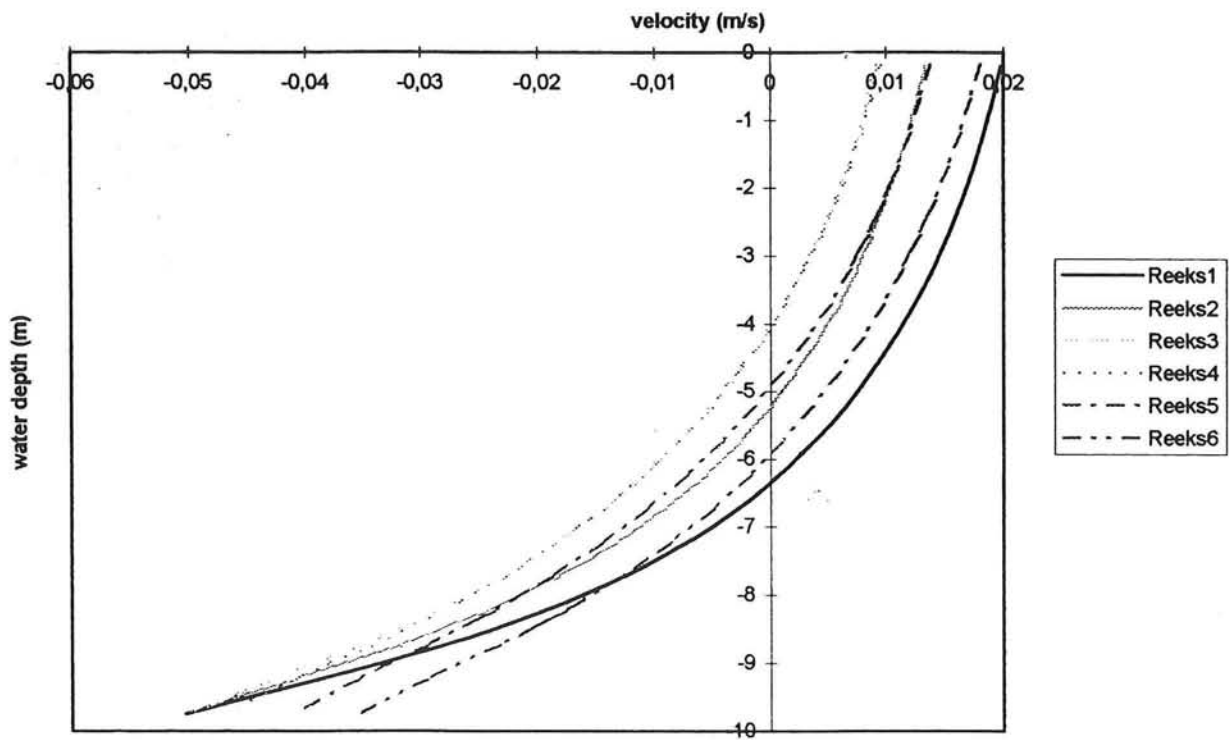
radial velocities 375 m upstream of the bend
velocity (m/s)



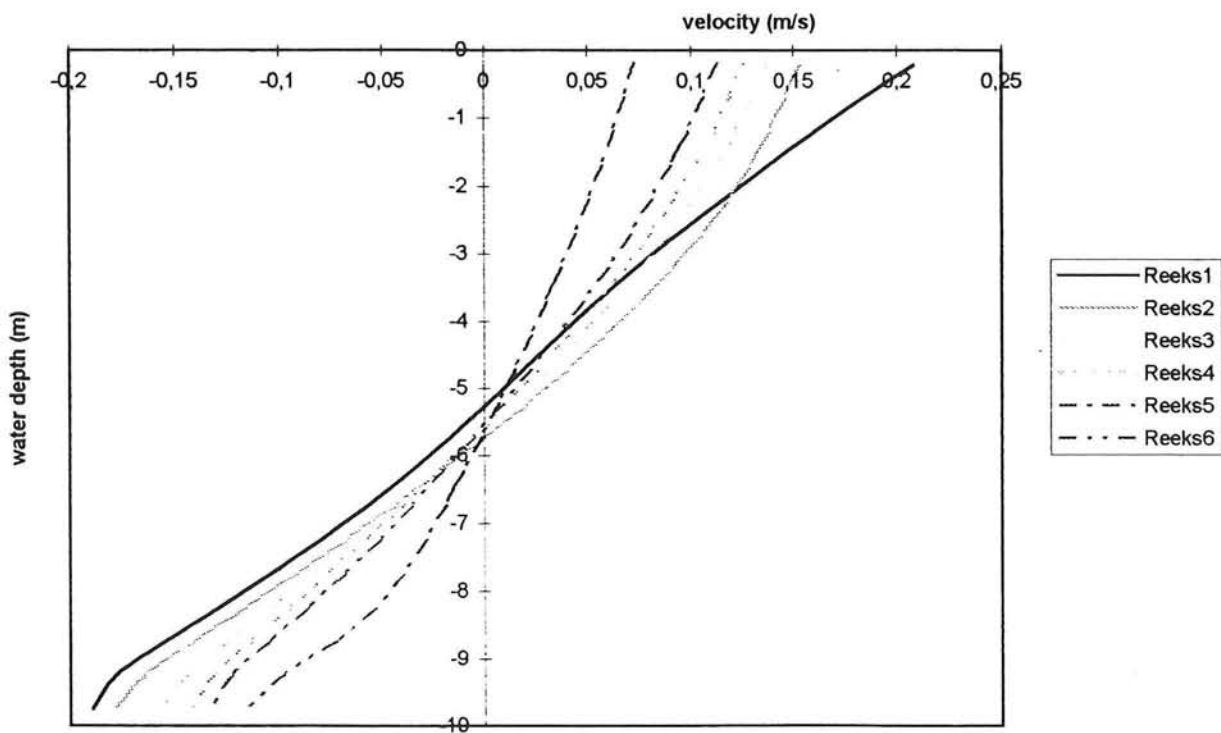
radial velocities at 125 upstream of the bend



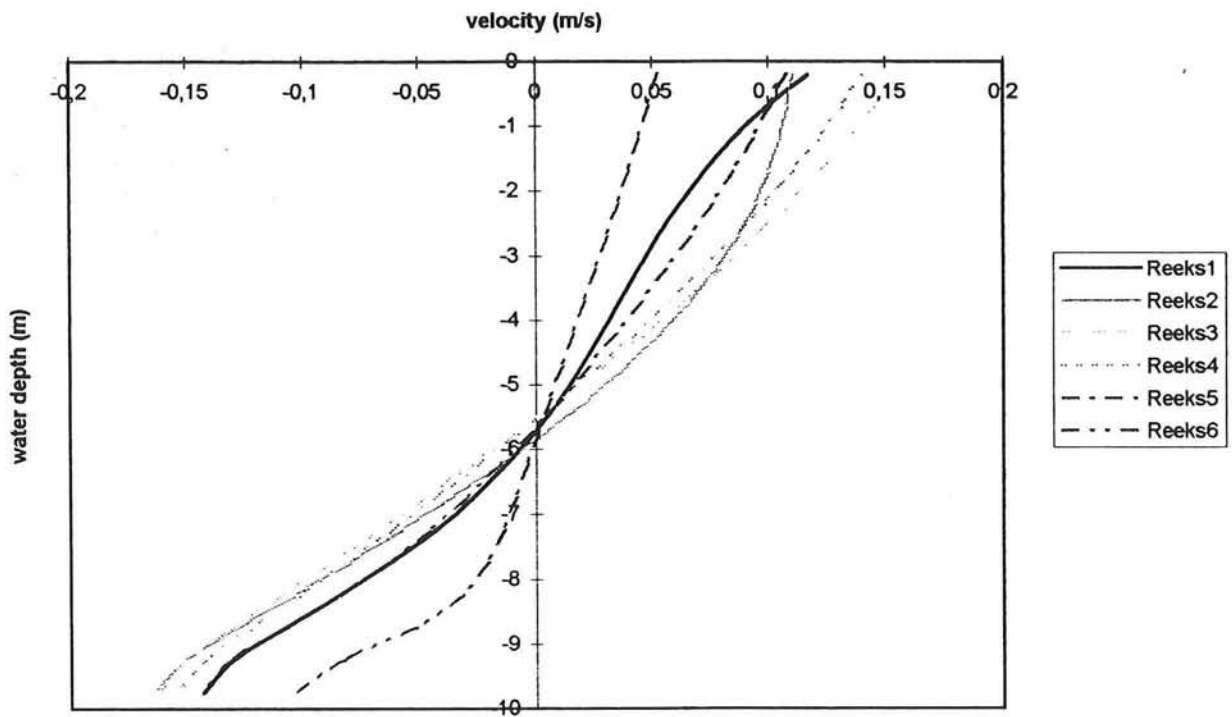
radial velocities at $\phi=3,75$



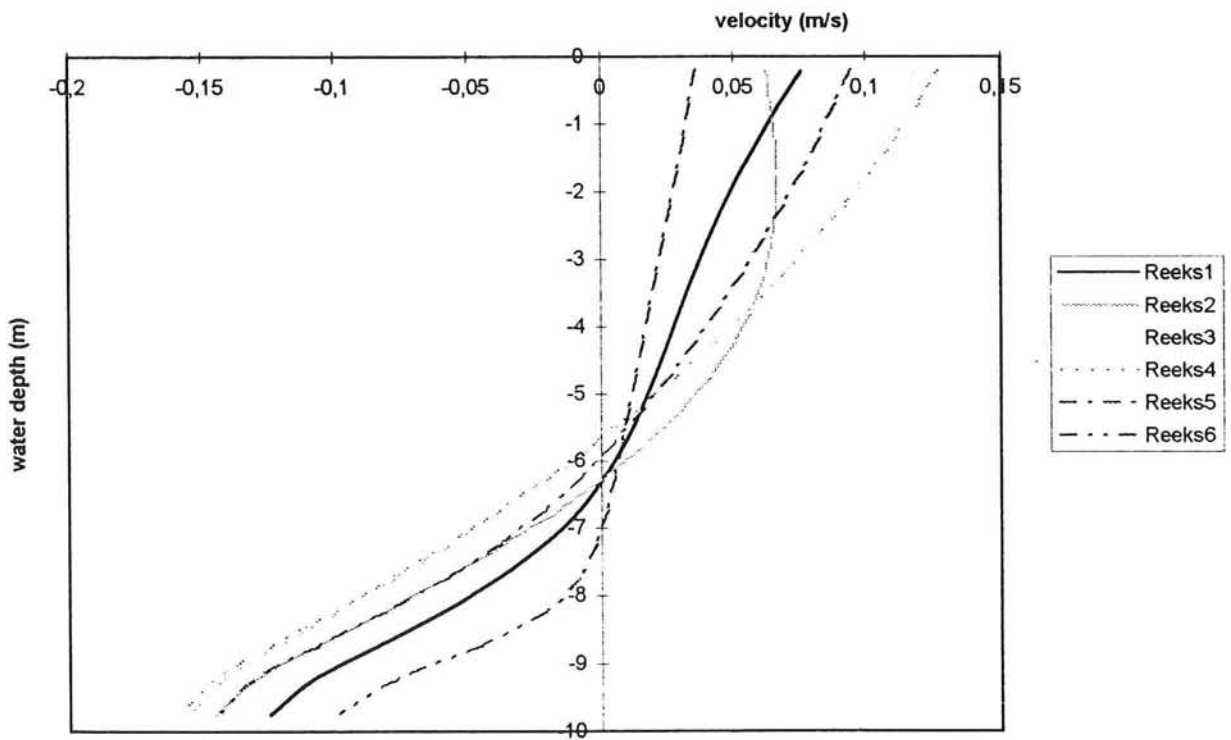
radial velocities at $\phi=45$



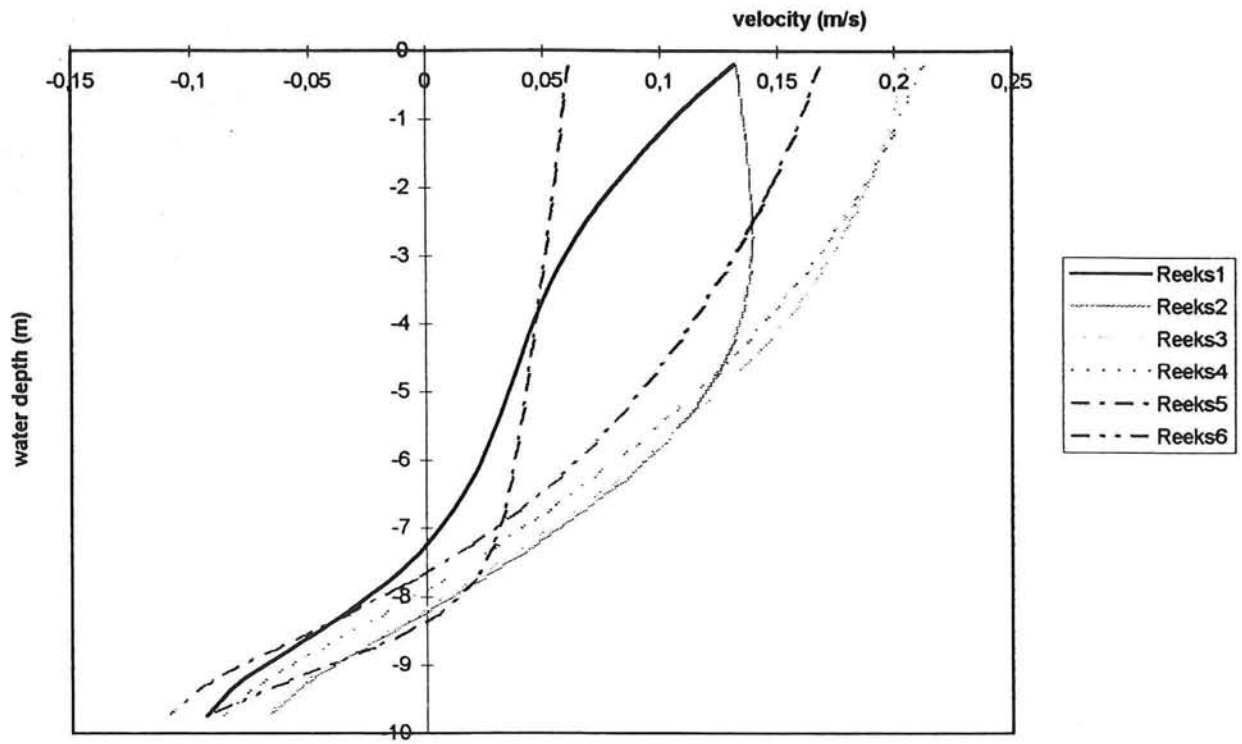
radial velocities at phi=90



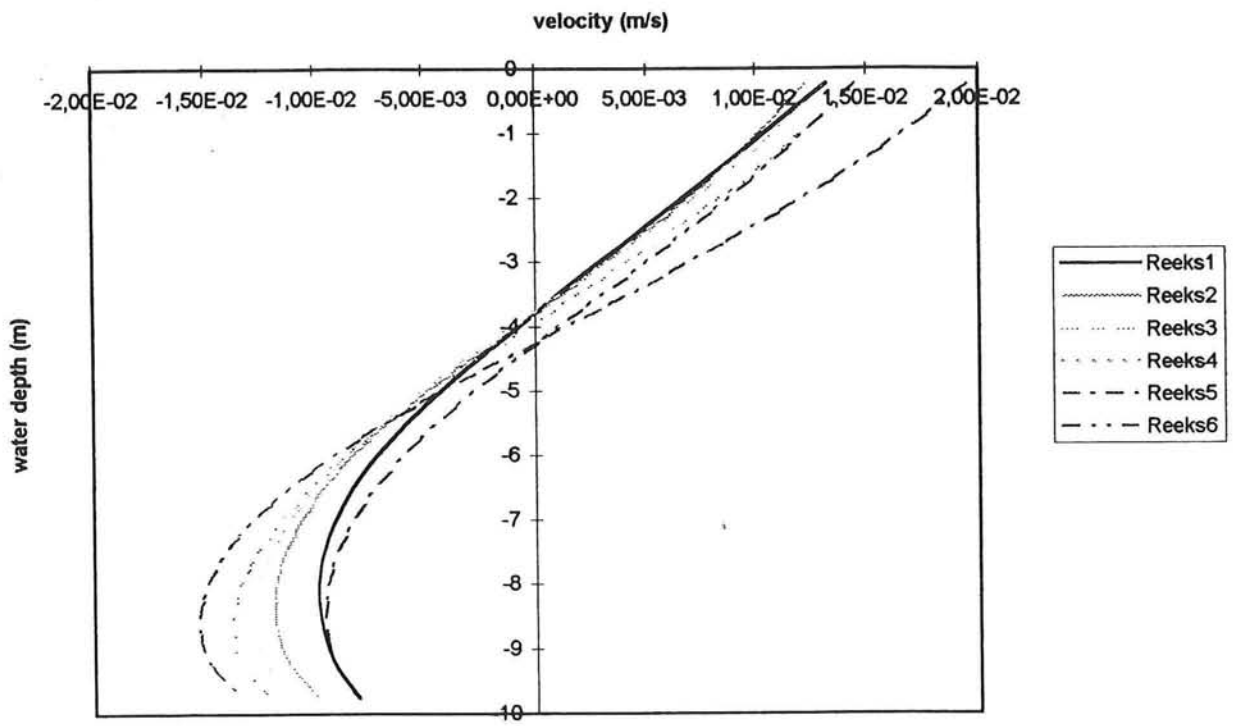
radial velocities at phi=135



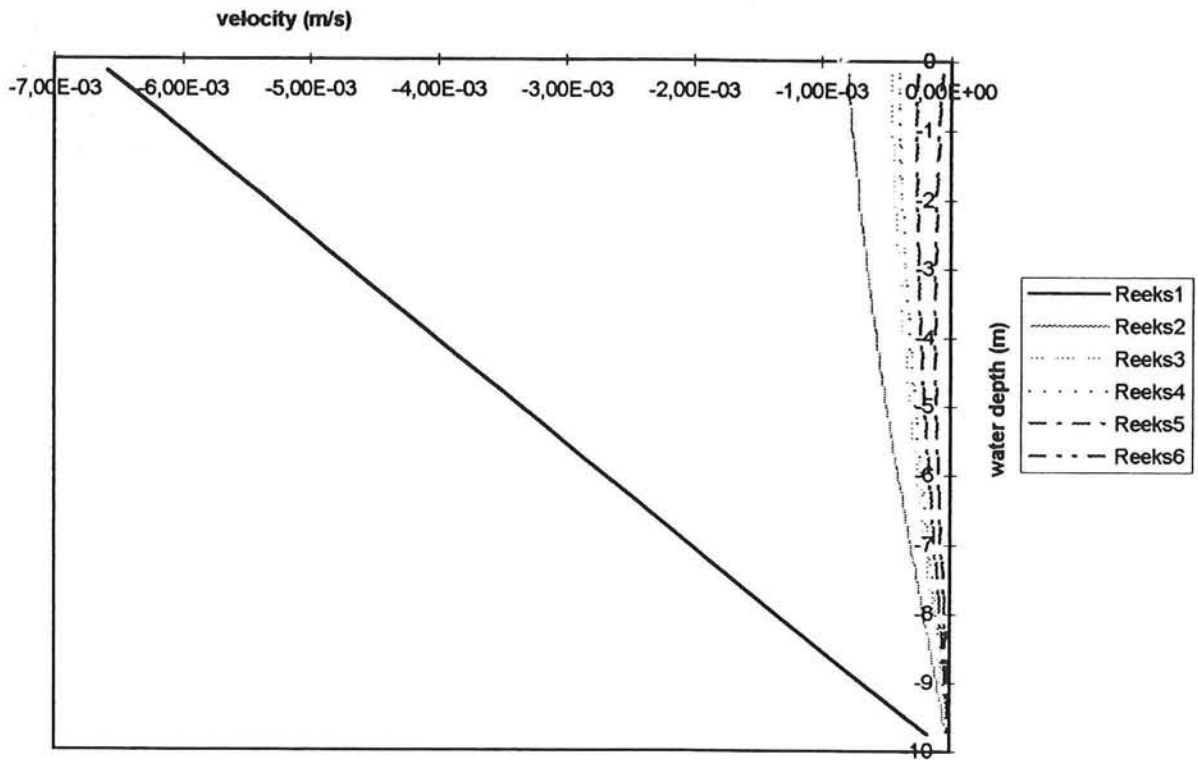
radial velocities at $\phi=177,25$



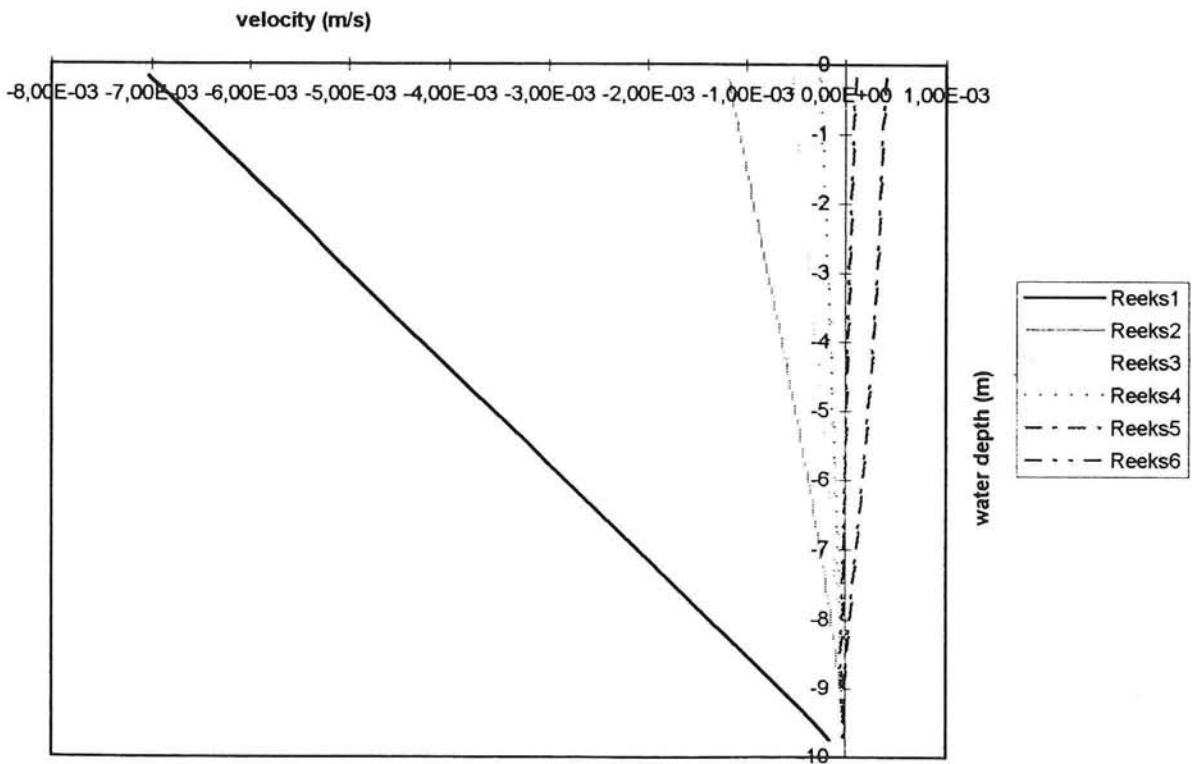
radial velocities 375 m downstream of the bend



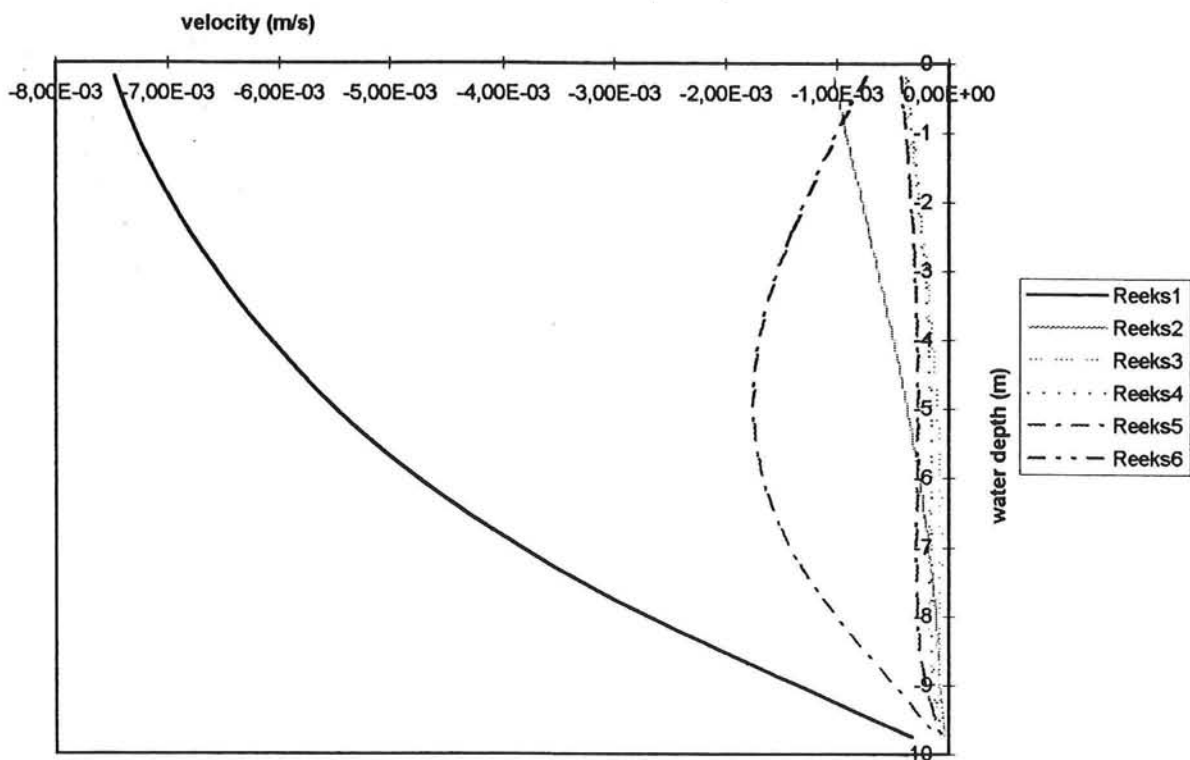
vertical velocities 375 m upstream of the bend



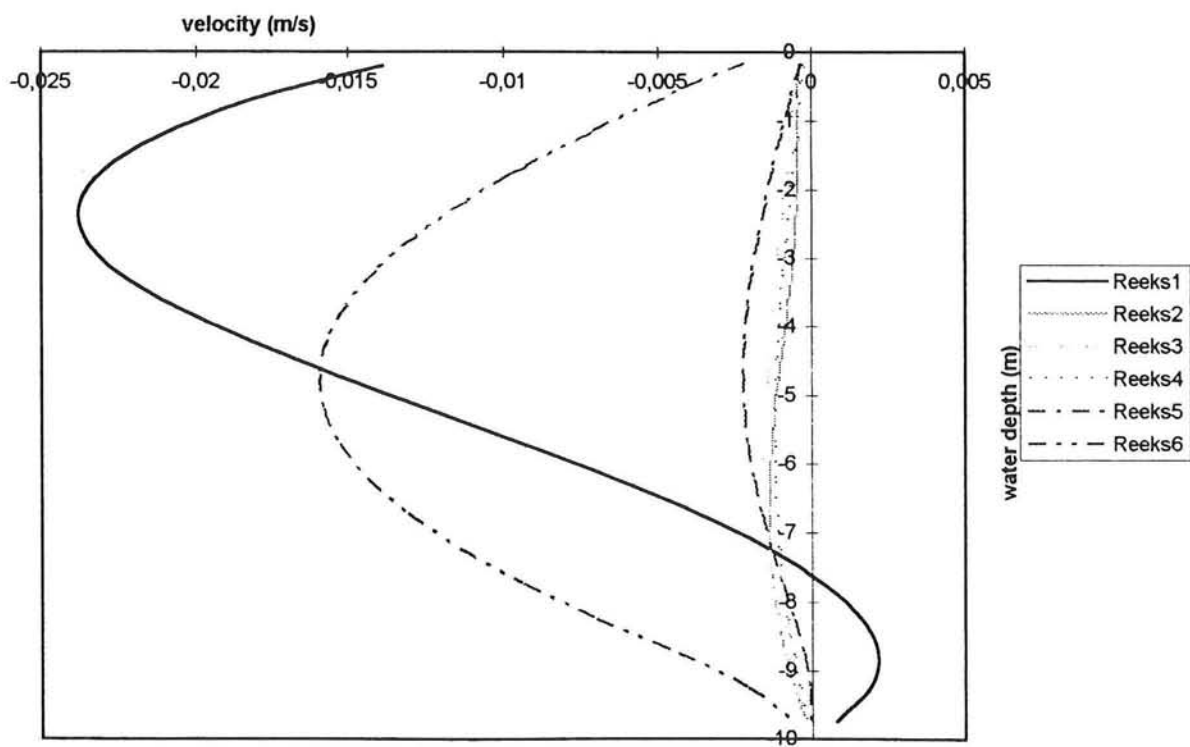
vertical velocities 125 m upstream of the bend



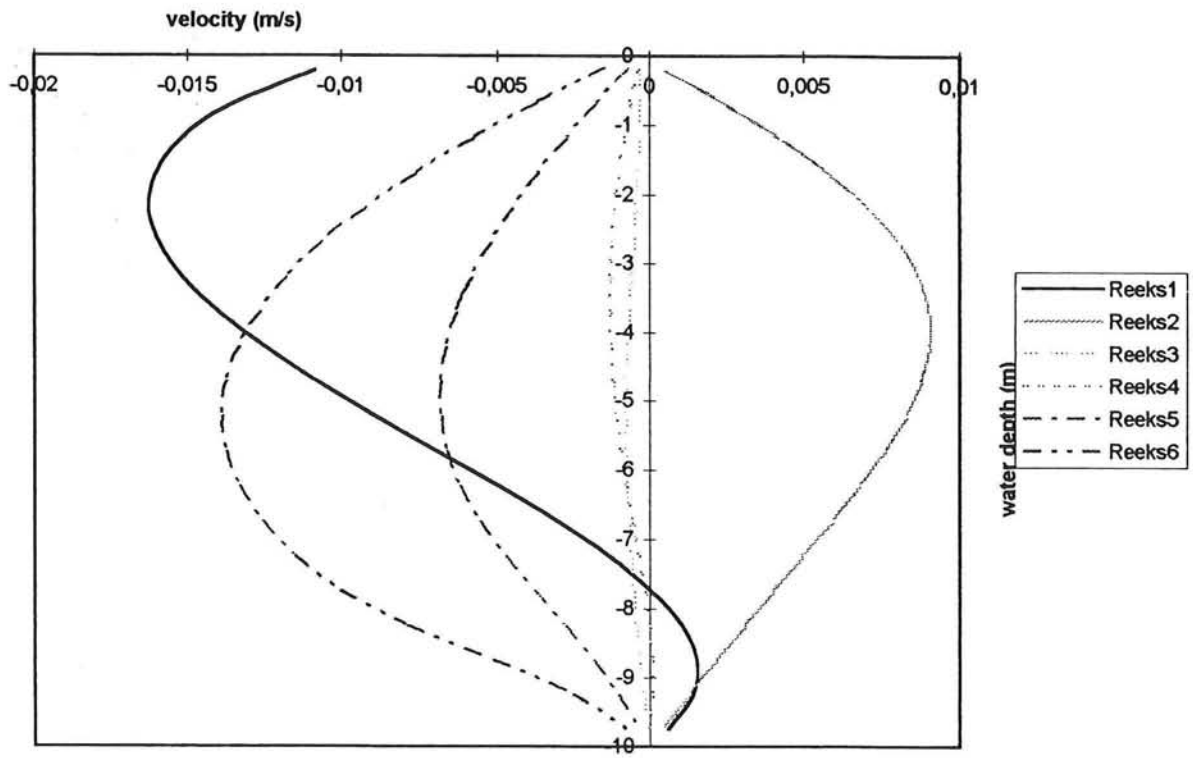
vertical velocities at $\phi=3,75$



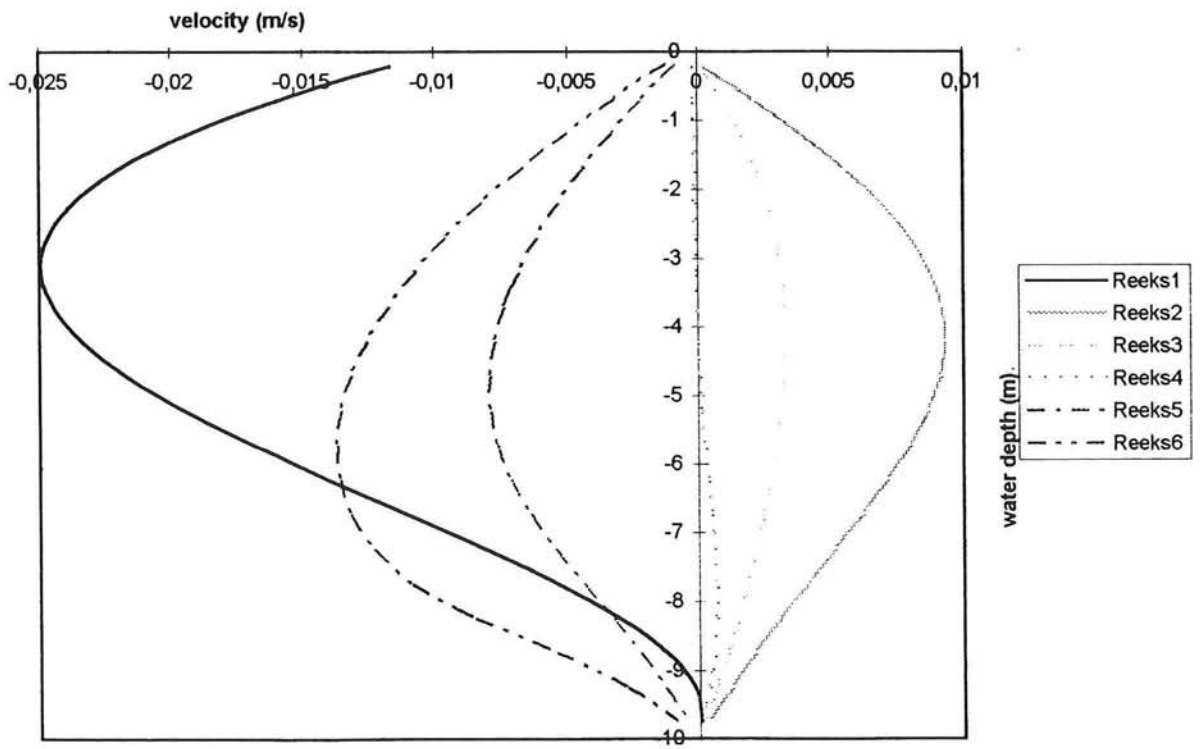
vertical velocities at $\phi=45$



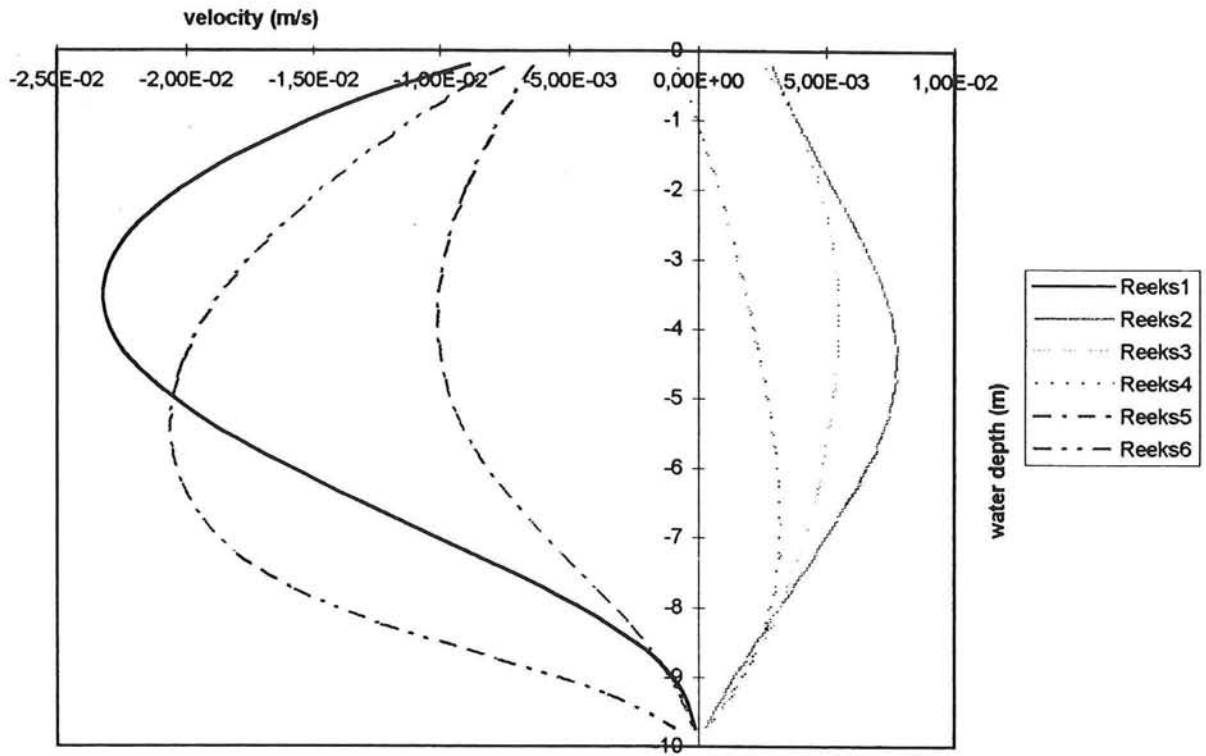
vertical velocities at $\phi=90$



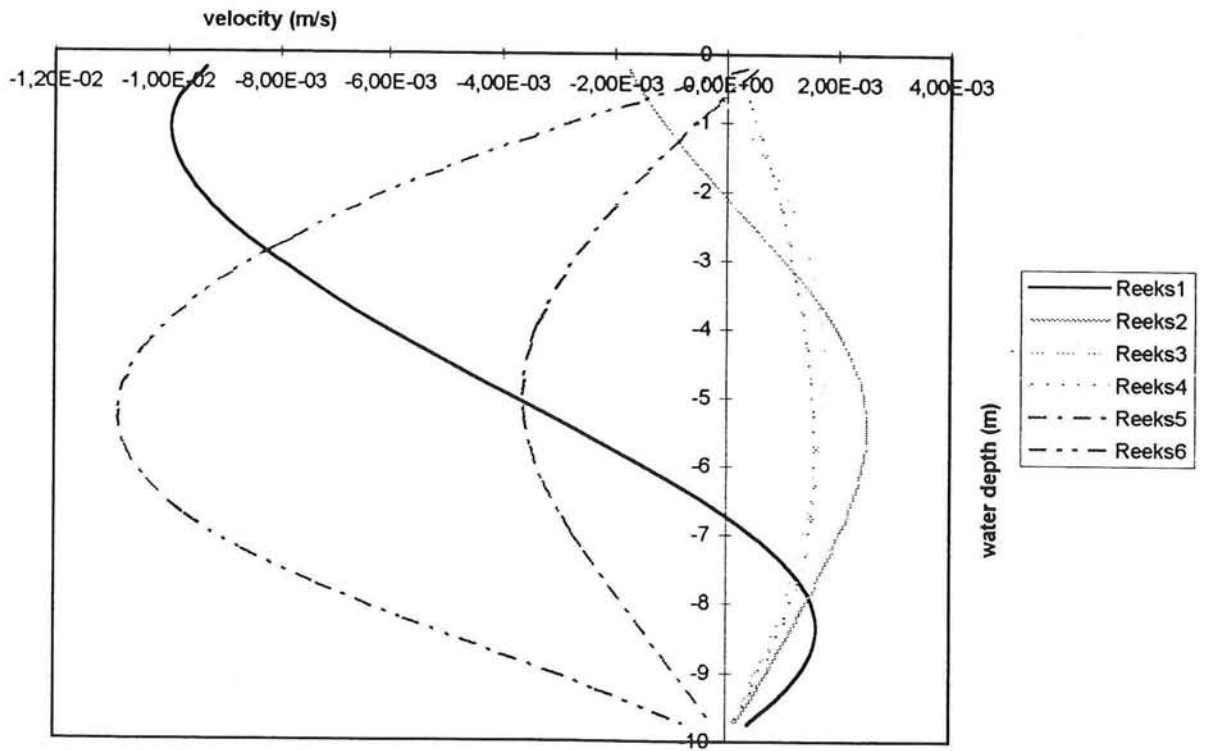
vertical velocities at $\phi=135$



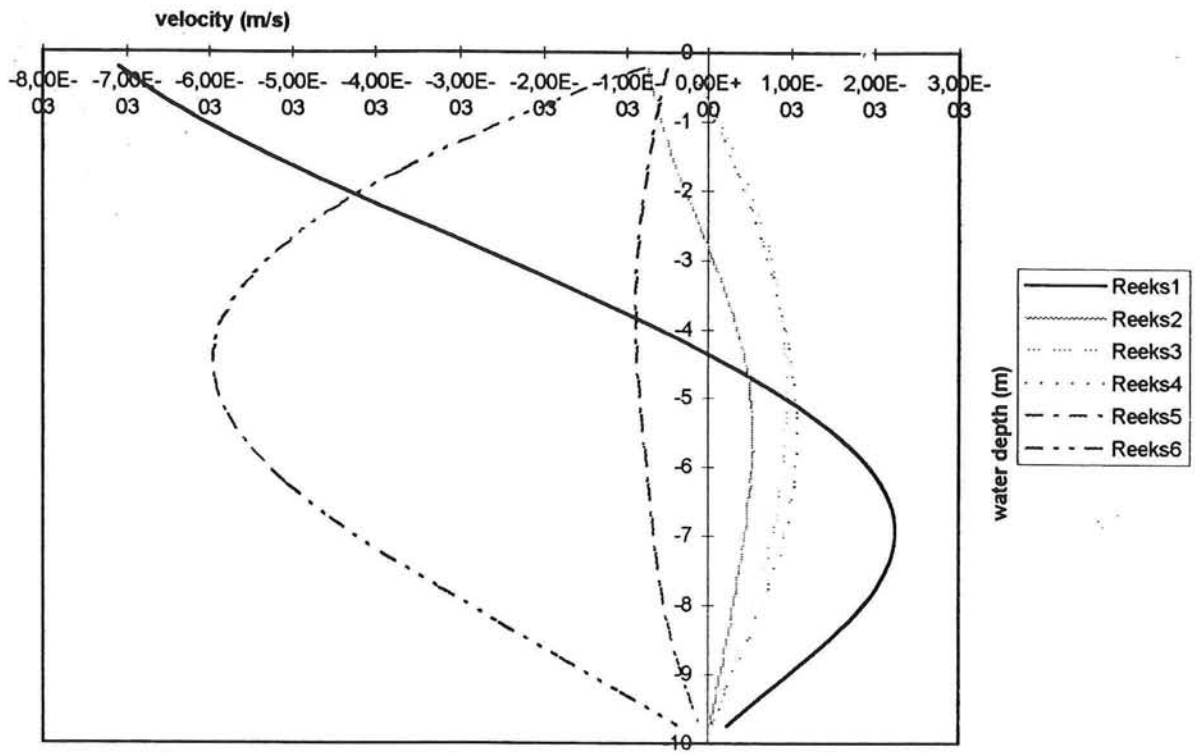
vertical velocities at $\phi=177,5$



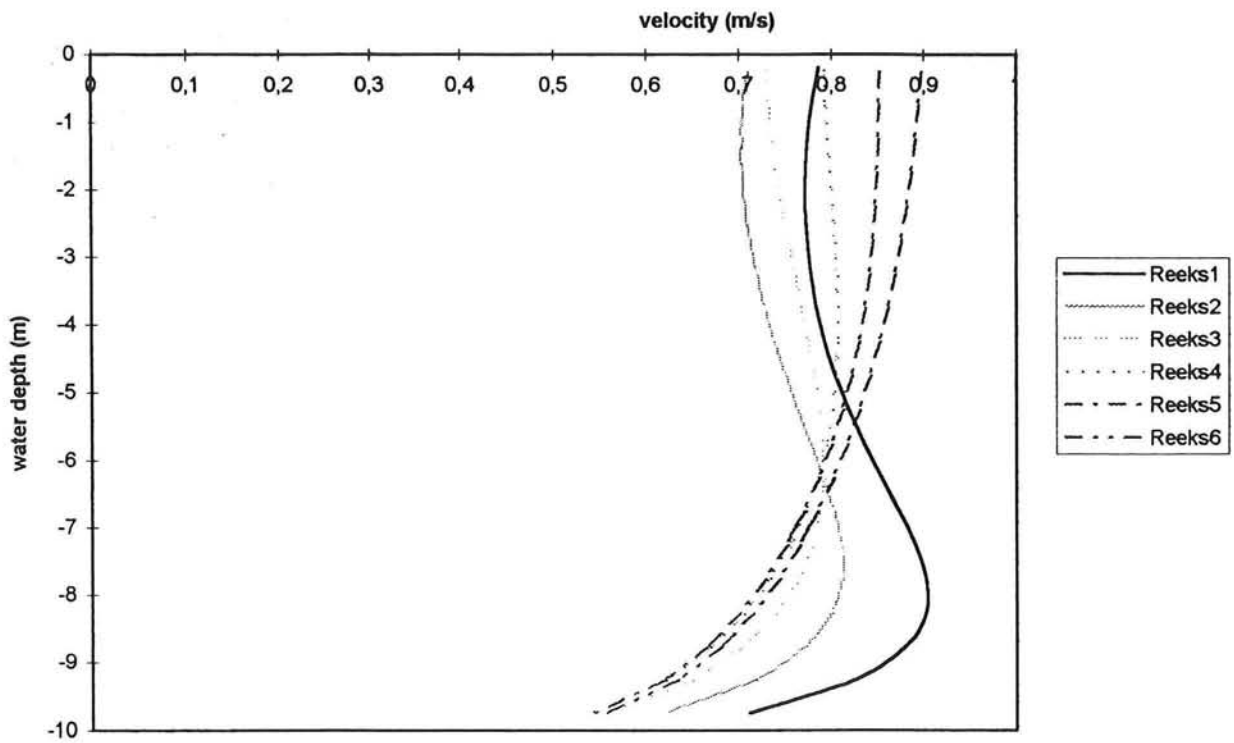
vertical velocities 125 m downstream of the bend



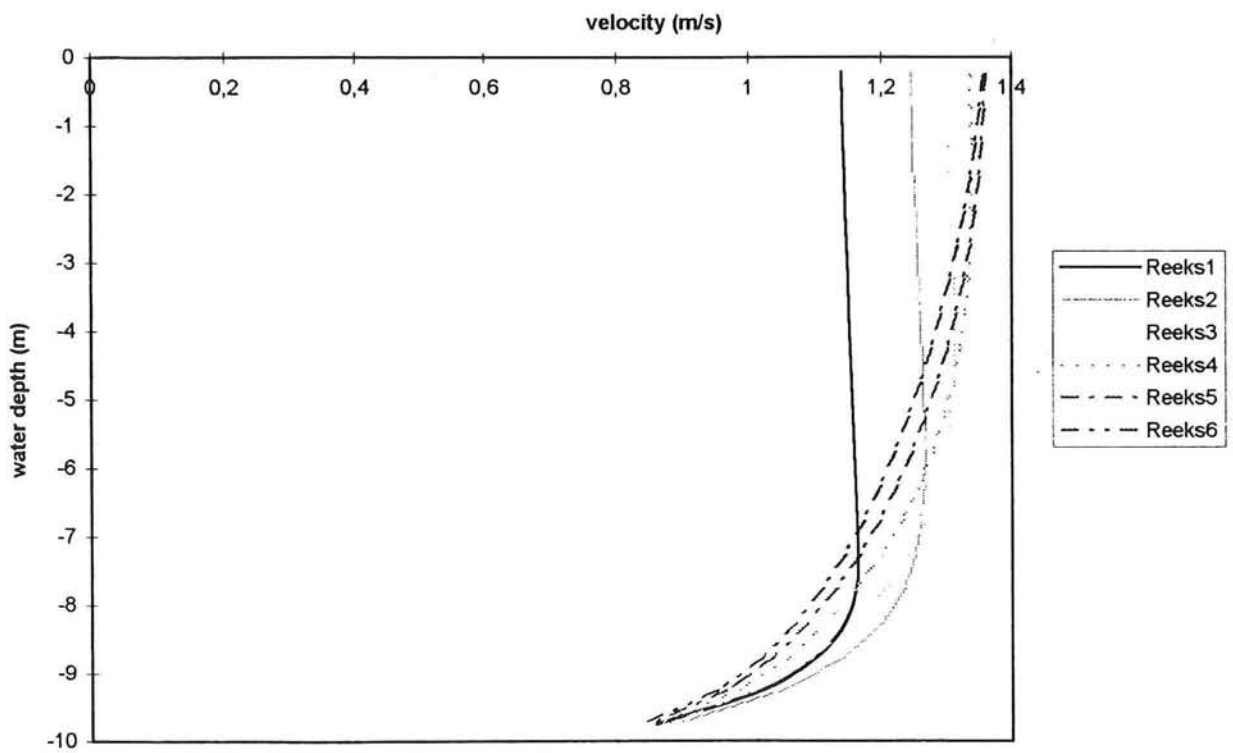
vertical velocities 375 m downstream of the bend



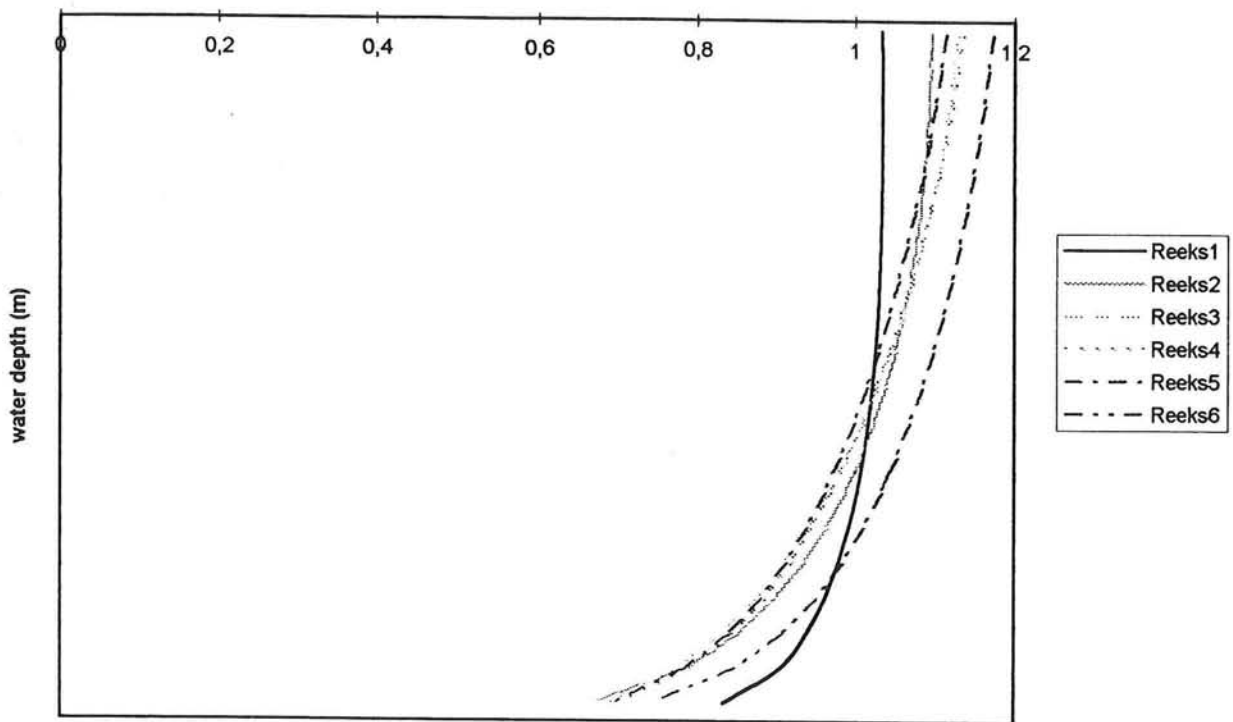
longitudinal velocities near the inner wall downstream of the bend



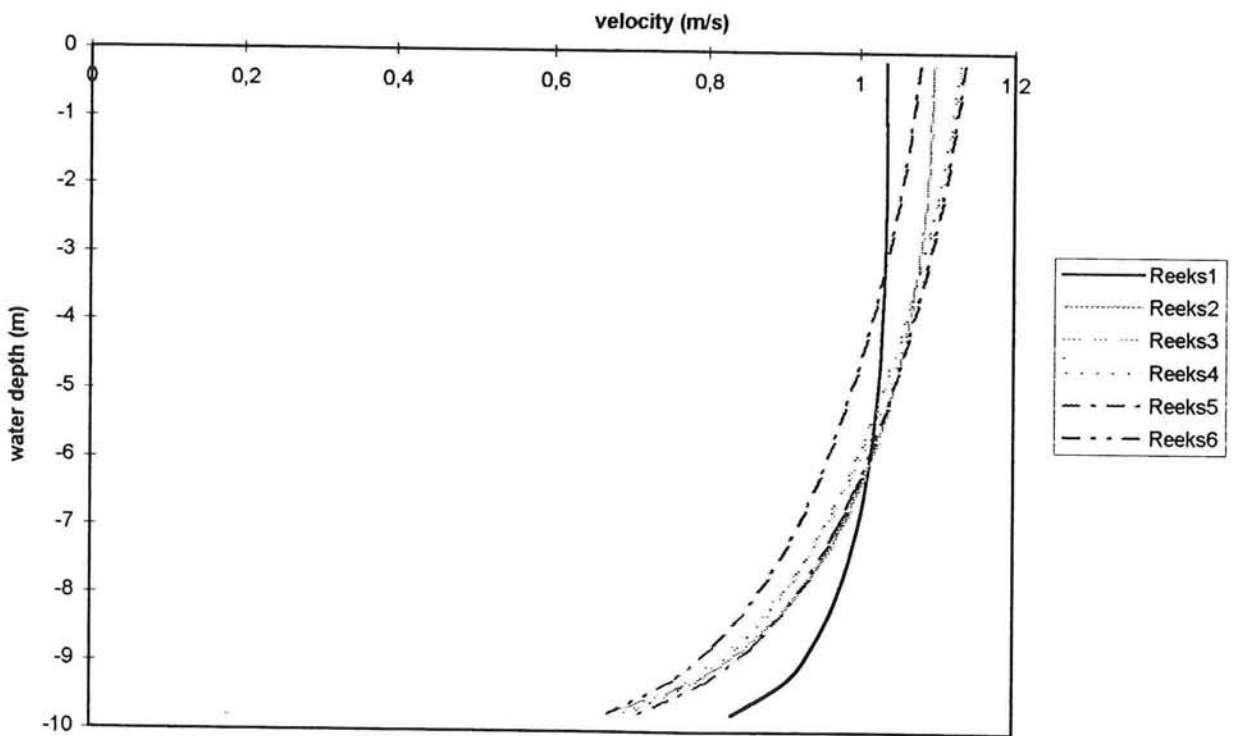
longitudinal velocities near the outer wall downstream of the bend



longitudinal velocities near the inner wall before the entrance of the bend



longitudinal velocities near the outer wall upstream of the bend

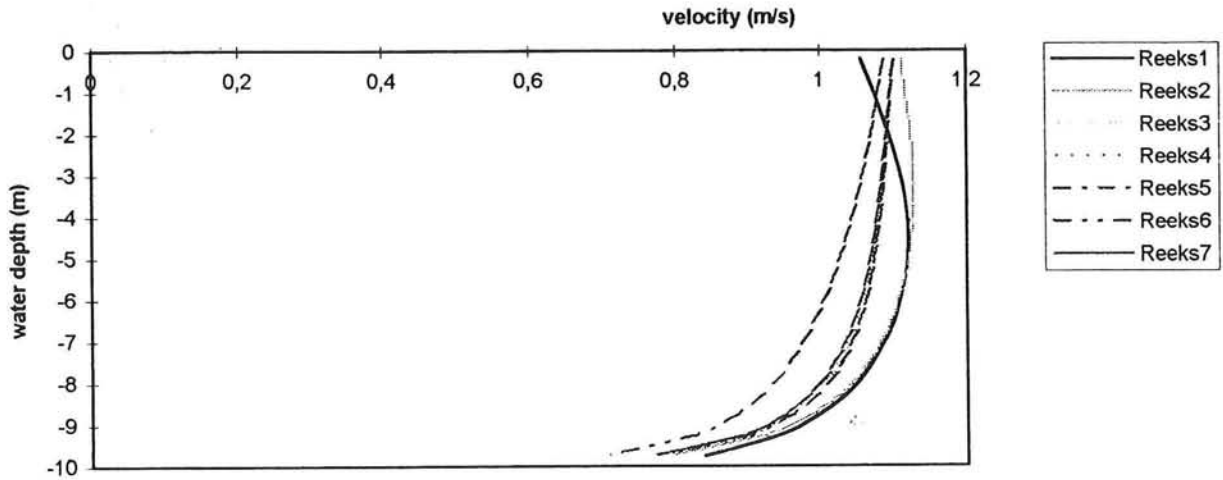


Appendix XI

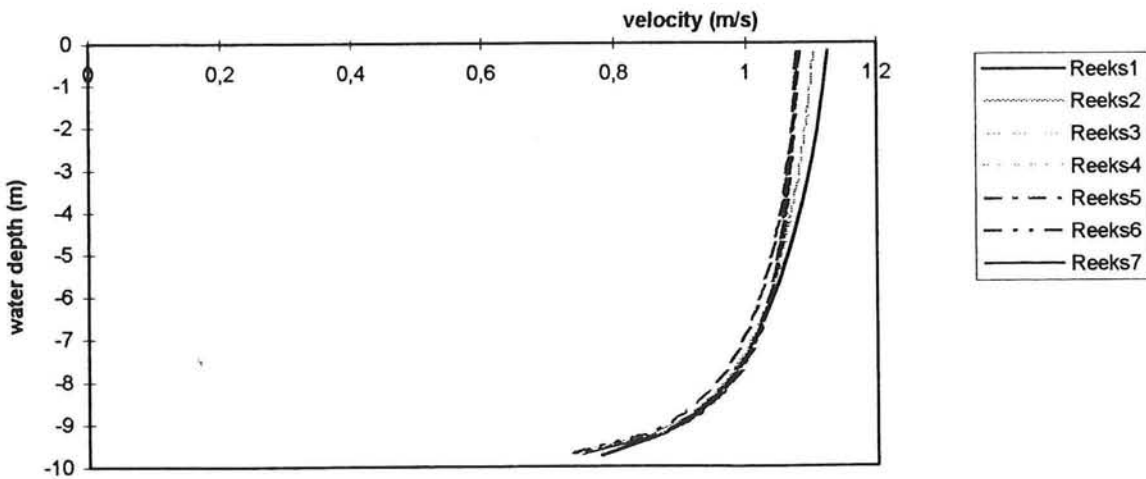
These figures show the influence of the used turbulence model in the simulation of the strongly curved bend

- reeks 1 is the k- ϵ model and the horizontal eddy viscosity $\nu_h = 1 \cdot 10^{-2} \text{ m}^2/\text{s}$
- reeks 2 is the k-L model and the horizontal eddy viscosity $\nu_h = 1 \cdot 10^{-2} \text{ m}^2/\text{s}$
- reeks 3 is a constant value for the vertical viscosity coefficient $\nu_v = 1 \cdot 10^{-6} \text{ m}^2/\text{s}$ and the horizontal eddy viscosity $\nu_h = 1 \cdot 10^{-2} \text{ m}^2/\text{s}$
- reeks 4 is a constant value for the vertical viscosity coefficient $\nu_v = 1 \cdot 10^{-2} \text{ m}^2/\text{s}$ and the horizontal eddy viscosity $\nu_h = 1,0 \text{ m}^2/\text{s}$
- reeks 5 is a constant value for the vertical viscosity coefficient $\nu_v = 1 \cdot 10^{-6} \text{ m}^2/\text{s}$ and the horizontal eddy viscosity $\nu_h = 1,0 \text{ m}^2/\text{s}$
- reeks 6 is a constant value for the vertical viscosity coefficient $\nu_v = 1 \cdot 10^{-6} \text{ m}^2/\text{s}$ and the horizontal eddy viscosity $\nu_h = 10,0 \text{ m}^2/\text{s}$
- reeks 7 is the algebraic model

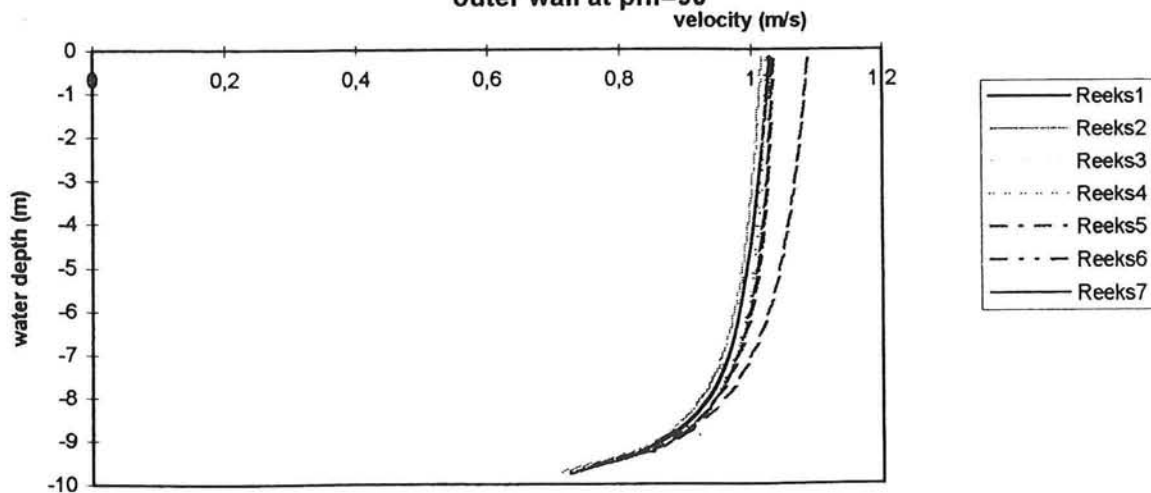
comparison of the turbulent models; for the longitudinal velocities near the inner wall at $\phi=90$



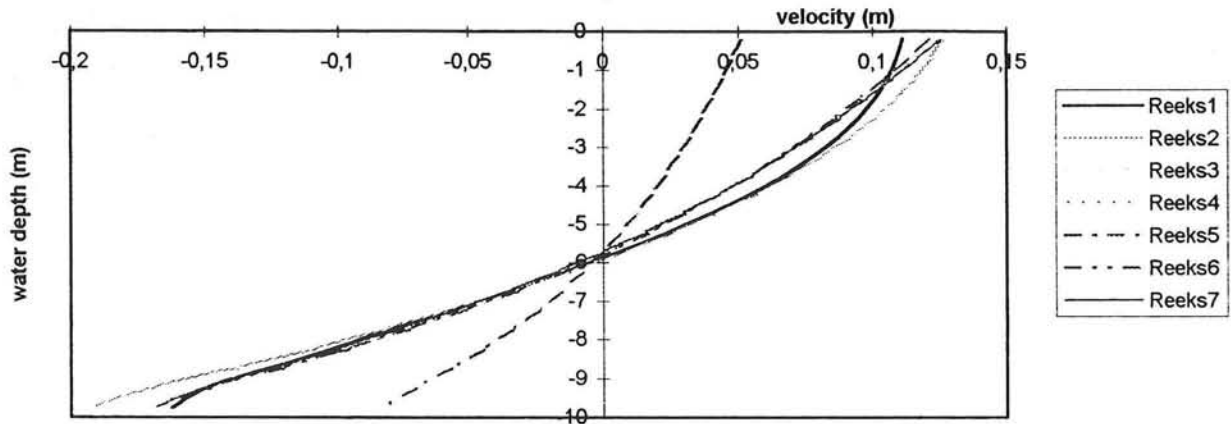
comparison of the turbulent models; for the longitudinal velocities in the middle of the cross-section at $\phi=90$



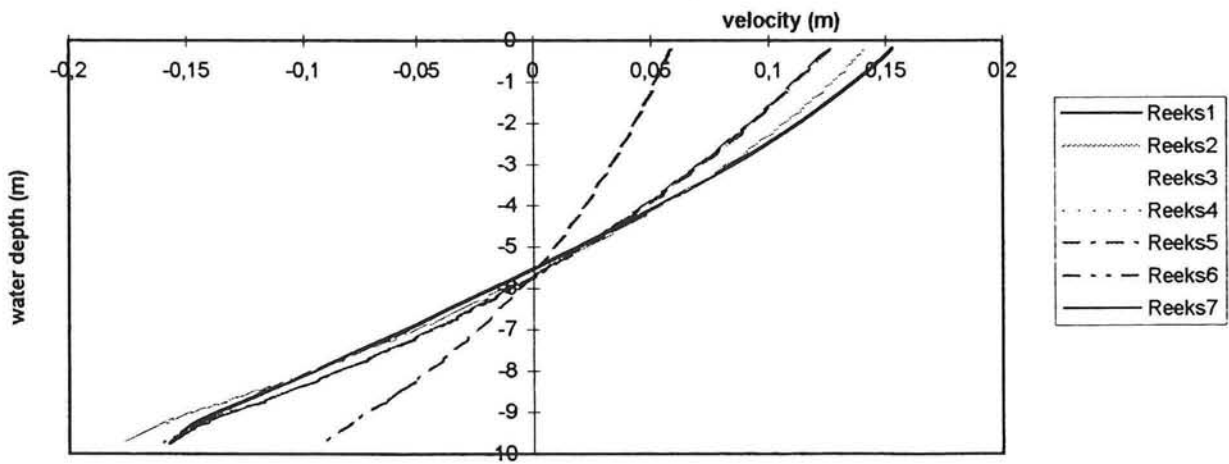
comparison of the turbulent models; for the longitudinal velocities near the outer wall at $\phi=90$



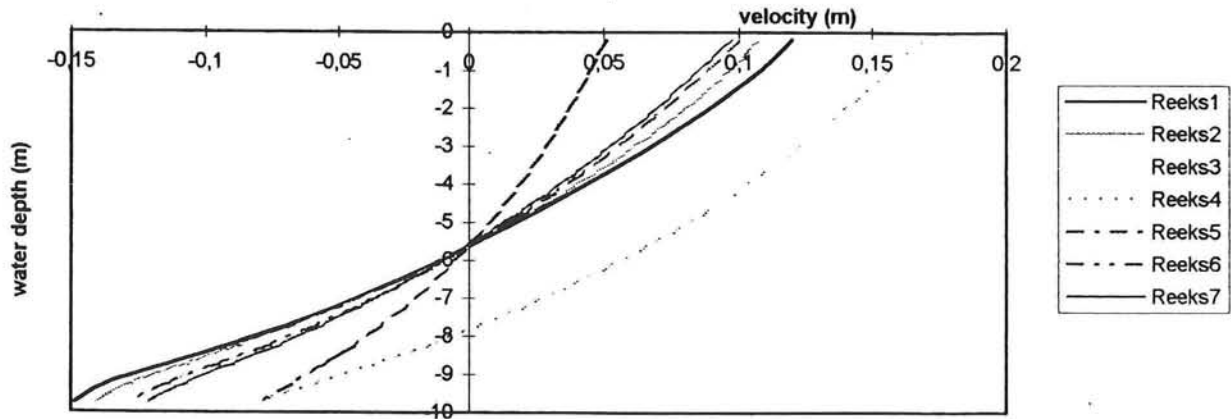
comparison of the turbulent models; for the radial velocities near the inner wall at $\phi=90$



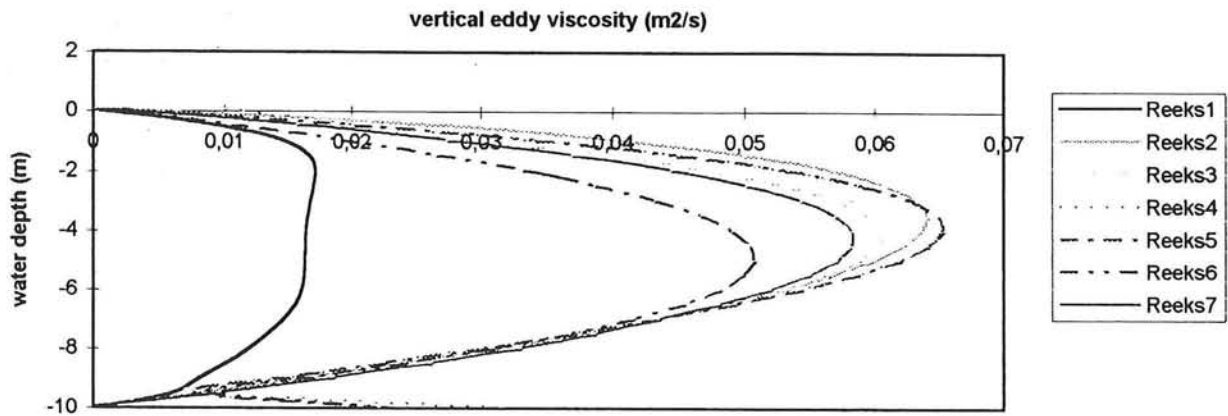
comparison of the turbulent models; for the radial velocities in the middle of the cross-section at $\phi=90$



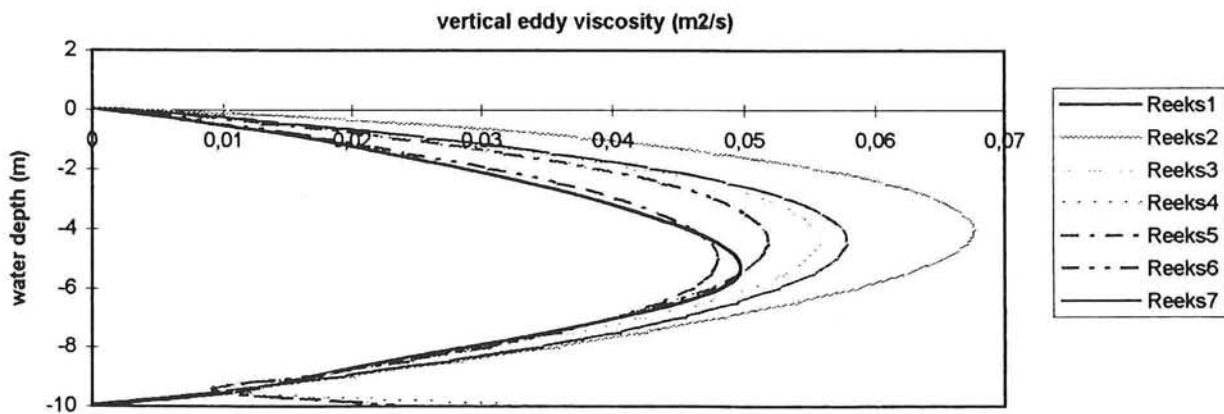
comparison of the turbulent models; for the radial velocities near the outer wall at $\phi=90$



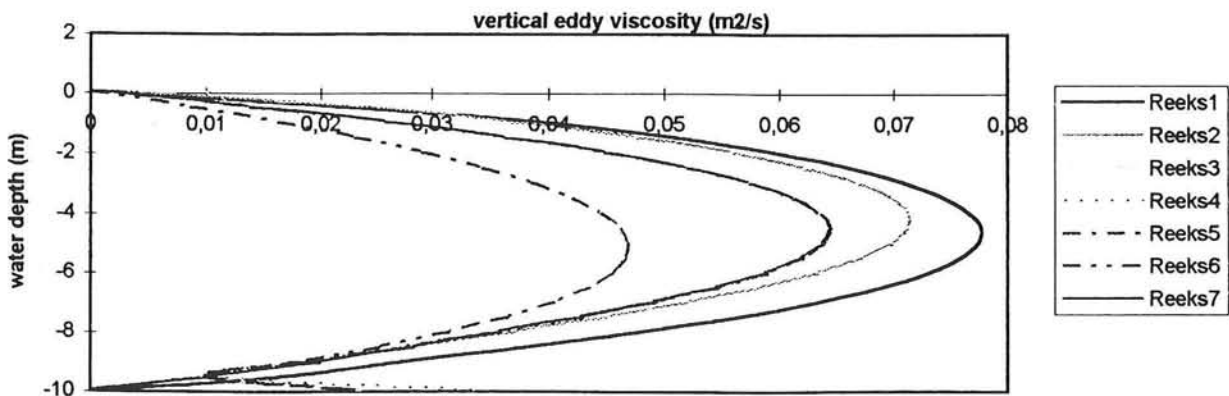
comparison of turbulent models for the vertical eddy viscosity at the first gridpoint at the inner wall at $\phi=90$



comparison of turbulent models for vertical eddy viscosity at the second gridpoint at the wall at $\phi=90$



comparison of turbulent models for vertical eddy viscosity in the middle of the cross-section at $\phi=90$



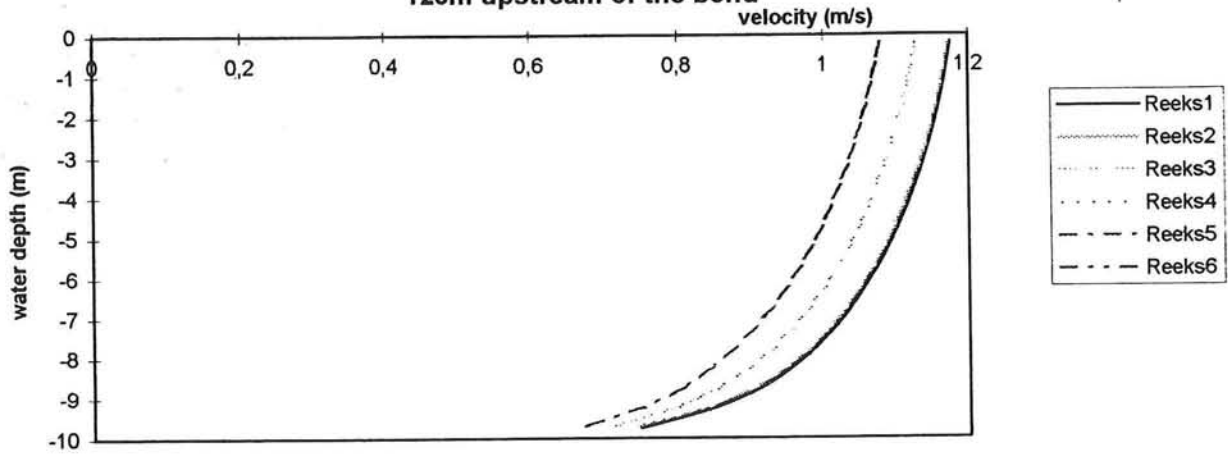
Appendix XII

These figures show the influence of the grid size in the simulation of the strongly curved bend. The velocities are taken at the positions 125m upstream of the bend, at $\phi=90^\circ$ and at 125m downstream of the bend at the 3rd, 10th and 20th grid point.

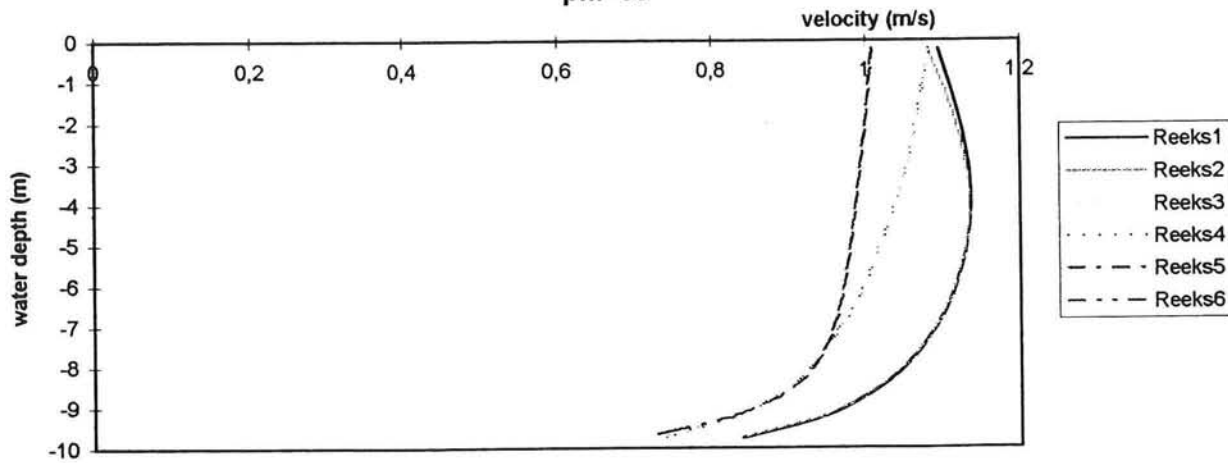
Reeks 1, Reeks 3, Reeks 5 $\Delta\phi=7,5^\circ$

Reeks 2, Reeks 4, Reeks 6 $\Delta\phi=15^\circ$

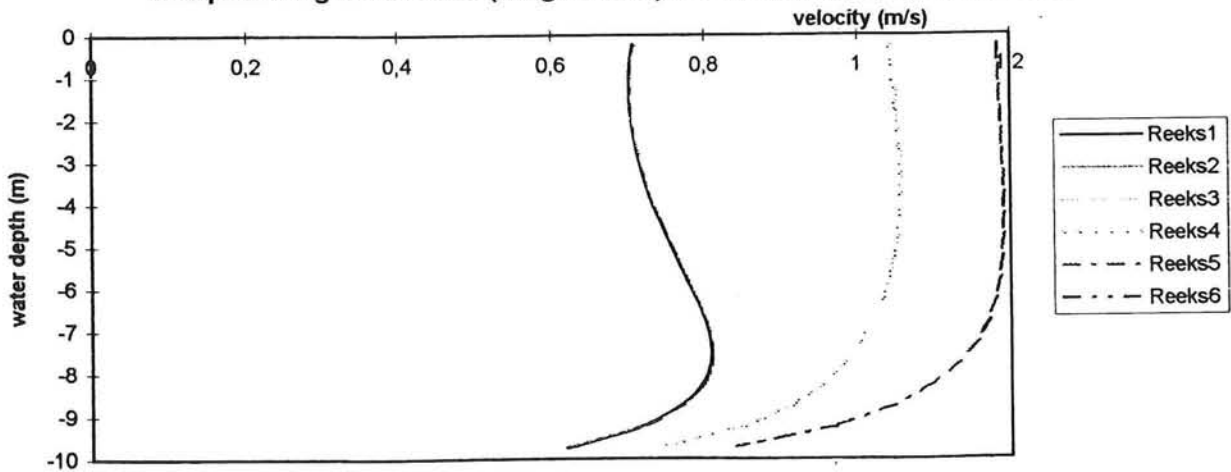
comparison of longitudinal velocities for different longitudinal grid sizes
125m upstream of the bend



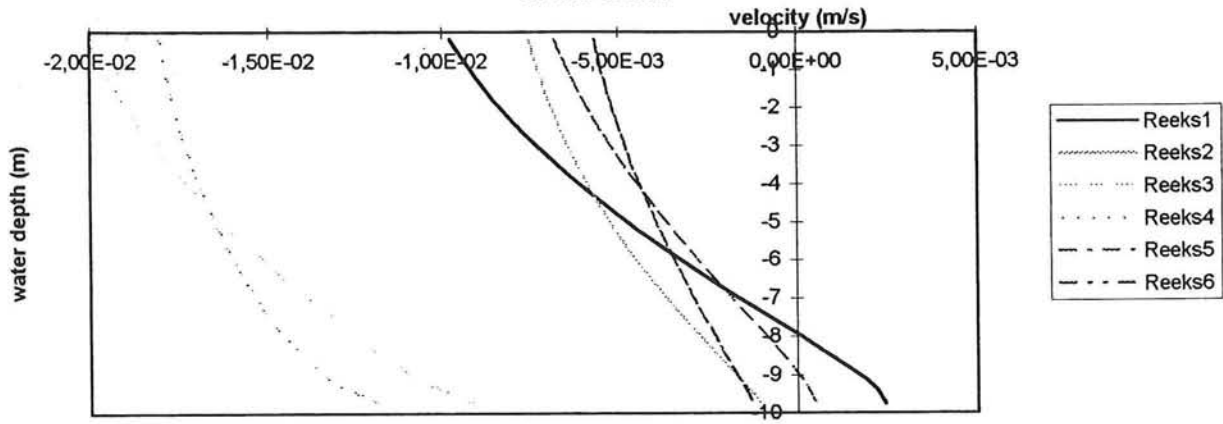
comparison of longitudinal velocities for different longitudinal grid sizes at
 $\phi=90$



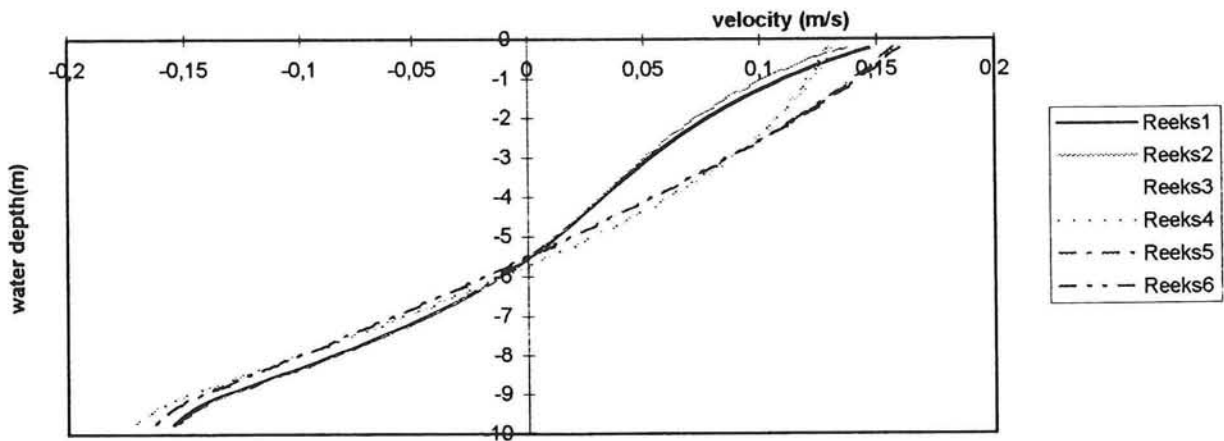
comparison grid distance (longitudinal) 125 m downstream of the bend



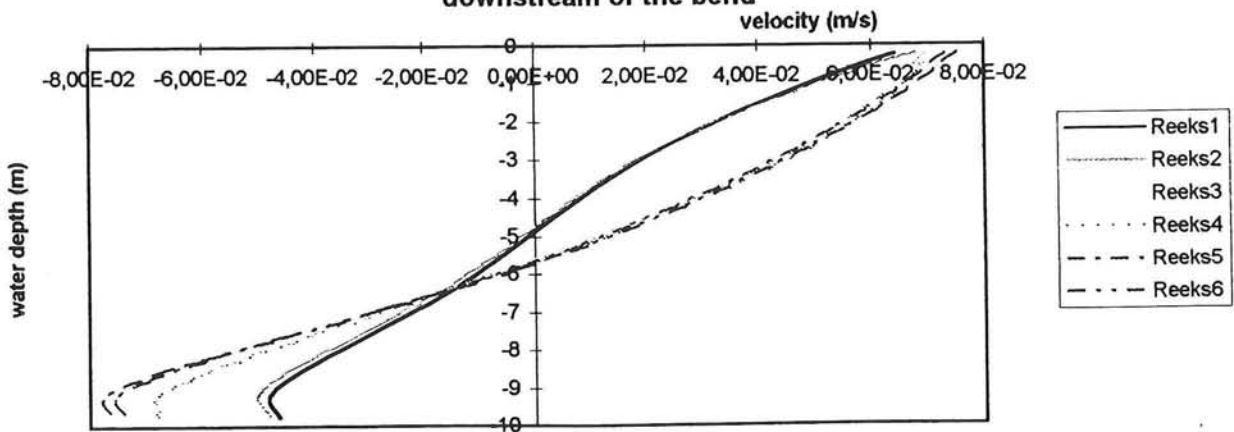
comparison of radial velocities for different grid-sizes (radial) 125 m upstream of the bend



comparison of radial velocities for different longitudinal grid sizes at phi=90



comparison of radial velocities for different longitudinal grid sizes 125 m downstream of the bend



Appendix XIII

These figures show the influence of the used time step in the simulation of the strongly curved bend

In these figures the lines represent the distributions with the full time step equal to, respectively;

reeks 1 $\Delta t=0,05\text{min}$

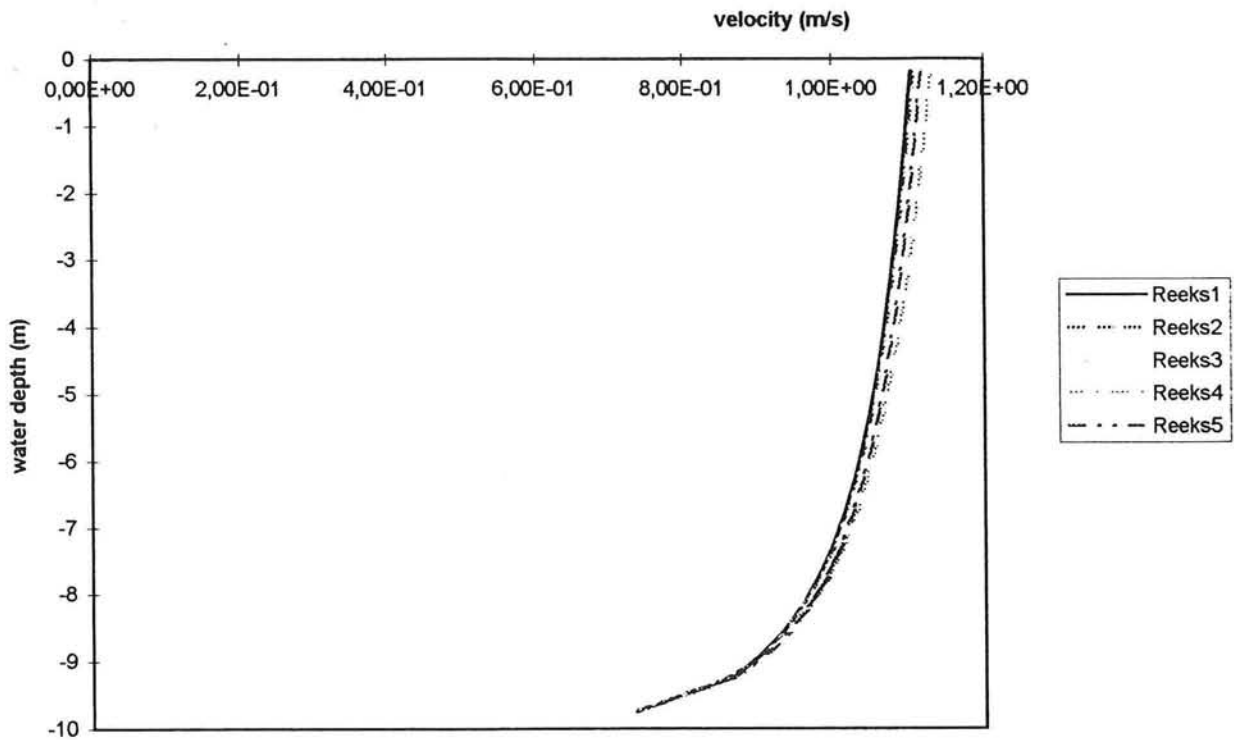
reeks 2 $\Delta t=0,5\text{min}$

reeks 3 $\Delta t=1,0\text{min}$

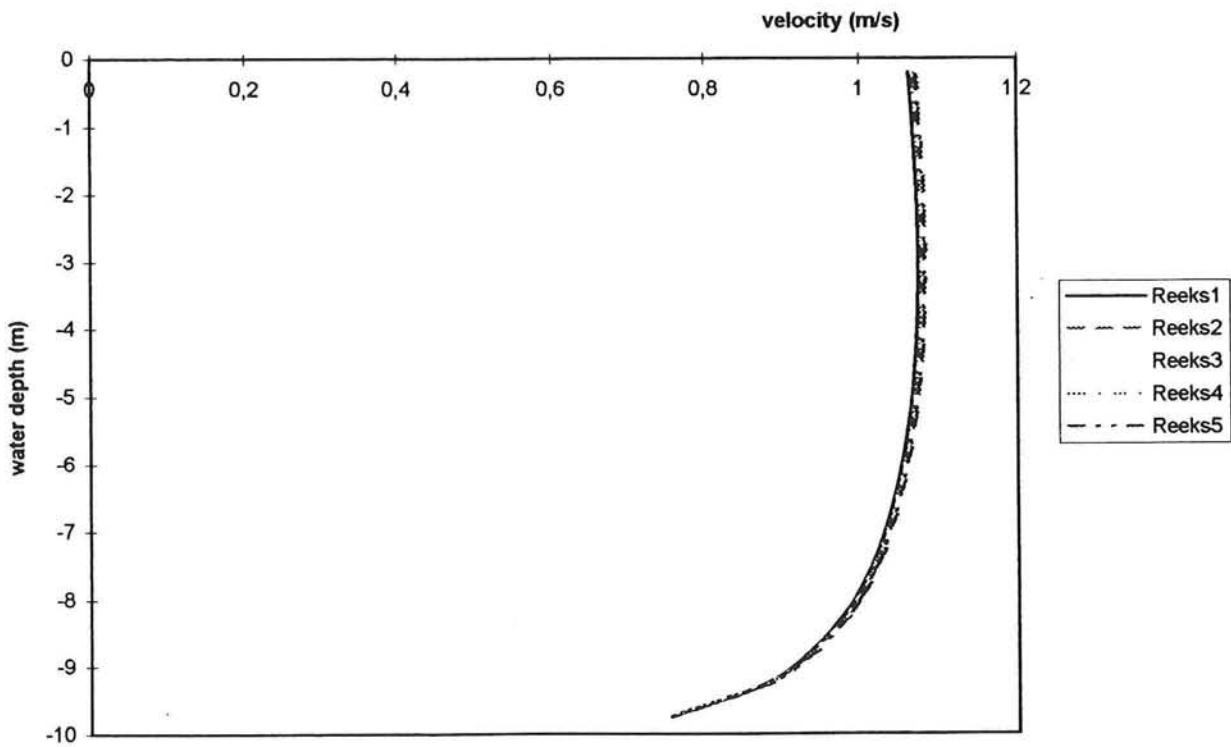
reeks 4 $\Delta t=2,0\text{min}$

reeks 5 $\Delta t=4,0\text{min}$

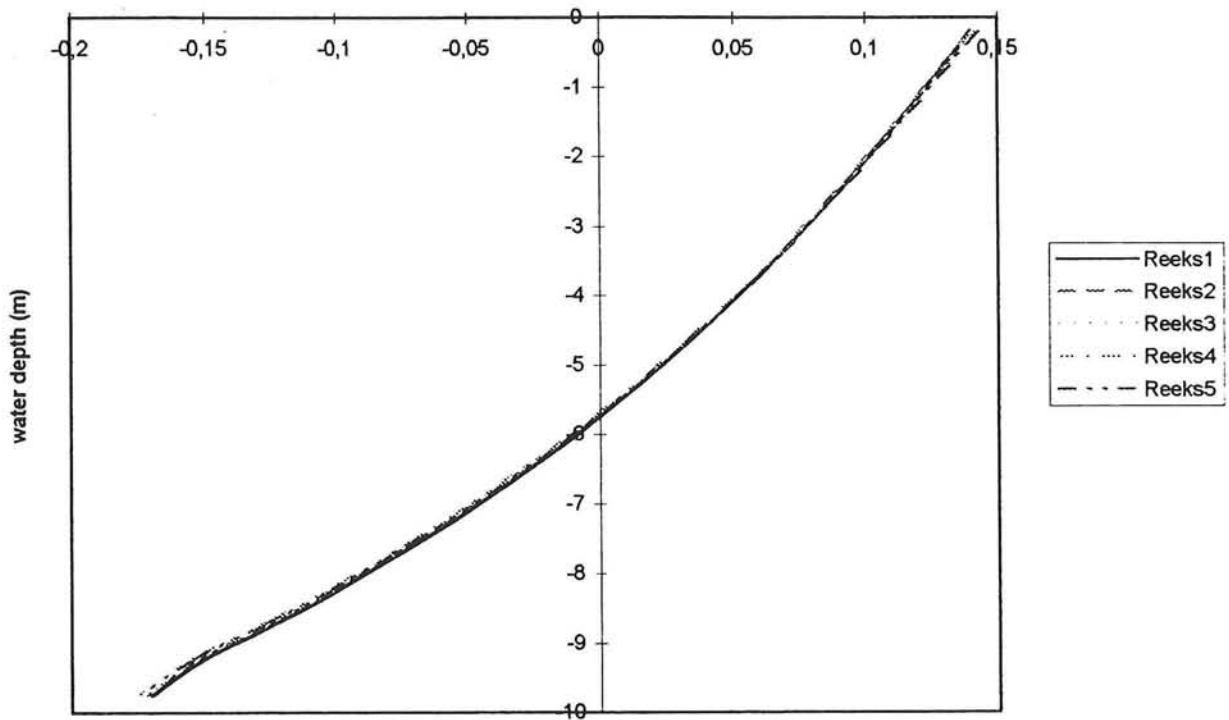
comparison of longitudinal velocities for different time steps in the middle of the cross-section at $\phi=90$



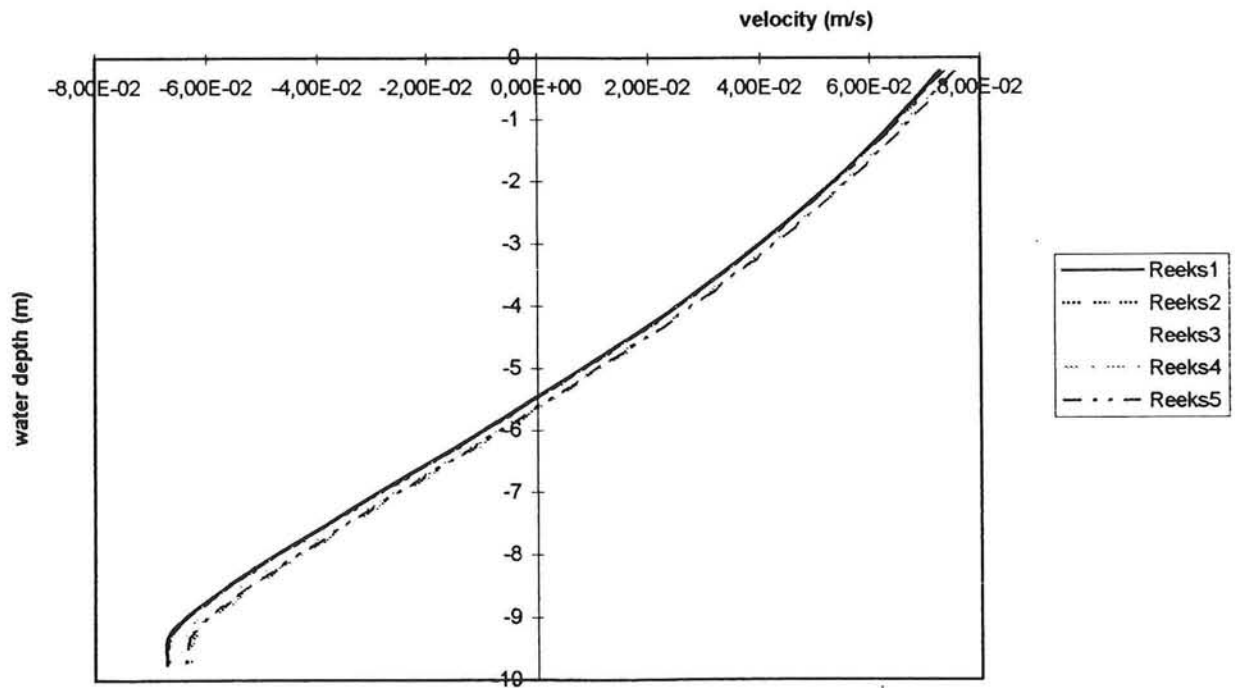
comparison of longitudinal velocities for different time steps in the middle of the cross-section 125 m downstream of the bend



comparison of radial velocities for different time steps in the middle of the cross-section at $\phi=90^\circ$ velocity (m/s)



comparison of radial velocities for different time steps in the middle of the cross-section 125 m downstream of the bend

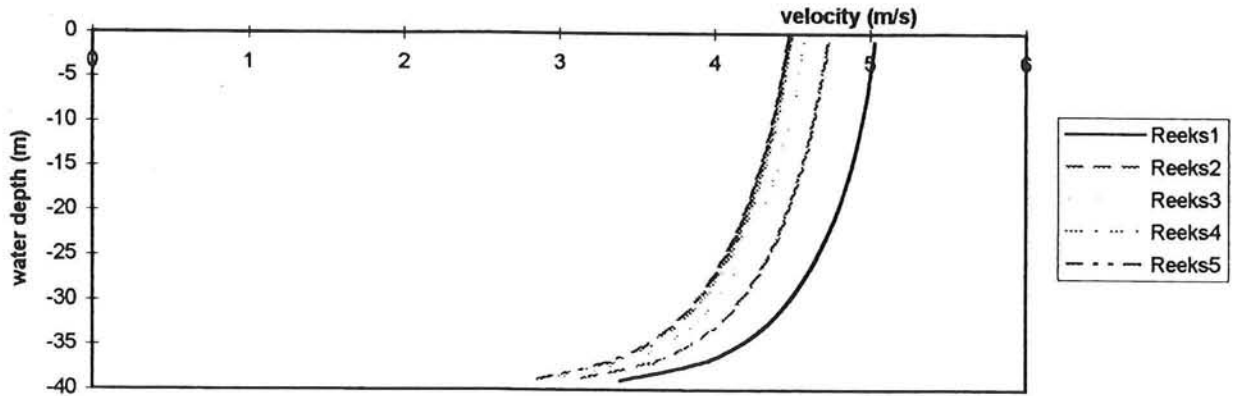


Appendix XIV

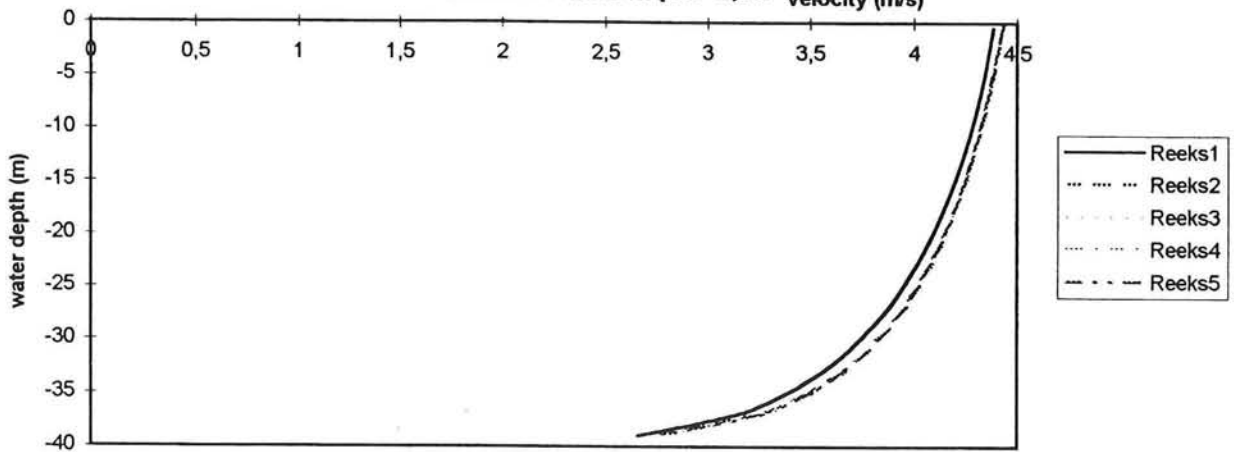
The influence of the radius of curvature is shown in this appendix. The lines represent the following radius of curvature:

reeks 1	R=125m
reeks 2	R=250m
reeks 3	R=500m
reeks 4	R=1000m
reeks 5	R=1500m

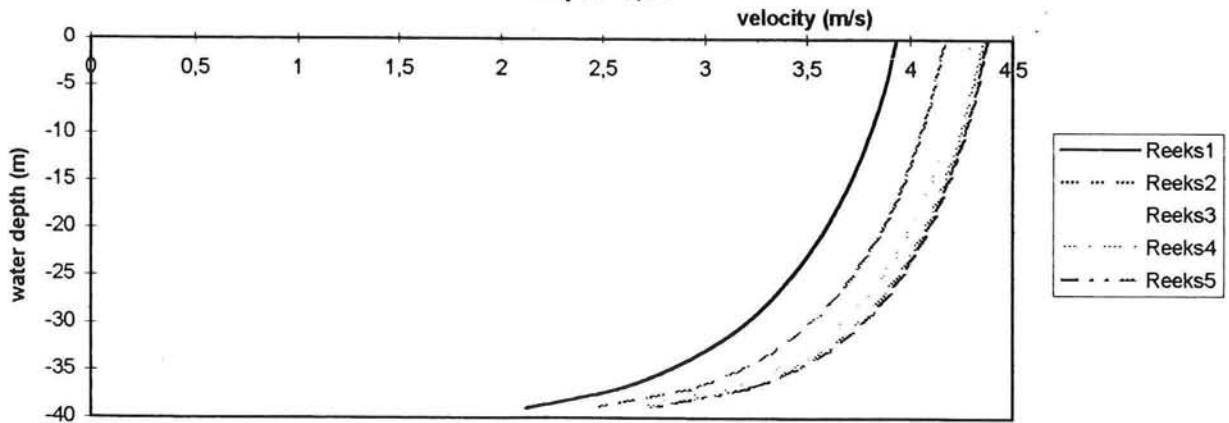
comparison of longitudinal velocities for different radii at the 6th grid point at $\phi=3,75$



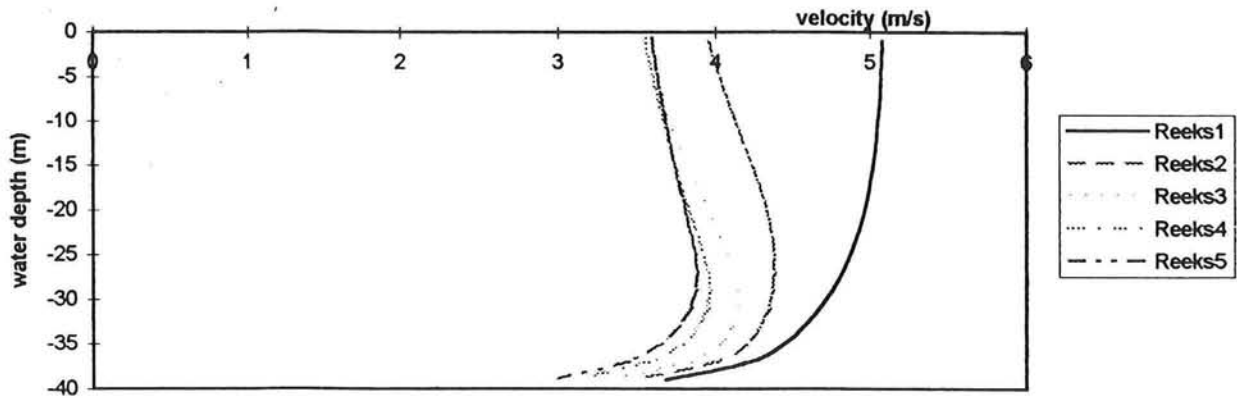
comparison of longitudinal velocities for different radii in the middle of the cross-section at $\phi=3,75$



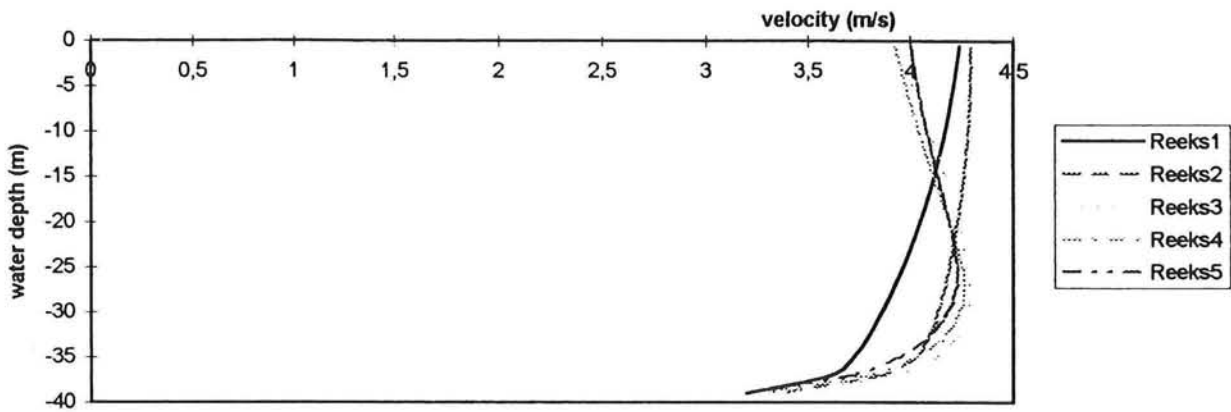
comparison of longitudinal velocities for different radii at the 16th grid point at $\phi=3,75$



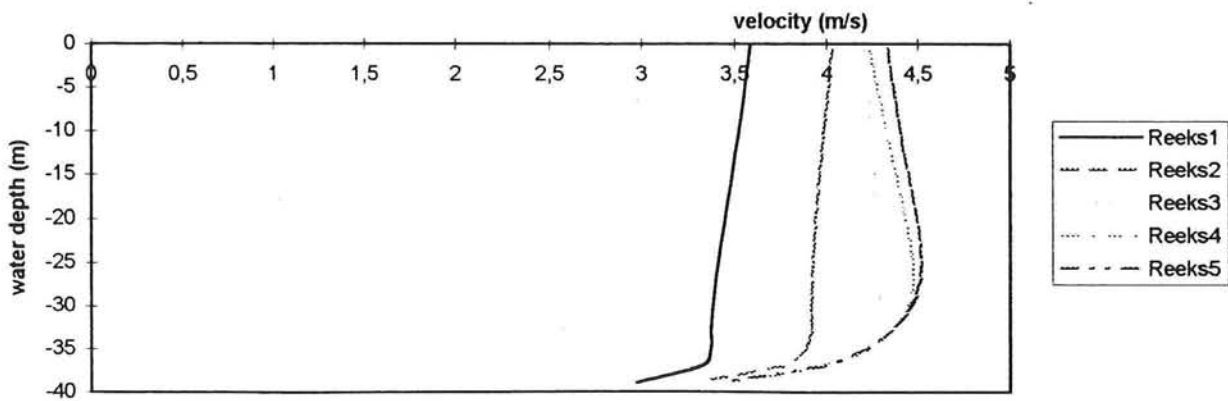
comparison of longitudinal velocities for different radii at the 6th gridpoint at $\phi=90$



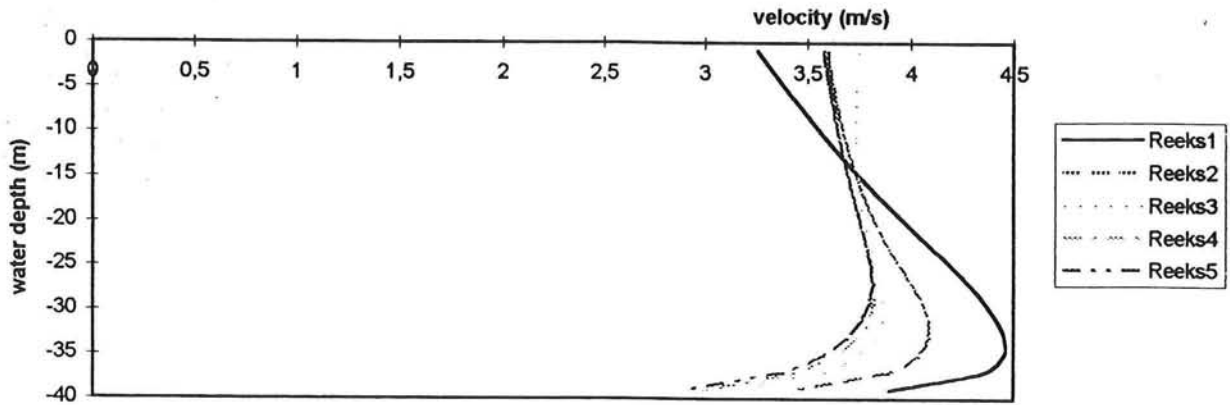
comparison of longitudinal velocities for different radii in the middle of the cross-section at $\phi=90$



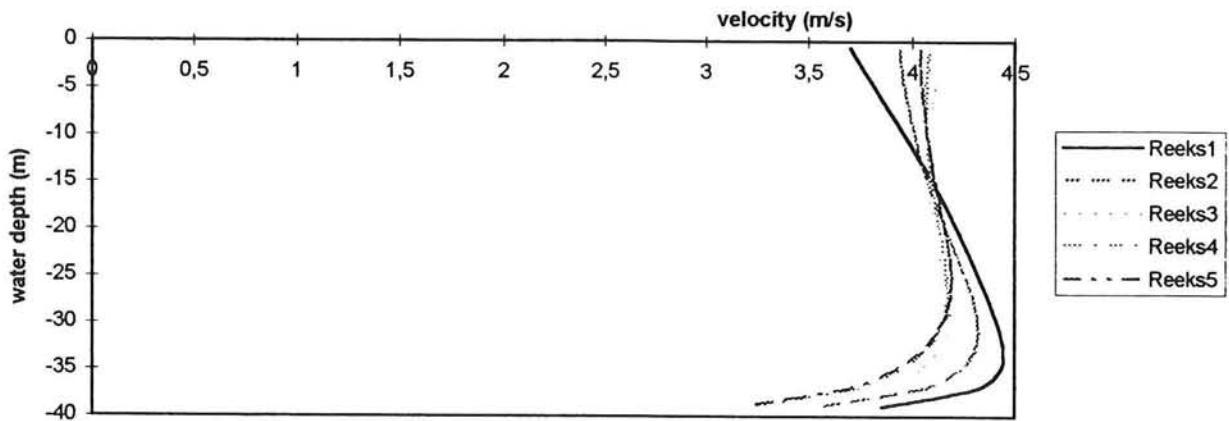
comparison of longitudinal velocities for different radii at the 16th grid point at $\phi=90$



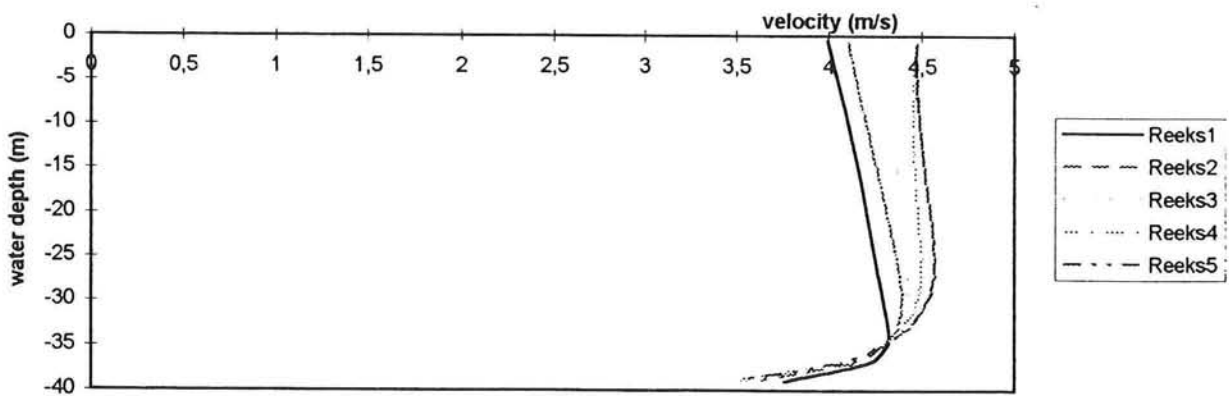
comparison of longitudinal velocities for different radii at the 6th grid point at $\phi=177,25$



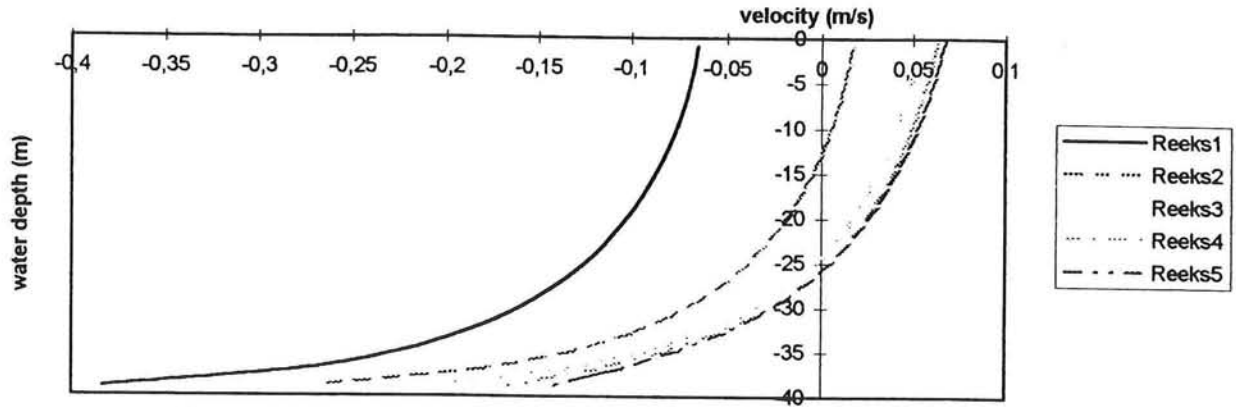
comparison of longitudinal velocities for different radii in the middle of the cross-section at $\phi=177,25$



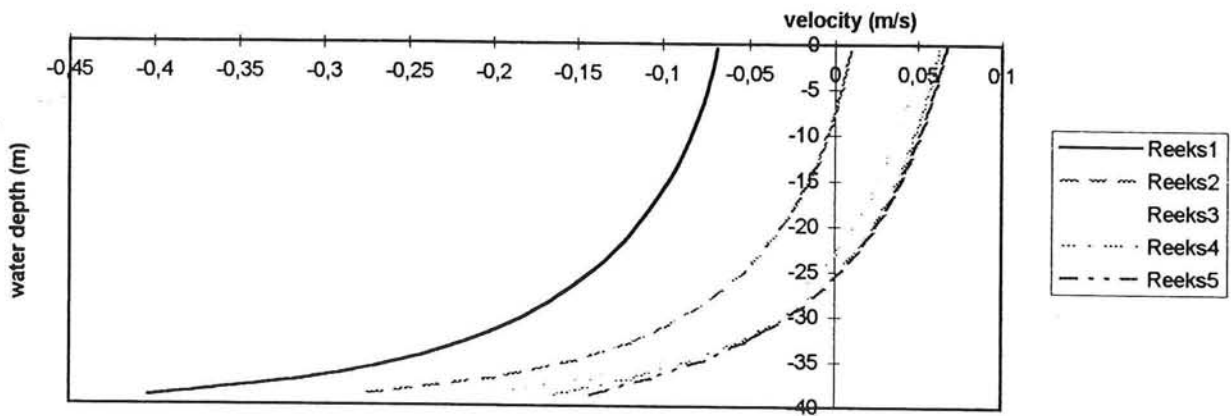
comparison of longitudinal velocities for different radii at the 16th grid point at $\phi=177,25$



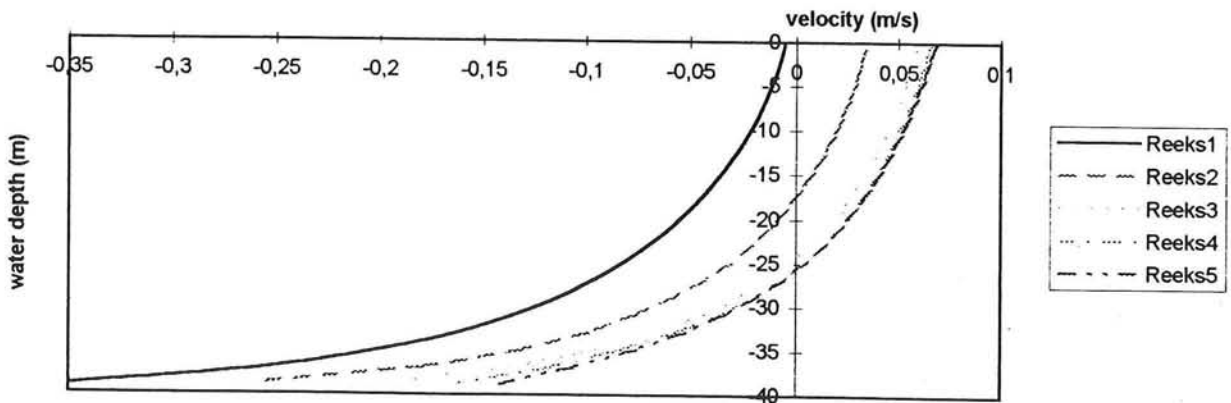
comparison of radial velocities for different radii at the 6th grid point at $\phi=3,75$



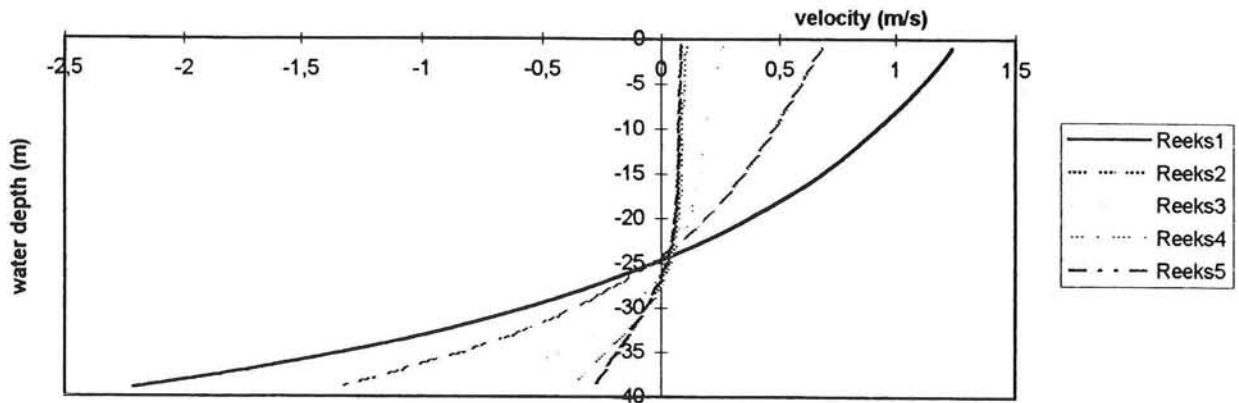
comparison of radial velocities for different radii in the middle of the cross-section at $\phi=3,75$



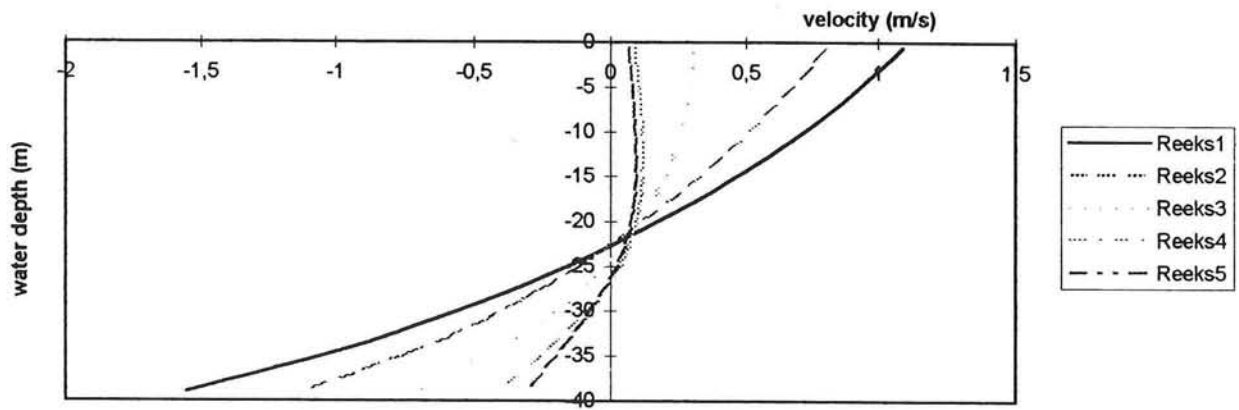
comparison of radial velocities for different radii at the 16th grid point at $\phi=3,75$



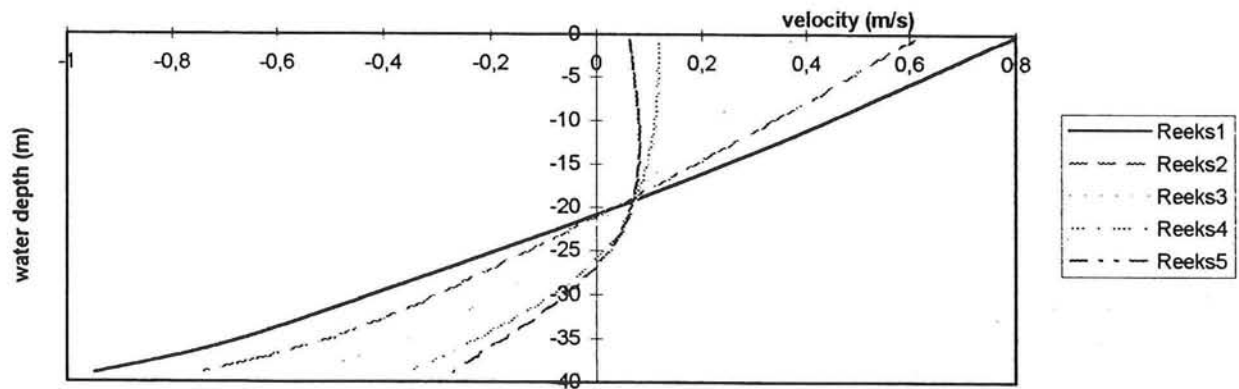
comparison of radial velocities for different radii at the 6th grid point at $\phi=90$



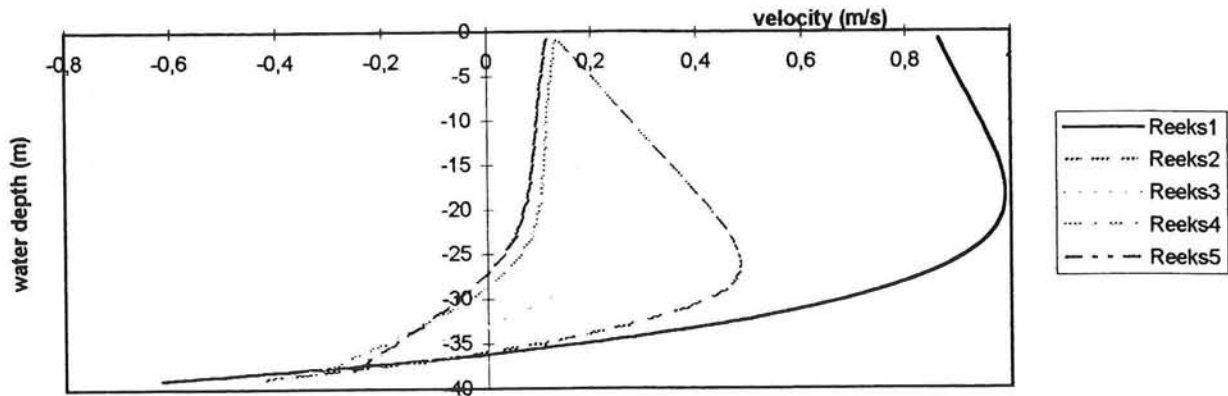
comparison of radial velocities for different radii in the middle of the cross-section at $\phi=90$



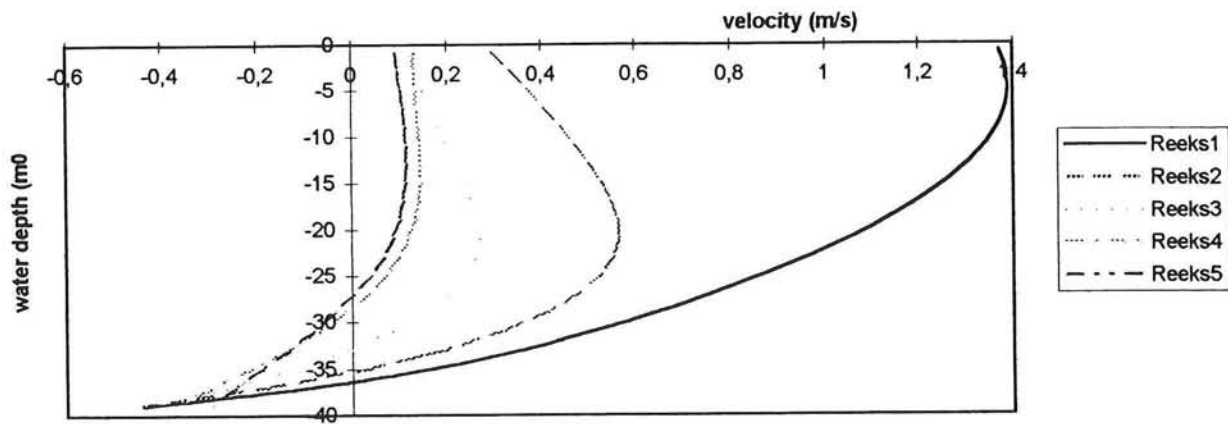
comparison of radial velocities for different radii at the 16th grid point at $\phi=90$



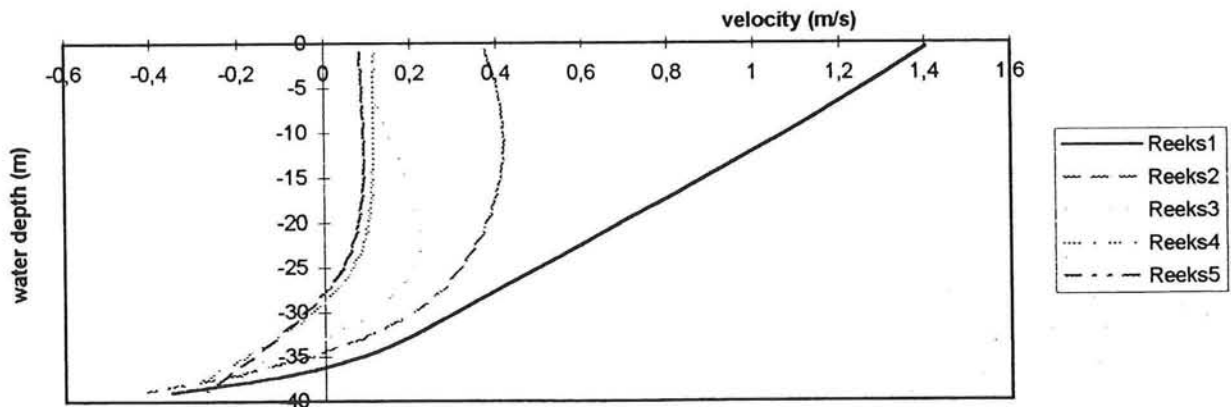
comparison of radial velocities for different radii at the 6 th grid point at $\phi=177,25$



comparison of radial velocities for different radii in the middle of the cross-section at $\phi=177,25$



comparison of radial velocities for different radii at the 16th grid point at $\phi=177,25$



Appendix XV

These figures show the influence of the inlet flow velocity in the simulation of the strongly curved bend.

The velocities are adimensional (they are shown as predicted velocity divided by the average inlet flow velocity)

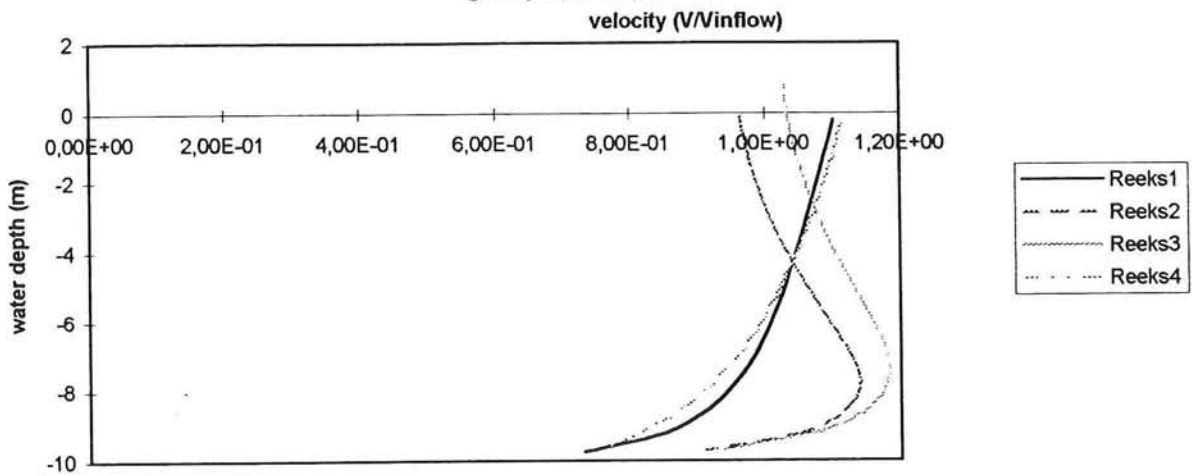
reeks 1 0,5 m/s

reeks 2 1,0 m/s

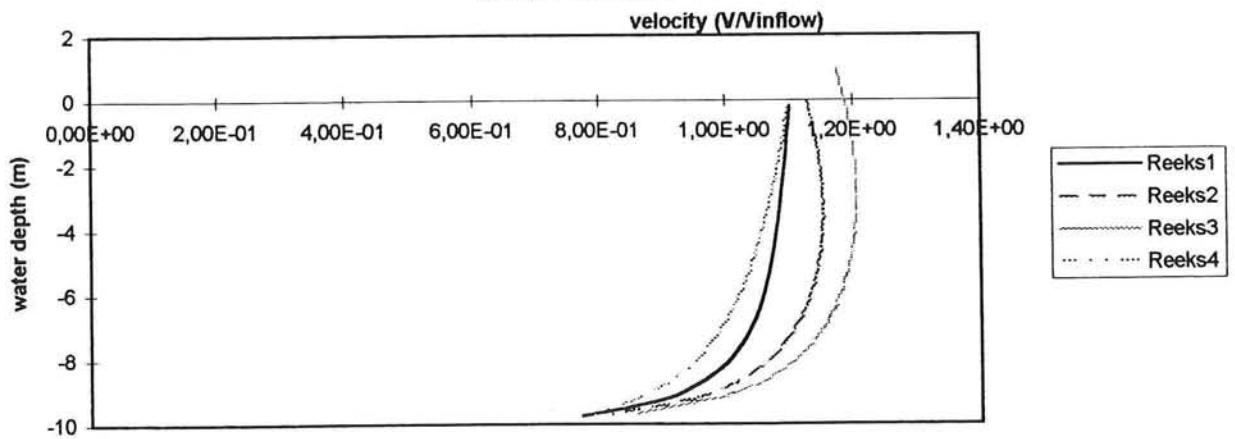
reeks 3 2,0 m/s

reeks 4 4,0 m/s

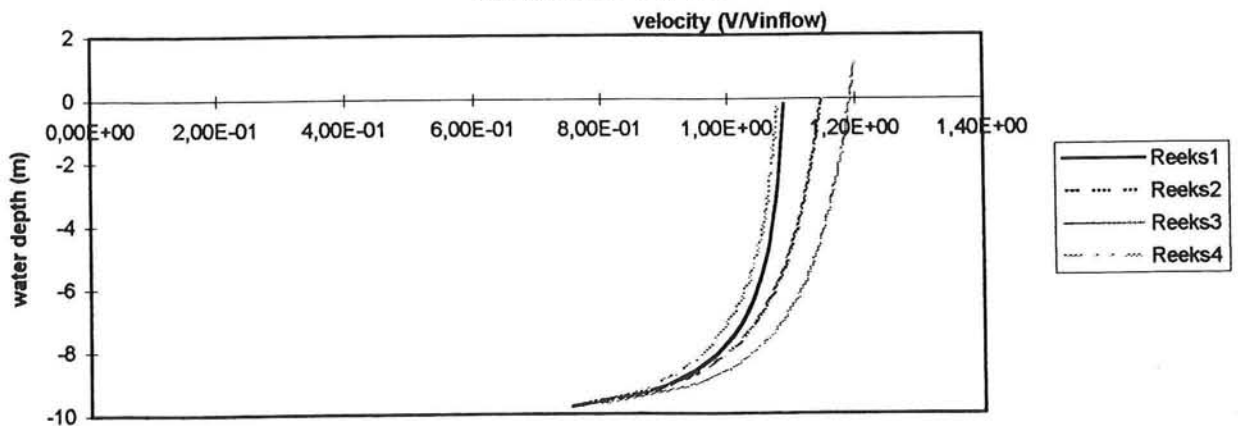
comparison of longitudinal velocities for different inflow velocities at the 3rd grid point at $\phi=90$



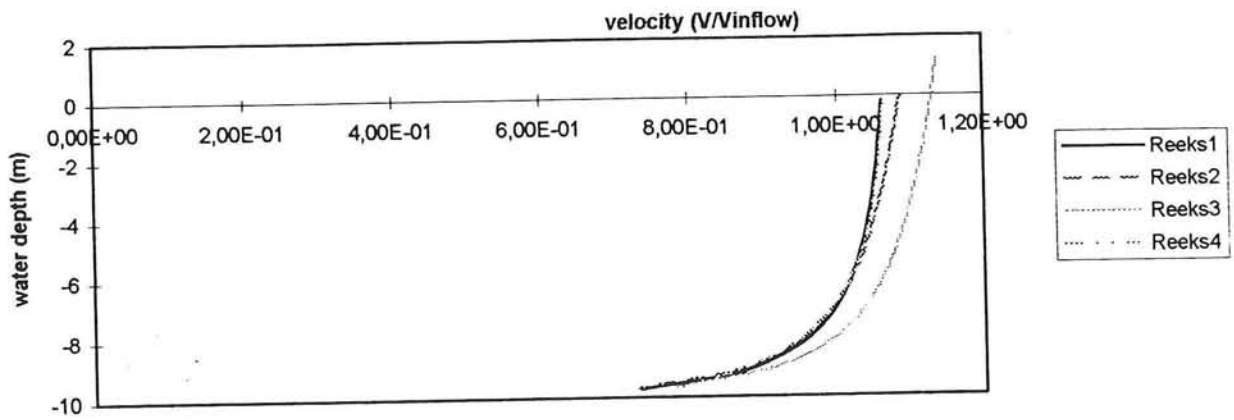
comparison of longitudinal velocities for different inflow velocities at the 6th gridpoint at $\phi=90$



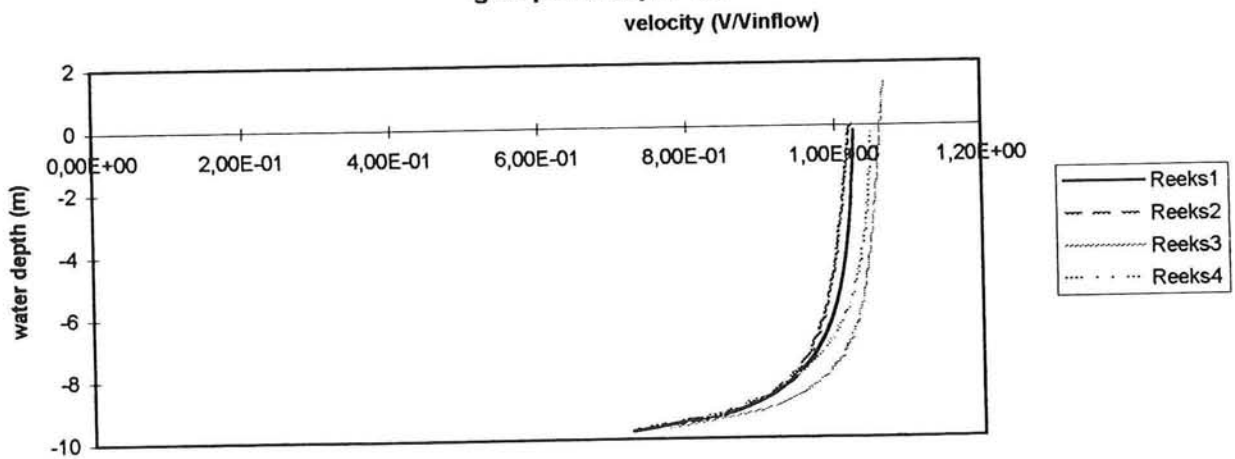
comparison of longitudinal velocities for different inflow velocities at the 10th gridpoint at $\phi=90$



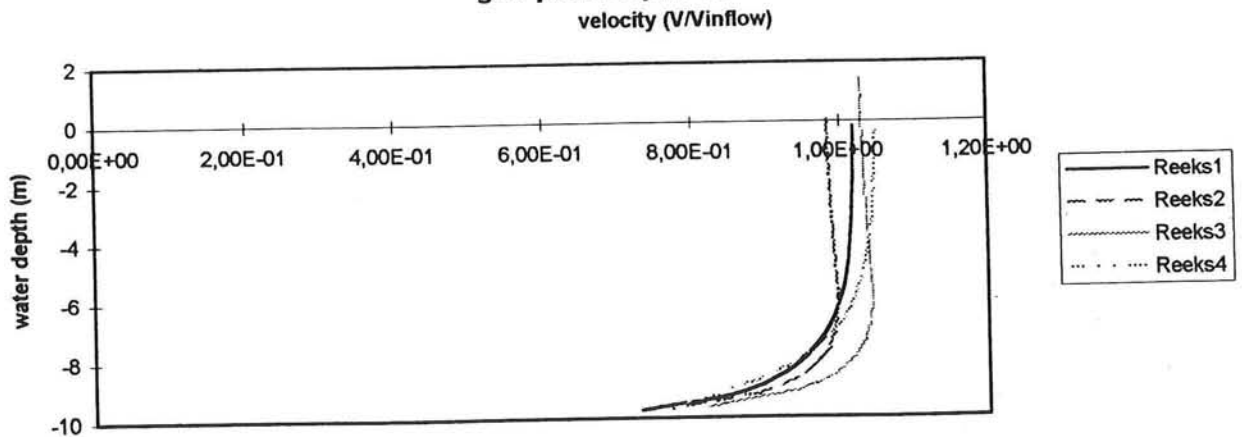
comparison of longitudinal velocities for different inflow velocities at the 13th grid point at $\phi=90$



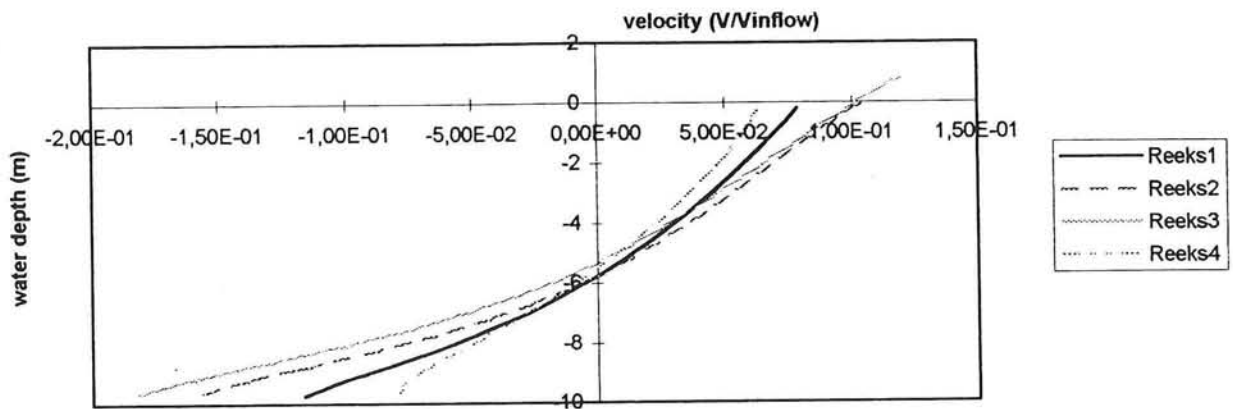
comparison of longitudinal velocities for different inflow velocities at the 17th grid point at $\phi=90$



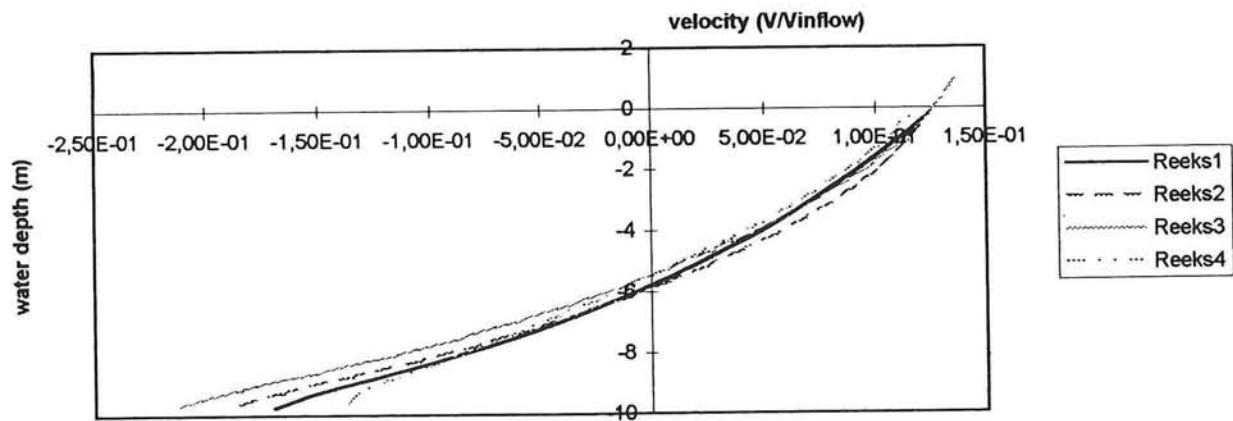
comparison of longitudinal velocities for different inflow velocities at the 20th grid point at $\phi=90$



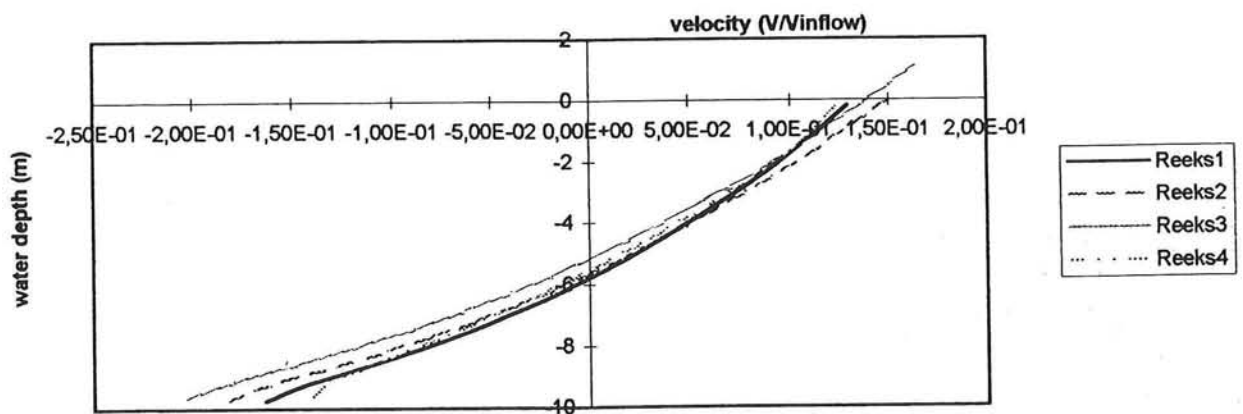
comparison of radial velocities for different inflow velocities at the 3rd grid point at $\phi=90$



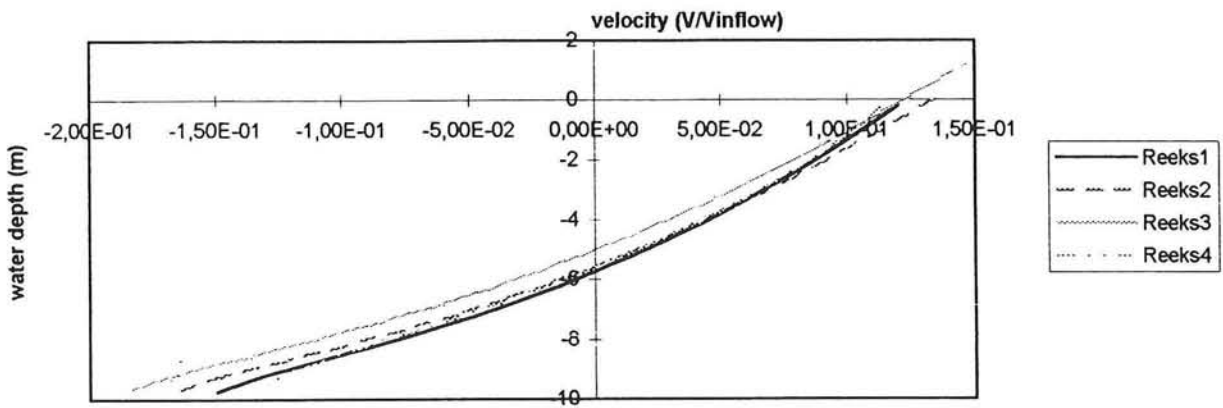
comparison of radial velocities for different inflow velocities at the 6th grid point at $\phi=90$



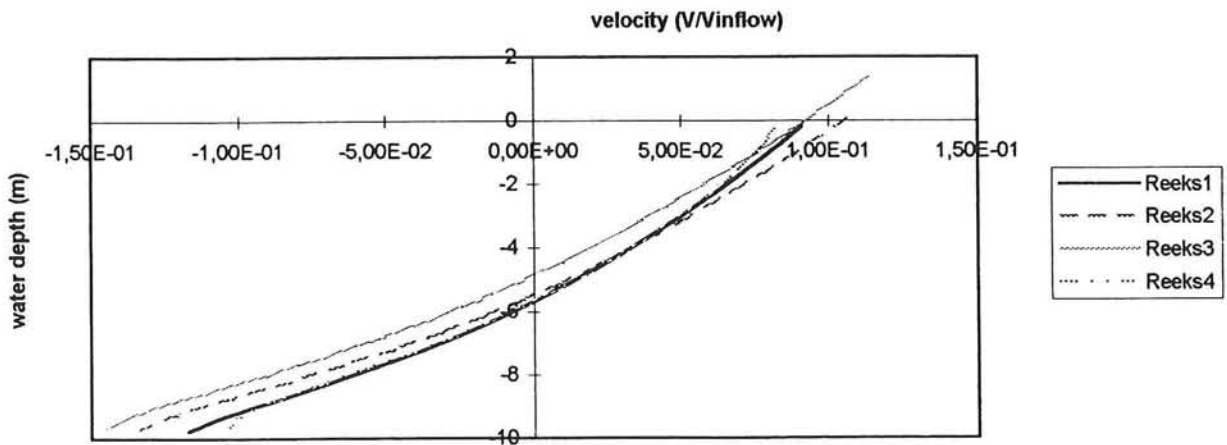
comparison of radial velocities for different inflow velocities at the 10th grid point at $\phi=90$



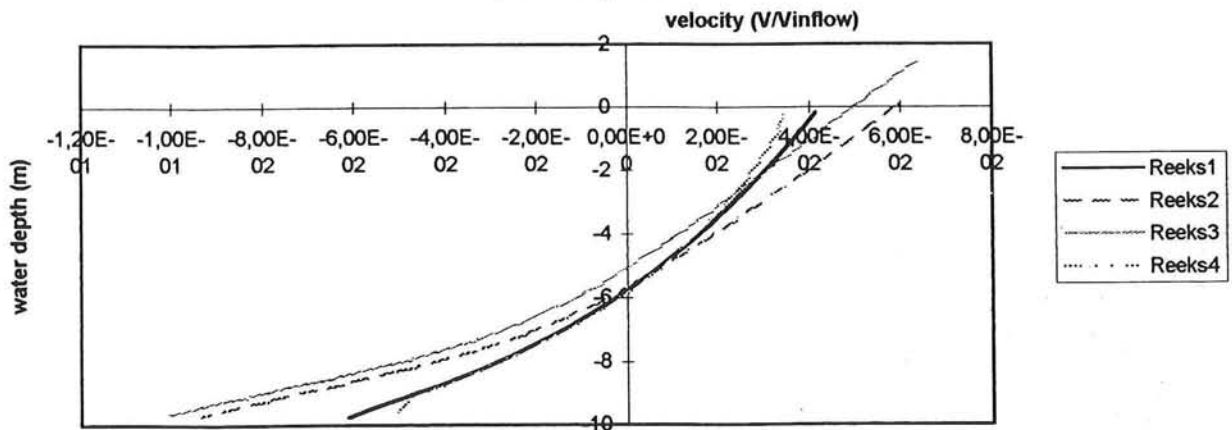
comparison of radial velocities for different inflow velocities at the 13 th grid point at phi=90



comparison of radial velocities for different inflow velocities at the 17th grid point at phi=90



comparison of radial velocities for different inflow velocities at the 20th grid point at phi=90



Appendix XVI

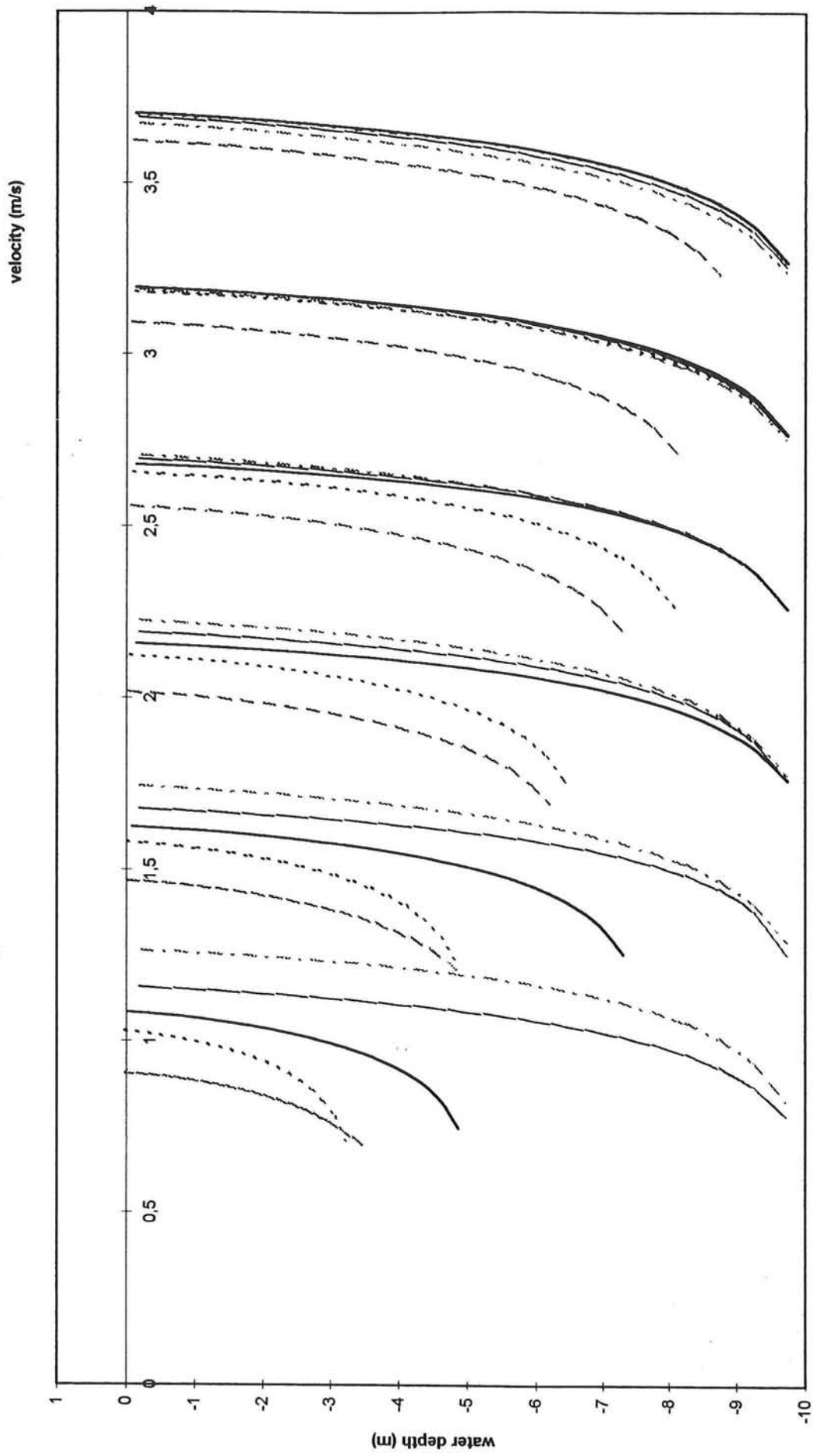
These figures show the influence of the cross-sectional profile in the simulation of the strongly curved bend.

The results of the velocity distributions are shown for every grid point in the radial direction and at three position; $3,75^\circ$ downstream of the entrance of the bend, halfway of the bend, $3,75^\circ$ upstream of the exit of the bend.

- rectangular cross-section
- channel profile with side walls 1:1 and a plane bottom
- channel profile with side walls 1:2 and a plane bottom
- channel profile with side walls 1:3 and a plane bottom
- river profile with a parabolic cross-section in the straight parts and a gradually changing profile, with steep side walls and a large depth near the outer wall and a smoothly sloping side wall and a small depth near the inner wall, at the entrance of the bend.

N.B. All the velocity distributions have their own vertical axis. This vertical axis represent the main velocity (in case of the radial velocity distributions this main velocity is zero). The scale of the velocity is only shown for the first velocity distribution.

longitudinal velocities near the inner wall at $\phi=7,5$



Longitudinal velocities in the middle of the cross-section at $\phi=7,5$

